Functional Materials for Rechargeable Li Battery and Hydrogen Storage

by

Guang He

A thesis

presented to the University of Waterloo

in fulfillment of the

thesis requirement for the degree of

Doctor of Philosophy

in

Chemistry

Waterloo, Ontario, Canada, 2012

AUTHOR'S DECLARATION

I hereby declare that I am the sole author of this thesis.

This is a true copy of the thesis, including any required final revisions, as accepted by my examiners.

I understand that my thesis may be made electronically available to the public.

Abstract

The exploration of functional materials to store renewable, clean, and efficient energies for electric vehicles (EVs) has become one of the most popular topics in both material chemistry and electrochemistry. Rechargeable lithium batteries and fuel cells are considered as the most promising candidates, but they are both facing some challenges before the practical applications. For example, the low discharge capacity and energy density of the current lithium ion battery cannot provide EVs expected drive range to compete with internal combustion engined vehicles. As for fuel cells, the rapid and safe storage of H_2 gas is one of the main obstacles hindering its application. In this thesis, novel mesoporous/nano functional materials that served as cathodes for lithium sulfur battery and lithium ion battery were studied. Ternary lithium transition metal nitrides were also synthesized and examined as potential on-board hydrogen storage materials for EVs.

Highly ordered mesoporous carbon (BMC-1) was prepared via the evaporation-induced self-assembly strategy, using soluble phenolic resin and Tetraethoxysilane (TEOS) as precursors and triblock copolymer $(\text{ethylene oxide})_{106}(\text{propylene oxide})_{70}(\text{ethylene oxide})_{106}$ (F127) as the template. This carbon features a unique bimodal structure (2.0 nm and 5.6 nm), coupled with high specific area (2300 m^2/g) and large pore volume (2.0 cm^3/g). The BMC-1/S nanocomposites derived from this carbon with different sulfur content exhibit high reversible discharge capacities. For example, the initial capacity of the cathode with 50 wt% of sulfur was 995 mAh/g and remains at 550 mAh/g after 100 cycles at a high current density of 1670 mA/g (1C). The good performance of the BMC-1C/S cathodes is attributed to the bimodal structure of the carbon, and the large number of small mesopores that interconnect the isolated

cylindrical pores (large pores). This unique structure facilitates the transfer of polysulfide anions and lithium ions through the large pores. Therefore, high capacity was obtained even at very high current rates. Small mesopores created during the preparation served as containers and confined polysulfide species at the cathode. The cycling stability was further improved by incorporating a small amount of porous silica additive in the cathodes.

The main disadvantage of the BMC-1 framework is that it is difficult to incorporate more than 60 wt% sulfur in the BMC-1/S cathodes due to the micron-sized particles of the carbon. Two approaches were employed to solve this problem. First, the pore volume of the BMC-1 was enlarged by using pore expanders. Second, the particle size of BMC-1 was reduced by using a hard template of silica. Both of these two methods had significant influence on improving the performance of the carbon/sulfur cathodes, especially the latter. The obtained spherical BMC-1 nanoparticles (S-BMC) with uniform particle size of 300 nm exhibited one of the highest inner pore volumes for mesoporous carbon nanoparticles of 2.32 cm^3/g and also one of the highest surface areas of 2445 m^2/g with a bimodal pore size distribution of large and small mesopores of 6 nm and 3.1 nm. As much as 70 wt% sulfur was incorporated into the S-BMC/S nanocomposites. The corresponding electrodes showed a high initial discharge capacity up to 1200 mAh/g and 730 mAh/g after 100 cycles at a high current rate 1C (1675 mA/g). The stability of the cells could be further improved by either removal of the sulfur on the external surface of spherical particles or functionalization of the C/S composites via a simple TEOS induced SiO_x coating process. In addition, the F-BMC/S cathodes prepared with mesoporous carbon nanofibers displayed similar performance as the S-BMC/S. These results indicate the importance of particle size control of mesoporous carbons on electrochemical properties of the Li-S cells.

By employing the order mesoporous C/SiO_2 framework, Li_2CoSiO_4/C nanocomposites were synthesized via a facile hydrothermal method. The morphology and particle size of the composites could be tailored by simply adjusting the concentrations of the base LiOH. By increasing the ratio of $LiOH:SiO_2:CoCl_2$ in the precursors, the particle size decreased at first and then went up. When the molar ratio is equal to 8:1:1, uniform spheres with a mean diameter of 300-400 nm were obtained, among which hollow and core shell structures were observed. The primary reaction mechanism was discussed, where the higher concentration of OH^- favored the formation of Li_2SiO_3 but hindered the subsequent conversion to Li_2CoSiO_4. According to the elemental maps and TGA of the Li_2CoSiO_4/C, approximately 2 wt% of nanoscale carbon was distributed on/in the Li_2CoSiO_4, due to the collapse of the highly ordered porous structure of MCS. These carbons played a significant role in improving the electrochemical performance of the electrode. Without any ball-mill or carbon wiring treatments, the Li_2CoSiO_4/C-8 exhibited an initial discharge capacity of 162 mAh/g, much higher than that of the sample synthesized with fume silica under similar conditions and a subsequent hand-mixing of Ketjen black.

Finally, lithium transition metal nitrides Li_7VN_4 and Li_7MnN_4 were prepared by high temperature solid-state reactions. These two compounds were attempted as candidates for hydrogen storage both by density functional theory (DFT) calculations and experiments. The results show that Li_7VN_4 did not absorb hydrogen under our experimental conditions, and Li_7MnN_4 was observed to absorb 7 hydrogen atoms through the formation of LiH, Mn_4N, and ammonia gas. While these results for Li_7VN_4 and Li_7MnN_4 differ in detail, they are in overall qualitative agreement with our theoretical work, which strongly suggests that both compounds are unlikely to form quaternary hydrides.

Acknowledgements

I would like to thank all people who have helped me during the past four and half years, especially my supervisor Prof. Linda F. Nazar. She contributed many brilliant ideas to my projects and assisted to resolve problems in research throughout my doctoral study. Without her, I would have been lost in the research works, and her erudition and enthusiasm will inspire me to continue the exploration of the nature of chemistry.

I thank my research committee members, Prof. Holger Kleinke, Prof. Pavle Radovanovic and Prof. Kathryn Preuss for their advice during my study. I would also like to thank Prof. Prouzet for his kind help in understanding mesoporous materials, and Dr. Neil Coombs at Univeristy of Toronto for the TEM works.

I also thank all of my collaborators: Dr. Jan F. Herbst at General Motor, Prof. Thomas Bein and Dr. Jörg Schuster at University of Munich.

I am grateful to our current and former group members: Dr. David, Ji, Dr. Ramesh, Brian Ellis, SiHyoung Oh, Rajesh Tripathi, Scott Evers, Kaitlin Town, Taeeun Yim, Antony Han, Jack Kan and many other lab members.

Finally, I wish to thank my wife and my parents. Their consistent support behind me is the primary motivation that encouraged me to finish the doctoral study!

Table of Contents

List of Figures

List of Tables

Glossary

AAO	Anodic alumina oxide
ACs	Activated carbons
BET	Brunauer-Emmett-Teller
BSE	Backscattered electrons
CNTs	Carbon nanotubes
CPSM	Colloidal phase separation mechanism
DFT	Density functional theory
DMC	Dimethyl carbonate
DME	1,2-Dimethoxy ethane
DOE	Department of Energy
DOL	1,3-Dioxolane
DSC	Differential scanning calorimetry
EC	Ethylene carbonate
EDAX/EDX/EDS	Energy dispersive X-ray analysis
EISA	Evaporation induced self-assembly
EO	Ethylene oxide
F127	$(\text{Ethylene oxide})_{106}(\text{propylene oxide})_{70}(\text{ethylene oxide})_{106}$
FFT	Fast fourier transform
FWHM	Full width at half maximum intensity
HRSEM	High resolution scanning electron microscopy
IUPAC	International Union of Pure and Applied Chemistry
LIB	Lithium ion battery

LiTFSI	Bis-(trifluoromethane)sulfonimide lithium
MCF	Mesostructured cellular foam
MMA	Methy methacrylate
MOF	Metal-organic framework
NiMH	Ni-metal hydride battery
NLDFT	Non localized density functional theory
NMP	N-Methyl-2-pyrrolidone
OCV	Open circuit voltage
OMC	Ordered mesoporous carbon
P123	$(\text{Ethylene oxide})_{20}(\text{propylene oxide})_{70}(\text{ethylene oxide})_{20}$
PEDOT	Poly(3,4-ethylenedioxythiophene)
PEG	Polyethylene glycol
PEMFC	Polymer electrolyte membrane fuel cell
PEO	Poly(ethylene oxide)
PF	Phloroglucinol/formaldehyde
PI-*b*-PEO	Poly(isoprene)-*block*-poly(ethylene oxide)
PMMA	Poly(methyl methacrylate)
PPO	Poly(propylene oxide)
PS-P4VP	Polystyrene-*block*-poly(4-vinylpyridine)
PVDF	Poly(vinylidene fluoride)
PXRD	Powder X-ray diffraction
RF	Resorcinol/formaldehyde
RGA	Residual gas analysis
SDS	Sodium dodecyl sulfate
SE	Secondary electrons

SEI	Solid electrolyte interface
SEM	Scanning electron microscopy
SiNW	Silicon nanowire
SLI	Starting, lighting and igniting
STEM	Scanning transmission electron microscope
TEM	Transmission electron microscopy
TEOS	Tetraethoxysilane
TGA	Thermal gravimetric analysis
THF	Tetrahydrofuran
TIPB	1,3,5-Triisopropylbenzene
TMB	1,3,5-Trimethylbenzene
VASP	Vienna ab initio simulation package

Chapter 1

Introduction

1.1 Rechargeable Lithium Batteries

1.1.1 History of rechargeable batteries

Nowadays, there is a large demand for clean, efficient and renewable energy for automotive transportation due to the limitations of the fossil fuel petroleum.[1] First of all, petroleum represents a non-renewable primary energy source which is experiencing rapid depletion. Secondly, the unfettered consumption of petroleum releases greenhouse gas CO_2 when it is burned. Along with the burning of coal, petroleum combustion is the largest contribution to the increase in atmospheric CO_2.

An alternative option to power vehicles is electrical energy which can be generated from many renewable energy sources such as wind or solar. Because these are intermittent, however, the energy must be stored in order for renewables to become part of a viable energy solution. The most convenient form to store electrical energy, especially for automotive transportation, is rechargeable batteries. A rechargeable battery is a device that converts chemical energy to electrical energy during discharge, and stores electrical energy via the reverse process during charge. Leading the first generation of these devices was the lead-acid battery, invented in 1859 by Gaston Planté, a French scientist. In spite of its low energy density (only 40 Wh/kg or 80 Wh/l), the good rate capability coupled with a low-cost make lead-acid very attractive in the auto industry. For example, most of the vehicles in the world use lead-acid batteries for

starting, lighting and igniting (SLI). The open circuit voltage (OCV) of a lead-acid cell is ~2.0 V, based on the following "bulk" electrode reactions:

$$positive: \quad PbSO_4 + 2H_2O \leftrightarrow PbO_2 + 4H^+ + SO_4^{2-} + 2e^- \tag{1-1}$$

$$negative: \quad PbSO_4 + 2e^- \leftrightarrow Pb + SO_4^{2-} \tag{1-2}$$

Another type of rechargeable battery-nickel cadmium (NiCd) battery, was developed by Waldemar Jungner in Sweden in 1899 but in the 1960s, the nickel-hydride (NiMH) battery was proposed to replace it owing to the toxicity of Cd. The electrochemical reactions are as follows, which also take place "in the bulk":

$$positive: \quad Ni(OH)_2 + OH^- \leftrightarrow NiO(OH) + 2H_2O + e^- \tag{1-3}$$

$$negative: \quad M + H_2O + e^- \leftrightarrow MH + OH^- \tag{1-4}$$

In the 1990s, the NiMH battery was considered to be the most advanced battery for portable electronic devices due to its higher energy density (75 Wh/kg or 200 Wh/l), and it is still widely used in hybrid vehicles such as the Toyota Prius which was released in 1997. However, despite great success, NiMH battery is not a suitable energy storage system for plug-in vehicles. First of all, its gravimetric energy density is still too low for all-electric plug-in vehicles. In addition, this type of battery suffers self-discharge which can account for losses as much as 10% in the first day after charging - a significant waste. Owing to the development of lithium ion battery, NiMH battery was gradually squeezed out of the portable device market after 2000.

The rechargeable lithium-ion battery (LIB) was first commercialized by Sony in 1990, although pioneering studies had been carried out as early as in 1970s by Whittingham and

Goodenough.[2,3] Most of their contributions focused on the development of cathode materials for LIB. The breakthrough on anode materials of LIB was much behind the cathode materials. In 1990, both Sony and Moli announced the commercialization of LIB based on petroleum coke as the anode. In the same year, Dahn and co-workers published their work on the principle of lithium intercalation chemistry with graphitic anodes.[4,5] The discovery of graphite as the anode brought the real commercialization of LIB. Since then, LIB has experienced an explosive growth in the next two decades and dominated most of the portable electronic device market, primarily due to the superior high gravimetric energy density (at least twice higher than NiMH) and long cycle life. Unlike the Pb-acid and Ni-MH batteries that work on the basis of "bulk" electrode reactions, Li-ion batteries work on the basis of intercalation chemistry, as discussed in the next section.

1.1.2 Overview of basic concepts in rechargeable batteries

For any rechargeable battery, the discharge is the conversion from chemical energy to electrical energy, and the charge is the reverse process. The amount of energy converted is determined by the difference of the chemical potentials between the positive and negative electrodes, which also determines the cell potential:

$$\mu_p - \mu_n = \Delta G = n*F*E \quad (1\text{-}5)$$

Here, μ_p, μ_n and are chemical potentials of the positive and negative electrodes, their difference ΔG is equal to the Gibbs free energy when the electrode reactions proceed in equilibrium; n is the number of electrons transferred in the reaction; F is the Faraday constant; and E is the cell potential.

During discharge, the negative electrode is oxidized and electrons flow through the external circuit to the positive electrode, where electrons are released to the active materials of the electrode via the reduction process. Thus, a positive electrode is also called a cathode and a negative electrode is called an anode. It should be noted that this designation is only correct in discharge process because the reverse reactions take place at the electrodes during charging, and consequently the positive electrode becomes the anode and the negative electrode becomes the cathode of the cell. However, the positive electrodes are usually called cathodes in the literature without clarification. In the thesis, this rule is followed and the term "cathodes" is used to describe the positive electrodes.

The amount of charge (Q) stored per unit mass (always denoted as mAh/g) is called the specific gravimetric capacity. If the capacity is valued volumetrically, it is usually denoted as mAh/cm^3 or mAh/l. Correspondingly, the specific energy density of a cell (Wh/g or Wh/l) can be evaluated by considering capacity (Q) times its cell voltage (V), as $W = Q*V$. Another important concept is the rate capability, which denotes the ability of a cell to charge and discharge at different current rates (or current density). Cyclability, or cycle life of a cell indicates the stability of the cell on cycling.

1.1.3 Rechargeable Li-ion battery

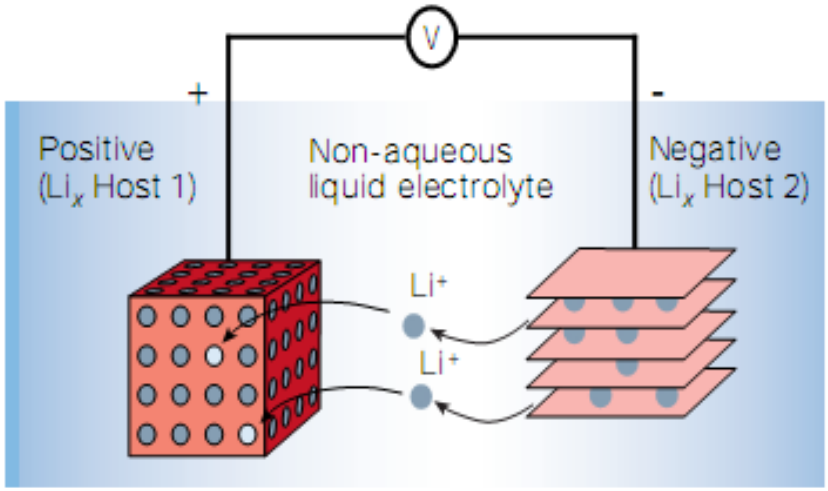

Figure 1.1 Schematic representation and operating principles of rechargeable Li-ion batteries.[6]

The reaction mechanism of lithium-ion batteries is illustrated in Figure 1.1. A single cell consists of a positive electrode (cathode), a negative electrode (anode) and non-aqueous electrolyte. The insertion of lithium ions at either cathode or anode is called an intercalation reaction, and the reverse process is called deintercalation. The typical electrode reactions of a LIB are as follows (considering $LiCoO_2$ as the cathode and graphite as the anode):

$$positive:\ LiCoO_2 \leftrightarrow Li_{1-x}CoO_2 + xLi^+ + xe^- \quad (1\text{-}6)$$

$$negative:\quad C + xe^- + xLi^+ \leftrightarrow Li_xC \quad (1\text{-}7)$$

1.1.3.1 Cathodes of Li-ion batteries

In the early stages, studies of the cathode materials of lithium ion battery primarily focused on layered-structure compounds such as $LiCoO_2$, $LiNiO_2$ and $LiMnO_2$.[7] $LiCoO_2$ was first

recognized as a cathode material by Goodenough in 1980.[3] It exhibits the α-$NaFeO_2$ structure with the oxygen in a cubic close-packed arrangement, where lithium is able to be reversibly inserted and extracted. The theoretical capacity of the cathode is ~270 mAh/g ($LiCoO_2 \leftrightarrow CoO_2$), and the average cell voltage is ~3.7 V (graphite as the anode). However, the commercialized cell has only a little more than half of the theoretical capacity because only ~0.7 Li can be reversibly cycled. On complete extraction of the lithium from the structure, the oxygen layers rearrange themselves to give hexagonal close packing of the oxygen in CoO_2.[8,9] The phase change slows down the intercalation/deintercalation rate of Li and leads to cathode instability. In recent years, many groups have made great efforts to improve the capacity of the $LiCoO_2$-based electrodes and some positive results have been achieved.[10,11,12]

$LiNiO_2$ is isostructural with $LiCoO_2$, but excess nickel atoms existing in the lithium layer impede the transportation of lithium ions.[13] Therefore, the composition of this compound is always given as $Li_{1-x}Ni_{1+x}O_2$. Layered $LiMnO_2$ with the same *R*-3*m* structure is very difficult to prepare directly, although it can be obtained by ion-exchange from $NaMnO_2$. It is not electrochemically stable and finally transforms to the spinel-structured $LiMn_2O_4$ on cycling.[14]

In addition to the single metal element compounds discussed above, substitutions with one or more other metals were also extensively investigated, such as $LiCo_xNi_{1-x}O_2$,[15,16] $LiCo_xMn_{1-x}O_2$[17,18,19] and $LiCo_xNi_{1-x-y}Mn_yO_2$.[20,21,22] Currently, lithium ion batteries based on these "NMC" cathodes dominate the portable electronics market and they are also being explored for automotive applications. The Tesla Motor company, for example, uses thousands of small-scale cells comprised of NMC cathodes for their battery packs, although the cells are spaced apart for safety concerns. Ultimately that issue may limit their application as a large-scale energy system for electric vehicles, but it is too soon to tell.[23,24,25] One alternative to layered

structure cathodes is the spinel $LiMn_2O_4$ because manganese is relatively an low-cost and environmentally benign element. Another advantage of $LiMn_2O_4$ is the chemically stable Mn (III)/Mn (IV) redox couple, which offers an operating voltage of 4.1 V. However, this material is plagued by capacity fading owing to Jahn-Teller distortion of Mn (III) under a deep discharge state.[26] Even so, its moderate capacity (130 mAh/g), high voltage and facile Li ion mobility make it one of the most promising candidates as a first-generation cathode material for automotive applications.[24]

Alternatives to lithium metal oxides have been investigated, including "polyanion" materials. The most well-known polyanion-based cathode material is the olivine $LiFePO_4$, first reported by Goodenough and his colleagues in 1997.[27] Several advantages make this material very attractive. First, it has a high discharge capacity (170 mAh/g) and relatively high cell voltage (3.5 V). Second, iron is a low-cost and abundant element on the earth. Third, it exhibits extraordinary cyclability, as there is no fading over many hundred cycles. Furthermore, compared with lithium metal oxide compounds, the safety issue is significantly improved due to the incorporation of the phosphate group. The disadvantage of $LiFePO_4$ is its low electronic conductivity, along with one dimensional Li-ion transport.[28] In principal, there are two strategies to solve the conductivity problem: (1) reduce the dimension of the particle size and (2) modify the surface of the particles. A good example of the former is the synthesis of uniform $LiFePO_4$ nanocrystallites with a mean particle size of ~40 nm via a low temperature precipitation method by Masquelier *et al.*[29] As for the surface modification, the most commonly employed strategy is coating conductive layers on $LiFePO_4$.[30] For example, a carbon-double-coated configuration of $LiFePO_4$/C exhibited 97% of the maximum theoretical capacity (161 mAh/g) at a current of 1C (defined as (de) intercalation of one lithium in one

hour) at 60 ℃. Similar results were also achieved by coating of conductive polymers such as poly(3,4-ethylenedioxythiophene) (PEDOT).[31] Moreover, our group found that the formation of metallic iron phosphides (FeP/Fe_2P) at the grain boundary of the $LiFePO_4$ nanocrystallites also improves the conductivity of the cathode.[32]

The great success in $LiFePO_4$ greatly inspired researchers to explore other types of polyanion cathode materials. One direction is the replacement of iron with other transition metals like Mn[33] and Co.[34] $LiMnPO_4$ and $LiCoPO_4$ also have the olivine structure, but they both suffer some serious problems (i.e. extremely low electronic conductivity or too high a cell voltage for most of the current LIB electrolytes).

Another direction to develop new polyanion-based cathode materials refers to the substitution of the anion P with Si and S. Since the first report of Li_2FeSiO_4 in 2005,[35] the new Li_2MSiO_4 silicate class of cathode materials (M = Fe, Mn and Co) has been drawing increasingly more attention. Compared with phosphate based compounds like $LiFePO_4$, the key feature of the Li_2MSiO_4 system is the possibility of extracting two lithium ions from the framework (M^{2+}-M^{3+}-M^{4+}), to achieve a theoretical capacity above 300 mAh/g.[36] Additionally, Si is one of the most abundant elements in the earth's crust and is widely distributed, making the relatively low price of silicates very commercially attractive. However, the electrical conductivity of the silicate family is extremely low. Previously reported conductivity values for Li_2FeSiO_4 and Li_2MnSiO_4 are 10^{-12} S/m and 10^{-14} S/m, respectively,[37,38] several orders of magnitude lower than for comparable phosphate-type cathode materials. The intrinsically low conductivity greatly impedes the extraction of lithium from the compounds. For example, early reports of Li_2FeSiO_4 indicated a reversible discharge capacity of ~160 mAh/g (equal to ~1.0 Li), but at an elevated temperature of 60 ℃ and a low current density of 16/C.[35] Similarly,

only 0.5 Li per formula unit of Li_2MnSiO_4 could be reversibly extracted according to the original experimental results.[39] As for Li_2CoSiO_4, the electrochemical activity of the pristine material is almost negligible.[40]

Various attempts have been made on improving the performance of silicate cathodes, among which carbon coating, or "wiring" is the most effective strategy to enhance the electronic conductivity of electrodes, as demonstrated for $LiFePO_4$. Another approach is the reduction of particle size of cathode materials to facilitate the migration of lithium ions in the structure. Muraliganth and co-workers prepared nanostructured Li_2FeSiO_4 and Li_2MnSiO_4 via a facile microwave-solvothermal method, and the carbon coating was achieved by a subsequent pyrolysis of sucrose on the silicates at 650 ℃ (Figure 1.2).[41] The Li_2MnSiO_4/C electrodes showed a high initial capacity of ~250 (equal to 1.5 Li) mAh/g at elevated temperature 55 ℃, but it faded to less than 50 mAh/g in 20 cycles, probably due to Jahn-Teller distortion as observed in other Mn containing electrode materials.[42] The Li_2FeSiO_4/C composite demonstrated a stable reversible capacity of above 200 mAh/g up to 20 cycles under similar conditions, indicating that more than one lithium could be extracted. Similar results were also obtained by Yang's group, where Li_2FeSiO_4/C synthesized via a solution-polymerization method displayed an initial discharge capacity of 220 mAh/g when cycled at a high cut-off potential of 4.8 V.[43] Most recently, nanoleaflets of Li_2FeSiO_4 and Li_2MnSiO_4 have been observed to undergo almost full two electron extraction-insertion.[44,45] However, the oxidation of Fe (II) to Fe (IV) is believed to be very difficult, and therefore, more investigation is necessary on this material to support these exciting results. If they are confirmed, the silicate material will be a good competitor amongst polyanion based cathodes.

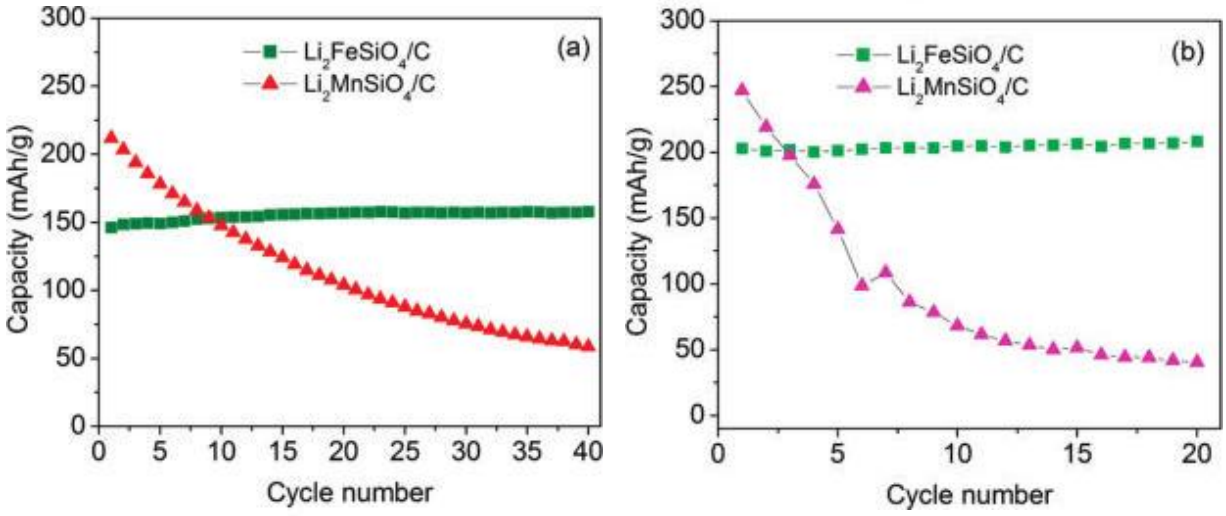

Figure 1.2 Electrochemical behavior of Li_2FeSiO_4/C and Li_2MnSiO_4/C at (a) 25 ℃ and (b) 55 ℃ at a current rate of C/20.[41]

Very recently, another type of polyanion cathode-lithium iron fluorosulfate $LiFeSO_4F$ was reported by Tarascon.[46,47] It has a voltage 3.6-3.9 V, depending on the structure, and moderate capacity ~120 mAh/g (80% of the theoretical capacity).

In summary, cathode materials developed on the basis of intercalation chemistry have dominated most of the rechargeable lithium battery market since the 1990s. Nonetheless, all these materials have some intrinsic limitations in terms of gravimetric energy density, which are derived from their redox mechanism of operation and structural aspects.[48] New systems with higher energy gravimetric and volumetric density are necessary to offer electric vehicles the long drive range to compete with combustion engine vehicles.

1.1.3.2 Anodes of Li-ion battery

Initially, metallic lithium was considered an ideal anode material of Li-ion battery because of its low standard electrode potential (-3.04 V) and high theoretical capacity (3860 mAh/g). However, it was later found that lithium dendrites grew on the anode upon continuous cycling. These needlelike crystals may pierce the separator and result in an internal short circuit, thermal runaway and even explosion.[4]

Since 1980s, the reversible intercalation of lithium ions into carbonaceous materials like graphite was gradually realized.[49] Graphite has a theoretical capacity of 372 mAh/g and an average potential of ~0.1 V versus lithium metal, based on the formation of LiC_6. Upon the first charge, a solid electrolyte interface (SEI) layer results on the surface of the graphite anode. Thanks to this passivation and protection layer, a graphite anode is stable up to many hundreds of cycles.[50] Other carbonaceous materials, like fullerenes,[51] carbon nanotubes (CNTs),[52] mesoporous carbons[53] and graphenes,[54] have also been studied as anodes of lithium ion batteries. However, despite offering much higher capacities than graphite, they suffer various problems and none have been commercialized so far.

Around 2000, nanoparticles of transition metal oxides were first reported as anode materials.[55] Unlike graphite which stores lithium ions via intercalation reactions, this class of anodes relies on reversible conversion reactions:[56]

$$2yLi + M_xO_y \leftrightarrow yLi_2O + xM \quad (1\text{-}8)$$

The potential of these reactions versus Li is ~0.9 V, slightly higher than for graphite. However, most of the M_xO_y anodes exhibit high capacity, as well as acceptable cyclability.[57] The success in metal oxides expanded the frontier of anode materials and since then, various binary

and ternary nano compounds like nitrides[58,59] and phosphides[60,61] have been developed as candidates of anode materials.

Lithium alloy anodes belong to another class of important anode materials, where lithium ions can form various alloys with many metals and semiconductors.[62] The most interesting examples are the Li-Sn[63,64] and Li-Si[65,66] systems, especially the latter which has a theoretical capacity 4212 mAh/g (4.4Li + Si↔$Li_{4.4}Si$, but $Li_{4.4}Si$ may not be an alloy any more), even higher than metallic lithium as the anode. In order to achieve this extraordinary high capacity, there are two obstacles to overcome. First, more than 300% expansion of the Si anode was detected during lithiation,[67] although it depends on the depth of discharge. The high volumetric expansion causes electrode pulverization and lithium trapping in the active material upon cycling. Consequently, active material is gradually consumed due to continual electrolyte exposure during expansion and contraction of the anodes.[68] The other problem is the low electronic conductivity of the Si anode. The pulverization of the electrode makes it more serious. The solution of the above problems is the dispersion of nanosized silicon on a carbon matrix. Jaephil Cho and Yi Cui reported on the use of various carbon matrixes such as carbon nanoparticles,[69] porous carbons,[70] carbon nanofibres,[71,72] and carbon nanoshells.[73] These matrixes provide enough space for Si expansion on cycling, and the electronic conductivity is significantly improved as well. More recently, C/Si granules were prepared by using carbon black as the matrix and silane as the silicon precursor. The facile synthetic route, combined with its highly reversible capacity, good rate capability, and much improved coulombic efficiency of the granular C/Si composite makes it very competitive among the various next generation of anode materials.[74] It is suggested that certain additive extracted from natural

organisms like brown algae seems also to help in preventing the volume changes during electrochemical alloying and de-alloying with lithium.[75]

1.1.4 Rechargeable Li-S batteries

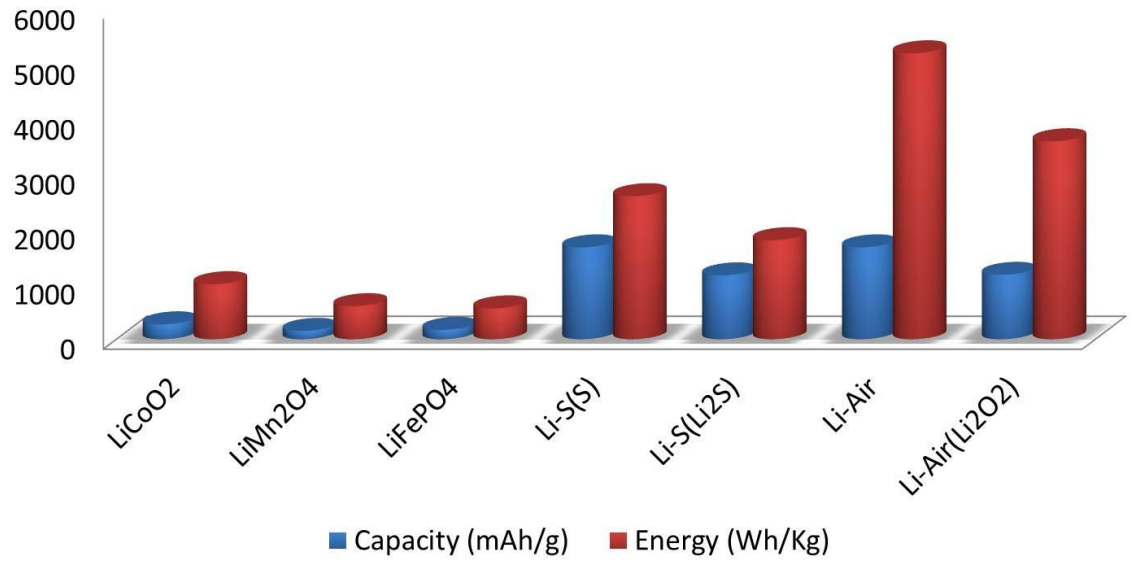

Figure 1.3 Theoretical capacity and energy density of various cathode materials of rechargeable lithium batteries.

After 20-year development of lithium ion batteries, lithium intercalation-based cathode materials have approached the theoretical energy density limit, and breakthroughs will probably come from the redox conversion reaction-based materials, similar to the evolution of anode materials from graphite to metal oxides and lithium alloys. Currently, two types of redox conversion cathodes, Li-S[76] and Li-Oxygen,[77] have drawn much attention and are considered to be the most promising cathodes for future-generation rechargeable lithium batteries. They both have much higher theoretical capacities and energy densities than lithium

ion batteries (Figure 1.3), but they also both face significant challenges in order to realize practical devices. Relatively speaking, Li-S is a more mature technology than Li-oxygen, since a number of fundamental problems are still not solved for the latter.[78]

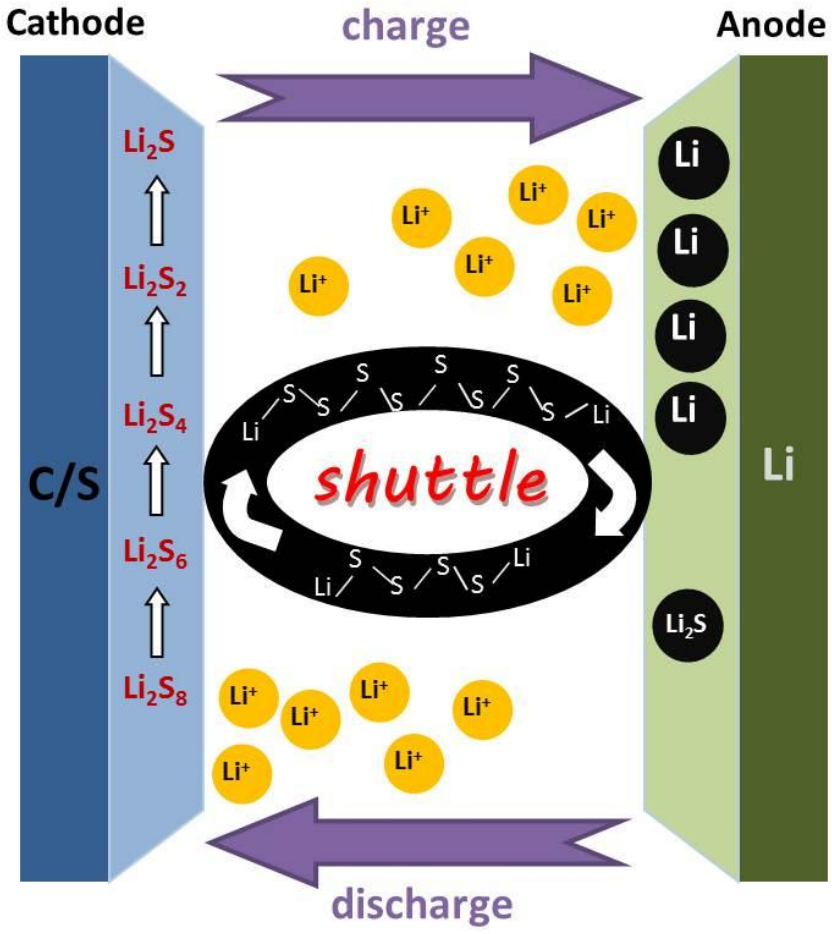

Figure 1.4 Schematic representation of a typical rechargeable Li-S cell.

A typical rechargeable Li-S cell consists of a sulfur cathode, a metallic or alloy lithium anode, non-aqueous electrolyte and a separator. The redox reactions at both electrodes can be illustrated in Figure 1.4. At the cathode, elemental sulfur S_8 is readily reduced to a series of intermediate lithium polysulfides (Li_2S_n) upon discharge. Most of these species are soluble in

the organic electrolytes except Li_2S_2 and Li_2S. Simultaneously, lithium is oxidized at the anode and lithium ions diffuse through the separator to the cathode to balance the negative charges. The overall reaction is written as:

$$S_8 + 16Li \leftrightarrow 8Li_2S \quad (1\text{-}9)$$

1.1.4.1 Cathodes of Li-S batteries

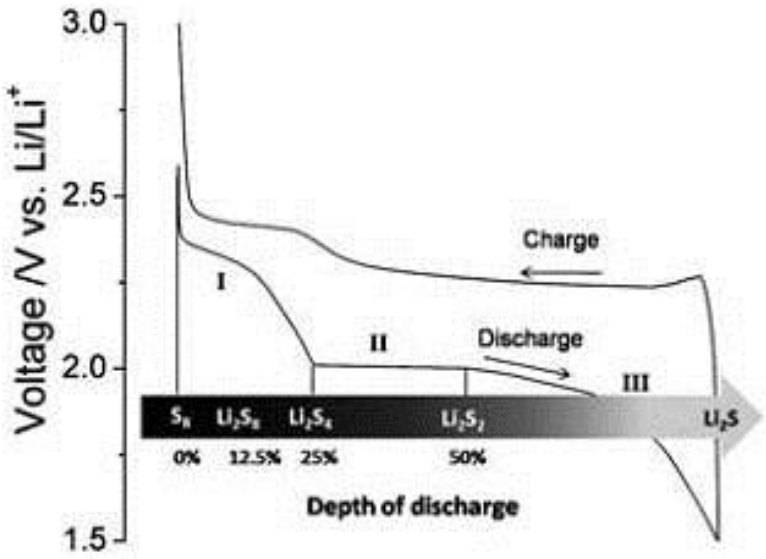

Figure 1.5 Typical discharge-charge profiles of a rechargeable sulfur cathode.[74]

In contrast to the insertion cathodes in lithium ion batteries, energy is electrochemically stored in the sulfur cathode via the reversible conversion between S and Li_2S. Figure 1.5 displays a typical discharge-charge profile of a sulfur cathode. Two discharge plateaus are identified at ~2.3 V and 2.0 V. The first one is attributed to the gradual reduction of molecular S_8 to polysulfide S^{4-} ions. At this stage, a complicated equilibrium exists among many soluble polysulfide intermediates such as S_8^{2-}, S_6^{2-} and S_4^{2-}. Further reduction of these long-chain polysulfide species produces non-soluble Li_2S_2, corresponding to the lower plateau at ~2.0 V.

The last step ($Li_2S_2 \rightarrow Li_2S$) is the most difficult because it is impeded by sluggishness of solid-state diffusion in the bulk.[74] In addition, the insoluble Li_2S/Li_2S_2 precipitates and forms an insulating layer on the cathode with prolonged cycles, which causes electrochemically inaccessibility and loss of active materials.[79]

During charge, the voltage increases rapidly to above 2.2 V at the initial stage of charging and then rises slowly until ~2.4 V. Finally, the curve ends with a sharp voltage raise. Two plateaus are present in the charge curve, indicating the formation of Li_2S_n ($n>2$) and elemental sulfur, respectively. It is worthy to note that the two charge plateaus usually merge into a continuous one (especially when the cells are run at high current rates), since the voltage difference is very small between them. Correspondingly, only one oxidation peak appeared at ~2.35 V in cyclic voltammograms of sulfur cells for a long-time in the past.[80] Very recently, the other peak associated with the higher plateau was observed at 2.45 V.[81]

There are several remarkable advantages making sulfur a promising cathode material for the next generation of lithium batteries:

1. It exhibits much higher theoretical energy density (2600 mAh/kg and 2800 Wh/l), assuming a complete conversion from elemental sulfur to Li_2S;[82]
2. It is non-toxic and environmentally benign;
3. The cells are fundamentally low cost.

However, despite these advantages, Li-S cells face some challenges. The first one is the low electronic conductivity of both sulfur and its final discharge product Li_2S. The difference in electronic conductivity between sulfur and $LiCoO_2$ is more than 15 orders of magnitude.[83,84] Moreover, sulfur is also a good ionic insulator. Therefore, sulfur cathodes have traditionally suffered from low discharge capacity and efficiency. For example, the sulfur cathodes

prepared by physical mixing of sulfur and carbon black exhibited an initial capacity of less than 500 mAh/g, which corresponds to about a quarter of the theoretical capacity.[85]

A further issue is the "polysulfide shuttle phenomenon" that is a problem for most Li-S cells.[86,87,88,] As discussed above, the long chain polysulfide ions S_n^{2-} formed in the cathode during discharge are soluble in the electrolyte. Due to the concentration gradient between cathode and anode, they diffuse through the separator to the anode, where they are reduced to insoluble Li_2S_2 or Li_2S. Once the lithium anode is fully coated, the diffused S_n^{2-} reacts with these reduced sulfides to form lower order polysulfides (S_{n-x}^{2-}) that become concentrated at the anode, then diffuse back to the cathode and are re-oxidized to S_n^{2-}, as shown in Figure 1.6. The above shuttle process takes place repeatedly, causing a decrease of active material at the cathode, capacity fading, inactivation of the anode, and self-discharge of the cell.[89 , 90] Mathematical modeling has been established to understand the shuttle phenomenon, as well as a complete Li-S cell. In these studies, polysulfide shuttles and other electrochemical properties of a cell, such as charge/discharge process and capacity, overcharge protection, self-discharge, multicomponent transport phenomena in the electrolyte and the charge transfer within and between solid and liquid phases, are quantitatively described.[91,92]

On realizing these problems, various optimizations of Li-S cells have been carried out. The anode and electrolyte parts will be discussed in the next sections separately and here the discussion is focussed on the progress on cathodes. The most common strategy is mixing of sulfur and carbon to improve the conductivity of the cathode. For example, various attempts have been made to fabricate C/S composites using carbon black,[83] activated carbons (ACs)[93] and carbon nanotubes (CNTs)[94,95]. Although some improvements resulted, the cathodes still suffered from inhomogeneous contact between the active materials and the electronic

conductors, due to the intrinsic small surface of these carbonaceous materials. In order to immobilize polysulfides in the cathodes, chemical sorption methods were studied. Some metal oxides like $Mg_{0.6}Ni_{0.4}O$[96] and Al_2O_3[97] as additives in the cathodes were proven to be helpful, especially when they are on the nanoscale. Addition of $LiNO_3$ in the electrolyte was also found to play a critical role on the formation of protection layer on a lithium anode. This layer prevents the corrosion of anodes by polysulfides.[98] Another approach to immobilize polysulfides relies on the formation of sulfur-polymer composites, which was developed by Wang and co-workers, along with many others. The coulombic efficiency could be greatly enhanced by using polyacrylonitrile-sulfur conductive composite as the cathodes, but a large capacity fade still existed on cycling.[99,100] Following studies showed that the stability of this kind of cathode was remarkably improved for those composites synthesized above 400 ℃, which was attributed to the unique structure of the dehydropyridine type matrix with S-S bond in side-chain[101] formed at elevated temperatures.

A major step forward in fabricating a uniform C/S composite was reported in 2009 by our lab. We employed CMK-3, an ordered mesoporous carbon (OMC) featuring high specific surface area and large pore volume as a scaffold.[102] As much as 70 wt% sulfur was incorporated into the uniform 3-4 nm mesopores (Figure 1.6a), and the cells exhibited discharge capacities up to 1000 mAh/g at moderate rates and the conductive polymer polyethylene glycol (PEG) modified cell even showed a capacity 1350 mAh/g and more than 1000 mAh/g was retained after 20 cycles (Figure 1.6b). Subsequently, our lab found mesoporous silicas such as SBA-15 is an excellent polysulfide adsorbent which acts to trap them at the cathodes, retain capacity and improve coulombic efficiency.[103]

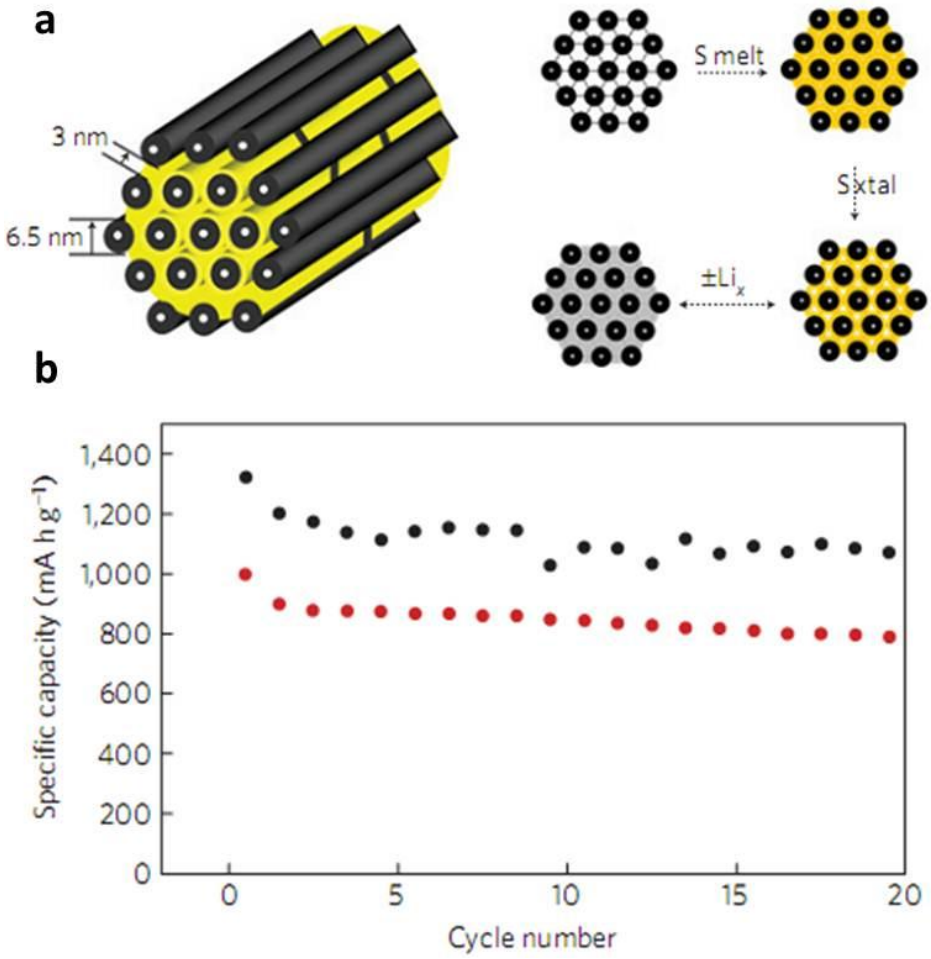

Figure 1.6 (a) Schematic representation of the CMK-3/S nanocomposite and (b) its electrochemical performance.[102]

These exciting results greatly boosted the enthusiasm of researchers on exploring other carbonaceous porous materials with high surface area and large pore volume sulfur cathode frameworks. Archer et al. reported sulfur infused nanoscale hollow porous carbon spheres prepared via an elaborate vapour-infusion method.[79] Despite the relatively poor rate capability of the cathodes, they displayed a remarkable cyclability and good capacity, further illustrating the advantages of nano-sized porous carbon in the sulfur cathodes. Cui and co-workers investigated graphene-wrapped sulfur composites as cathodes and claimed a stable capacity up

to 600 mAh/g over 100 cycles.[104] In addition, 1-D and 3-D hollow carbon arrays were also prepared by hard template methods and employed as sulfur matrixes.[105,106,107] Very recently, some non-carbonaceous porous materials like metal-organic framework (MOF) [108] and polypyrrole[109]/polythiophene[110] were also suggested to reduce the polysulfide shuttle.

The influence of frameworks on the performance of sulfur cathodes varies depending on the specific porous architecture. In principal, smaller pores (< 3 nm) are believed to have a better polysulfide retention effect. For example, sulfur/microporous carbon composites exhibit more stable capacity than other sulfur/mesoporous composites.[111,112] However, the mobility of lithium ions in microporous pores is restricted, too. Therefore, the rate capability is always sacrificed when a microporous C/S configuration is established. Conversely, ultra large-pore carbons favor rapid diffusion of lithium ions, but the large size pores give rise to extensive dissolution of intermediate polysulfide species formed on charge and discharge cycles into the electrolyte.[113] Indeed, finding proper ways to achieve practical high "C" rate (>1500 mA/g current density) cells in a sulfur system without the attendant problem of low capacity and capacity fading, is a big challenge, in addition to the conductivity and shuttle problems. High rates are possible for catholyte-type sulfur cells where all the redox active species are in solution; but such cells have low volumetric capacities and require negative electrode passivation.[114] In contrast, sulfur contained-cathode cells have an estimated theoretical volumetric capacity of up to 1300 Wh/l respectively for a full cell, assuming a 30% inactive carbon content, and a residual porosity within the cathode of 10% for the electrolyte.

Recently, a promising activated mesoporous carbon with a bimodal structure achieved by KOH activation, was reported by Liang et al.[115] The sulfur cathodes prepared with this carbon show a large retainable capacity at a high discharge current rate, which was attributed to the

creation of small mesopores. In spite of the low energy density of the cathode (less than 12 wt% sulfur in the carbon for the material with the best performance), this work shows that the existence of the small pores (<3 nm) is a key factor for polysulfide retention while the large pores aid in high rate charge/discharge. Therefore, the application of bimodal structured carbon is a new and promising approach for lithium sulfur batteries. Optimization of the porous structure, taking into consideration pore size, surface area and pore volume, is still necessary to realize high-performance Li-S cathodes, however. Such efforts to tailor nanostructures have shown very promising results with mesoporous intercalation oxides[116] - and it is as, if not more - important in this case.

1.1.4.2 Anodes of Li-S batteries

Because of the special configuration of Li-S cells (no lithium ion available at the cathode), the anode has to serve as a Li source that provides sufficient lithium ions for the redox reactions. Thus, many lithium-free anode materials used in lithium ion batteries such as graphite, metal oxides and alloys are not suitable. Metallic lithium is always the first choice of an anode material in a Li-S cell. However, safety issue caused by the formation of dendrites on lithium metal on cycles is a key issue as discussed above.

Cui developed prelithiated silicon nanowire (SiNW) by a self-discharge method for lithium-free cathodes.[117] Through a time-dependent study, 20 min of prelithiation loaded ~50% of the full capacity into the SiNWs and the nanostructure was maintained by SEM and TEM. These lithiated SiNWs showed a high capacity of ~1000 mAh/g in a full cell with sulfur/CMK-3 as the cathode, but faded to 500 mAh/g in 20 cycles. The authors proposed three possible reasons to explain the fast capacity fading: (1) limited Li source in a full cell, (2) loss of Li the electrodes due to the dissolution of polysulfides in the electrolyte and (3) failure in voltage

control of the cathode or anode. Instead of prelithating the anode, Cui also studied the prelithation of the sulfur cathode by using n-butyllithium.[118] The full cell, composed of Li_2S/CMK-3 as the cathode and SiNWs as the anode was evaluated. Again, fast fading resulted.

Attempts of assembling Li_2S cathodes like Li_2S/M (M = Fe, Co and Cu) to provide metallic lithium anode-free cells were also made by other groups.[119,120,121] The transition metals served both as conducting agents and Li_2S decomposition catalysts at the cathodes, but the cathodes still suffered from low conductivity and dissolution of polysulfide species during cycling.

The above examples indicate the importance of sulfur cathodes in Li-S cells. Because the major problems of Li-S battery are caused by the cathodes like low conductivity and polysulfide shuttle, without solving these issues first, the development of new anode material alone cannot improve the performance of a full Li-S cell.

1.1.4.3 Electrolytes of Li-S batteries

Electrolyte plays significant roles in the performance of Li-S batteries because solid-liquid and liquid-solid transitions of active materials occur during redox reactions in the electrodes. Moreover, the polysulfide shuttle phenomenon also originates from the facile dissolution of polysulfides into the electrolytes as many organic solvents such as dimethylsulfoxide, sulfones, sulfolanes, cyclic acetals or ethers like tetrahydrofuran (THF) and glymes provide Li_2S_n exceeding several M/L. Some glymes, sulfone or sulfolane type solvents exhibit higher viscosity. This is good for polysulfide retention in the cathodes, but a high capacity is only attained at rates substantially below 1C by using these solvents. Mikhaylik suggested to use a mixture of low viscosity 1,3-dioxolane (DOL) and 1,2-dimethoxy ethane (DME).[122] These solvents provide a compromise between several factors like sulfur utilization, rate capability and lithium anode cycle-ability. Specifically, DOL has lower polysulfide solubility and

kinetics, but forms a more stable solid electrolyte interface (SEI) on the metallic lithium surface and has one order of magnitude higher conductivity than do THF:toluene-rich electrolytes.[85] DME, on the other hand, is more reactive with lithium, but higher polysulfides solubility makes for good kinetic behavior for cathode operation.[120] Similar results on the sulfur cathodes were obtained by Wang *et al*. with $LiClO_4$ as the salt and DOL/DME as the solvents.[123] They found too high content of DME in electrolytes could raise the interfacial resistance of battery due to the impermeable layer formed on the surface of sulfur cathodes, which led to bad cycling performance, while the increase of DOL could partially solve this problem. The optimal composition of electrolyte, through their experiments, is DME:DOL = 2:1 (v/v).

Ionic liquids were found to have low polysulfide solubility, but the Li-S cells fabricated with them as electrolyte still suffered rapid capacity fading within only 20 cycles.[124,125] This is probably due to the gradual precipitation of Li_2S on the surface of the cathodes, which prevents the access of electrolyte to the active material.

Scrosati and co-workers assembled solid-state configuration Li-S cells with polymer gel $PEO_{20}LiCF_3SO_3Li_2S$+10 mass% ZrO as the membrane electrolyte and separator, Li_2S/C as the cathode and Sn/C as the anode. The membrane also served as an envelope with liquid electrolyte trapped inside.[126] The cell operated at 60 ℃ had a reversible capacity of ~1000 mAh/g in terms of Li_2S at a current rate of C/20. Overcharge still occurred because the release of the electrolyte in the liquid zone could not be totally excluded. Subsequently, this group fabricated all-solid-state of Li-S cells by using only polymer gel as the electrolyte, Li_2S/C and the cathode and metallic lithium as the anode.[127,128] At 70 ℃, the cell had an initial discharge capacity of ~ 550 mAh/g in terms of Li_2S at a very low current density of 30 mA/g (~C/40).

By increasing the current density to 120 mA/g (~C/10), the initial capacity dropped to only ~160 mAh/g. More recently, glass-ceramic electrolytes such as Li_2S-P_2S_5 were studied by Nagao for sulfur batteries.[129] The cell performance was highly dependent on the mixing conditions of the electrolyte and the sulfur/carbon electrode. At room temperature, a ball-mixed sulfur/carbon/electrolyte exhibited an initial capacity of 1550 mAh/g (92.5% of the theoretical capacity) at a current rate of 0.064 mA/cm^2, and ~1400 mAh/g was retained after 10 cycles with almost 100% coulombic efficiency. However, unlike the liquid Li-S systems, the two discharge plateaus merged together, which was probably associated with the special glass-ceramic electrolyte.

1.2 Hydrogen Storage

Utilization of hydrogen energy is very attractive because hydrogen is abundant on earth and environmentally benign. Currently, there are two approaches to use hydrogen energy: (1) in Ni-metal hydride batteries (NiMH) and (2) in fuel cells, especially in the polymer electrolyte membrane type fuel cells.

1.2.1 Hydrogen storage in Ni-metal hydride batteries (NiMH)

A brief review of NiMH batteries has been presented in section **1.1.1**. In a typical NiMH cell, hydride alloys serve as the anode (negative electrode) to store hydrogen electrochemically, by obtaining protons from water. A good hydrogen storage electrode alloy must satisfy the following criteria:[130,131] (1) high reversible hydrogen storage capacity, (2) inherent catalytic properties to enable hydrogen charge and discharge, (3) easy activation and excellent corrosion resistance in alkaline electrolyte, (4) operation under a suitable hydrogen equilibrium pressure,

(5) good charge/absorption and discharge/desorption kinetics for efficient operation and (6) long cycle life and low cost.

Commercialized hydrogen storage alloys basically meet all the above criteria. They usually consist of two or more elements: a strong hydride-forming element A and a weak hydriding element B that form alloys with intermediate thermodynamic affinities for hydrogen. Some well-known intermetallic compounds/alloys and their hydrogen storage gravimetric capacities are summarized in Table 1.1.[132]

Table 1.1 Intermetallic compounds and their hydrogen storage capacities.

Type	Alloy	Hydride	H mass%
AB_5	$LaNi_5$	$LaNi_5H_6$	1.37
AB_2	ZrV_2	$ZrV_2H_{5.5}$	3.01
AB	FeTi	$FeTiH_2$	1.89
A_2B	Mg_2Ni	Mg_2NiH_4	3.59

Due to the presence of heavy rare-earth/transition metals, most alloys have very low gravimetric hydrogen storage capacities. For example, $LaNi_5$, the most commonly used anode material of NiMH batteries, can form a hydride $LaNi_5H_6$, accounting for 1.7 mass% of hydrogen content, which is 372 mAh/g if converted to electrochemical capacity. The practical capacity is only 80% (~300 mAh/g) of this theoretical capacity, and the cell voltage of NiMH batteries is 1.2 V, about 1/3 of that of typical lithium ion batteries. Therefore, the energy density of a NiMH battery is lower with respect to a lithium ion battery. However, safety is not

an issue for NiMH batteries because the electrolyte is aqueous, and alloys are also very stable even in the charged state under high impact.

1.2.2 On-board hydrogen storage

Compared with electrochemical hydrogen storage in NiMH batteries, the storage of H_2 gas has drawn much more attention owing to the rapid development of polymer electrolyte membrane fuel cells (PEMFC). The basic principle of H_2 storage is similar to electrochemical hydrogen storage and all the alloys listed in Table 1.1 are capable of absorbing H_2 because of their strong affinity with H_2 molecules. H_2 molecules are split into atoms at the surface of the metal and then enter the metallic lattice in their atomic form, and diffuse through the metal via interstitial sites to form a hydride phase with a more or less ordered hydrogen sub-lattice. The hydrogen *s* electron can be partly donated to the metal conduction band if the metallic lattice contains *d* or *f* electron states at the Fermi level. Hence, these bare protons can move relatively freely through the metal lattice due to the electrostatic force screened by electrons at the metal Fermi surface. In the desorption process, the opposite takes place; *i.e.*, hydrogen atoms diffuse out from the alloy lattice and recombine to form H_2 again.

The target set by the US Department of Energy (DOE) for on-board hydrogen storage in 2015 is a gravimetric capacity of 5.5 wt% H_2 by the storage system to fulfill a long driving range of the PEMFCs. None of the intermetallic alloys comprised of rare-earth metals in Table 1.1 meet this requirement. Currently, most of the attempts focus on the complex hydrides which consist of light elements such as $NaAlH_4$,[133,134] $LiBH_4$[135,136] and $LiNH_2$-LiH[137]. These compounds have very high hydrogen capacities, but they all suffer thermodynamic or kinetic challenges to desorb hydrogen from the structure. For example, $LiNH_2$-LiH is a well-known and highly promising system that was first developed by Chen in 2002.[138] Up to 11.4 wt %

hydrogen could be released according to the equation: $LiNH_2 + 2LiH \leftrightarrow Li_2NH + LiH + H_2 \leftrightarrow Li_3N + 2H_2$. However, the storage capacity of the 2nd step can only be achieved at a temperature of 400 ℃, much higher than the operating temperature range of PEMFC vehicles. This reaction temperature can be decreased, to some extent, by incorporating other light elements such as Mg,[139] B[140] and Al[141] into this system, but still cannot meet the criteria of the PEMFCs. Recently, it was found the addition of KH remarkably improved the reaction kinetics of the $Mg(NH_2)_2$-LiH system by forming K-N-containing intermediates.[142] Reversible hydrogen release and uptake were achieved at a temperature as low as 107 ℃ in a few hours. Other potassium salts like KOH, KF or K_2CO_3 showed a similar effect.

Another example of hydrogen storage by a complex hydride is ammonia borane (AB, NH_3BH_3) and its derivatives, which has one of the highest achievable hydrogen densities of 19.6 wt%. AB releases hydrogen through 3 steps: $NH_3BH_3 \rightarrow NH_2BH_2 \rightarrow NHBH \rightarrow BN$ at 120 ℃, 145 ℃ and above 500 ℃.[143] By ball milling LiH and AB, lithium amidoborane ($LiNH_2BH_3$) is formed upon release of H_2. This compound has remarkably improved hydrogen-release performance: up to 11 wt% (2 equivalents of moles) of H_2 was released at ~92 ℃ in 19 h and no borazine was detected. Conversely, ball milled AB released only about 5.3 wt% under similar conditions, indicating that rapid near-room-temperature hydrogen release may be feasible if kinetic barriers can be overcome by catalytic modification.[144] Subsequent investigations showed the reaction of LiH and AB in THF released almost 3 equivalent moles of H_2 at very moderate temperatures of ~50 ℃.[143,145] Inspired by these exciting results, many other amidoboranes like $NaNH_2BH_3$,[146] $Ca(NH_2BH_3)_2$[147] and $Li(NH_2BH_3) \cdot NH_3BH_3$[148] were also developed. They all exhibited high hydrogen release ability at mild conditions. However, the dehydrogenation product cannot be re-hydrogenated directly

by pressurized hydrogen as other materials can. Hence, recycling of the AB type compounds is a big challenge.

Nanostructured hydrogen storage materials can significantly improve the reaction kinetics, reduce the enthalpy of formation and lower the hydrogen absorption and release temperatures through destabilization of the metal hydrides and multiple catalytic effects in the system. On the other hand, nanostructures can also lead to poor cyclability, degradation of the sorption properties, and a significant reduction of the thermal conductivity that could make metal hydrides impractical for hydrogen storage.[149] Additionally, if a scaffold like porous carbon or silica is employed for the hydrides, it should be chemically inert.[150] For example, mesoporous silica materials are unsuitable for nano-confinement of $LiBH_4$ due to the irreversible formation of lithium silicates (Li_2SiO_3 or Li_4SiO_4) upon dehydrogenation.[151, 152] Several types of nanostructured hydrogen storage materials such as $NaAlH_4$ nanoparticles,[153] nanoscaffold BH_3NH_3,[154, 155] and MgH_2/Mg[156, 157] nanocomposites have been reported, revealing the potential to solve thermodynamic or kinetic problems for bulk materials, but there is still a long way to go before practical application of these hydrides in fuel cell vehicles can be achieved.

1.3 Mesoporous Materials

1.3.1 Mesoporous silica

A mesoporous material is a material containing pores with diameters between 2 and 50 nm. One of the earliest reports of a tailor-designed mesoporous material dates back to 1992, when scientists at Mobil prepared a series of novel, mesoporous molecular sieves and named them MCM-41 (Mobil Composition of Matter).[158] MCM-41 was prepared by using cetyltrimethylammonium chloride as a cationic surfactant and tetramethylammonium silicate

solution as the silica resource. It exhibits a hexagonal structure, with high surface area (> 1000 m^2/g), large pore volume (0.8 cm^3/g) and narrow pore size distribution (2-3 nm). The structure could be switched to a cubic symmetry termed MCM-48 by simply adjusting the ratios of the surfactant and the silica precursors. [159] A liquid crystal templating reaction mechanism of both mesoporous silicas was proposed by the authors, although a more accurate cooperative self-assembly mechanism has been widely accepted nowadays (Figure 1.7).[160]

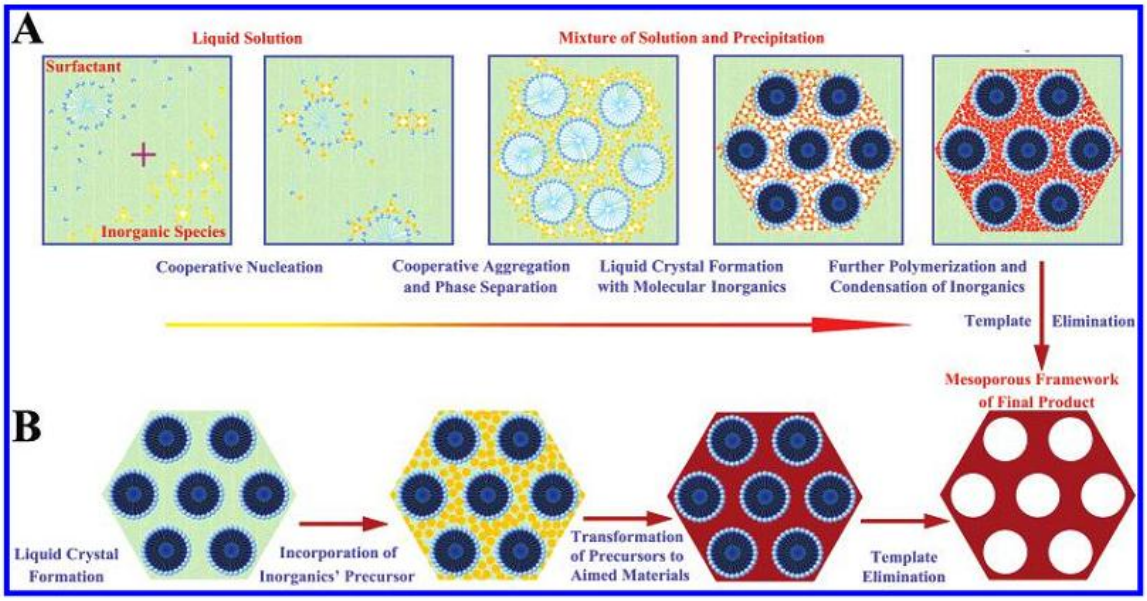

Figure 1.7 Schematic diagram of the two formation mechanisms of mesoporous materials: (a) cooperative self-assembly and (b) liquid-crystal templating process.[158]

The report of MCM-41 opened a new era of investigations on porous materials and in the following two decades, it has become one of the most popular topics in inorganic and material chemistry. Many intriguing mesoporous materials have been developed. However, silicas of the SBA-type, [161] MSU-type [162] and the KIT-type, [163] are still the most extensively studied materials. The three letter acronym refers to the institution where they were invented.

SBA-15, a well-known ordered mesoporous silica of the SBA family, was developed in 1998 at UC Santa Barbara by Stucky's group.[164] The mesostructure of SBA-15 was readily formed in acidic condition, using nonionic surfactant triblock copolymer poly(ethylene oxide)-poly(propylene oxide)-poly(ethylene oxide) (PEO-PPO-PEO) (P123) as the template. The general reaction process can be described as follows: an acidic P123 surfactant aqueous solution is first prepared; once the silicate precursor tetraethoxysilane (TEOS) is added to this solution, the hydrolysis of the TEOS is immediately catalyzed by the acid to produce a sol of silicate oligomers, which interacts with the surfactant micelles. Cooperative assembly and aggregation of the silicates result in precipitation from the sol. Subsequent reorganization further proceeds to form an ordered mesostructure. Hydrothermal treatment is then carried out to induce complete condensation and solidification, and improve the organization of the mesostructure. After the removal of the P123 template by pyrolysis, a well ordered hexagonal mesostructured silica is obtained. The porous structure is affected by various synthetic parameters such as reaction/hydrothermal temperature, chain length of the surfactant, and system pH. The silica synthesized under optimized conditions has a specific BET surface area of ~1000 m^2/g and pore volume of ~1.3 cm^3/g, with a mean pore size of 5 nm. Similar to the MCM type of silica, a cubic structure always results (i.e. SBA-6[165] and SBA-16[166]) by increasing the ratio of silica to surfactant in the precursors. This rule is found to be applicable to most of the preparation of mesoporous materials.

The pore size of SBA-15 silicas is tunable by the addition of pore expanders (or swelling agents) like 1,3,5-trimethylbenzene (TMB). For example, the pore size increases to 12 nm by adding some TMB during the synthesis of SBA-15. Further increase of TMB expands the pores to 30 nm, but leads to a phase transformation from an ordered *P*6*mm* mesostructure to a

meso-structured cellular foam (MCF) structure.[167] In 2005, a low-temperature pathway was reported by Zhao *et al*. to synthesize a highly ordered face-centered cubic mesoporous silica (*Fm3m*) with a large pore size up to 27 nm.[168] An alternative method is the use of surfactants with tailored hydrophobic/hydrophilic regions (ie "di and tri block" polymers) to enlarge the diameter of the micelles. For example, Wiesner and co-workers prepared large pore (>20 nm) ordered mesoporous silica using their lab-synthesized diblock copolymer poly(isoprene)-*block*-poly(ethylene oxide) (PI-*b*-PEO) as the template.[169]

Morphology tuning of mesoporous silicas can be realized via kinetic control, by varying the synthetic conditions. Mono-dispersed MCM-48 and MCM-41 nanospheres were obtained via a modification of Stöber's method,[170,171] with tunable particle size between 150-1200 nm.[172] Zhao *et al.* systematically studied the influence of various synthetic conditions such as temperature, stirring rate, ionic strength, acidity and reactant ratios on the morphology of SBA-15.[173] They found that low temperatures, low acidity and low ionic strength usually increased the induction time and gave rise to mesoporous silica morphologies with increased curvatures. Moreover, it was found stirring rate played an important role on morphology as well. For example, rod like SBA-15 silica is only obtained with vigorous stirring, which was explained by a colloidal phase separation mechanism (CPSM). Additionally, the average diameter of the rods can be reduced from 300-400 nm to ~100 nm just by diluting the precursor concentrations.[174]

Mesoporous silica with chiral channels and helical morphology was reported in 2004 by Che *et al*.[175] It has a very special structure, in which twisted and hexagonally shaped rods with 2D chiral channels run inside and parallel to the ridge edge (Figure 1.8). At first, this structure was believed to be the result of using a chiral anionic surfactant as the template. However, it

was later found that similar helical mesoporous silica could also form in the presence of other non-chiral surfactants like sodium dodecyl sulfate (SDS) and or CTAB.[176,177] An entropically driven model was proposed to explain the helical structure. Guided by this theory, a series of helical mesoporous silica materials have been successfully prepared.[178,179]

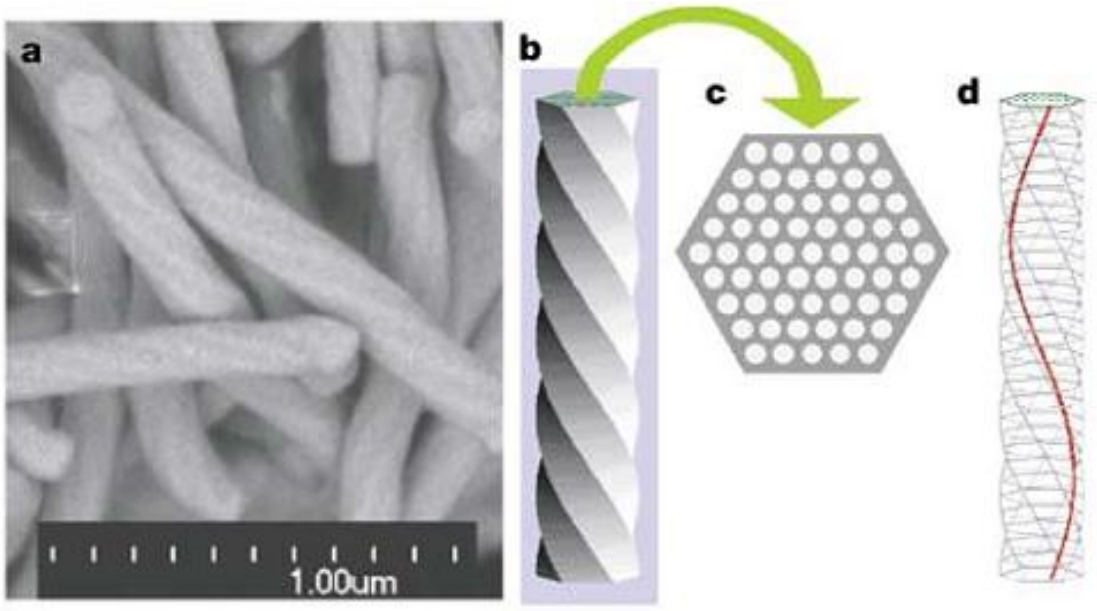

Figure 1.8 The SEM image and schematic diagram of a structural model of the chiral mesoporous silica.[173]

1.3.2 Mesoporous carbon

1.3.2.1 Hard-template strategy

The preparation of ordered mesoporous carbon through a hard-template method (nanocasting process), was successfully developed by Ryoo in 1999, although some attempts of synthesizing porous carbons traced back to 1980s.[180,181,182] This strategy makes use of the voids of the mesoporous silica to incorporate carbon precursors. A replica structure is formed after the pyrolysis of the silica/carbon-precursor composite, and the hard-template (silica)

removal by HF or NaOH solutions. In order to obtain highly ordered mesostructures by this hard-template route, four requirements should be considered:[183] (1) the mesoporous templates should possess high order and durable thermal stability; (2) a full impregnation of the desired precursors within the voids of templates is necessary and such precursors should be easily converted to the desired solid structures with as little volume shrinkage as possible; (3) the parent templates should be easily and completely removed in order to achieve a faithful replica; (4) in order to control the morphology of the replica of hard-templates, the morphology of mesoporous templates should be controlled.

The first ordered mesoporous carbon prepared through a nanocasting process employed mesoporous silica MCM-48 as the hard-template, sucrose as the carbon precursor and sulfuric acid as the catalyst for carbonization.[184] A highly ordered mesoporous carbon inverse replica (CMK-1) was obtained with a mean pore size of ~3 nm. However, transformation was detected between the replica CMK-1 ($I4_1/a$) and the silica template MCM-48 ($Ia3d$). Therefore, CMK-1 did not replicate the hard-template precisely. Subsequent studies showed the structural transformation was due to the change in the relative position of the two non-interconnecting mesopore systems filled with carbon in MCM-48 after the silica template was removed.[178,185]

Later, another ordered mesoporous carbon CMK-3 with a hexagonal structure was synthesized by the same group, using SBA-15 as the hard-template.[186] The high-resolution TEM images clearly displayed a cylindrical carbon nanorod arrangement. The rods were 7 nm in diameter, and the distance between the centers of two adjacent rods was 10 nm. Hence, the channels among the rods were ~3 nm. Three well resolved peaks were observed from the low angle XRD patterns of CMK-3, quite similar to those of the silica template SBA-15. The successful obtaining of the "true" reverse replica of the template was attributed to the

interconnection of the hexagonal pores in SBA-15, formed due to the penetration of the PPO chains of the surfactant into the silica walls during synthesis.[187] Therefore, CMK-3 consists of carbon nanorods in a hexagonal pattern with connecting bridges between them.

By partial impregnation of the cylindrical pores of SBA-15 with furfuryl alcohol as carbon precursor, Ryoo prepared a bimodal mesoporous carbon CMK-5, where the nanorods in CMK-3 became nanopipes.[188] The inside pore size is ~6 nm and the distance of the channels between two pipes is ~4 nm. Owing to this bimodal structure, the specific BET surface area of CMK-5 is 2000 m^2/g, much higher than that of CMK-3 (1300 m^2/g). However, the porous structure of CMK-5 is not as stable as CMK-3 due to the thin walls of the nanopipes. Mesoporous carbons were also synthesized through a similar nanocasting strategy, but using other silica templates such as MSU-1,[189] KIT-6,[190] as well as colloidal silica nanoparticles.[191,192] Most of these carbons exhibited narrow pore size distribution, large pore volume and high surface area.

It should be noted that the surfactants used in the synthesis of mesoporous silica can also serve as carbon sources to prepare mesoporous carbon, instead of using a external carbon precursors.[193,194] In these cases, sulfuric acid was always introduced in the preparation of mesoporous silicas to catalyze the dehydration process of the surfactant. Otherwise, the surfactants decomposed to gaseous products after pyrolysis.

1.3.2.2 Soft-template strategies

In spite of the great success in preparing mesoporous carbon through the nanocasting strategy, the use of mesoporous silica as a sacrificed scaffold makes the process complicated, high cost and time consuming, and in turn, unsuitable for large-scale production and industrial application.[195] In 2004, Dai and co-workers first reported the direct soft-template synthesis of ordered mesoporous carbon films, with resorcinol/formaldehyde as the carbon sources and the

diblock copolymer polystyrene-*block*-poly(4-vinylpyridine) (PS-P4VP) as the soft template.[196] Since then, the past few years have witnessed many significant developments in this technology.

Liang and Dai summarized the four key factors for the successful synthesis of mesoporous carbon materials via soft templates:[178] (1) the ability of the precursor components to self-assemble into the nanostructures; (2) the presence of at least one pore-forming component and at least one carbon-yielding component; (3) the stability of the pore-forming component that can sustain the temperature required for curing the carbon-yielding component but can be readily decomposed with the least carbon yield during carbonization; (4) the ability of the carbon-yielding component to form a highly cross-linked polymeric material that can retain its nanostructure during the decomposition or the extraction of the pore-forming component.

Only a few materials can meet all the four requirements so far. For example, not all the surfactants used to synthesize mesoporous silica are suitable for preparation of mesoporous carbon. The most commonly used soft templates for synthesis of mesoporous carbon are PEO-PPO-PEO type nonionic triblock copolymers such as F127, P123 and F108. The hydrophilic parts (PEO) of these nonionic surfactants can form strong hydrogen bonds with the hydroxyl groups of the carbon precursors including resorcinol/formaldehyde (RF), [197] phloroglucinol/formaldehyde (PF) [198] and water-soluble phenolic resin (resol). [199] More importantly, these copolymers completely decompose to gasses during carbonization under inert atmospheres. In contrast, cationic surfactants like CTAB or CTAC and Briji ($C_nH_{2n+1}(EO)_x$) produce - high carbon residues after carbonization, which block most of the pores.[200,201]

Dongyuan Zhao's group made great contributions towards this soft-template strategy. They developed highly ordered mesoporous carbon C-FDU-15 (hexagonal structure) and C-FDU-16 (cubic structure) through a solvent evaporation induced self-assembly (EISA) method,[202] which is a versatile strategy to prepare mesostructures.[203,204,205] The synthesis procedures include five major steps (Figure 1.9), as summarized by Zhao: (1) resol precursor preparation; (2) the formation of an ordered hybrid mesophase by the organic-organic self-assembly during the solvent evaporation; (3) thermopolymerization of the resols around the template to solidify the ordered mesophase; (4) template removal; (5) carbonization.

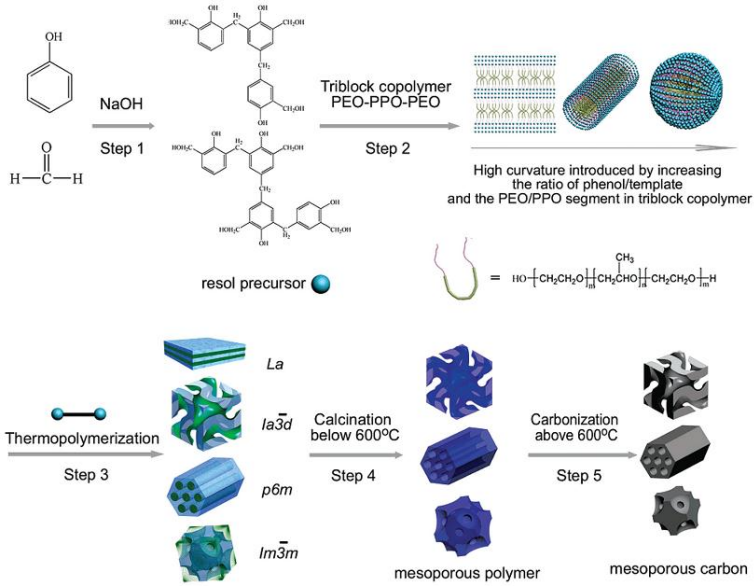

Figure 1.9 Schematic representation of the procedures employed to prepare mesoporous polymers and carbon frameworks.[206]

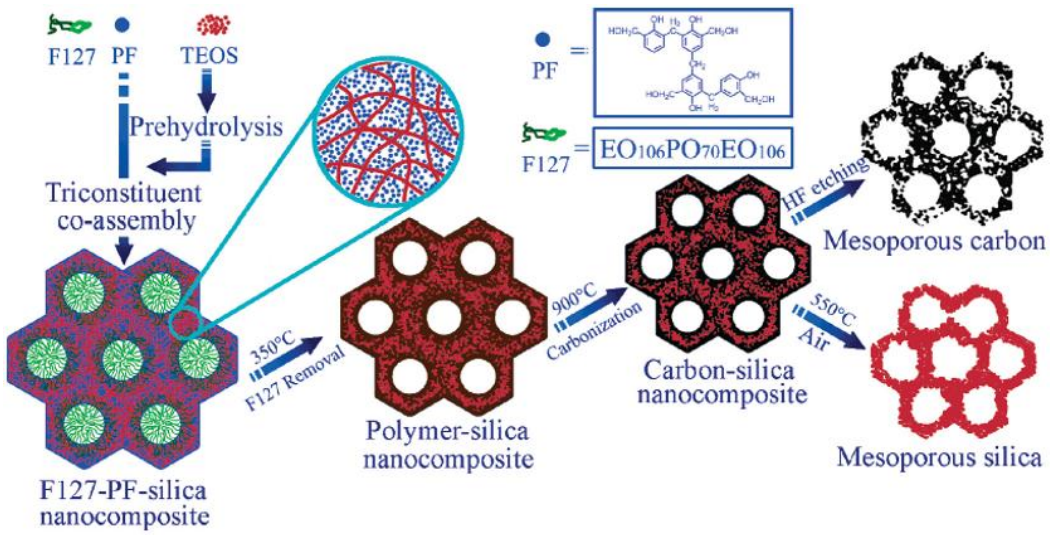

Figure 1.10 Schematic representation of the tri-constituent co-assembly to ordered msoporous polymer-silica, carbon-silica nanocomposites, as well as the corresponding ordered mesoporous silica and carbon frameworks.[207]

Compared with the hard-template method, one of the major drawbacks of the ordered mesoporous carbons synthesized via a soft-template is severe skeleton shrinkage during the high-temperature carbonization procedure which results in low surface areas, small pore sizes and low pore volumes.[207,208] For example, the C-FDU-15 carbonized at 900 ℃ only exhibited a pore volume of 0.56 cm^3/g, less than half of that of the carbons prepared by nanocasting such as CMK-3. In order to solve this problem, Zhao *et al*. developed a tri-constituent co-assembly approach to prepare well-ordered mesoporous carbons, by using resols as the carbon precursor, silicate oligomers TEOS as the inorganic precursor and triblock copolymer F127 as the template (Figure 1.10).[209] This route is similar to the synthesis of FDU-15. However, since TEOS was added as one of the precursors, ordered mesoporous carbon-silicate nanocomposites were formed after pyrolysis. The presence of the rigid silicates acted as "reinforcing-steel-bars", which dramatically inhibited framework shrinkage during pyrolysis.

Mesoporous carbon obtained after silica extraction from the carbon-silica composites has a mean pore size of ~6.7 nm, more than twice than that of C-FDU-15 (~2.9 nm) prepared without silica addition. More interestingly, this process also created a large amount of small nanopores (<3 nm), which was evident by the pore size distribution analysis.[193] This result originates from the co-assembly between TEOS, resol and F127 during the hydrolysis of TEOS in weakly acidic conditions. The subsequent polymerization of resol, decomposition of the surfactant and pyrolysis of the resol/silica composites yielded numerous small nanocrystallites of silica imbibed in the walls of the mesoporous carbon framework. Finally, the nanocrystallites were removed by HF etching, leaving 2-3 nm voids on the walls. This unique bimodal porous structure renders the material one of the largest surface areas (2100 m^2/g) and pore volumes (2.0 cm^3/g), amongst all reported ordered mesoporous carbons.

Another drawback of surfactant-templated mesoporous carbon is the difficulty in controlling morphology and particle size. Films and monoliths are the most common morphologies of the mesoporous carbons synthesized via this method, due to the limitations of the synthetic procedures,[210,211,212] Liang and Dai prepared mesoporous carbon fibres by using a fibre drawing machine.[196] An alternative method to prepare mesoporous carbon fibres is the employment of hard templates such as anodic alumina oxide (AAO) membranes. For example, Chen et al. synthesized mesoporous carbon fibre arrays using resol as the carbon source, F127 as the template and AAO as the hard-template. The diameter of these fibres was ~200-300 nm, depending on the pore size of the AAO membranes.[213] Similar results were also reported by other groups.[214,215] By using an aerosol-assisted EISA pathway, or a suspension-assisted strategy, mesoporous spheres could be synthesized with tunable particle size.[216,217] Very recently, Zhao's group prepared ordered mono-dispersed spherical mesoporous carbon with a

highly uniform particle size through a low-concentration hydrothermal approach.[218] The particle size of the nanospheres varied between 20 nm and 140 nm by controlling the precursor concentrations. The ordered mesopore arrays could be clearly observed from HRSEM images. Surprisingly, there are only less than 10 pores in one sphere of the 20 nm size sample, suggesting one unit cell of body-centered cubic (Im3-m) mesostructure in one particle.

1.3.3 Other mesoporous materials beyond silica and carbon

In addition to silica and carbon, various studies have focused on mesoporous metal oxide materials as well. Pioneering studies were carried out by Peidong Yang's group, using nonionic surfactant P123 as the soft-template, metal chlorides as the metal sources and ethanol as the solvent.[219] Thermally stable, ordered and large pore (up to 14 nm) metal oxides were fabricated, including binary compounds TiO_2, ZrO_2, Al_2O_3, Nb_2O_5, Ta_2O_5, WO_3, HfO_2, SnO_2, and ternary compounds $SiAlO_{3.5}$, $SiTiO_4$, $ZrTiO_4$, Al_2TiO_5 and ZrW_2O_8. More systematic studies on mesoporous metal oxides were later reported by the same group with more than 20 different metal precursors examined.[220] Later, the "acid-base pair" mechanism was proposed to explain the self-adjusted inorganic-inorganic (II) interplay between two or more inorganic precursors, and an overall "framework" was produced for the sophisticated combination of synergic inorganic acid-base precursor pairs.[221] A wide variety of well ordered, large pore, homogenous and multi-component mesoporous solids were synthesized under this theory, including metal phosphates, silica-aluminophosphates, metal borates, as well as various metal oxides and mixed metal oxides.

Fabrication of mesoporous metal oxides by a nanocasting process was also studied by employing mesoporous silica or carbon frameworks as hard-templates. For example, Peter Bruce's group synthesized a series of metal oxides or lithium metal oxides as electrode

materials of lithium-ion batteries, including $LiCoO_2$,[222] Fe_2O_3,[223] Li-Mn-O[224] and TiO_2.[225] In order to obtain binary porous metal oxides, a metal salt such as cobalt nitrate was first dissolved in a solution containing a hard-template (KIT-6) to make the salt homogeneously impregnate into the pores. The metal-salt/silica composites were then heated in air to convert the salt to oxide. Finally, the silica template could be washed out with basic solution at elevated temperatures. The ternary lithium-containing metal oxide compounds were prepared by treating the as-prepared binary mesoporous oxides with lithium hydroxide through a solid state reaction. Other metal oxides such as CeO_2, Co_3O_4, Cr_2O_3, CuO, β-MnO_2, Mn_2O_3, Mn_3O_4, NiO and $NiCoMnO_4$ can be obtained in a similar way.[226] A good example of fabricating mesoporous metal oxides via mesoporous carbon is the synthesis of mesoporous MgO. Magnesium oxide is soluble in both HF and NaOH solutions, so silica is not suitable as a sacrificable scaffold. However, mesoporous carbon is an ideal hard template since it can be easily removed during the conversion of the magnesium salts to MgO in air.[227,228]

The hard-template nanocasting strategy can be extended to prepare mesoporous metal nitrides as well. Zhao prepared ordered mesoporous CoN and CrN by using SBA-15 as the silica-template. Similar impregnation and pyrolysis process discussed above applied, but then the metal-oxide/template composites were treated in an NH_3 atmosphere at high temperatures. The conversion of oxides to nitrides and the meso-structural retention were confirmed by XRD. However, a large number of CrN nanowires with a diameter of 4 nm were observed from TEM, indicating the partial collapse of the mesostructure.

Lately, a type of new mesoporous material - g-C_3N_4 - has been developed by using various silica hard-templates such as mesoporous silica monolith,[229] commercially available silica colloidal particles (LUDOX),[230] or the ordered mesoporous framework SBA-15.[231] Cyanamide

or its dimer and trimer (dicyandiamide and melamine) serve as the precursors which polymerize at elevated temperature in an inert atmosphere, to yield g-C_3N_4 by elimination of the amino groups.[232] g-C_3N_4 has a similar layered structure to that of graphite, and is very stable in ambient conditions. However, it thermally decomposes to gaseous products above 600 ℃. Making use of this feature, TiN and VN nanoparticles with an average size below 10 nm were successfully prepared using mesoporous g-C_3N_4 as the confinement, as well as the nitrogen source.[233]

1.4 The Motivation and Scope of This Thesis

The motivation of this thesis is to explore high efficient functional materials for energy storage and conversion, i.e. cathode materials of rechargeable lithium batteries and hydrogen storage materials for polymer electrolyte membrane fuel cells (PEMFC). Hydrogen is the lightest and simplest element and lithium is the lightest metal in nature. The gravimetric energy densities of both H-containing and Li-containing materials are much higher than most of the other heavy-element-containing compounds. Furthermore, either of the cathode materials or hydrogen storage materials represents a crucial barrier to utilization of rechargeable lithium battery or PEMFC system on electric vehicles. Thus, the development of novel materials for these two technologies covers most of the topics in this thesis. The morphologies and structures of these functional materials were carefully controlled since they significantly influence the properties of batteries and fuel cells. For example, the tailored porous sulfur cathodes always allow a more homogeneous distribution of the active material in/on the carbon frameworks, and consequently, greatly improve the capacity and stability of lithium sulfur cells. All the active materials of the cathodes in this thesis (**Chapter 3-5**) are

based on or associated with mesoporous architectures. That is why mesoporous materials (especially mesoporous carbons) were extensively reviewed in this chapter.

Specifically, **Chapter 2** describes the main characterization techniques employed in this thesis such as TGA, powder XRD, BET, SEM, TEM, EDAX and electrochemical studies of cells; **Chapter 3** presents the synthesis of a novel highly ordered bimodal mesoporous carbon framework with high surface area and large pore volume and its utilization in sulfur cathodes; **Chapter 4** discusses morphology and size control of the bimodal mesoporous carbon and its significant influence on the performance of sulfur cathodes; **Chapter 5** discusses a strategy to coat carbon nanoparticles in/on the Li-ion battery cathode material Li_2CoSiO_4, which can be potentially extended to other silicate-based cathodes. The last part, **Chapter 6**, introduces the possibility of developing and using lithium metal nitride materials (Li_7VN_4 and Li_7MnN_4) for on-board hydrogen storage, both theoretically and experimentally.

In **Chapter 4**, the mesoporous carbon spheres and fibers were synthesized by Dr. Jörg Schuster in University of Munich, Germany, and in **Chapter 6**, the theoretical calculations and hydrogen sorption experiments were conducted by Dr. Jan Herbst and colleagues in General Motor, USA. I really appreciate their great contributions to this thesis.

Chapter 2

Characterization Methods

Various techniques were employed to understand and characterize the materials in this thesis. In this chapter, the fundamental principles of these techniques such as TGA, XRD, SEM, TEM, EDAX, BET, and galvanostatic cycling of cells were presented.

2.1 Thermal gravimetric analysis (TGA)

Thermal gravimetric analysis (TGA) is a type of measurement preformed on samples to determine changes in weight in relation to a temperature program. Except the Li_7VN_4 and Li_7MnN_4 samples in **Chapter** 6, all the other TGA measurements were performed with a SDT Q600 analyzer, with which the atmospheres and heating rates could be controlled. The differential scanning calorimetry (DSC) results could also be obtained simultaneously with the TGA measurements.

In **Chapter 6**, hydrogenation experiments were conducted in a Cahn2151 high pressure thermal gravimetric analyzer and mixed gas experiments were conducted in a Hiden Model IGA-3 thermal gravimetric analyzer (IGA).

2.2 Powder X-ray diffraction (PXRD)

X-ray diffraction (XRD) is one of the most important techniques to understand the crystal structures. Pioneering works were carried out by Laue in 1912. He gave three equations (Laue

Equations) to describe the relationship between X-ray wavelengths and diffraction angles in a crystal. This approach is a rigorous and mathematically correct way to describe diffraction by crystals, but they are cumbersome to use. The alternative theory, known as Bragg's Law, is much simpler and is used almost universally in solid state chemistry.[1] Bragg' Law is based on the assumption that crystals build up in layers or planes, and each plane acts as a semi-transparent mirror. Some of the X-rays are reflected off a plane with the angle of reflection equal to the angle of incidence, but the rests are transmitted to be subsequently reflected by succeeding planes. Bragg's Law describes the relationship between the incident angle (also called Bragg angle), the wavelength and the distance of the two adjacent planes (d-spacing) as:

$$\lambda = 2d * sin\theta \tag{2-1}$$

In a real experiment, Bragg's Law is applied by varying θ degrees of sample stage with respect to the incident beam to probe various d-spacings of crystallographic planes in the lattice.

Among various XRD techniques, powder XRD (PXRD) is the most widely used one for the identification and characterization of crystalline solids. In order to prepare a PXRD sample, careful grinding is needed to obtain fine particles which produce a distinctive diffraction pattern during a scan. Both the positions and the relative intensity of the lines are indicative of a particular phase and material, providing a "fingerprint" for comparison, with the help of a comprehensive database. The crystal domain size of a sample characterized by PXRD can be calculated according to the Scherrer Equation:

$$D = K * \lambda / (\beta * cos\theta) \tag{2-2}$$

where D is the mean size of the domains, K is the shape factor (always a constant), λ is the wavelength of the X-ray, θ is the Bragg angle, and β represents the full width at half maximum intensity (FWHM) in radians.

Post-heat treated PXRD measurements of Li_7VN_4 and Li_7MnN_4 were performed with a Siemens D5000 diffractometer (Cu-Kα radiation, λ=1.5418 Å) in **Chapter** 6. All other PXRD patterns, no matter in low angle or wide angle, were collected on a D8-Advance power X-ray diffractometer operating at 40 kV and 30 mA and employing Cu-Kα radiation (λ=1.5406 Å). Since there are no single crystal XRD investigations in this thesis, PXRD is simply denoted to "XRD" everywhere.

2.3 Scanning electron microscopy (SEM)

Scanning electron microscopy (SEM), inception in the middle of the 20th century, is one of the most versatile methods available for imaging of nanoscale features of solid state materials. Specifically, an SEM image is obtained by scanning the sample with a high energy beam of electrons in a raster scan pattern. The beam interacts with the sample surface and creates a large number of various signals like secondary electrons (SE), backscattered electrons (BSE) and characteristic X-rays, which provide useful information about morphology, composition and surface topography. Features up to tens of microns in size can be seen and the resulting images have a definite 3-D quality. At the other extreme, high resolution scanning electron microscopy (HRSEM) is capable of giving information on the atomic scale by direct lattice imaging. In spite of wide applications of SEM, this technique suffers some drawbacks. First of all, high-vacuum environment during the analysis limits its utilization for samples that readily decompose under vacuum. Secondly, poor images could be resulted at high magnifications for

insulators or semi-conductive samples, because they tend to charge when scanned by the high energy electron beams. Therefore, a thin layer of Au coating on the surface of samples is employed via sputter process under vacuum condition. Unless specified, all the SEM samples in this thesis were pre-treated by sputtering before analysis. Finally, only surface region of samples can be viewed by SEM.

Most of SEM images in the thesis were taken on a LEO 1530 field emission SEM instrument under the backscattering detection mode. In **Chapter 4** and **Chapter 5**, some images were taken from a Hitachi S-2000 scanning transmission electron microscope (STEM), and some of them were performed on a JEOL JSM-6500F scanning electron microscope equipped with a field emission gun, at 10-15 kV.

2.4 Transmission electron microscopy (TEM)

In transmission electron microscopy (TEM), electrons are accelerated to 100 KeV or higher, penetrate through a thin specimen (always less than 500 nm), and interact with the sample to create signals. The greatest advantages that TEM offers are the high magnification ranging from 50 to 10^6, and capable of providing both image and diffraction information from a single sample. The magnification, or resolution of a TEM is dependent on the electron wavelength λ, which is given by the de Broglie relationship:[2]

$$\lambda = h / (2 * m * q * V)^{1/2} \qquad (2\text{-}3)$$

where m and q are the electron mass and charge, h is Planck constant, and V is the potential difference through which electrons are accelerated. Therefore, a higher operating voltage of TEM instrument gives high energy waves with a smaller wavelength, and then a greater

resolution. Another advantage of higher voltage is the more possibilities of penetrating thicker samples. However, even in a very high voltage, it is difficult to get information with a sample in micron size because electrons are usually completely absorbed by thick particles and results in little peneration.

Except some of the images in **Chapter 4**, all the other TEM images in this thesis were carried out on Hitachi S-2000 scanning transmission electron microscope (STEM). STEM combines the features of SEM and TEM, which can be considered as a collection of individual TEM analysis by scanning the samples step by step. TEM images in **Chapter 4** were obtained on a JEOL JEM 2011 microscope at an acceleration voltage of 200 kV.

2.5 Energy dispersive X-ray analysis (EDAX)

Energy dispersive X-ray analysis (EDAX, or EDX or EDS) is an analytical technique used for the elemental analysis or chemical characterization of a sample, which relies on the investigation of an interaction of X-ray excitation and a sample. It is usually used in conjunction with a SEM or TEM instrument. When a sample is bombarded by the electron beam, electrons are ejected from the surface atoms of the sample. The resulting electron vacancies are filled by electrons from higher state, and an X-ray is emitted to balance the energy difference between the two states. These characteristic X-rays could reflect a unique atomic structure of each element and its relative abundance in the sample.

Elemental mapping is the extension of EDAX technique. Characteristic X-ray intensity is measured relatively to lateral position on the sample. Variations in X-ray intensity at any characteristic energy value indicate the relative concentration for the applicable element across the surface. One or more maps are recorded simultaneously using image brightness intensity as a function of the local relative concentration of the element present. This technique is

extremely useful for displaying element distribution in a textural context, such as the dispersion degree of sulfur in mesoporous carbon frameworks.

In **Chapter 3** and **Chapter 6**, the elemental maps and EDAX spectrum were taken from LEO 1530 SEM instrument, while the elemental maps in **Chapter 4** and **Chapter 5** were obtained from Hitachi S-2000 scanning transmission electron microscope (STEM).

2.6 Porous structure analysis

2.6.1 Nitrogen adsorption isotherm

Gas adsorption is the most popular method to characterize porous structures because it allows assessment of a wide range of pore sizes (from 0.35 nm up to 100 nm), including the complete range of micro- and mesopores and even macropores.[2] There are two types of gas adsorption depending on the strength of the adsorbent and the adsorbate gas: chemical adsorption and physical adsorption. The former process is gas selective because it is based on reactivity of adsorbent and adsorbate gas, and chemisorbed molecules may react or dissociate after the measurements. For example, the first-stage adsorption process of hydrogen storage in intermetallic alloys can be considered as a chemical adsorption. The latter category, in contrast, is a completely reversible phenomenon associated only with van der Waals' forces. It takes place whenever an absorbable gas is introduced in contact with the surface of the solid adsorbent. Most of the modern adsorption characterizations on porous materials are based on physical adsorption.

The International Union of Pure and Applied Chemistry (IUPAC) defined six types of sorption isotherms in 1985 (Figure 2.1).[3] Type I (Langmuir isotherm) is exhibited by microporous solid like molecular sieve zeolites. Type II is obtained in case of nonporous or

macroporous materials. Type III is uncommon, and a well-known example is the adsorption of water on nonporous carbon.[4] Type IV is typical for mesoporous absorbent. The initial part is similar to type II isotherm. Type V is rare. The initial is related to type III, but the pores in the mesoporous range exist. Type VI is a special case, which represents a stepwise multilayer adsorption on a uniform, non-porous surface, particularly by spherically symmetrical, non-polar adsorbate gases.[3,5]

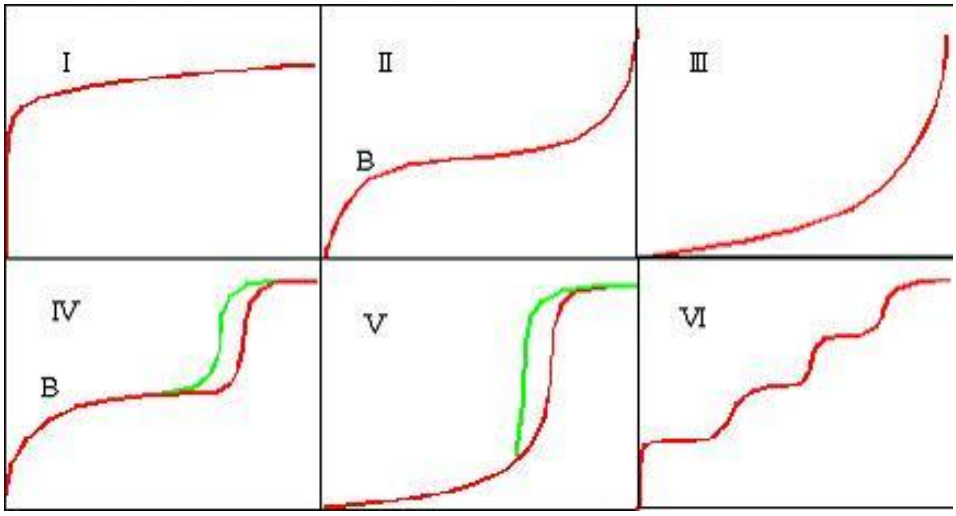

Figure 2.1 The six types of sorption isotherms defined by IUPAC.[6]

Various gases such as N_2, Ar, CO_2 and Kr, can serve as adsorbates for physical adsorption analysis. The selection of a specific gas should consider both of the adsorbent structures and physical properties of the gas such as saturation pressure and temperature, as well as the molecular size. For example, N_2 is the most suitable one for mesoporous frameworks.

The total pore volume of an adsorbent can be derived from the amount of vapour adsorbed at a relative pressure close to unity by assuming pores are fully filled with liquid adsorbate.

For example, if the adsobte is N_2, the adsorbed volume of N_2(g) can be converted to N_2(l) using the Ideal Gas Law:

$$P(g) * V(g) = n * R * T = \rho(l) * V(l) * R * T / M \quad (2\text{-}4)$$

Therefore, the volume of liquid N_2 is expressed as

$$V(l) = P(g) * V(g) * M / \rho(l) * R * T \quad (2\text{-}5)$$

where $P(g)$ and T are ambient pressure and temperature, $V(g)$ is the gaseous volume of N_2 absorbed, M is the molar mass, R is the ideal gas constant and $\rho(l)$ is the density of N_2 at boiling point (0.808 g/cm^3).

2.6.2 Surface area analysis

The Brunauer-Emmett-Teller (BET) theory, first reported in 1938, is the most important and widely used approach to determine surface areas of solid state materials.[7] The equation is described as:

$$\frac{1}{v\left(\frac{P}{P_0} - 1\right)} = \frac{1}{v_m C} + \frac{C - 1}{v_m C}\frac{P}{P_0} \quad (2.6)$$

in which v is the volume of gas adsorbed at a relative pressure P/P_0, v_m is the volume of adsorbate constituting a monolayer of surface coverage and C is the BET constant. By picking up several P/P_0 points in the range of 0.05 to 0.35, a linear plot should be obtained (also called BET plot). The slope S and intercept I of the BET plot are

$$S = (C - 1) / (v_m * C) \quad (2\text{-}7)$$

$$I = 1 / (v_m * C) \quad (2\text{-}8)$$

The volume of a monolayer adsorbate v_m can be obtained by solving the above two equations. The relationship of the total surface area of the sample is

$$S_{total} = v_m * N * s / V \quad (2\text{-}9)$$

where N is Avogadro's number, V is the molar volume of the adsorbate gas and s represents the molecular cross section area of the adsorbate molecule. For hexagonal closed-packing nitrogen monolayer at 77 K, the cross section area for N_2 is 16.2 $Å^2$.[7]

The microporous surface area and volumes are always determined by V-t plot method.[8] It assumes that in a certain isotherm region, the micropores are already filled up, whereas the adsorption in larger pores occurs according to a simple equation, which should approximate adsorption in mesopores, macropores and on a flat surface in a narrow pressure range just above complete filling of micropores, but below vapor condensation in mesopores.[9] Moreover, the adsorbent is assumed to be covered by a uniform film to obtain the so-called statistical thickness from the gas adsorption isotherms. The calculation procedures are very similar as that employed in the BET surface area measurement.

2.6.3 Pore size analysis

The average pore size could be roughly estimated since pores that would not be filled below a relative pressure of unity have a negligible contribution to the total volume and the surface area, but accurate pore size information like pore size distributions have to rely on some mathematical methods. Several models have been established for meso-structural pore size analysis, such as DFT method, BJH method and DH method, among which the BJH method works well for cylindrical mesopores below 10 nm.[10]

In this thesis, the porous structure analyses in **Chapter 3** and **Chapter 5** were carried out on a Quantachrome Autosorb-1 at 77 K. The carbon samples were degassed on a vacuum line at 100-300 ℃ prior to measurements, while C/S samples were degassed at room temperature. The total pore volumes of samples were calculated at a relative pressure of 0.995 (P/P_0), and the surface area and pore size distribution data were calculated via BET method and BJH method, respectively. Samples in **Chapter 4** were also evaluated using a Quantachrome Autosorb-1, but the pore-size distribution was calculated with a DFT method.

2.7 Electrochemical measurements

2.7.1 Assembly of coin cells

Electrochemical performance was evaluated using 2325 coin cells. The preparation procedures of working electrodes and electrolytes were specified in each chapter. A metallic lithium foil stuck on a stainless steel or copper spacer was used as anode materials. All the operations of cell-assembly were carried out in an Ar-filled glove box. Typical assembly of a coin cell is shown in Figure 2.2.

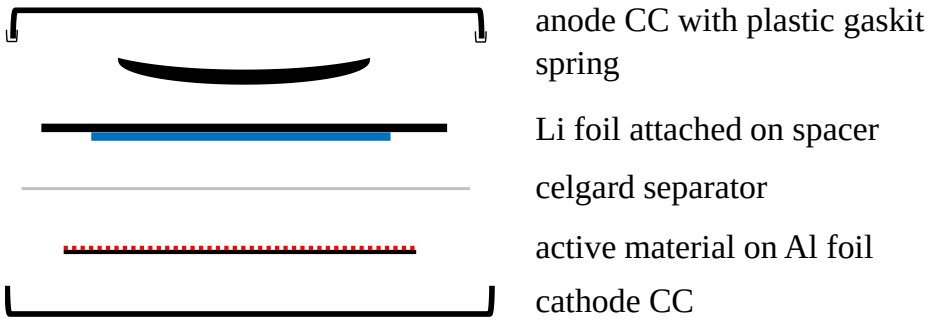

Figure 2.2 Schematic representation of a typical coin cell assembly (CC = current collector).

2.7.2 Galvanostatic cycling

All the coin cells were performed with an Arbin BT-2000 system at room temperature under the galvanostatic mode. In this mode, a desired constant current is applied, based on the calculation of active materials in the cell. The voltage is recorded as the function of time or capacity. Therefore, a voltage-capacity profile could be obtained in each cycle, as well as the cyclability of a cell with the accumulation of cycles.

Chapter 3

High Rate Performance of Li-S Cathodes Scaffold by Bulk Ordered Bimodal Mesoporous Carbon

3.1 Introduction

Despite the high specific capacity (1675 mAh/g) and energy density (2600 Wh/kg)[1] which is a factor of 3-5 times higher than any commercial lithium ion cells, Li-S batteries suffer from some serious problems as described in **Chapter 1**, such as poor electronic and ionic conductivity,[2,3] poor cyclability and rate capability,[4,5,6] and self-discharge.[7,8] A major step forward in fabricating a uniform sulfur/carbon cathodes was reported by our lab in 2009.[9] The C/S nano configurations were prepared by employing ordered mesoporous carbon CMK-3, and the corresponding electrodes displayed high discharge capacity of above 1300 mAh/g (~80% of the theoretical capacity) at a current rate of C/10. In this chapter, I attempt to find an effective way to improve the performance of the sulfur cathodes at high current rates. To achieve this goal, a new mesoporous carbon with a bimodal structure (denoted as BMC-1) was successfully synthesized via EISA method, and applied as a framework of sulfur cathodes. All these carbon-sulfur cathodes, with as much as 60 wt% sulfur incorporated, demonstrate high capacities and good cycling stability at high current rates (up to 5C). The performance of the cathodes could be further improved either by adding hydrophilic mesoporous silica (SBA-15) or by optimizing the porous structure (pore volume and surface area) of the BMC-1.

3.2 Experimental

3.2.1 Synthesis of BMC-1, M-BMC-1, MP-C-36*, C-FDU-15 and SBA-15

The bulk bimodal mesoporous carbon (BMC-1) was prepared by the evaporation-induced self-assembly (EISA) strategy.[10,11,12] The carbon/silica/surfactant ratio was optimized to obtain the desired porous structure compared with ref. 13. The first step is the preparation of water-soluble phenolic resin. In a typical synthesis, 6.1 g of phenol was melted at 40 ℃ and stirred with 1.0 g 20 wt% NaOH solution for 10 min; then 10.5 g of formalin was added and stirred for another 50 min at 65 ℃. After the mixture was cooled down to room temperature, the pH was adjusted to about 7.0 with dilute HCl. Water was then removed by evacuation at room temperature. The final product was dissolved in ethanol to form a 20 wt% solution of water-soluble phenolic resin. To synthesize BMC-1, 1.6 g of triblock copolymer poly(propylene oxide)-*block*-poly(ethylene oxide)-*block*-poly(propylene oxide) (F127, M_w=12,700) was dissolved in a solution of 8.0 g ethanol and 1.0 g 0.2 M HCl via stirring. Next, 2.08 g of tetraethyl orthosilicate (TEOS) and 5.0 g phenolic resin solution were added to this solution and stirred for 5 h at 40 ℃. The mixture was transferred to Petri dishes to evaporate the ethanol overnight, and held at 100 ℃ for 24h to thermopolymerize the phenolic resin. The as-made product was collected from the dishes, hand milled in a mortar for 10 min, and heated under Ar flow at 900 ℃ for 4 h, at a rate of 1 ℃/min below 600 ℃ and 5 ℃/min above 600 ℃. Finally, the product was washed with 10 wt% HF for 12 h to remove the silica.

Bimodal mesoporous carbon MP-C-36* was also prepared following the method developed by Zhao *et al*.,[13] where the number "36" represents the percentage of the carbon-compound

content in the carbon-silica nanocomposite after 900 °C calcination, and the star "*" indicates a bimodal structure.

Ordered mesoporous silica SBA-15 was prepared by hydrothermal method.[14] First, 2.0 g of triblock copolymer poly(ethylene oxide)-*block*-poly(propylene oxide)-*block*-poly(ethylene oxide) (P123, M_w = 5800) was dissolved in 60 mL of 2.0 M HCl at 36 ℃ to give a clear solution. Next, 4.2 g of TEOS was added and vigorously stirred for 10 min. The mixture was kept under static conditions for 24 h, then transferred to an autoclave and heated at 100 ℃ for another 24 h. The solid products were collected by filtration, washed with water and dried at 70 ℃. Finally, the resultant powder was calcined at 550 ℃ for 4 h to remove the polymer template.

Mesoporous carbon C-FDU-15 was prepared by EISA method.[15] First, 5.0 g of triblock copolymer F127 was dissolved in 20.0 g ethanol by sonication at room temperature. Next, 5.0 g phenolic resin solution prepared above were added to this solution and stirred for 10 min to form a homogenous solution with the molar composition of F127/phenol/formaldehyde/ethanol of 0.012:1:2:67. The mixture was transferred to Petri dishes to evaporate the ethanol overnight and held at 100 ℃ for 24 h to thermopolymerize the phenolic resin, like the procedures of preparing BMC-1. The as-made product was collected from the dishes, hand milled in a mortar for 10 min. Finally, it was carbonized at 800 ℃ for 2 h under inert gas atmosphere.

Modified BMC-1 (M-BMC-1) carbons were prepared via a similar method like BMC-1 with some modifications. First of all, different amounts of additives such as decane, 1,3,5-trimethylbenzene (TMB), 1,3,5-triisopropylbenzene (TIPB) were used during the preparation;

Secondly, the reaction temperature was set at 13 ℃. This cooling bath was home-made by mixing P-xylene and ice at room temperature. Since ice kept melting gradually, it was supplemented every 2-3 h; thirdly, both templates P123 and F127 were employed; finally, the ratios between phenolic resin and template were varied to obtain the best porous structure. Detailed information of the synthesis is available in the section 3.3.2.1 (Table 3.3).

3.2.2 Preparation of the C/S nanocomposites

The BMC-1/S nanocomposites were prepared following a melt-diffusion strategy. Mesoporous carbon obtained above was ground together with different masses of sulfur to achieve either 40 wt%, 50 wt% or 60 wt% of sulfur in the resultant C/S composites, and then maintained in an oven at 155 ℃ overnight. MP-C-36*/S-60, C-FDU-15/S-50 and M-BMC-1/-T2-2/S-Y (Y = 50, 60 and 70) were also prepared in this method with different sulfur ratios in the C/S composites. Silica doped BMC-1/S-50 samples was prepared by hand-grinding SBA-15 and BMC-1/S-50 for 15 min in a mortar.

3.2.3 Electrochemistry

The C/S cathode materials were slurry-casted from cyclopentanone onto a carbon-coated aluminium current collector. Typically, 82 wt% of C/S composite, 10 wt% Super S carbon and 8 wt% poly(vinylidene fluoride) (PVDF) were mixed with cyclopentanone. The slurries were coated on C-coated aluminium current collectors and dried at 60 ℃ overnight. Each current collector contained between 0.7-0.8 mg/cm^2 active materials. The equivalent current density for the 334 mA/g current density (C/5) is 0.25 mA/cm^2; 1.25 mA/cm^2 for the 1675 mA/g current density (C) and 2.5 mA/cm^2 for a current density of 3340 mA/g (2C). The

electrochemical performance of the prepared cathodes was evaluated using 2325 coin cells cycled at room temperature between 1.5 V and 3.0 V, with lithium metal foil as the anode. The electrolyte was 1 M bis-(trifluoromethane)sulfonimide lithium (LiTFSI) in a mixed solvents of dimethoxyethane (DME) and 1,3-dioxolane (DOL) with a volume ratio of 1 : 1. This electrolyte was chosen to optimize high-rate behaviour because of its lower viscosity (compared to other systems we used previously such as ethyl methyl sulphone). Here "C" rate is defined as two lithium discharge/charge in one hour. Charge/discharge rates are reported in units of current per mass of sulfur cathode, mA/g, as well as the C-rate convention, or C/n, where n is the time (h) for complete charge or discharge at the nominal (theoretical) capacity measured at low rates, here taken to be 1675 mAh/g.

3.3 Results and discussion

3.3.1 Bulk bimodal mesoporous carbon BMC-1

3.3.1.1 Formation mechanism of BMC-1 and C/S nanocomposites

Bimodal mesoporous carbon was prepared via EISA method with phenolic resin as the carbon precursor, TEOS as the silica precursor and amphiphilic triblock copolymer F127 as the soft template. First, TEOS was hydrolyzed with the catalyst of dilute HCl to form oligomers with Si-OH groups. These hydrophilic OH- groups, together with the OH- groups from the water-soluble phenolic resin interacted with the EO parts of the block copolymer template F127 via strong hydrogen bonds, and arranged around F127 micelles. There is a

complicated balance in the solution among inorganic-inorganic (silicate-silicate), organic-inorganic (F127-silicate and phenolic resin-silicate) and organic-organic (F127-F127, F127-phenolic resin, phenolic resin-phenolic resin) interaction.

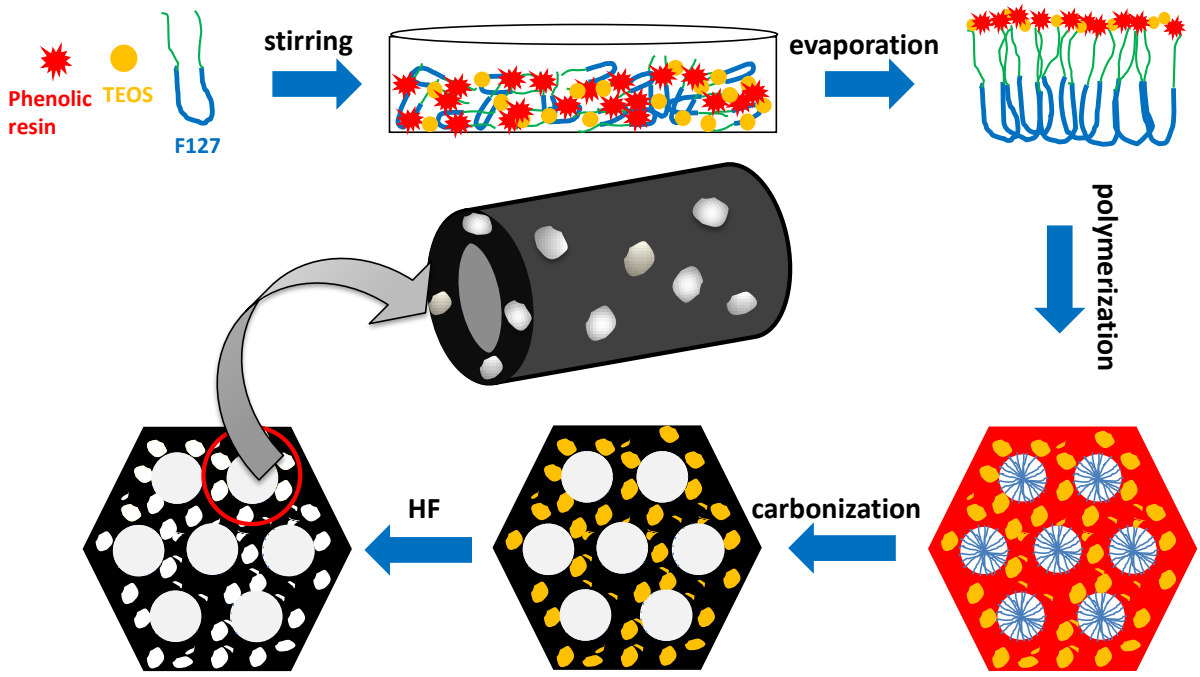

Figure 3.1 Schematic diagrams of the synthetic procedures of the bimodal mesoporous carbon (BMC-1).

With the evaporation of ethanol, the silica-F127-phenolic resin experienced co-assembly, and the mesophase started to form. Simultaneously, the silica species themselves cross-linked with each other and condensed to form the frameworks. The further heat treatment at 100 ℃ promoted the polymerization of the phenolic resin to form 3D networks, which interpenetrated with the silica frameworks. C/SiO_2 nanocomposites could be obtained by burning out the

copolymer template F127 at 350 ℃, and the following carbonization of resin at 900 ℃ in N_2 or Ar atmosphere. The large hexagonal pore, created by the co-assembly of the template F127, was achieved at this step. Finally, the etching of SiO_2 with HF solution produced the small pores onto/into the wall of the large hexagonal pores.

BMC-1/S nanocomposites were obtained by a sulfur diffusion strategy. Since both sulfur and BMC-1 are highly hydrophobic, it is readily to wet the pores of the carbon with melted sulfur by capillary force at 155 ℃, at which sulfur has the lowest viscosity.[16] It should be noted that the density of sulfur varies with temperatures. At the molten state, the density is 1.82 g/cm^3, while it increases to 2.07 g/cm^3, when sulfur cools down to solid state. The density variation makes the sulfur layer in the pores thinner when it is at room temperature than in the molten state, which reserves more space for both of the volume expansion and electrolyte diffusion at the cathodes (ρ_{sulfur} = 1.66 g/cm^3) during battery tests.

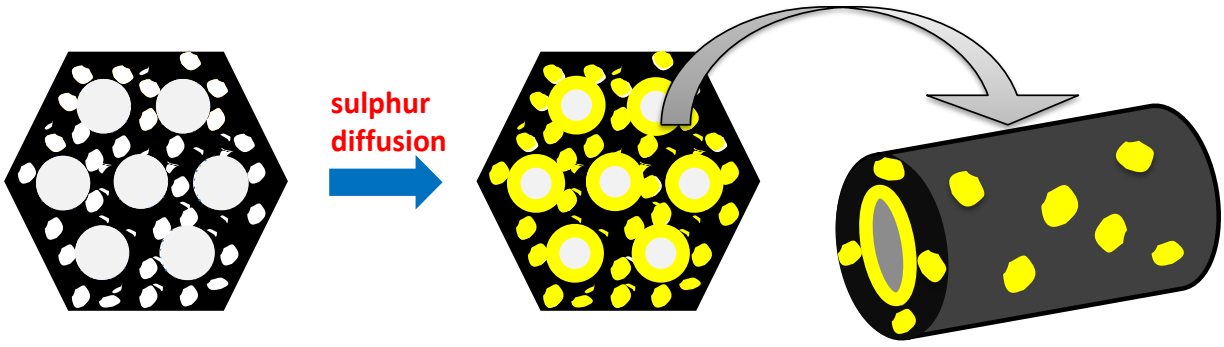

Figure 3.2 The preparation of BMC-1/S nanocomposites via the sulfur-diffusion strategy.

3.3.1.2 Physical characterizations of BMC-1 and BMC-1/S

The complete combustion of the BMC-1 at 500-600 ℃ in air (TGA curve) coupled with the typical exothermic carbon-burning peak at 550 ℃ (DSC curve), as shown in Figure 3.3, indicates the successful removal of silica by HF etching.

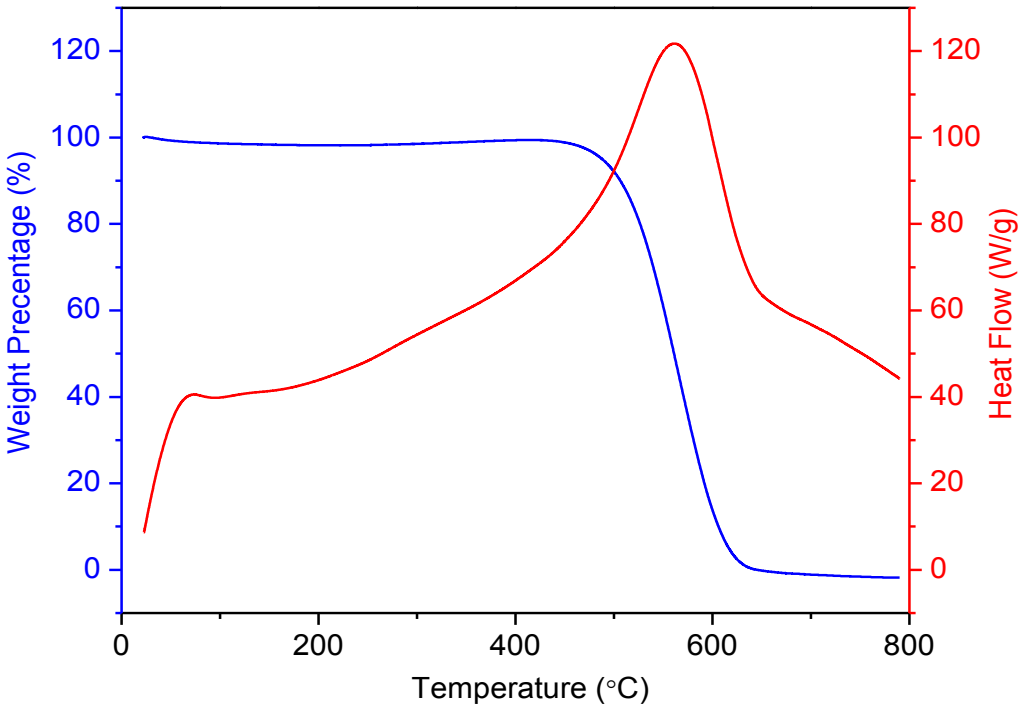

Figure 3.3 TGA (blue) and DSC (red) curves of the BMC-1.

The low angle XRD pattern of BMC-1 (Figure 3.4) clearly shows two diffraction peaks at 2 theta values of 0.91 ° and 1.54 °, and another weak but still recognizable peak at 2.36 °. These three peaks can be indexed as the 100, 110 and 210 reflections of a 2D hexagonal unit cell with a lattice constant (a) of 11.2 nm, indicating a highly ordered mesostructure with p6mm symmetry. Inset of Figure 3.4 is the wide angle XRD of the BMC-1 showing the amorphous

structure of the carbon evidenced by the broad peak at 43.5 °(100 reflection). The strong peak at 17 °as well as the shoulder at 25 °is due to the plastic holder.

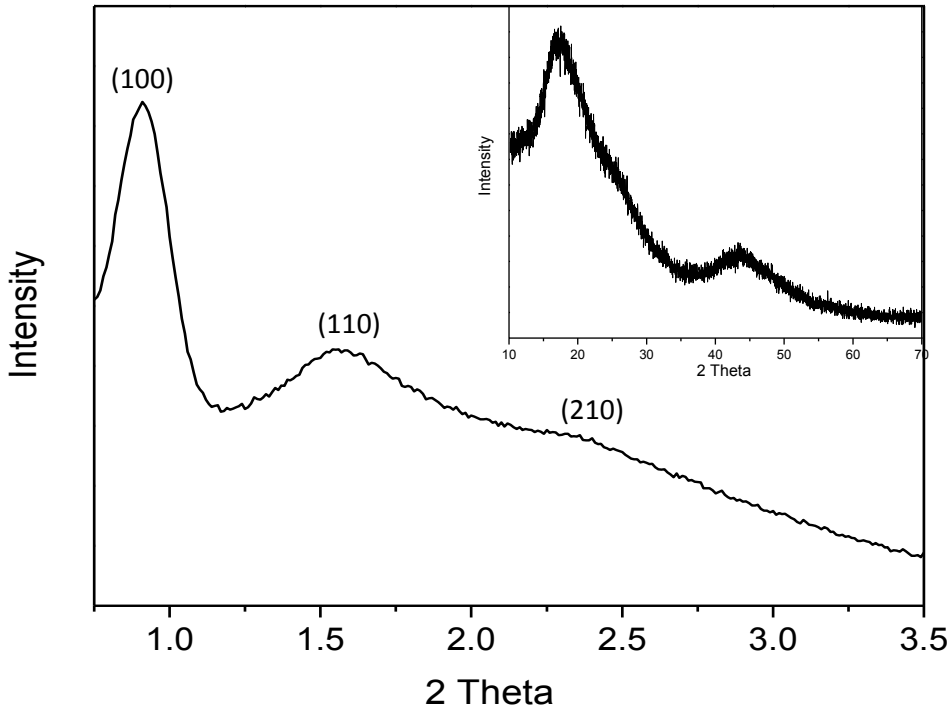

Figure 3.4 Low angle and wide angle (inset) XRD patterns of the BMC-1 carbon.

SEM image of the polymer/silica sample reveals the resin polymer film is less than 10 μm in thickness (Figure 3.5a). The polymer/silica films scraped off from Petri dishes were ground carefully for at least 10 min before calcination. Even though, the particle size of BMC-1 is still in microns (Figure 3.5b). In principal, either the thickness of the polymer film or particle size of BMC-1 is tunable simply by using different amount of dishes during the solvent evaporation process. For example, some groups have reported on the preparation of thin film polymer resin and carbon, or carbon/silica with mesoporous structures via the EISA strategy.[17,18,19,20] However, it is found that the pyrolysis of 2-D hexagonal thin films with

p6mm symmetry templated by F127 always yielded a disordered porous structure following the template removal, while thin films obtained from P123 exhibited well-ordered cylindrical pores after the template was removed.[21] The mechanism behind this phenomenon is not clear so far, but it seems the particle size of the BMC-1 carbon cannot be significantly reduced just by making very thin polymer films.

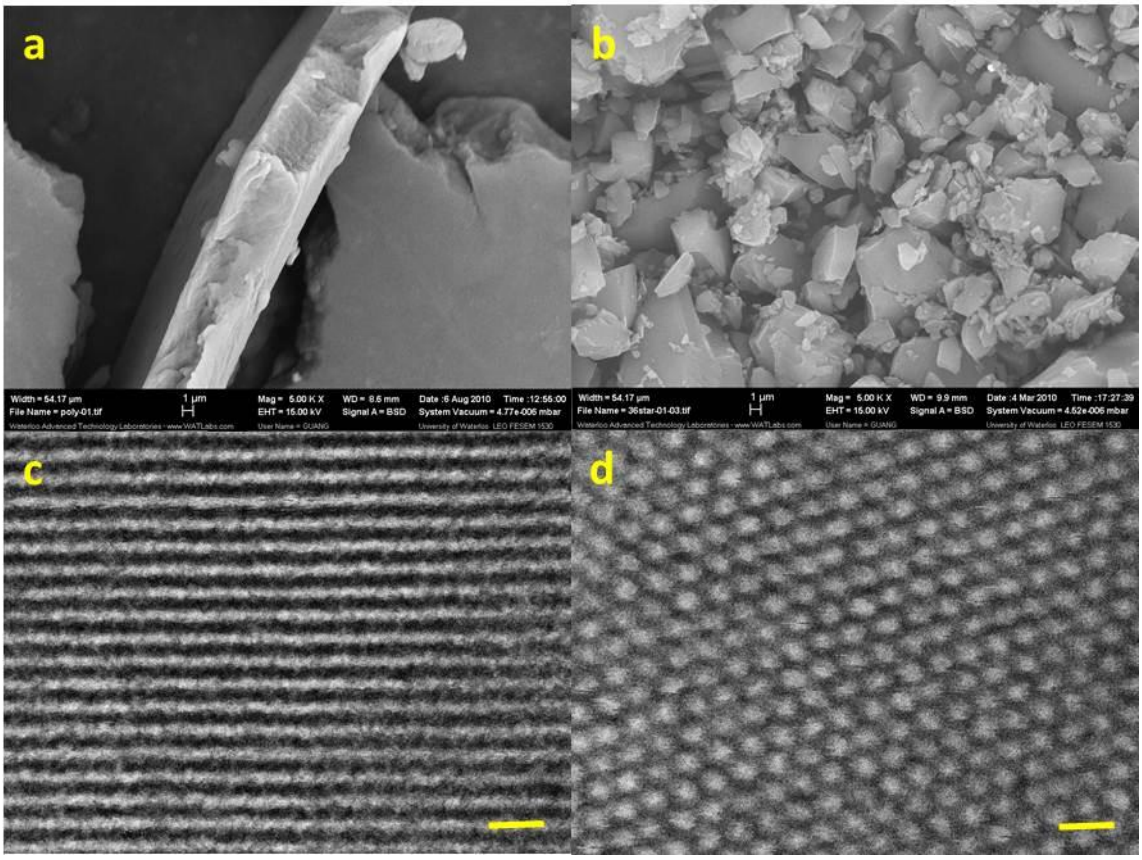

Figure 3.5 SEM images of (a) the polymer/silica sample before carbonization (a) and as-prepared BMC-1 (b), and TEM images of BMC-1 down two unit cell directions, (c) [110] and (d) [001]. The scale bars are 20 nm for both c and d.

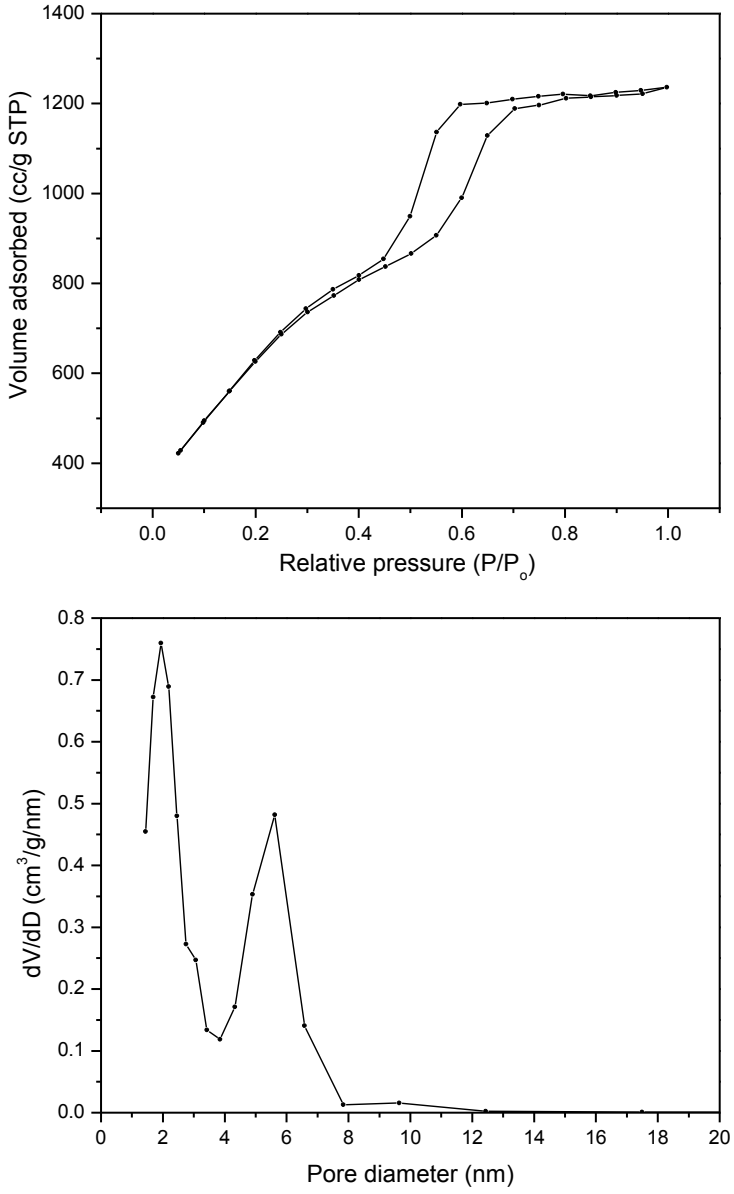

Figure 3.6 (a) N_2 sorption isotherm and (b) pore size distribution analyzed by the BJH method of the BMC-1 carbon.

The large domain regularity of the BMC-1 is verified by TEM images viewed down the [110] and [001] directions in Figure (c) and (d) (Note that the zone axis is slightly off in the latter image). From their expanded versions, the cell parameter a is estimated to be 11 nm

which is in very good agreement with the calculation from the low angle XRD pattern. The inner pore diameter estimated from Figure 3.5d is 5.5 nm. The nitrogen sorption isotherm of the BMC-1 (Figure 3.6a) displays a typical IV curve with a sharp capillary condensation step at a relative pressure of 0.45-0.70 P/P_0, reflecting a narrow pore size distribution. The specific BET surface area is 2300 m^2/g, similar to that of MP-C-36*. The pore size distribution curve (Figure 3.6b) exhibits two narrow peaks at 5.6 nm and 2.0 nm, corresponding to mesopores and super-micropores (or small mesopores), respectively. This result is in excellent accord with the estimation obtained from TEM (5.5 nm of the hexagonal pores). The large hexagonal cylindrical pores were obtained from the self-assembly of the copolymer F127 and the small pores were attributed to the addition of TEOS. Compared with MP-C-36*, both the large and small pore sizes of the BMC-1 are slightly smaller; however, there is a greatly increased contribution to the total pore volume from the small pores (Figure 3.6b).

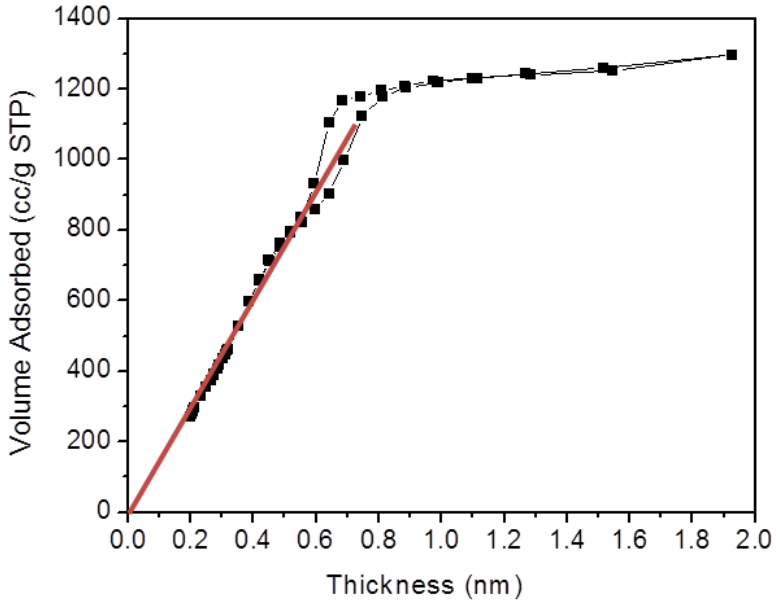

Figure 3.7 Micropore analysis (d < 1.5 nm) of BMC-1 using the V-t plot method, showing their contribution is negligible to the total pore volume.

More detailed data shows that the small pore (1.5 nm<D<3.0 nm) volume is 0.95 cm^3/g in BMC-1, which corresponds to almost half of the total volume (2.0 cm^3/g). The contribution of micropores (D<1.5 nm) is negligible as revealed by the V-t plot method in Figure 3.7.

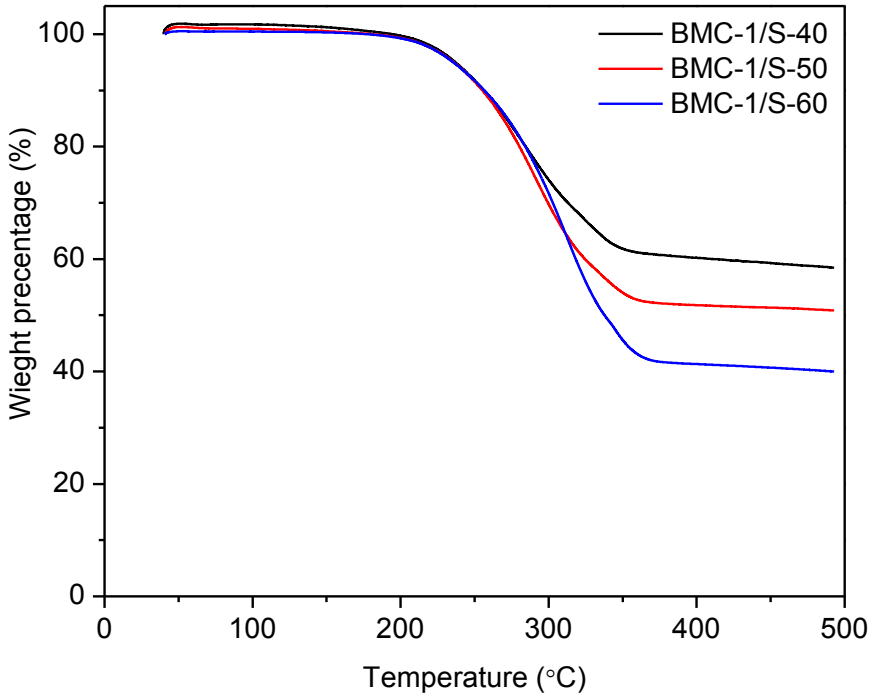

Figure 3.8 TGA curves of BMC-1/S-40, BMC-1/S-50 and BMC-1/S-60.

Three C/S samples BMC-1/S-40, BMC-1/S-50 and BMC-1/S-60 were prepared with various gravimetric sulfur contents in the composites by a melt-diffusion strategy. The detailed ratios of sulfur in each sample are 41.5 wt%, 50.2 wt% and 60.0 wt% respectively (Figure 3.8).

SEM image and the corresponding elemental maps of sulfur and carbon of BMC-1/S-50 show that sulfur is homogeneously distributed into the pores, and no obvious large sulfur masses are evident. However, in spite of the strong affinity, some sulfur probably exists as a light coating on the external surface as well, especially for the BMC-1/S-50 and BMC-1/S-60 samples.

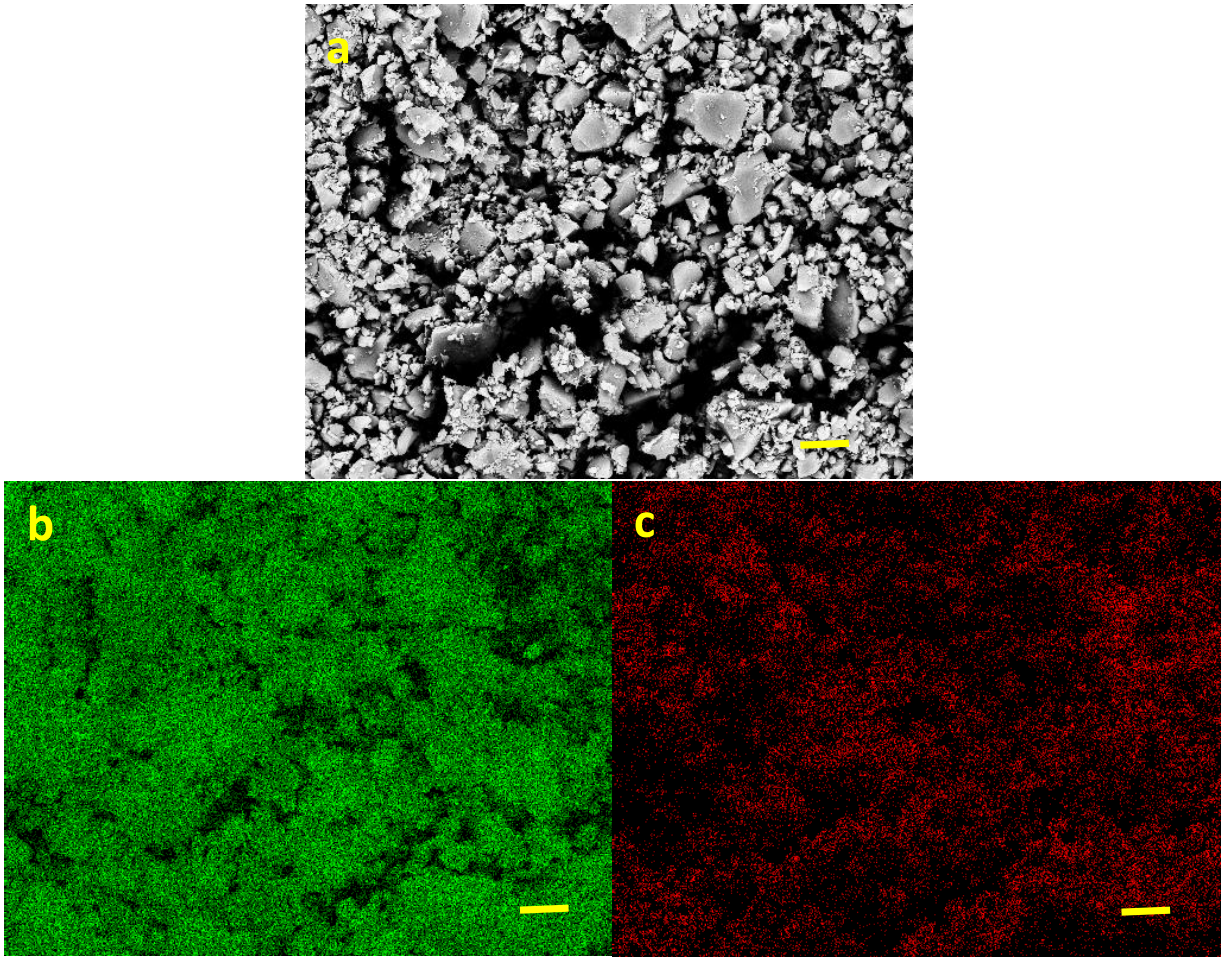

Figure 3.9 (a) The SEM image of BMC-1/S-50 and corresponding elemental maps of (b) sulfur and (c) carbon.

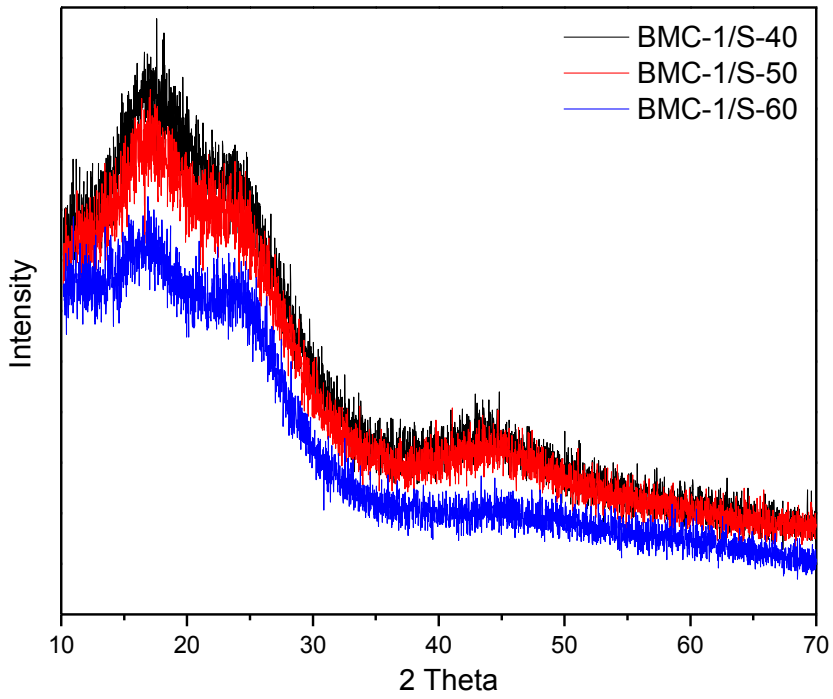

Figure 3.10 Wide angle XRD patterns of BMC-1/S-40, BMC-1/S-50 and BMC-1/S-60.

Wide angle XRD patterns of the C/S samples are similar with pristine BMC-1 carbon (Figure 3.10), implying no crystalline sulfur exists in the composites. The successful impregnation of sulfur into the pores is also evidenced by the low angle XRD patterns in Figure 3.11. The [100] peaks of all the three samples shift to higher angle (>1.1 °) with respect to pristine BMC-1 (0.9 °). According to the Bragg's Law, this shift is a result of the smaller C/S cell parameter (a). Additionally, with the increase of sulfur in the composites, peaks at low angles become less intensive and wider gradually. For example, although it is much weaker than in BMC-1, the [110] reflection of BMC-1/S-40 is still recognizable. However, it completely disappears in the BMC-1/S-60 low angle pattern. All these variations are the reflections of filling sulfur into the pores step by step.

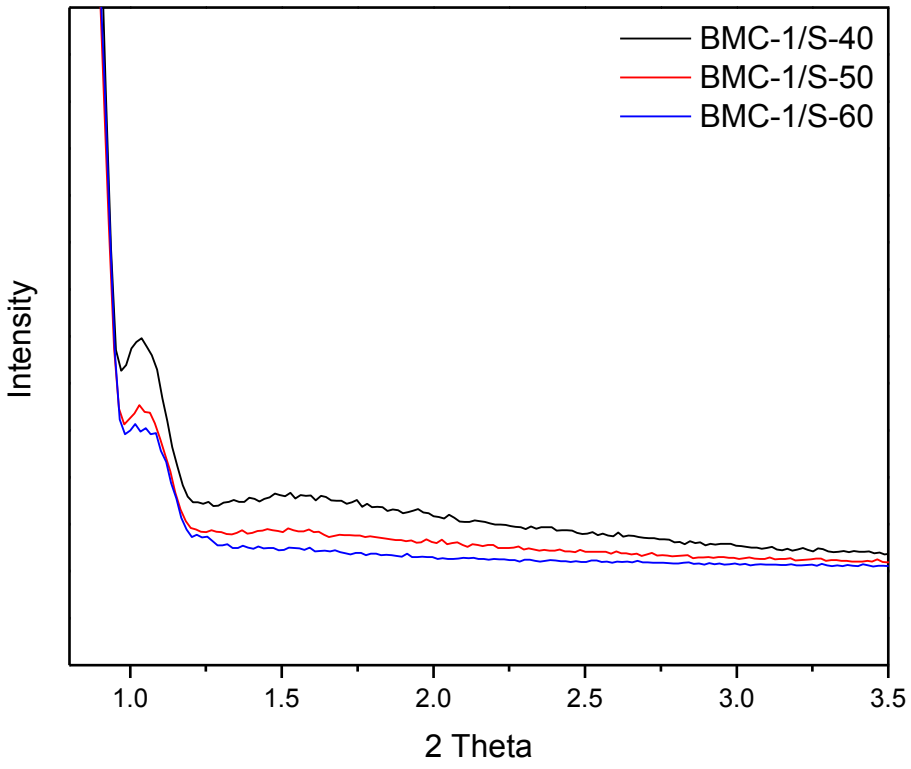

Figure 3.11 Low angle XRD patterns of BMC-1/S-40, BMC-1/S-50 and BMC-1/S-60, showing the diminution of the 100 and 110 peaks.

Nitrogen sorption isotherms in Figure 3.12a illustrate that the capillary condensation effect becomes weaker and the hysteresis region becomes wider with increased sulfur loading, corresponding to a systematic decrease of the specific surface area, pore volume and pore size. Table 3.1 summarizes the data. The small-pore volume decreases much faster on sulfur loading than that of the large pores. For example, the volumes of the two types of pores are almost equal (1.0 cm^3/g) before sulfur infiltration. After loading the C/S composite with 40 wt% of sulfur, the small pore volume is reduced to 0.35 cm^3/g, which is half of the large pore volume. An increase of the sulfur ratio to 60 wt% of the C/S composite results in a negligible

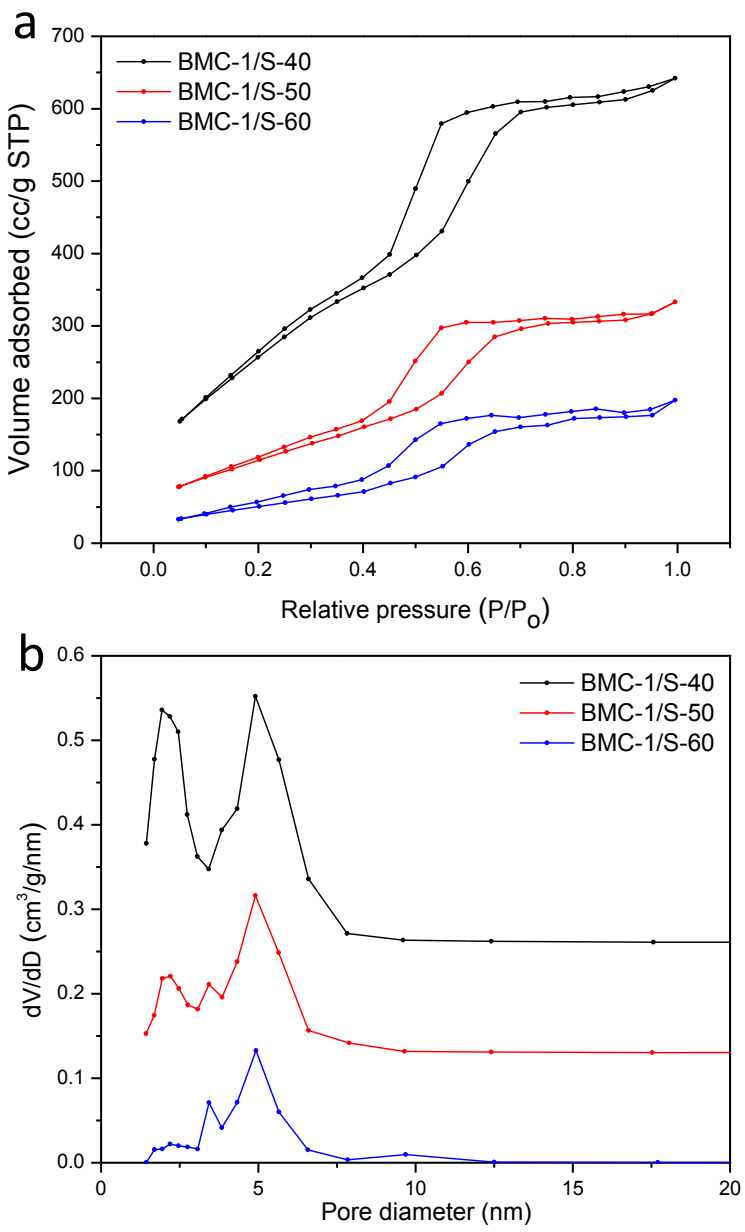

Figure 3.12 (a) N_2 sorption isotherms and (b) pore size distribution analysed by the BJH method of the BMC-1/S composites .

small-pore volume of 0.03 cm^3/g, which is 1/9 of the large pore volume. This is in accordance with the pore size distribution of the three samples seen in Figure 3.12b, which shows the

broadening and decreasing intensity of the peaks with increased sulfur content, until the small peak disappears when the mass ratio of sulfur reaches 60 wt%. Additionally, this signals the appearance of a new peak at 3.5 nm that grows in intensity from BMC-1/S-50 to BMC-1/S-60, which is easily understood. With an increase of sulfur loaded into the pores of the BMC, the inner diameter of the cylindrical pores decreases from 5.6 nm to 3.5 nm due to the deposition of sulfur on the walls.

Table 3.1 Physicochemical properties of BMC-1 and the three C/S composites (see text)

	S_{BET} (m^2/g)	V_t (cm^3/g)	V_s (cm^3/g)	V_l (cm^3/g)
BMC-1	2300	2.0	0.95	1.05
BMC-1/S-40	1000	1.05	0.35	0.70
BMC-1/S-50	435	0.53	0.21	0.32
BMC-1/S-60	194	0.30	0.03	0.27

S_{BET} is the specific BET surface area; V_t is the total specific pore volume; V_s is the specific pore volume of the small pores; V_l is the specific pore volume of the large pores.

3.3.1.3 Electrochemical properties of BMC-1/S-x (x = 40, 50 and 60) electrodes

Electrochemistry of the C/S composites was evaluated with metallic lithium as the anode in coin cells, and LiTFSI in 1,3-DOL and DME was selected as the electrolyte to optimize the high rate performance of the cells.[22,23,24]

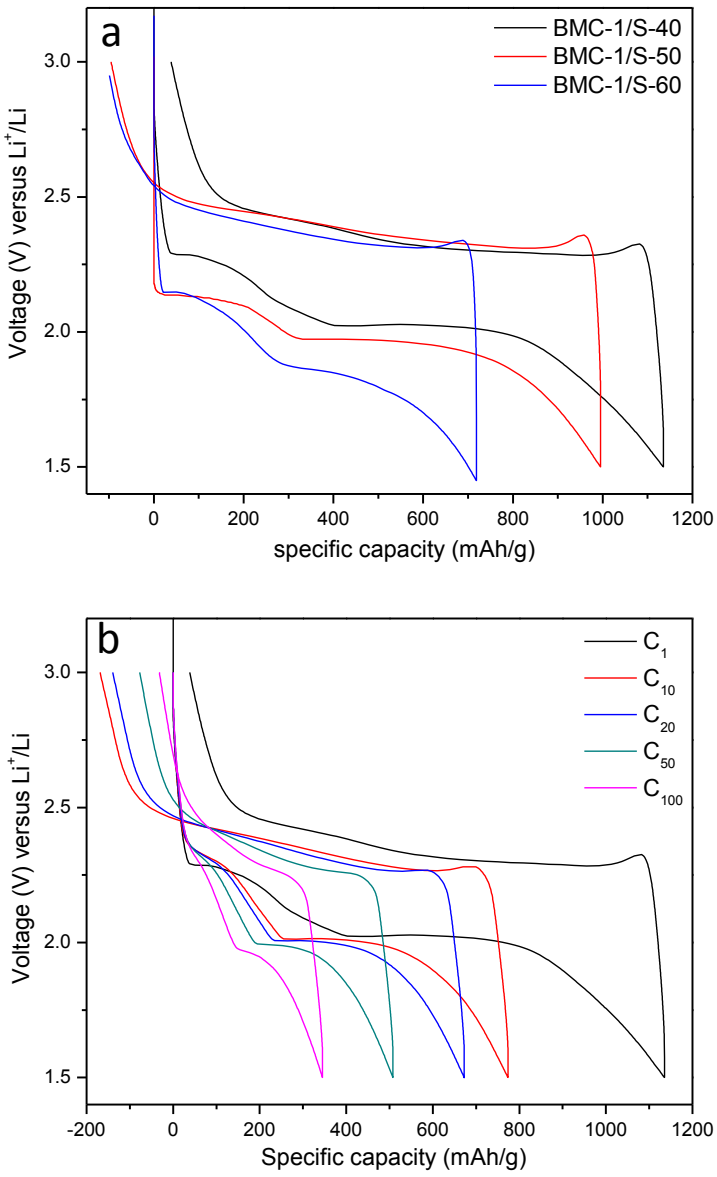

Figure 3.13 (a) Discharge-charge profiles of the three BMC-1/S samples and (b) discharge-charge profiles BMC-1/S-40 at various cycles at C rate.

The voltage vs. capacity discharge profiles of the three BMC-1/S samples on the first cycle at a 1C discharge rate (two Li in one hour, 1675 mA/g) are shown in Figure 3.13a. The initial discharge capacity of BMC-1/S-40 sample was 1135 mAh/g and the curve displays two plateaus at 2.0 V and 2.3 V, indicative of the two stages of the reduction of sulfur. At the higher voltage, elemental sulfur S_8 is reduced to S_n^{2-} ($n > 4$) and balanced by lithium ions to form lithium polysulfides Li_2S_n. These long chain polysulfides are further reduced to Li_2S_2 or Li_2S at low potential (<2.3 V). The charge curve also displays two plateaus at 2.3 V and 2.4 V, which corresponds to the oxidation of Li_2S_2 and Li_2S to elemental sulfur. It is noted that the initial profile does not show any overcharge capacity like other cells reported previously,[25,26] which means the polysulfide shuttle is completely inhibited. The slight irreversible capacity of ~50 mAh/g is probably caused by Li_2S. As described in Chapter 1, the conversion between Li_2S and Li_2S_2 is a diffusion controlled reaction, and it is the most difficult among the whole redox reactions at the cathode. In this case, there is always a little amount of Li_2S remaining after charge which becomes inactive materials. Initial charge-discharge profiles of BMC-1/S-50 and BMC-1/S-60 exhibit similar curves like BMC-1/S-40 with capacities of 995 mAh/g and 718 mAh/g, but the discharge plateaus are a little lower for both. Additionally, unlike BMC-1/S-40, an overcharge capacity of ~120 mAh/g exists for either of the two samples, probably resulted from the dissolution sulfur coating on the external surface of the BMC-1. Overcharge capacity is also observed on the following cycles of BMC-1/S-40 as shown in Figure 3.13b, implying that the dissolution and shuttle of polysulfide species took place step by step on cycling.

The cycling stability of the three cathodes BMC-1/S-40, and BMC-1/S-50 and BMC-1/S-60 studied at a discharge/charge rate of 1C are shown in Figure 3.14. The initial capacity is closely related to the amount of sulfur loading. Higher sulfur content results in a lower initial capacity, which is in agreement with previous findings.[3] After 100 cycles, the BMC-1/S-40 cell retains a capacity of 345 mAh/g, demonstrating a relatively low stability among the three samples. The BMC-1/S-60 cathode has the best cycling performance, but the initial capacity was only 718 mAh/g. When both capacity and cycling stability are considered, BMC-1/S-50 exhibits the best electrochemical performance. This cell had an initial capacity of 995 mAh/g and maintains a capacity of 550 mAh/g after 100 cycles at a high charge/discharge rate of 1C. The details are summarized in Table 3.2.

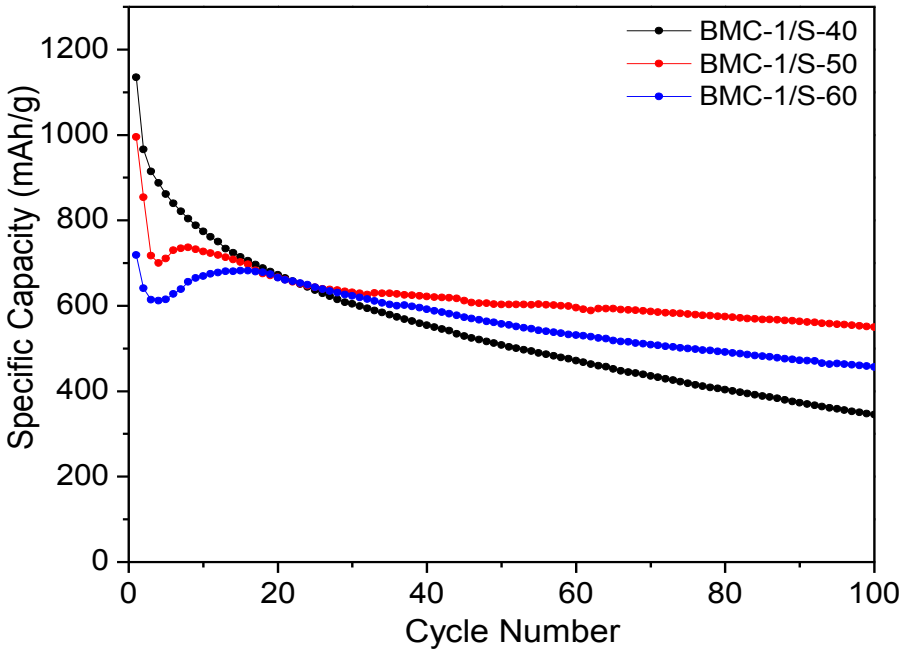

Figure 3.14 Cycling performance of the three BMC-1/S samples at C rate.

Table 3.2 Summary of capacity retention of BMC-1/S-40, BMC-1/S-50 and BMC-1/S-60.

	$C_{initial}$ (mAh/g)	C_{100} (mAh/g)	$C_{100}/C_{initial}$
BMC-1/S-40	1135	345	30.4%
BMC-1/S-50	995	550	55.3%
BMC-1/S-60	718	457	63.6%

$C_{initial}$ is the initial discharge capacity and C_{100} is the discharge capacity at 100 cycles.

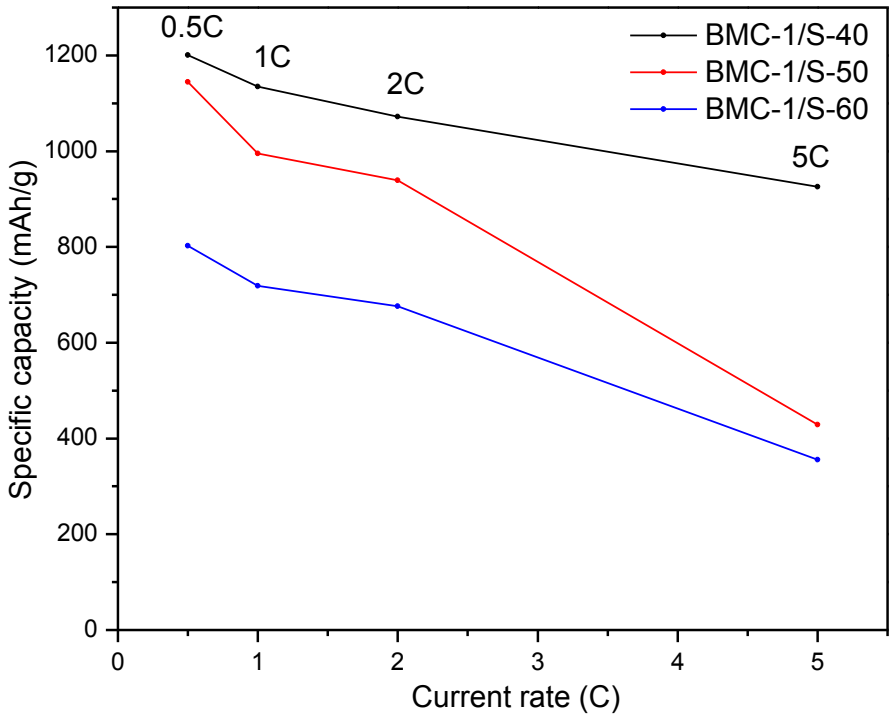

Figure 3.15 Rate capabilities of the three BMC-1/S samples.

BMC-1/S-40 shows good rate capability even at 5C (8375 mA/g) in which the initial discharge capacity is 925 mAh/g (Figure 3.15, black curve). As for BMC-1/S-50 and BMC-

1/S-60, high capacities are obtained up to 2C (3375 mA/g), but they distinctly drop down when the rate is up to 5C. Less sulfur in the C/S composites allows a good contact with carbon and improves the efficiency of the active materials at the cathodes. This probably explains the different performance between BMC/S-40 and the other two samples at higher current densities.

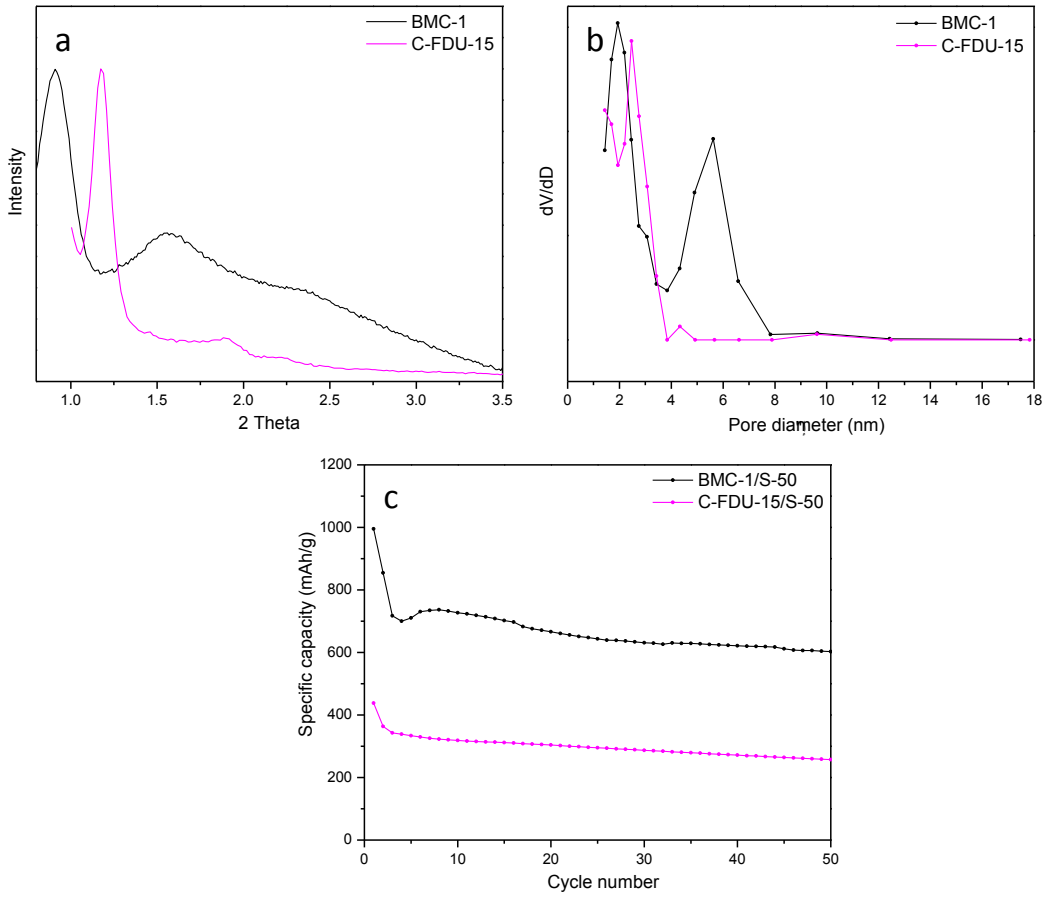

Figure 3.16: (a) Low angle XRD patterns, (b) pore size distribution and (c) Cycling performance of BMC-1/S-50 and C-FDU-15/S-50 at C rate.

The excellent performance of the BMC-1/S composite cathodes is attributed to the complex bimodal structure of the mesoporous carbon. This advanced carbon was prepared by using triblock-copolymer as a template and low molecular phenolic resin and TEOS as precursors. The addition of TEOS serves as an internal stabilizer to reduce the shrinkage of the structure. The "mother material" of this bimodal carbon, C-FDU-15[15, 27], also exhibits well-ordered porous structure (Figure 3.16a) and uniform pore size of around 2.7 nm (Figure 3.16b), while our BMC-1 has large cylindrical pores of 5.6 nm. These facilitate the transportation of electrolyte and solvated Li-ions, especially at a high current rate, which explains the distinct difference of BMC-1/S-50 and C-FDU-15/S-50 in electrochemistry (Figure 3.16c).

More importantly, unlike activated carbons (Ref. 3) which acquire small pores through treatment with KOH, the uniform small pores of BMC-1 are derived from the removal of homogeneous nanocrystalline silica that has a particle size of 2.0 nm. These small pores form numerous "holes" in the walls of the large hexagonal cylindrical pores and interconnect the isolated cylindrical pores. This unique structure also facilitates the transfer of Li ions in the electrolyte. As discussed above, previous studies[28,29] have shown that super-micropores, or small mesopores can serve as micro-containers for the polysulfides and mitigate the shuttle phenomenon. The numerous small pores of this carbon, which contribute to over half of the total pore volume, are believed to have a similar role.

The comparison of the electrochemical performance of BMC-1/S-60 and MP-C-36*/S-60 is shown in Figure 3.17. In spite of the comparable specific surface area and pore volume of the two carbons, the discharge capacities of the 1st and 50th cycles of MP-C-36*/S-60 are 618

mAh/g and 453 mAh/g respectively, which are 86% and 81% of the corresponding capacities of BMC-1/S-60. These results clearly show the importance of optimization of the bimodal carbon. As the molar ratio of phenolic resin to F127 surfactant in MP-C-36* is lower than that of the BMC-1, the carbon obtained is less dense and its electronic conductivity is predicted to be poorer than BMC-1. Furthermore, the modification creates more small pores in BMC-1, which benefit both high rate discharge and maintenance of polysulfide species at the cathodes.

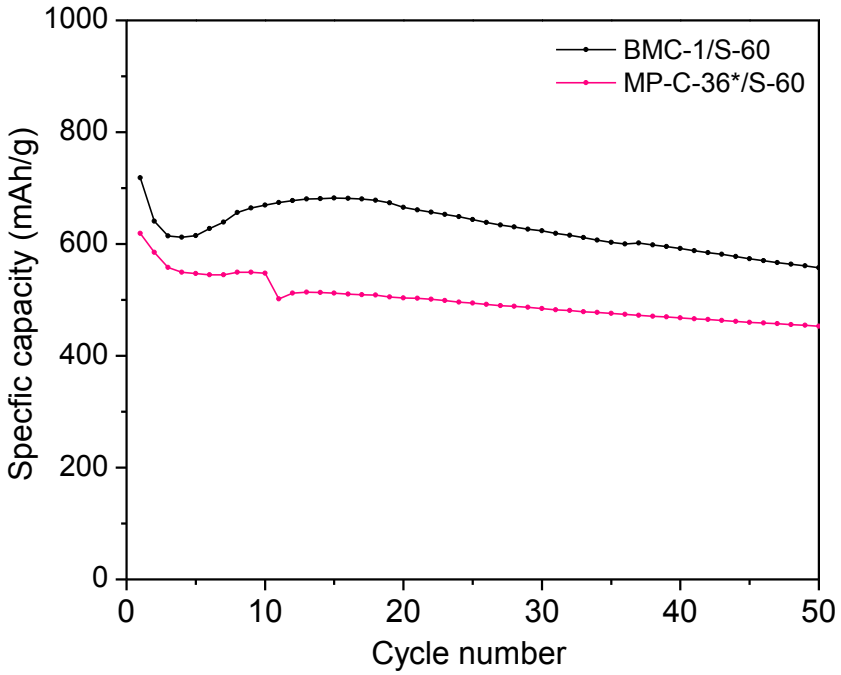

Figure 3.17 Comparison of the cycling performance of BMC-1/S-60 and MP-C-36*/S-60 at C rate.

It is known that doping with absorbents or surface modification of the host carbon can improve both electronic and ionic conductivity and immobilize polysulfides.[30,31] For example, previous work of our lab shows that functionalizing the carbon with polyethylene glycol (PEG) increases the surface hydrophilicity and traps more polysulfides within the cathode.[9] More

recently, mesoporous silica that has pore dimensions on the order of the size of the intermediate polysulfide anions were developed as an additive for sulfur/carbon cathodes to improve the cycling stability.[32] It was found that their relatively high hydrophilicity and large uniform mesopores can be tailored to the absorption of the polysulfide species in the cathodes via weak binding on absorption, and also permit reversible desorption and release during the reversible electrochemical redox reactions. Here, mesoporous silica SBA-15 is employed as an additive to optimize the sulfur cathodes.

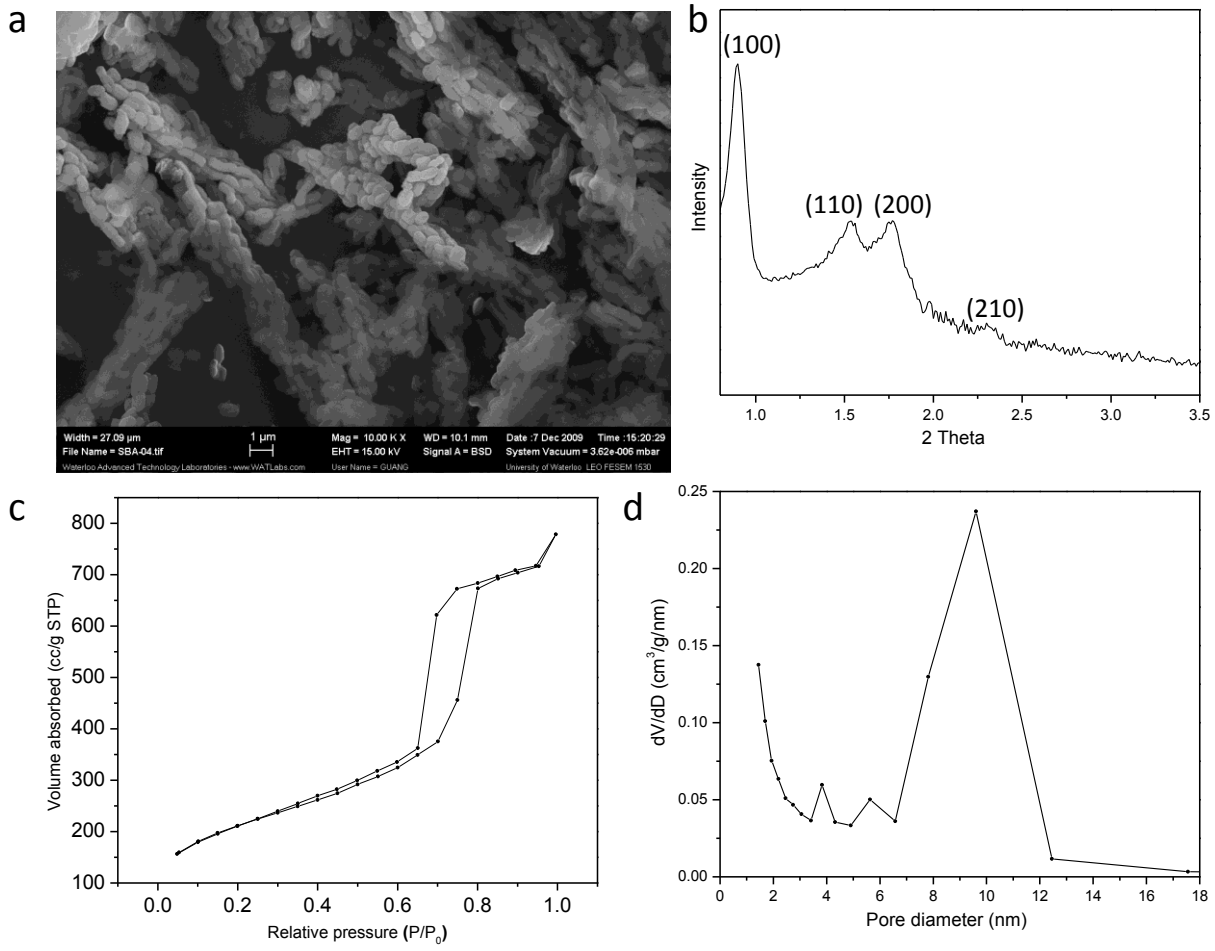

Figure 3.18: (a) SEM image; (b) low angle XRD pattern; (c) N_2 sorption isotherm and (d) pore size distribution analysed by the BJH method of the as-prepared SBA-15.

Figure 3.18 summarizes the physical characters of SBA-15. The particle size of this mesoporous silica is in sub-micron, as shown from the SEM image (Figure 3.18a). The low angle XRD pattern (Figure 3.18b) displays four well-resolved diffraction peaks associated with 100, 110, 200 and 210 reflections of 2D hexagonal symmetry. The long-range order porosity is also confirmed by the N_2 sorption isotherm (Figure 3.18c). This type IV curve with a sharp capillary condensation step at P/P_0 = 0.68-0.80 and an H_1-type hysteresis loop are typical of large cylindrical mesoporoes. BET specific surface area and pore volume are 760 m^2/g and 1.2 cm^3/g, respectively. The mean pore size is calculated to be 9.5 nm based on BJH method, as shown in Figure 3.18d.

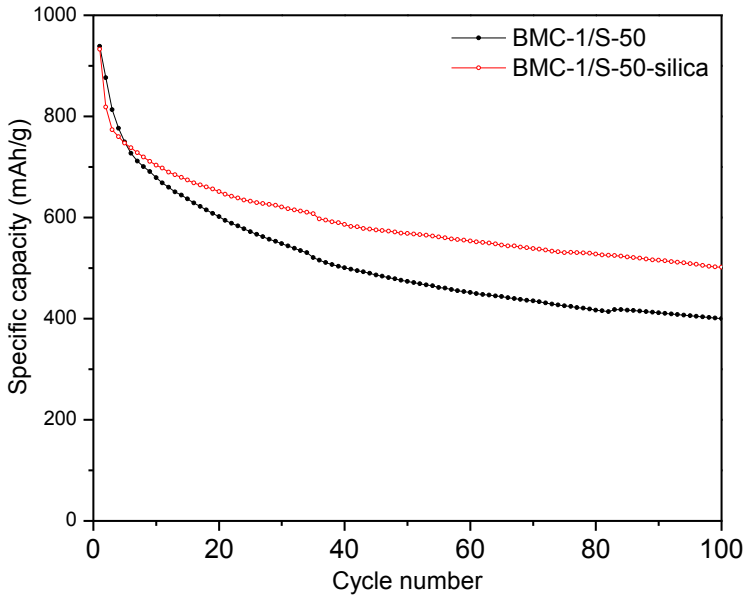

Figure 3.19 Cyclability of BMC-1/S-50 electrodes with and without the SBA-15 additive. Cells were operated at a current rate of 2C.

By doping 10 wt% of SBA-15 into the BMC-1/S-50 composite, the initial discharge capacity of the cell is almost the same as the one without the additive (932 mAh/g and 938 mAh/g, respectively in Figure 3.19) at high discharge rate of 2C (3340 mA/g). However, the

difference is very obvious after 100 cycles. The doping cell shows a remaining capacity of 501 mAh/g, which is more than 25% higher than the cell without the additive (400 mAh/g).

3.3.2 Modified bimodal mesoporous carbon M-BMC-1

3.3.2.1 Influence of templates, additives and precursor ratios on the porous structure

In spite of the good performance of the C/S electrodes, the BMC-1/60-S sample showed relatively low discharge capacity with respect to BMC-1/S-40 and BMC-1/50. This is because it is difficult to make sulfur diffuse into the pores completely when it counts 60 wt% in the C/S composite. The density of molten sulfur is 1.82 g/cm^3 and the specific pore volume of BMC-1 is 2.0 g/cm^3. Ideally, as much as 78 wt% of sulfur can be accommodated into the pores. However, wetting all the pores with sulfur in reality is very difficult, especially when the particle size of the BMC-1 framework is in microns. There are two methods to solve this problem: (1) by increasing the pore volume and surface area, and (2) by decreasing the particle size to nanometers to facilitate the diffusion of sulfur. The first approach is discussed in this section, and the latter will be in the next chapter.

Previous investigations have shown that hydrophobic additives like TMB and TIPB (also called swelling agents), can serve as pore expanders during the preparation of mesoprous silica.[33,34] Moreover, these additives also help improve the ordering of the porous structure which leads to higher surface area and pore volume.[35,36] Here, we investigate the influences of three different additives: decane, 1,3,5-trimethylbenzene (TMB) and 1,3,5-triisopropylbenzene

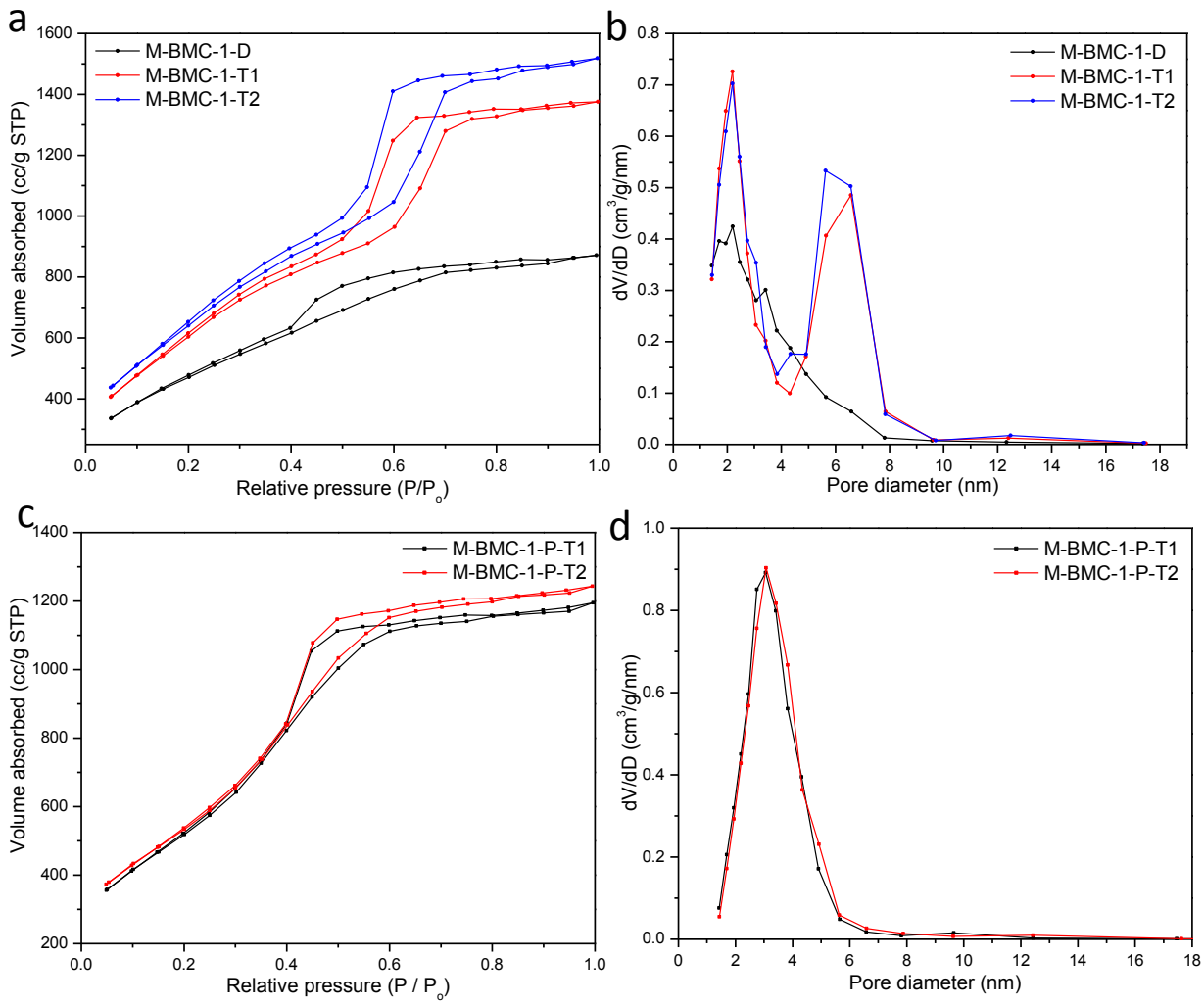

Figure 3.20 N_2 sorption isotherms (a and c) and the corresponding pore size distribution curves by the BJH method (b and d). Figure a and b exhibit the influence of the different additives and figure c and d show the influence of the different templates.

(TIPB). The modified carbons synthesized with 0.5g of the above additives were denoted as M-BMC-1-D, M-BMC-1-T1 and M-BMC-1-T2. Figure 3.20a shows that with TMB and TIPM added in the precursor solutions, the N_2 isotherm curves display typical type IV curves and H_1-type hysteresis loop, similar with BMC-1. The pore size distribution curves of the two samples

display almost the same peak at 2.2 nm (Figure 3.20b), indicating a slight pore expansion compared with BMC-1 (2.0 nm). The mean size of the large pores of M-BMC-1-T1 is 6.5 nm, about 1 nm larger than BMC-1. As for M-BMC-1-T2, the large pore is partially expanded, but the effect is not as obvious as M-BMC-1-T1. Very different with the roles of TMB and TIPB, the regularity of the hexagonal structure was destroyed by the addition of decane, which are evidenced by both Figure 3.20a and b.

The influence of TMB and TIPB were also studied with P123 employed as the template. The mass ratio of the phenolic resin and P123 was 1:1. The N_2 sorption isotherms of these samples exhibit similar hysteresis loop of small pore mesoporous materials like MCM-41[37] or CMK-3[38] (Figure 3.19c). The pore diameter is 3.5 nm, while no bimodal structure is observed, as shown in Figure 3.19d. It is known that the main difference of P123 and F127 is the length of the hydrophilic PEO parts, which plays an important role in the pore size of the final product.[39] Even with the pore expanders such as TMB and TIPB added, relatively small pores in M-BMC-1-P-T1 and M-BMC-1-P-T2 still yielded. Although there is only one peak in the pore size distribution curve, there must be plenty of "voids" on the walls of both samples in term of the high surface areas (~2000 m^2/g) and large pore volumes (~2.0 cm^3/g).

Influences of ratios between carbon precursor phenolic resin, template F127 and additive TIPB were studied in Figure 3.21. By decreasing phenolic resin solution to 3.5 g, the N_2 sorption curve does not change too much, but with the increase of the resin solution to 7.5 g, the shape of the hysteresis loop is not a typical H_1-type, indicating the formation of a mixture phase (hexagonal *p*6*mm* and cubic *Im*-3*m*), as shown in Figure 3.21a. The effect of the TIPB on pore size expansion is partially offset by this phase transformation (Figure 3.21b).

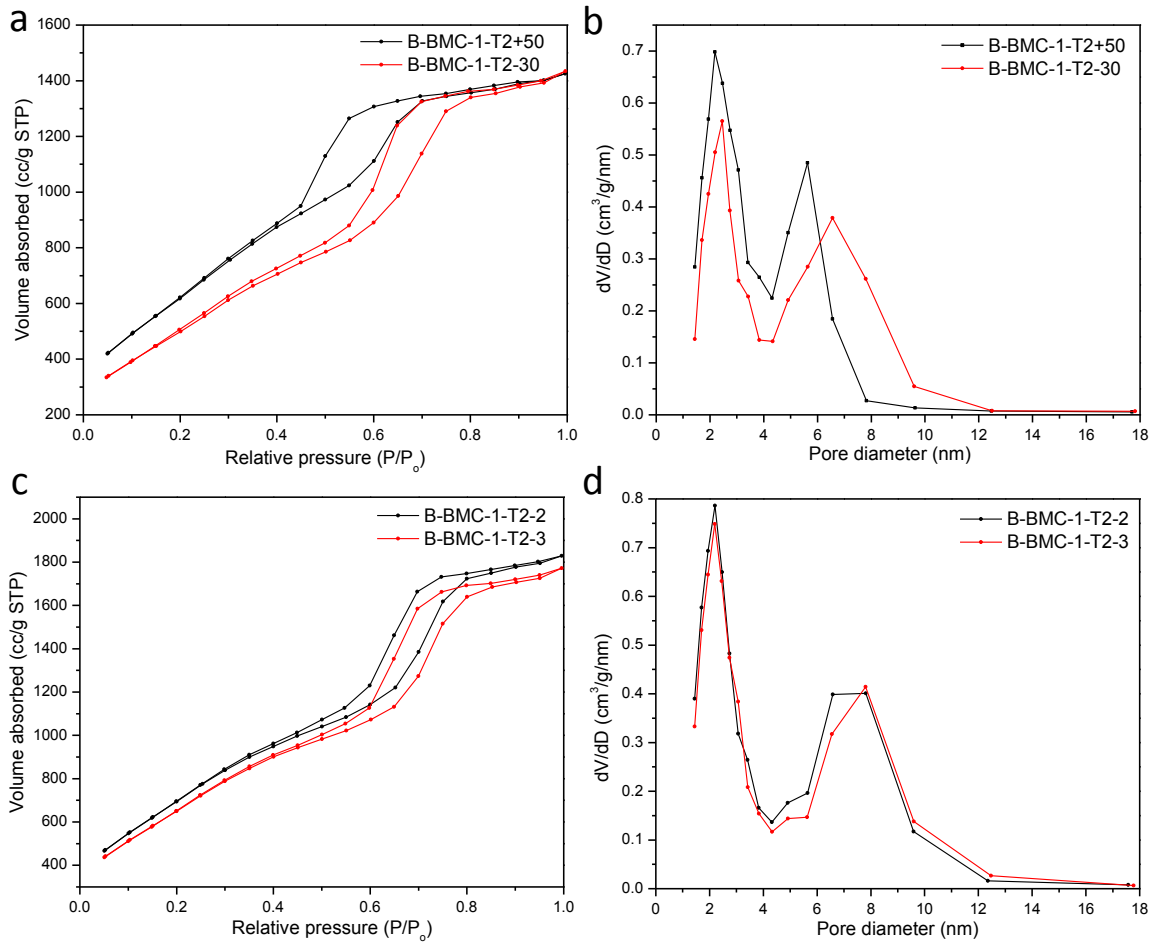

Figure 3.21 N_2 sorption isotherms (a and c) and the corresponding pore size distribution curves by the BJH method (b and d). Figure a and b exhibit the influence of different amounts of resin solutions and figure c and d show the influence of different amounts of TIPB.

By increasing the amount of TIPB to1.0 g, pore volume and surface area (Figure 3.21c) of the carbons were greatly enlarged. For example, the total pore volume of M-BMC-1-T2-2 is ~3.0 g/cm^3, 50% larger than for BMC-1 and 20% larger than for M-BMC-1-T2. With even more TIPB (1.5g), the pore size is expanded to ~8 nm (Figure 3.21d), but the pore volume and

surface area become to decrease. The physical characteristics of all the M-BMC-1 carbons are summarized in Table 3.3.

Table 3.3 Physicochemical properties of the BMC-1 and M-BMC-1 carbons (see text).

Samples	Templates	Additives	M_R (g)	M_A (g)	S_{BET} (m^2/g)	V (cm^3/g)	D_m (nm)	
							D_L	D_S
BMC-1	**F127**	**-**	**5.0**	**0.5**	**2300**	**2.0**	**5.6**	**2.0**
B-BMC-1-D	**F127**	**decane**	**5.0**	**0.5**	**1731**	**1.3**	**3.4**	**2.2**
B-BMC-1-T1	**F127**	**TMB**	**5.0**	**0.5**	**2310**	**2.3**	**6.5**	**2.2**
B-BMC-1-T2	**F127**	**TIPB**	**5.0**	**0.5**	**2437**	**2.5**	**5.6-6.5**	**2.2**
B-BMC-1-P-T1	**P123**	**TMB**	**5.0**	**0.5**	**1970**	**2.0**	**3.0**	**-**
B-BMC-1-P-T2	**P123**	**TIPB**	**5.0**	**0.5**	**2012**	**2.1**	**3.0**	**-**
B-BMC-1-T2-30	**F127**	**TIPB**	**3.5**	**0.5**	**1915**	**2.4**	**6.5**	**2.2**
B-BMC-1-T2+50	**F127**	**TIPB**	**7.5**	**0.5**	**2367**	**2.4**	**5.6**	**2.2**
B-BMC-1-T2-2	**F127**	**TIPB**	**5.0**	**1.0**	**2673**	**3.0**	**6.5-7.8**	**2.2**
B-BMC-1-T2-3	**F127**	**TIPB**	**5.0**	**2.0**	**2503**	**2.9**	**7.8**	**2.2**

M_R is the mass of phenolic resin solution; M_A is the mass of assistive; S_{BET} is the specific BET surface area; V is the total specific pore volume; D_m is the mean pore diameter; D_L is the mean large pore diameter and D_S is mean small pore diameter.

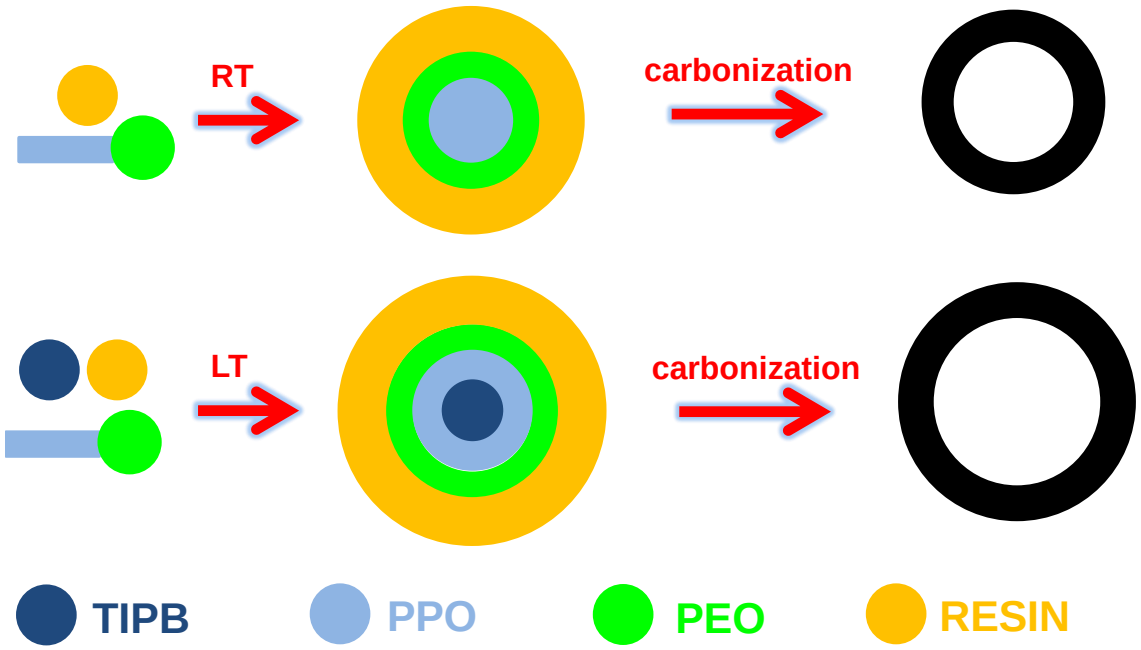

Figure 3.22 Scheme of the formation of porous structure with and without additives such as TIPB. RT is room temperature and LT is low temperature (13 ℃).

The pore expansion mechanism can be illustrated in Figure 3.22. For the synthesis of BMC-1, the hydrophobic PPO blocks of co-polymer F127 stayed at the core of a micelle, and the hydrophilic PEO blocks formed hydrogen bonds with phenolic resin (and also the hydrolyzed TEOS). After polymerization and carbonization, a porous carbon was obtained. Once a certain amount of pore expander (like TIPB) was added in the system, it could penetrate into the micelles and agglomerate with the PPO blocks at the core of the micelles. Therefore, the pore size of the carbon enlarged due to the expansion of the micelles. It should be noted that temperature played a significant role in obtaining large pores during the synthesis process. Previous study has shown that low temperature facilitated the additive (pore expander) to penetrate through the EO blocks because the association number of the micelles remarkably

decreased from 20 to 10 ℃.[40] In our experiments, the temperature was precisely controlled at 13-14 ℃ by using a p-xylene/ice cooling bath to allow the penetration of TIPB through the hydrophilic EO blocks .

Among all the M-BMC carbons, M-BMC-1-T2-2 has highest surface area and pore volume (Table 3.3). The large regularity of the porosity of this sample is confirmed by the low angle XRD pattern, as shown in Figure 3.23. Compared with BMC-1, the three peaks of M-BMC-1-T2-2 shift to the low angle by ~0.5 °. For example, the 110 peak is at 0.85 °, which gives the unit cell parameter (a) of 11.9 nm, larger than BMC-1.

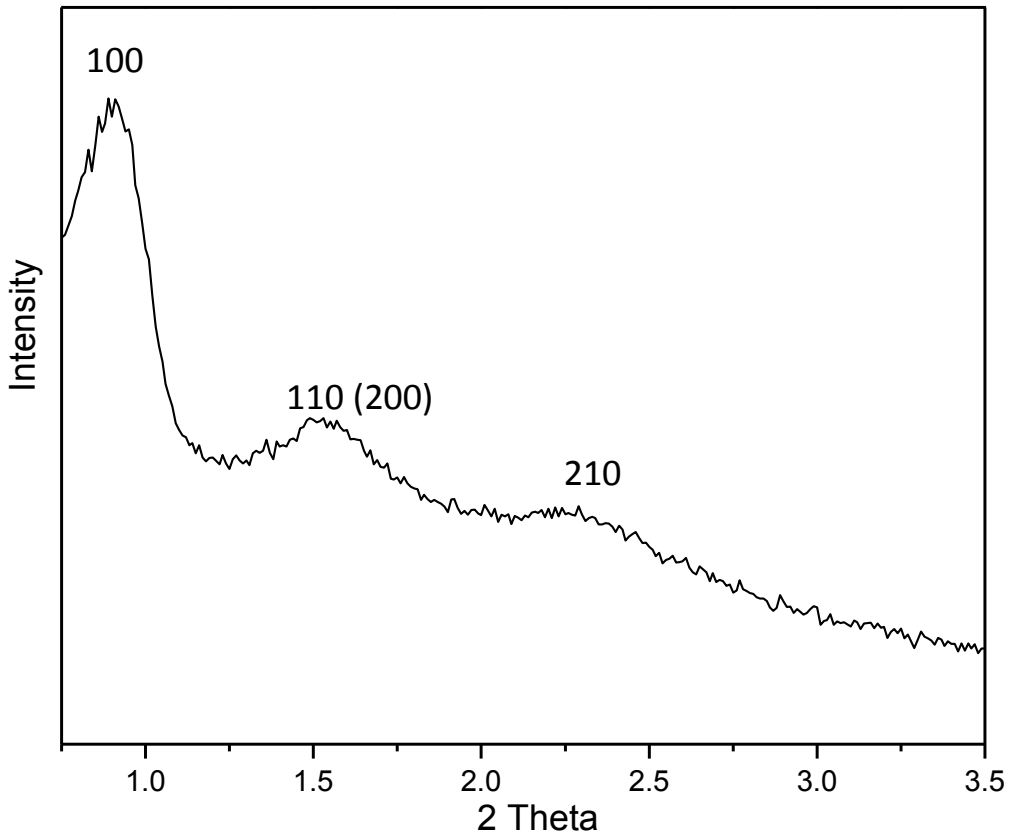

Figure 3.23 Low angle XRD pattern of the M-BMC-1-T2-2.

3.3.2.2 Electrochemical performance of M-BMC-1/S-x (x=50, 60, 70) composites

Since the surface area and pore volume are much improved than for BMC-1, three M-BMC-1-T2-2/S nanocomposites with higher sulfur content 50 wt%, 60 wt% and 70 wt%, were prepared by the method described above. The samples were denoted as M-BMC-1/S-50, M-BMC-1/S-60 and M-BMC-1/S-70. The average particle size of M-BMC-1/S-70 is a little smaller than M-BMC-1T2-2, as shown in Figure 3.24. This is probably due to the extra grinding of the C/S in the mortar. In addition, no sulfur agglomeration is detected.

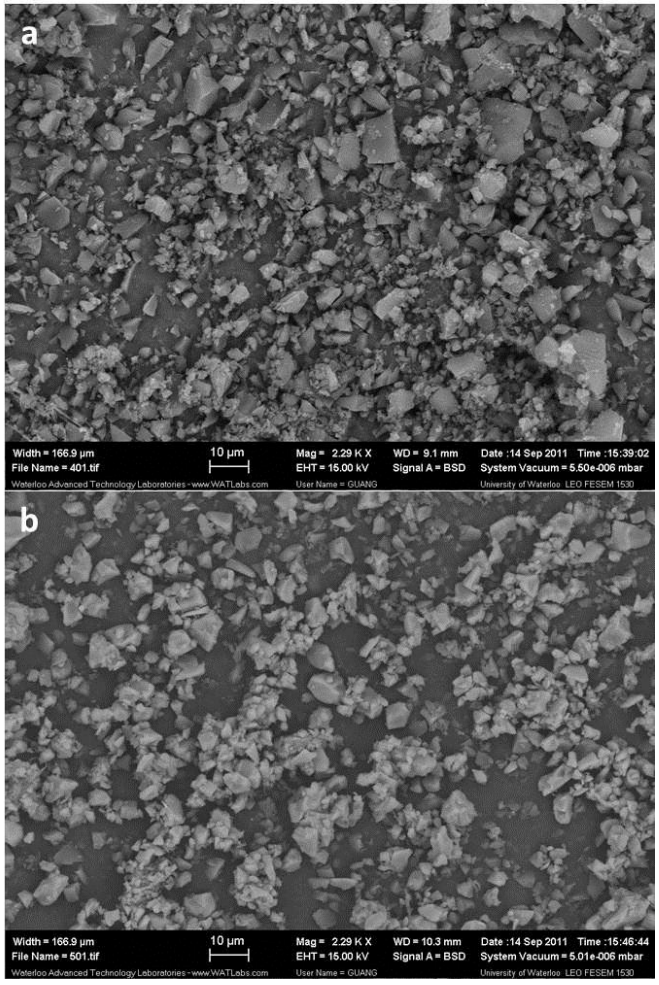

Figure 3.24 SEM images of (a) M-BMC-1-T2-2 and (b) M-BMC-1/S-70.

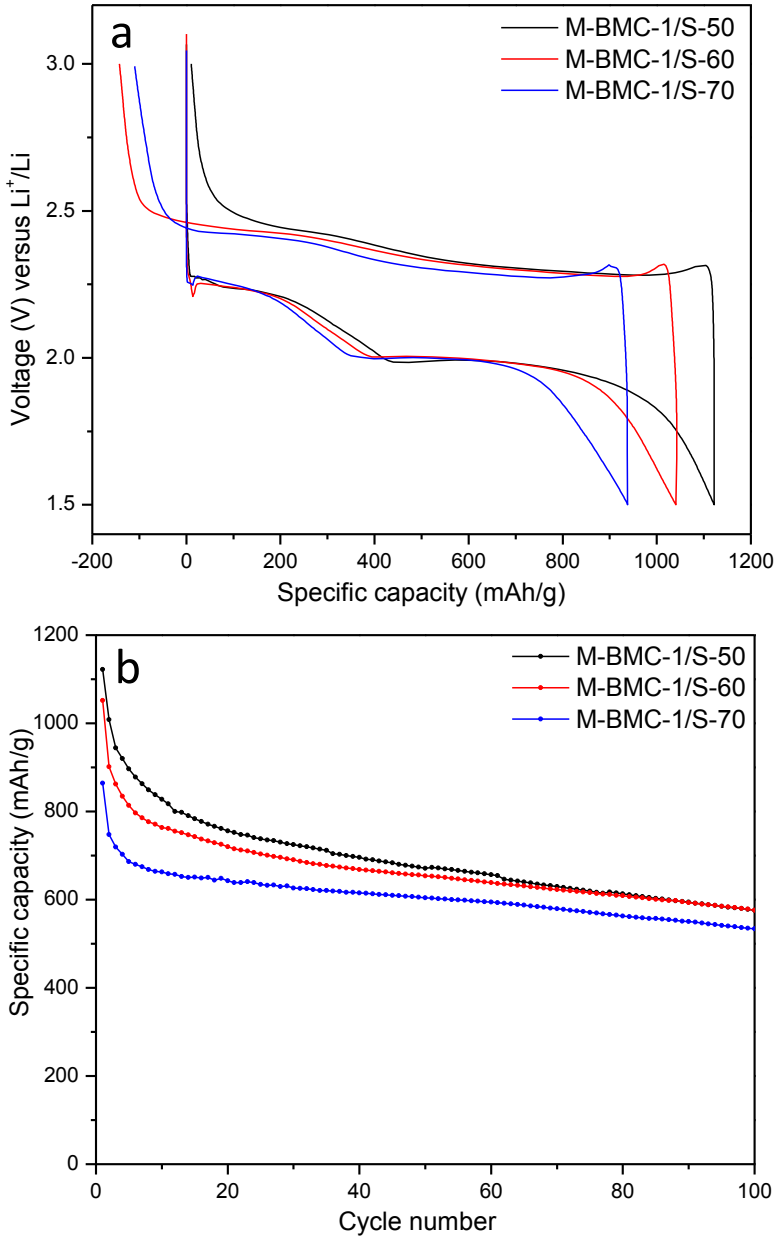

Figure 3.25 (a) Initial charge-discharge profiles and (b) cycling stability of the three samples at C rate.

All the initial charge-discharge profiles of the three samples (Figure 3.25a) exhibit two plateaus similar like BMC-1/S composites. However, the capacities of the M-BMC-1/S samples are much higher than those BMC-1/S composites that have the same sulfur content.

For example, the capacities of M-BMC-1/S-50 and M-BMC-1/S-60 are 1122 mAh/g and 1051 mAh/g (995 mAh/g and 718 mAh/g for BMC-1/S-50 and BMC-1/S-60, respectively). Even with 70 wt% sulfur, M-BMC-1/S-70 displays an initial discharge capacity of 864 mAh/g, higher than BMC-1/S-60. Also different with BMC-1/S-50, no overcharge capacity is observed on the first cycle on M-BMC-1/S-50, indicating a more homogeneous distribution of sulfur into the pores. After 100 cycles, all the M-BMC-1/S samples retain capacities above 530 mAh/g (Figure 3.25b). The comparison between M-BMC-1/S and BMC-1/S composites is clearly demonstrated in Figure 3.26 and summarized in Table 3.4.

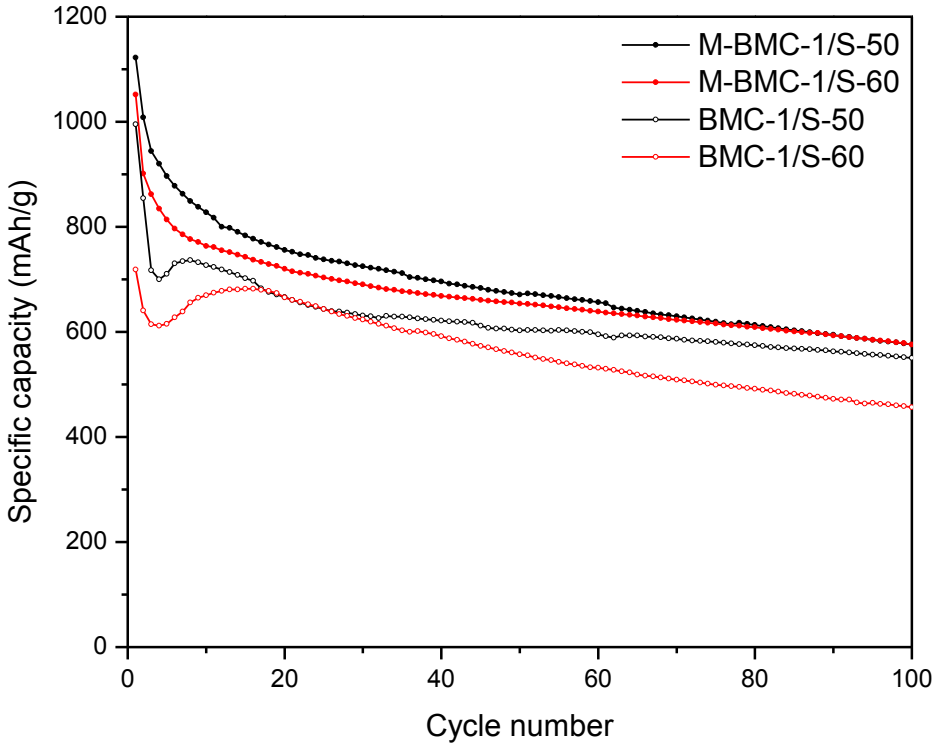

Figure 3.26 Cycling performance of M-BMC-1/S-60 and BMC-1/S-60 at C rate.

Table 3.4 Summary of capacity retention of M-BMC-1/S and BMC-1/S composites with 50 wt% and 60 wt% sulfur.

	$C_{initial}$ (mAh/g)	C_{100} (mAh/g)	$C_{100}/C_{initial}$
M-BMC-1/S-50	1122	576	51.3%
M-BMC-1/S-60	1051	576	54.8%
BMC-1/S-50	995	550	55.3%
BMC-1/S-60	718	457	63.6%

$C_{initial}$ is the initial discharge capacity and C_{100} is the discharge capacity at 100 cycles.

The different electrochemical results of the two BMC-1/S and M-BMC-1/S composites should be attributed to the variations in the pore structure. First of all, larger pore volume and surface area of the M-BMC-1 allowed more sulfur homogeneously distributed into the pores. This is the key factor of higher capacities of M-BMC-1/S over BMC-1 when the sulfur content is the same for both composites. Figure 3.27 compares the SEM images of M-BMC-1, M-BMC-1/S-60 and BMC-1/S-60 at high magnifications. In spite of the almost identical surface morphology of M-BMC-1 and BMC-1, M-BMC-1/S-60 and BMC-1/S-60 look quite different. First, the different brightness of the samples in Figure 3.27b and c indicates the formation of a thicker layer of sulfur on the surface of the BMC-1/S-60 sample. Additionally, many small bumps (~100 nm) and wires (~20 nm) are clearly seen in Figure 3.27c, revealing the existence of sulfur residues. Apparently, sulfur had a better distribution in the M-BMC-1/S-60 sample.

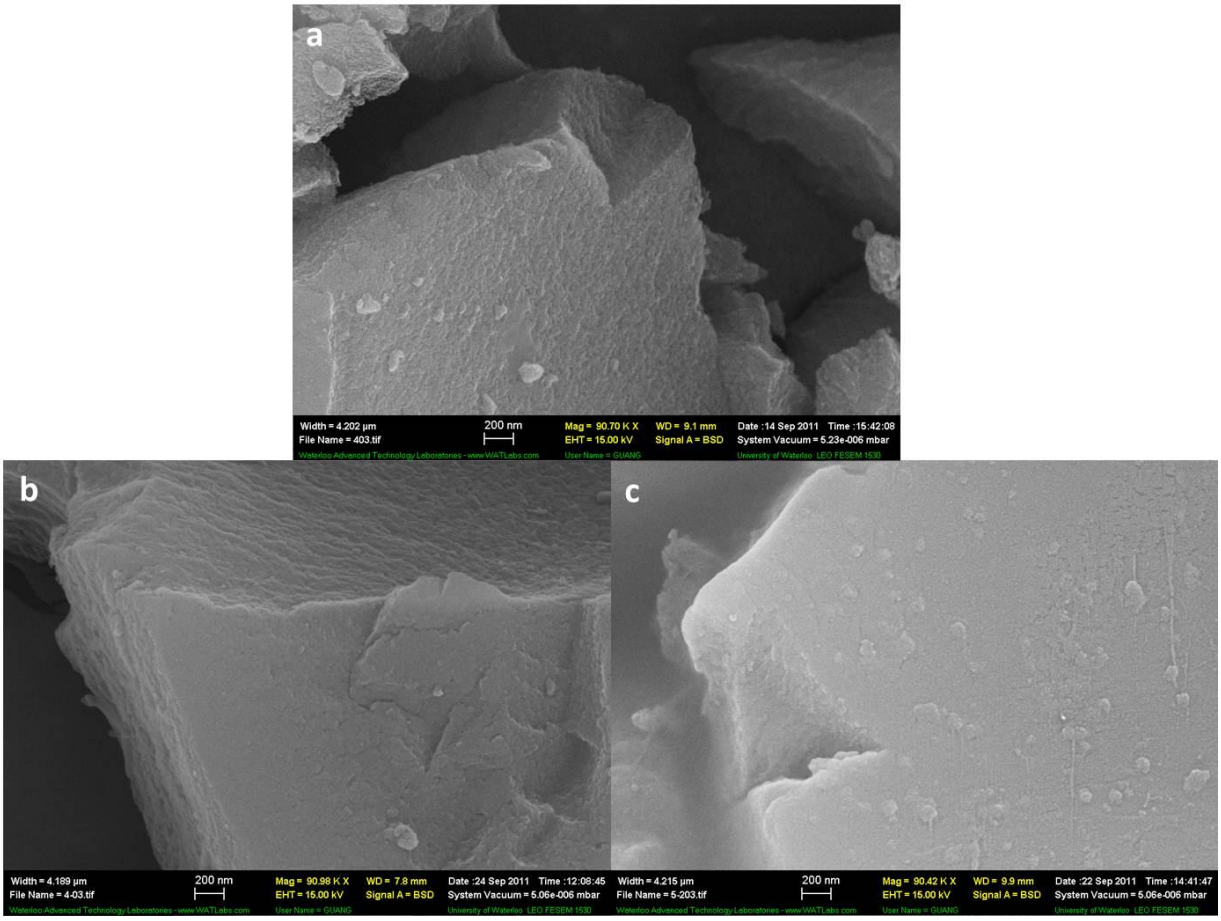

Figure 3.27 SEM images of (a) M-BMC-1, (b) M-BMC-1/S-60 and (c) BMC-1/S-60.

Secondly, the additive TIPB distinctly changed the volume ratio of small pores and large pores in M-BMC-1, where the small pore only accounts for less than ¼ of the total pore volume (0.65 cm^3/g). The great volume expansion of the large pores facilitated the sulfur distribution into the pores and transportation of lithium ions, but on the other side, the reduced ratio of small pores affected the retention of sulfur polysulfides at the cathodes. Therefore, capacity fading of the M-BMC-1/S composites is relatively faster than in BMC-1 ($C_{100}/C_{initial}$), as shown in Table 3.4.

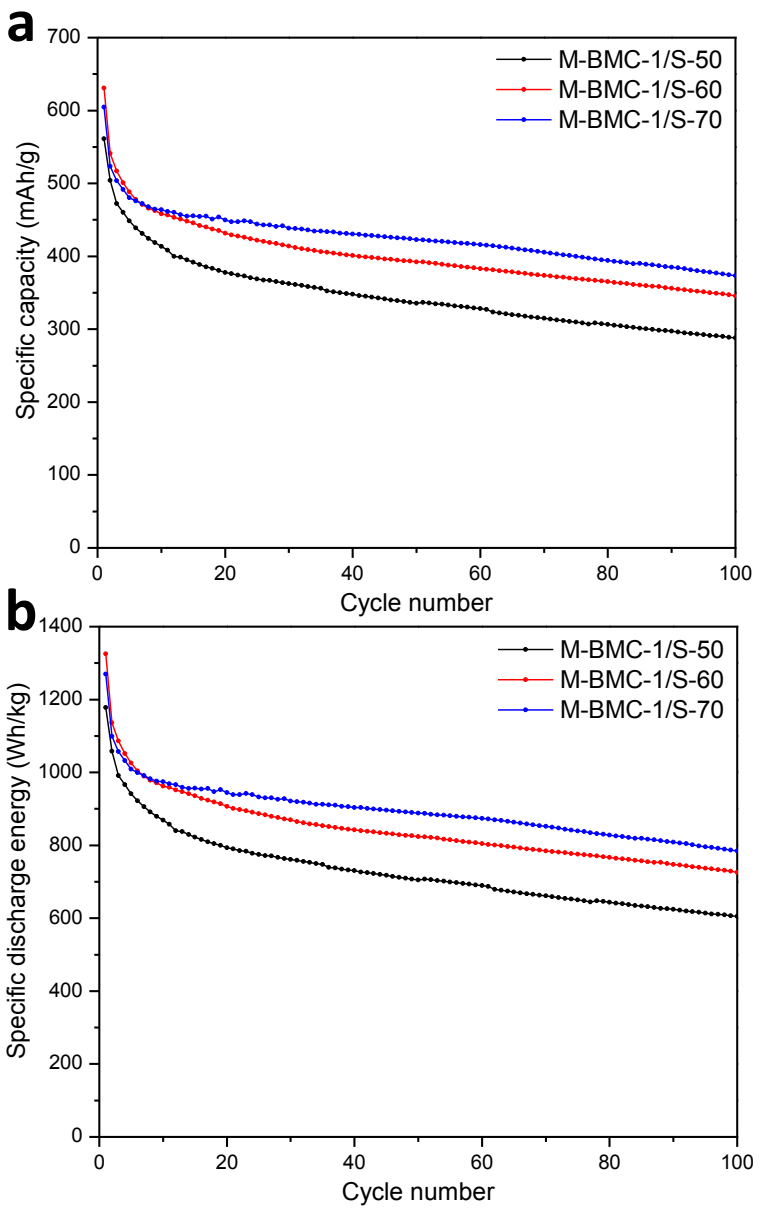

Figure 3.28 Specific discharge capacities and energy densities based on C/S composites at C rate. The energy densities were calculated by using an average voltage of 2.1V.

In order to compare the performance of the C/S electrodes and lithium ion battery cathodes, the specific discharge capacity and energy density were calculated based on the M-BMC-1/S composites (Figure 3.28). Among the three electrodes, M-BMC-1/S-70 exhibits the best

comprehensive property than the other two composites, thanks to its higher sulfur content (70 wt%) than the other two samples. The comparison of this electrode and other common studied lithium-ion battery cathodes is summarized in Table 3.5. In spite of relatively fast fading and low cell voltage, the M-BMC-1/S-70 cathode exhibits the highest capacity and energy density over the first 100 cycles than any others.

Table 3.5 Electrochemical properties of M-BMC-1/S-70 and other lithium ion battery cathodes (Lithium ion battery data is obtained from Wikipedia).

	Specific capacity (mAh/g)	Voltage (V)	Specific energy density (Wh/kg)
M-BMC-1/S-70	605-373*	2.1**	1270-784*
$LiCoO_2$	140	3.7	518
$LiMn_2O_4$	100	4.0	400
$Li(Co_{1/3}Ni_{1/3}Mn_{1/3})O_2$	160	3.6	576
$LiFePO_4$	150	3.3	495

* values of the 1^{st} and 100^{th} cycles

** estimation of average voltage (2.3V and 2.0V)

3.4 Conclusions

Ordered mesoporous carbon BMC-1 was synthesized via the EISA strategy, using soluble phenolic resin the carbon precursor, TEOS as the silicate precursors and triblock copolymer F127 as the template. This carbon has a unique porous structure, which features high specific area (2300 m^2/g), large pore volume (2.0 cm^3/g) and bimodal mesopores (5.6 nm and 2.0 nm).

Carbon/sulfur (C/S) nanocompsoites were prepared with this carbon via a melt-diffusion approach and employed as cathodes of rechargeable lithium sulfur batteries. The initial capacity of BMC-1/S-50 was 995 mAh/g and remains at 550 mAh/g after 100 cycles at a current rate of 1670 mA/g (1C). The good performance of the C/S cathodes is attributed to the bimodal structure of the carbon, and the large number of small mesopores. The small pores interconnect the isolated cylindrical pores (large pores), which facilitates the transfer of polysulfide anions and lithium ions through the large pores. Therefore, high capacity was obtained even at very high current rates. Small mesopores created during the preparation served as containers and confined polysulfide species at the cathode. Further investigation showed that cycling stability was improved by incorporating a porous silica additive in the cathodes.[41]

By using additives like TMB and TIPB, the porous structure of BMC-1 could be further optimized, with the specific surface area and pore volume of M-BMC-1 enlarged to 2673 m^2/g and 3.0 cm^3/g. The corresponding electrodes exhibit a high reversible capacity up to 1122 mAh/g with as much as 70 wt% sulfur incorporated.

Chapter 4

Ordered Mesoporous Carbon Nanoparticles with Specific Morphologies for Li-S Batteries

4.1 Introduction

In the previous chapter, the utilization of ordered mesoporous carbon BMC-1 as a framework of sulfur cathodes has been discussed, and we know that the high surface area, large pore volume, and special bimodal porous structure of this carbon are favorable for good performance of Li-S cells. However, the relatively large particle size of this carbon made the homogeneous distribution of a large amount of sulfur (>50 wt%) into the pores very challenge. In order to solve this problem, there are two options. One is to enlarge the specific pore volume to produce more space for sulfur accommodation, which has been discussed in **Chapter 3**. The other way is to nanosize the carbon particles to reduce the sulfur diffusion path. Only few examples of ordered mesoporous carbon (OMC) nanoparticles have been reported so far, including templating with PMMA colloidal crystals[1] or mesoporous silica nanoparticles[2], aerosol-assisted synthesis[3], ultrasonic emulsification[4] or hydrothermal synthesis[5]. Unfortunately, most of these carbons are unsuitable for applications in Li-S cells, due to low pore volume and/or surface area. Recently, Lei et al.[6] reported the synthesis of 65 nm mesoporous carbon nanospheres, with both 2.7 nm mesopores and high textural porosity (surface area of 2400 m^2/g; total pore volume of 2.9 cm^3/g). These showed promising supercapacitor properties.

In this chapter, nano mesoporous carbon spheres with a bimodal structure were developed and measured as frameworks for sulfur cathodes. The spherical OMC nanoparticles of 300 nm in diameter, prepared by a two-step casting process, exhibited extremely high porosity. The corresponding C/S electrodes showed high reversible discharge capacity of up to 1200 mAh/g and good cycling stability. The performance of the cells could be further improved by either removing the external sulfur on the surface or by adding a thin coating of SiO_x. A comparison between nano-size and bulk carbon reveals that the excellent electrochemical properties of the cells should be attributed to the nanoscale morphology of the mesoporous carbon, which facilitates the preparation of homogeneous C/S composites and aids in charge transfer. The strategy of nanosizing carbon particles is generally applicable to other C/S composites. For example, it also applies to other nanoscale carbon morphologies such as fibres, as long as they have comparable particle size, pore volume and surface area.

4.2 Experimental

4.2.1 Synthesis of mesoporous carbon nanospheres (S-BMC)

For the preparation of PMMA spheres 98 ml of distilled water were degassed with nitrogen for 15 minutes. 5 mg SDS (288.4 g/mol, 0.017 mmol) and 35.5 g MMA (100.1 g/mol, 0.35 mmol) were added. The mixture was held at 90 ℃ for 1 h under reflux conditions in nitrogen atmosphere. The initiator solution containing 56 mg $K_2S_2O_8$ (270.3 g/mol, 0.21 mmol) in 2 ml distilled water was added to the suspension. The white colloidal suspension was washed three times by centrifugation (20 min, 20000 rpm) and redispersed in water. To remove small amounts of larger spheres (> 500 nm), an additional centrifugation and washing step was

performed (2 min, 5000 rpm). The final solution exhibited a sphere concentration of about 20 wt%. The colloidal stock solution was dried in a plastic petri dish for 12 h at 60 °C. The obtained pieces of densed packed colloidal crystals had a size of several mm^3 and are directly used for further liquid impregnation of a silica sol-gel solution.

For silica sol-gel solution 4 ml of ethanol were mixed with 6 ml TEOS (26.9 mmol), 3 ml water and 1 ml concentrated hydrochloric acid (1.19 g, 12 mmol HCl). The colloidal crystal structures were crushed to powders and put on a filter paper in a Büchner funnel. While applying vacuum to the funnel, the silica sol-gel solution was dripped over the surface to completely wet the PMMA. The silica/PMMA composite was heated to 550 °C with a ramp of 1 °C/min and calcined for 5 h. The density of the silica inverse opal is much lower than for the PMMA opal. Therefore, the yield was only around 10 %.

In a typical preparation of carbon nanospheres, 1.0 g of Pluronic F127, 10.0 g of ethanol, and 1.0 g of 0.2 M HCl were mixed well at 40 °C. Then 2.08 g TEOS and 2.5 g of the 20 wt % resol solution (as described in **Chapter 3)** were added, and stirring was continued for 5 h at 40 °C. The precursor solution was cast in a glass vial together with the silica inverse opal with a mass ratio for precursor solution/silica of 100:1, which is equivalent with a ratio for precursor solution to initial PMMA spheres of 10:1 for a silica yield of 10 %. The ratio is based on the assumption that the final porous carbon product has a density which is up to five times lower than the density of the non porous PMMA spheres and therefore, needs up to five times more space. The OMC yield of the precursor solution is only 1.5 %. Therefore, the weight ratio of the precursor solution to OMC is 66:1. Due to five times higher density of the PMMA spheres, the maximum ratio for precursor solutions to the initial PMMA spheres

should be below 66:5 or 13:1. The chosen ratio of 10:1 was much lower. The solvent evaporated and the composite was thermopolymerized for 24 h at 100 °C. Afterwards, the material was carbonized at 900 °C in nitrogen, the heating sequence was 1 °C/min to 350 °C (3 h dwell time), then 1 °C/min to 600 °C and 5 °C/min to 900 °C (2 h). After carbonization, the carbon-silica nanocomposites were immersed in 10 wt % HF solution for 24 h. Afterwards the carbon was filtered and washed with water.

4.2.2 Synthesis of mesoporous carbon nanofibres

Ordered mesoporous carbon nanofibres (F-BMC) were synthesized by using macroporous silica as a hard template. Typically, 4 ml of ethanol were mixed with 6 ml TEOS, 3 ml water and 1 ml concentrated hydrochloric acid. The carbon nanofibers MF-C150 (received from YOUR-TOOL GmbH (Ø = 80-150 nm, length 2-25 µm)) were suspended in ethanol and filtered on a Büchner funnel. While applying vacuum to the funnel the silica sol-gel solution is dripped over the surface to completely wet the nanofibers. The silica/carbon composite is heated to 1000 °C with a ramp of 2 °C/min and calcined for 3 h. The silica yield is normally around 25 wt % of the initial carbon fibers. Next, 1.0 g of Pluronic F127, 10.0 g of ethanol, and 1.0 g of 0.2 M HCl were mixed well at 40 °C. Then 2.08 g TEOS and 2.5 g of the resol solution were added, and stirring was continued for 5 h at 40 °C. The precursor solutions were cast in glass vials together with the macroporous silica template obtained above with a mass ratio for precursor solution/porous silica of 40:1. The solvent was evaporated and the composites were thermopolymerized for 24 h at 100 °C. Afterwards, the product was

carbonized at 900 ℃ with a heating ramp of 1 ℃/min and the dwell time 3 h. Finally, the carbon-silica nanocomposites were immersed in 10 wt % HF solution for 24 h.

4.2.3 Preparation of C/S composites and the functionalization

The S-BMC/S and F-BMC/S nanocomposites were prepared following a melt-diffusion strategy as described in **Chapter 3**. Typically, S-BMC and F-BMC obtained above were ground together with different masses of sulfur to achieve either 50 wt%, 60 wt% or 70 wt% of sulfur in the resultant C/S composites, and then maintained in an oven at 155 ℃ overnight.

The CS_2 washed sample was prepared by filtering 50 mg C/S composite (70 wt% sulfur) with 8 ml EtOH-CS_2 mixture (v:v = 9:1), washing with EtOH for several times and drying at 50 ℃ overnight.

The C/S composite with 70 wt% sulfur was soaked in neat TEOS and kept in a glove box at room temperature for a specific duration time. The SiO_x-coated C/S composites were collected by filtration and dried at room temperature for 1 day.

The C/S cathode materials were prepared as in **Chapter 3**. Briefly, slurry was casted from cyclopentanone onto a carbon-coated aluminium current collector. Typically, 82 wt% of C/S composite, 10 wt% Super S carbon and 8 wt% PVDF were mixed with cyclopentanone. The slurries were coated on aluminium current collectors and dried at 60 ℃ overnight. The electrochemical performance of the prepared cathodes was evaluated in coin cells cycled at room temperature between 1.5 V and 3.0 V, with lithium metal foil as the anode. The electrolyte used was 1 M LiTFSI in a mixed solvent of DME and DOL with a volume ratio of 1:1. LiTFSI in DOL and DME was selected as the electrolyte to optimize the high rate behaviour.

4.3 Results and discussion

4.3.1 Physical characterizations of carbon nanospheres (S-BMC)

The scanning electron microscopy (SEM) images in Figure 4.1 depict the morphologies at different steps of the synthesis. The 400 nm PMMA spheres, close packed in an opal structure, (Figure 4.1a) were used as the template for a silica precursor solution. A highly ordered inverse silica opal structure (Figure 4.1b) was formed after calcination. The silica was then used in a second casting step as a template for an artificial opal made of OMC spheres (Figure 4.1c, d). The particle size of the OMC spheres (Figure 4.1c) is around 300 nm, indicating little shrinkage occurred at 900 ℃.

The OMC spheres exhibit the close packing of the PMMA spheres and the silica inverse opal. The representative TEM micrographs in Figure 4.1d and e reveal their 2D-hexagonal mesostructure P6mm. In agreement with the SEM results, the mean particle size was 300 nm ± 40 nm. Figure 4.1d depicts the hexagonal structure projected along the columns. The FFTs clearly show the hexagonal symmetry of the projections with d-spacings of 12.5 nm. Tilting up to 30 ° showed no other zone axes; this excludes a 3D structure and verifies the 2D-hexagonal mesostructure. Figure 4.1e shows the 2D-hexagonal structure tilted out of the columnar projection, where the cylindrical pores can be clearly observed. Thus the spherical nanoparticles exhibit the same structure as the bulk material described by Zhao and coworkers synthesized from the same precursor solution.[7] On grinding for TEM preparation, the OMC opal aggregates separated into small clusters (e.g. in Figure 4.1d) or even single particles (e.g. in Figure 4.1e), indicating that they are only loosely bound.

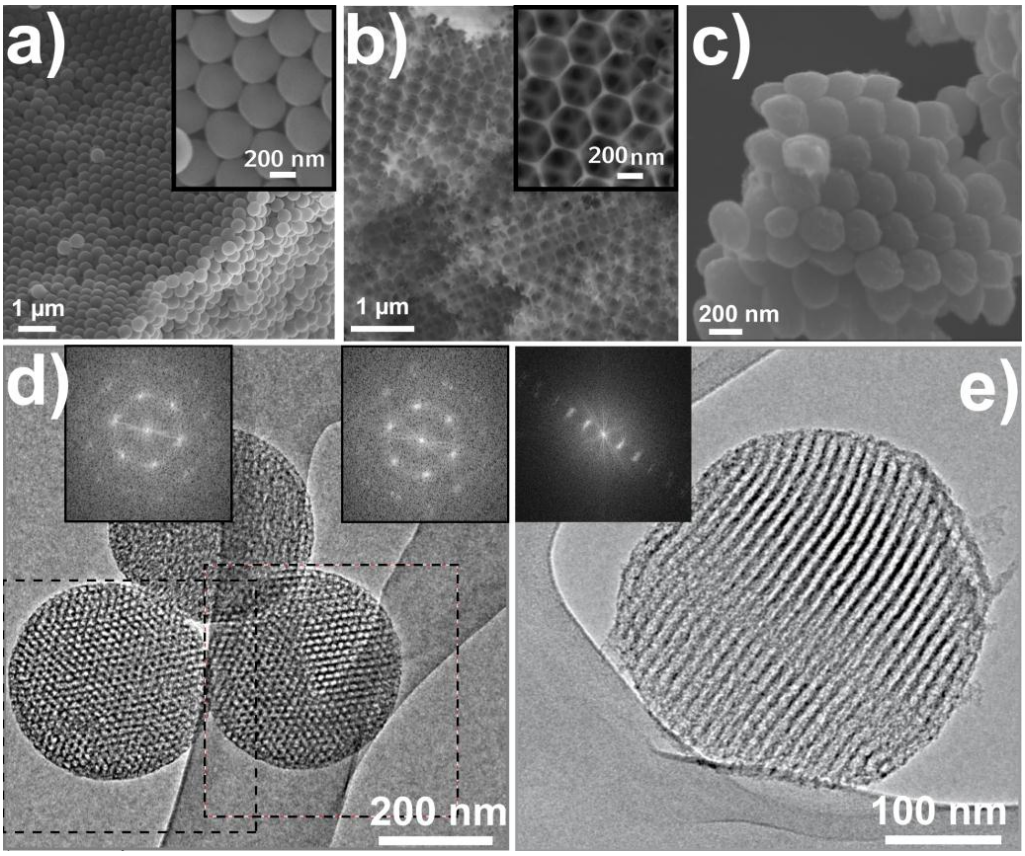

Figure 4.1 SEM images: a) PMMA spheres ordered in close packing with an inset at higher magnification; b) Silica inverse opal structure with an inset at higher magnification; c) OMC spheres ordered in opal structure. TEM micrographs of spherical OMC nanoparticles showing the 2D-hexagonal structure: d) projected along the columns, with insets of Fast Fourier Transforms (FFT) of the squares; e) tilted out of the columnar projection with FFT inset.

The OMC spheres show excellent porosity properties as Figure 4.2 illustrates. They exhibit a BET surface area of 2445 m^2/g, an inner pore volume of 2.32 cm^3/g ($p/p_0 = 0.82$, pores < 13 nm) and a total pore volume of 2.63 cm^3/g ($p/p_0 = 0.98$). The Type IV isotherm

shows hysteresis due to capillary condensation in mesopores. The bimodal pore size distribution (NLDFT adsorption branch) shows a maximum for large pores of 6.0 nm but also smaller pores with a maximum of 3.1 nm. This can be explained by porous walls that were formed through etching the silica out of the former carbon/silica nanocomposite walls. For better comparison with literature data the pore sizes were also determined with the BJH model, which gives maxima at 5.3 and 2 nm. In addition, the isotherm shows adsorption at very high partial pressures due to textural porosity of the packed 300 nm spheres.

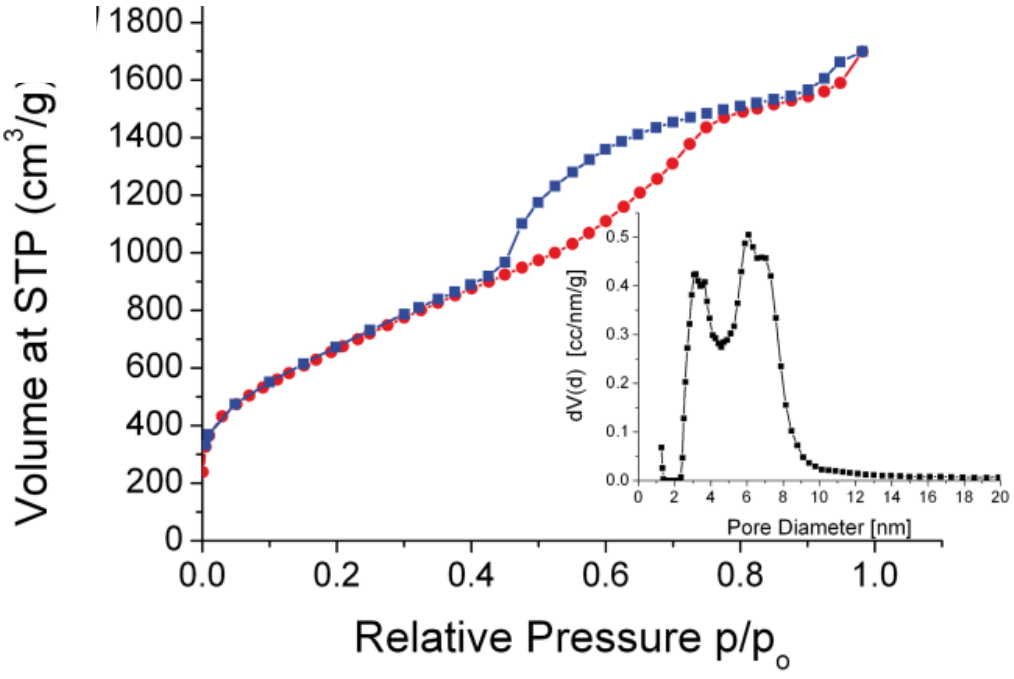

Figure 4.2 Nitrogen sorption isotherm and pore size distribution.

4.3.2 Characterization of S-BMC/S composites

Three C/S samples denoted as S-BMC/S-50, S-BMC/S-60 and S-BMC/S-70 were prepared (spherical-bimodal mesoporous carbon). The sulfur content of each sample was confirmed (Figure 4.3) by thermogravimetric analysis (TGA): 49.7 wt%, 61.4 wt% and 69.9 wt%, respectively.

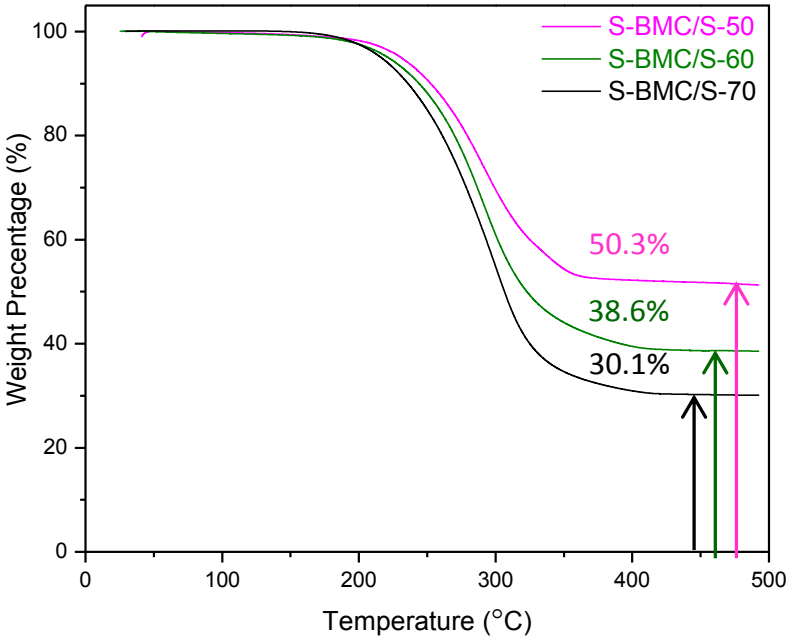

Figure 4.3 TGA data collected in N_2 (10 ℃/min) of the three S-BMC/S samples.

It is well known that both carbon and sulfur are hydrophobic, and accordingly, sulfur exhibits strong affinity for porous carbons.[8,9] SEM image of the S-BMC/S-70 sample (Figure 4.4) shows that the morphology of the S-BMC was maintained with 70 wt% of sulfur was incorporated. This result revealed that the homogeneous distribution of sulfur within nanosized mesoporous carbon was much more favored than in bulk carbon, although we believe there must be a thin layer of sulfur existing on the external surface of the carbon framework.

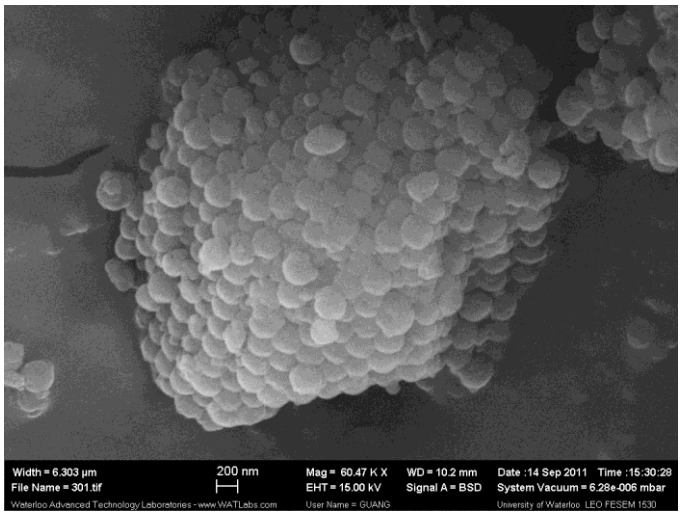

Figure 4.4 SEM image of S-BMC/S-70 showing the uniform distribution of sulfur.

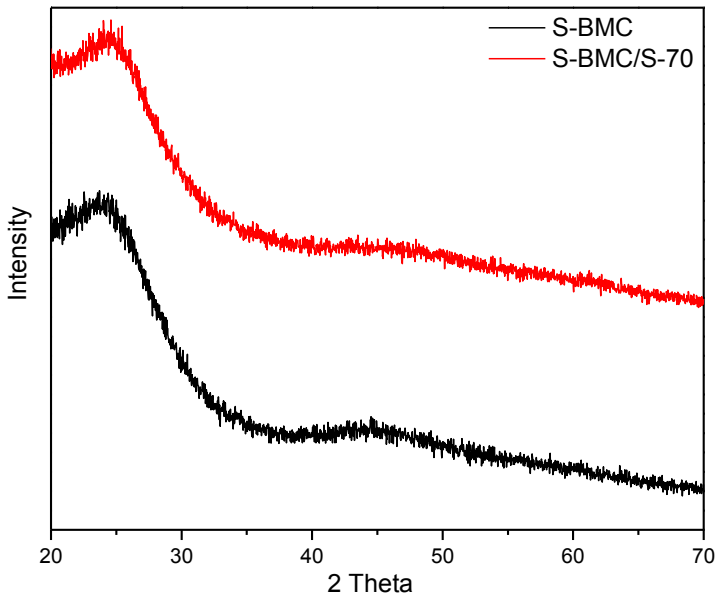

Figure 4.5 XRD patterns of S-BMC and S-BMC/S-70, indicating the amorphous state of sulfur in the C/S composite.

In Figure 4.5, no crystalline sulfur can be seen from the wide angle XRD pattern of S-BMC/S-70 sample, implying that the layer formed is very thin. The TEM (Figure 4.6) image

and the corresponding elemental maps of a single BMC/S-70 particle further confirms that sulfur was uniformly distributed into the pores of the S-BMC frameworks and there was no agglomeration observed.

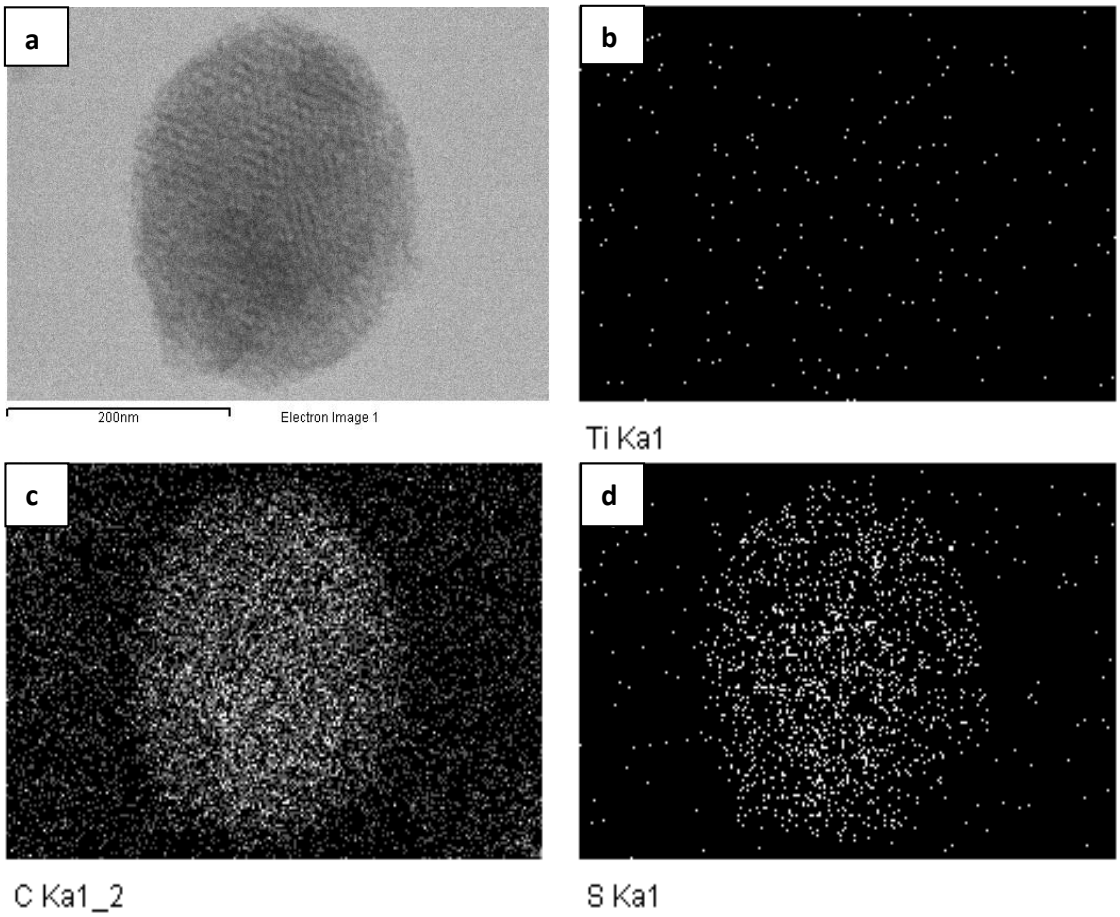

Figure 4.6 (a) TEM image of S-BMC/S-70 and the elemental maps of Ti (reference element) (b), carbon (c) and sulfur (d), implying the uniform distribution of sulfur.

4.3.3 Electrochemical performance of S-BMC/S composites

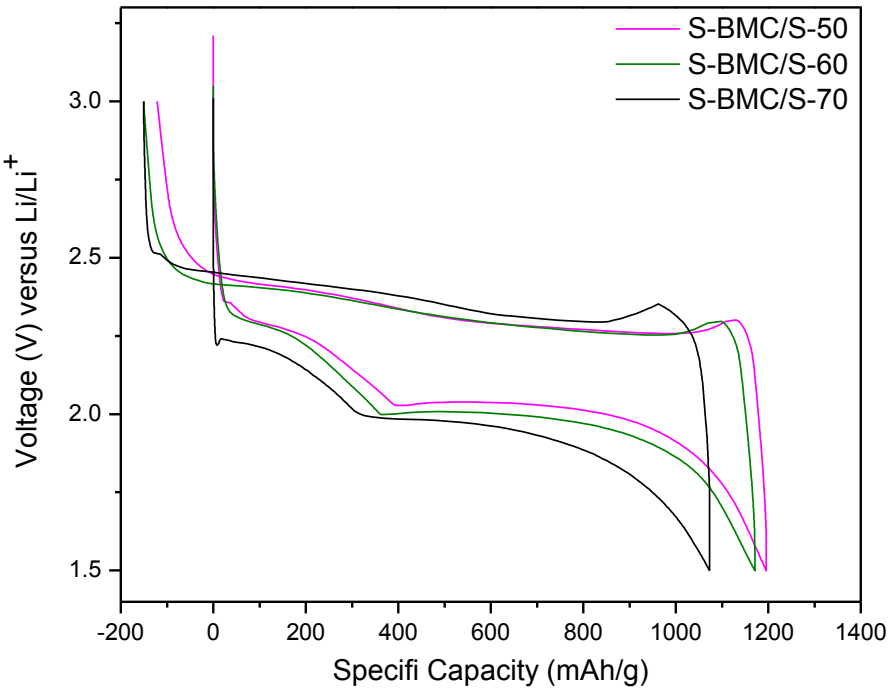

Figure 4.7 Initial charge-discharge profiles of the three S-BMC/S samples at C rate.

All the three initial discharge profile of S-BMC/S-50, S-BMC/S-60 and S-BMC/S-70 show two plateaus, similar to those of the BMC-1 initial profiles (Figure 4.7). The voltage difference between discharge and charge gradually extended with more sulfur loaded intot the carbon, indicating the polarization occured during dicharge/charge. Furthermore, an overcharge capacity about 120-150 mAh/g is observed for all the three samples, which is probably attributed to the dissolution of the reduced surface polysulfide species that engage in the shuttle mechanism during the electrode redox reactions.

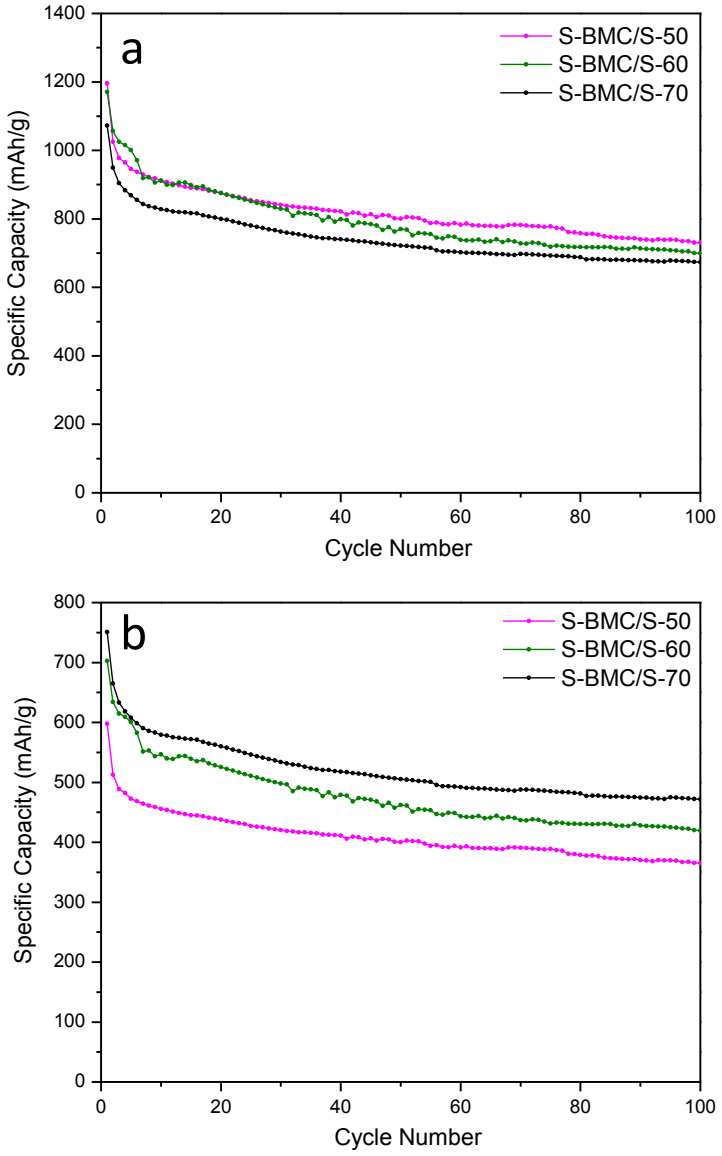

Figure 4.8 Cycling stability of the three S-BMC/S samples at C rate, based on (a) sulfur and (b) C/S as active materials.

S-BMC/S-50 (Figure 4.8a) shows the highest reversible discharge capacity of 1200 mAh/g. After 100 cycles this cell maintained a capacity of 730 mAh/g at a high current density of 1C (1675 mA/g). Strikingly, unlike the results in BMC-1, the electrochemical performance of the C/S nano composites was not strongly affected by increasing the sulfur content to 60 wt% and

even 70 wt%. For example, S-BMC/S-60 displays an initial capacity of 1170 mAh/g with 700 mAh/g retained after 100 cycles, comparable to S-BMC/S-50. However, if the capacity is calculated based on the whole C/S composites, S-BMC-/S-70 exhibits an initial discharge capacity of 750 mAh/g and more than 470 mAh/g is retained after 100 cycles, the best performance among the three samples. The detailed information is available in Table 5.1.

All three samples show a drop in capacity during the first two cycles, followed by good stability on subsequent cycling. We believe this is consistent with the obervation of the overcharge capacities in Figure 4.7, also caused by the dislutions of the sulfur on the external surface of the S-BMC framework.

Table 4.1 Summary of capacity retention of the S-BMC/S-50, S-BMC/S-60 and S-BMC/S-70 composites.

	$C_{initial}$ (mAh/g)	C_{100} (mAh/g)	$C_{100}/C_{initial}$
S-BMC/S-50 (S)	1196	730	61.0%
S-BMC/S-60 (S)	1171	699	59.7%
S-BMC/S-70 (S)	1073	674	62.8%
S-BMC/S-50 (C/S)	598	365	61.0%
S-BMC/S-60 (C/S)	702	420	59.7%
S-BMC/S-70 (C/S)	751	471	62.8%

$C_{initial}$ is the initial discharge capacity and C_{100} is the discharge capacity at 100 cycles.

The electrochemical performance of S-BMC/S-50 electrode was evaluated at higher current rates of 2C, 3C and 5C, as shown in Figure 4.9. The discharge capacities at 2C (3350 mA/g) are ~870 mAh/g and ~605 mAh/g for the first cycle and the 100th cycle, respectively. With the increase of the current rate to 3C (5025 mA/g), the initial capacity drops to ~550 mAh/g, but ~437 mAh/g is retained after 100 cycles. Even at very high current rate of 5C (8375 mA/g), the first discharge cycle capacity is still ~500 mAh/g, indicating a good rate capability of the S-BMC/S-50 electrodes.

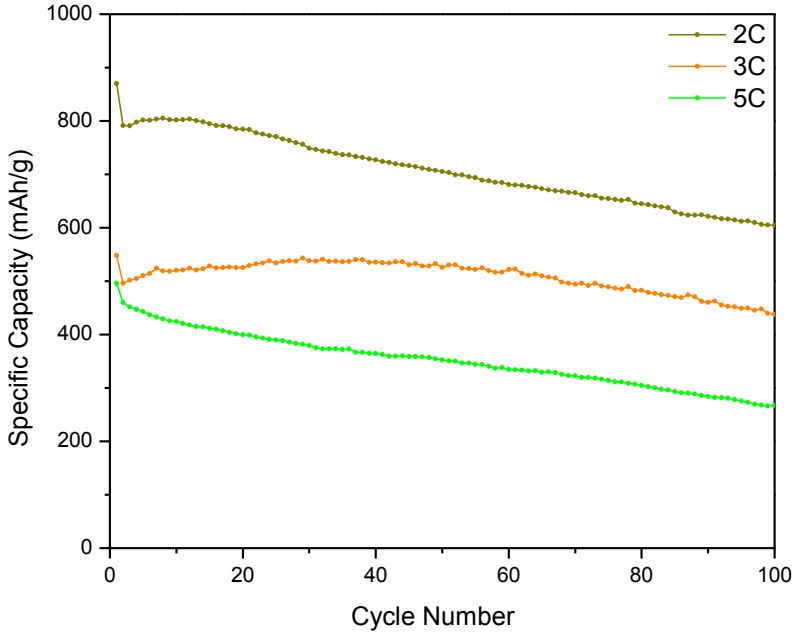

Figure 4.9 Capacity and cyclability of S-BMC/S-50 at higher current rates of 2C (3350 mA/g), 3C (5025 mA/g) and 5C (8375 mA/g).

Comparison of the nano-spherical S-BMC bimodal mesoporous carbon with the previously investigated bulk material BMC-1 is illustrated in Fig. 4.10, which clearly demonstrates the

advantages of S-BMC. The more sulfur is incorporated, the more obvious is the advantage. As discussed above, we attribute this result to the nanoscale morphology of the carbon phase. The small particle size of S-BMC allows the sulfur to distribute more homogeneously into the pores, which greatly enhances the electrochemical behaviour of the corresponding electrodes, compared with the bulk mesoporous carbon BMC-1.

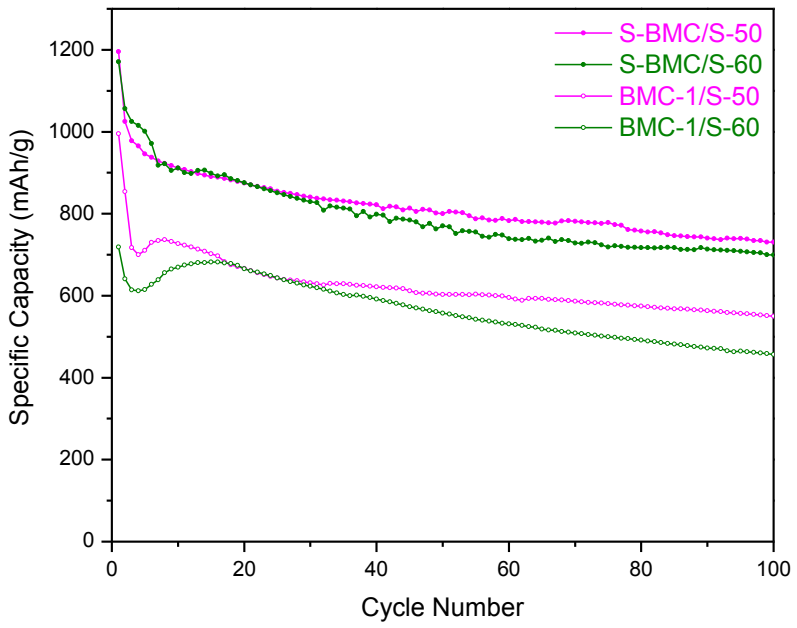

Figure 4.10 Comparison of electrodes prepared from BMC-1 and S-BMC, showing the importance of particle size on the electrochemical performance. All the cells were operated at C rate (1675 mA/g).

The influence of particle size on electrochemical performance was also evidenced by the mesoporous carbon nanofibers which have comparable surface area and pore volume with the nanospheres. The mesoporous nanofibers were prepared by employing phenolic resin (resol) as

carbon resources, TEOS as inorganic precursors and F127 surfactant as a soft-template. The fibrous morphology, achieved by a two-step casting process, is confirmed by the SEM image (Figure 4.11a). The average diameter of the fibers is ~100 nm and the length is several microns. Additionally, some of the fibers exhibit hollow structure, probably a result of insufficient infiltration of resol-TEOS-F127 solutions into the channels of the silica template (see experimental section). The TEM images (Figure 4.11b and c) in different magnifications clearly show the ordered mesoporous structure.

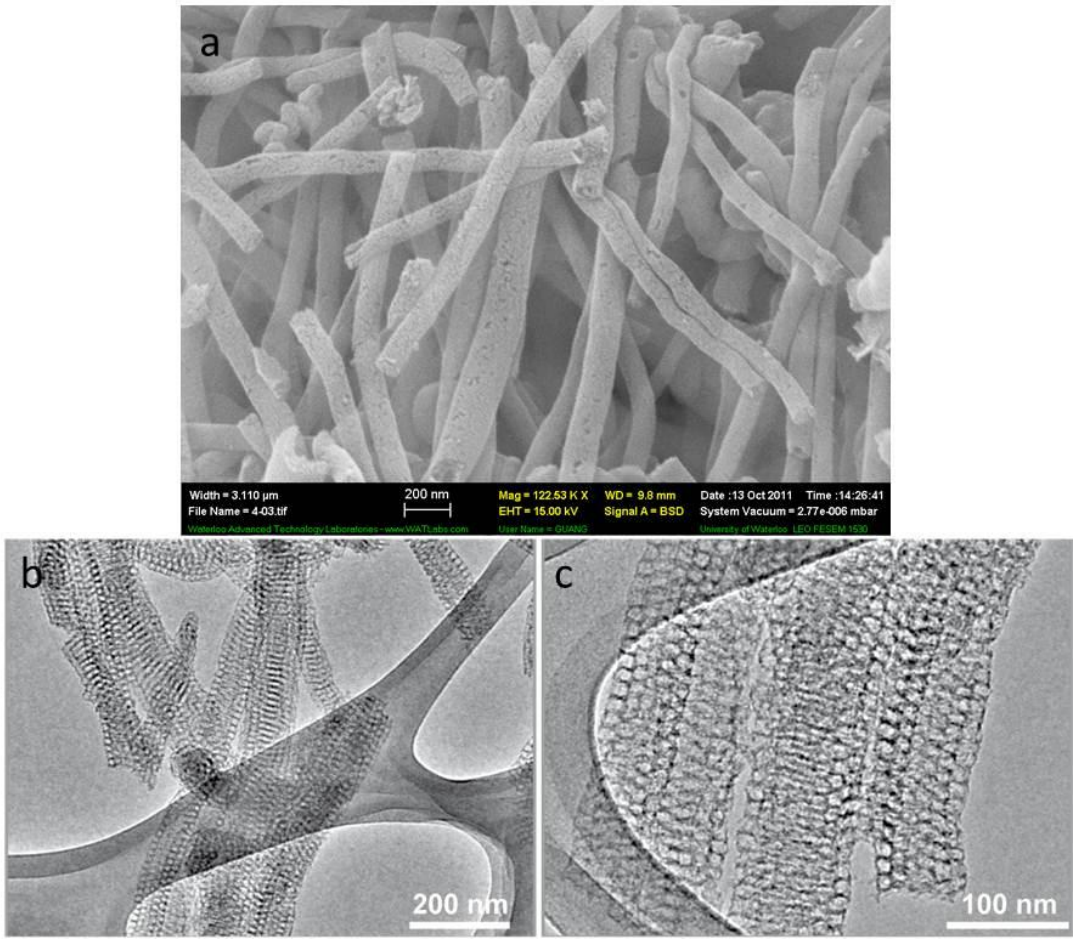

Figure 4.11 (a) SEM and (b, c) TEM images of the mesoporous carbon nanofibers.

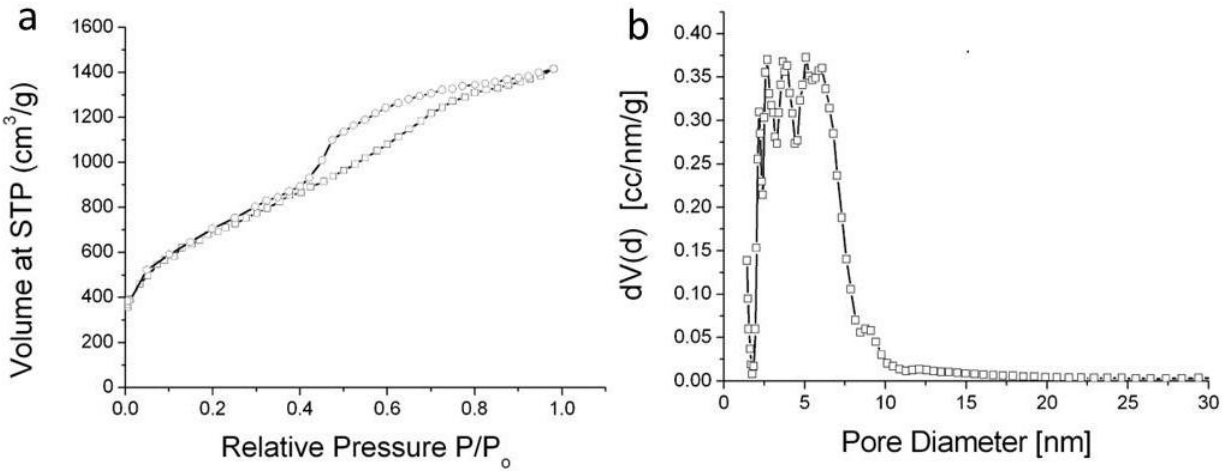

Figure 4.12 (a) Nitrogen sorption isotherm and (b) pore size distribution of the mesoporous carbon nanofibers calculated via the NLDFT mode.

Nitrogen sorption isotherm in Figure 4.12a displays Type IV isotherm curve and similar hysteresis loop like that of the nanospheres, which is indicative of the mesostructure. The corresponding BET surface area is 2480 m^2/g and total pore volume of 2.2 cm^3/g ($p/p_0 = 0.98$), with a pore size range of 2.7-5.9 nm (Figure 4.12b).

F-BMC/S-50 composite was prepared through the melt-diffusion strategy with a sulfur content of 50 wt%. The electrode exhibits almost the same performance as S-BMC/S-50 (Figure 4.13), except for a slightly lower initial capacity (~1060 mAh/g). In contrast, the performance of BMC-1/S-50 is much inferior, since there is a discharge capacity difference of ~150-200 mAh/g when compared to the other two electrodes. This example implies that the electrochemistry of the electrodes is not influenced by the morphology, but by the particle size. Therefore, sulfur is distributed more homogeneously in mesoporous carbon nanoparticles no

matter what is the morphology, than in bulk carbons. Correspondingly, the electrochemical performance can be significantly improved.

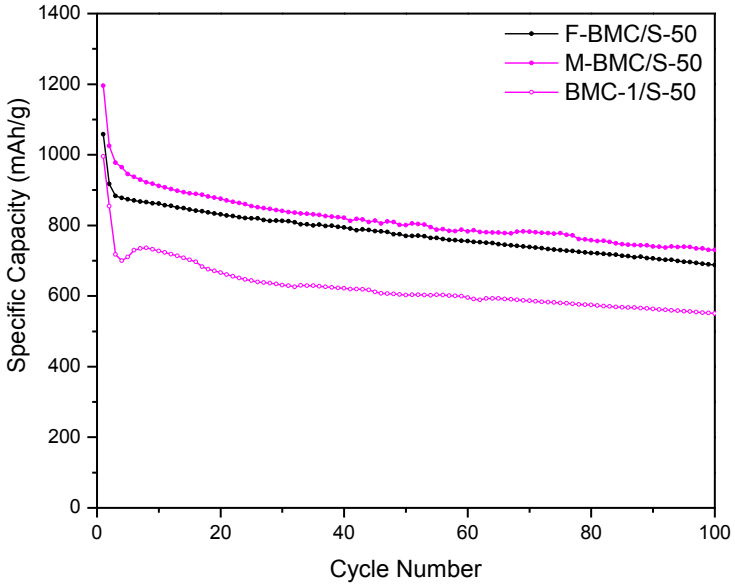

Figure 4.13 Comparison of electrodes prepared from F-BMC, S-BMC and BMC-1. All the cells were operated at a current rate of 1C (1675 mA/g).

4.3.4 Functionalization of S-BMC/S-70 composite

In spite of the great progress made on the nanopherical sulfur electrodes, the large overcharge capacity could possibly be reduced by further optimization of the C/S composites. Two approaches were followed to overcome it. First, S-BMC/S-70 was treated with CS_2 to remove excess external sulfur. Another approach to avoid overcharge was to modify the sample S-BMC/S-70 with a thin SiO_x coating. It has been established that additives play important roles in the sulfur electrodes to suppress the polysulfide shuttle,[10,11,12,13,14] among which mesoporous silica is particularly promising,[15] as discussed in **Chapter 3**.

Samples obtained via the above processes were denoted as S-BMC/S-70-W and S-BMC/S-70-Si. TGA data (Figure 4.14) showed that about 14% of the sulfur was extracted for both two samples, and the real sulfur content was ~56 wt% in the C/S composites. Moreover, the SiO_x in the S-BMC/S-70-Si sample was ~2 wt% from the TGA result. It is worth to note that there might be an error in this number because of the limitations of this technique. Considering this, the SiO_x layer should be in the range of 1-3 wt%, but this small error does not affect the calculations of the capacity very much. The coating is also confirmed by the elemental maps of the composites in Figure 4.15, where SiO_x layer is uniformly distributed on the surface of a single C/S particle.

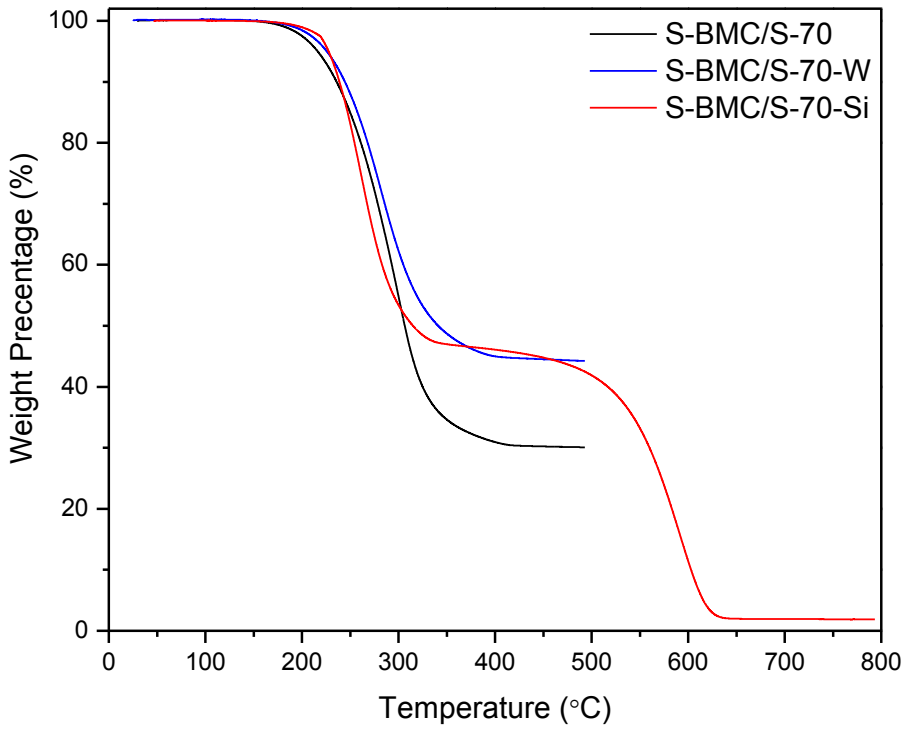

Figure 4.14 TGA data of S-BMC/S-70, S-BMC/S-70-W and S-BMC/S-70-Si. The former two were collected under N_2 and the last one was under air.

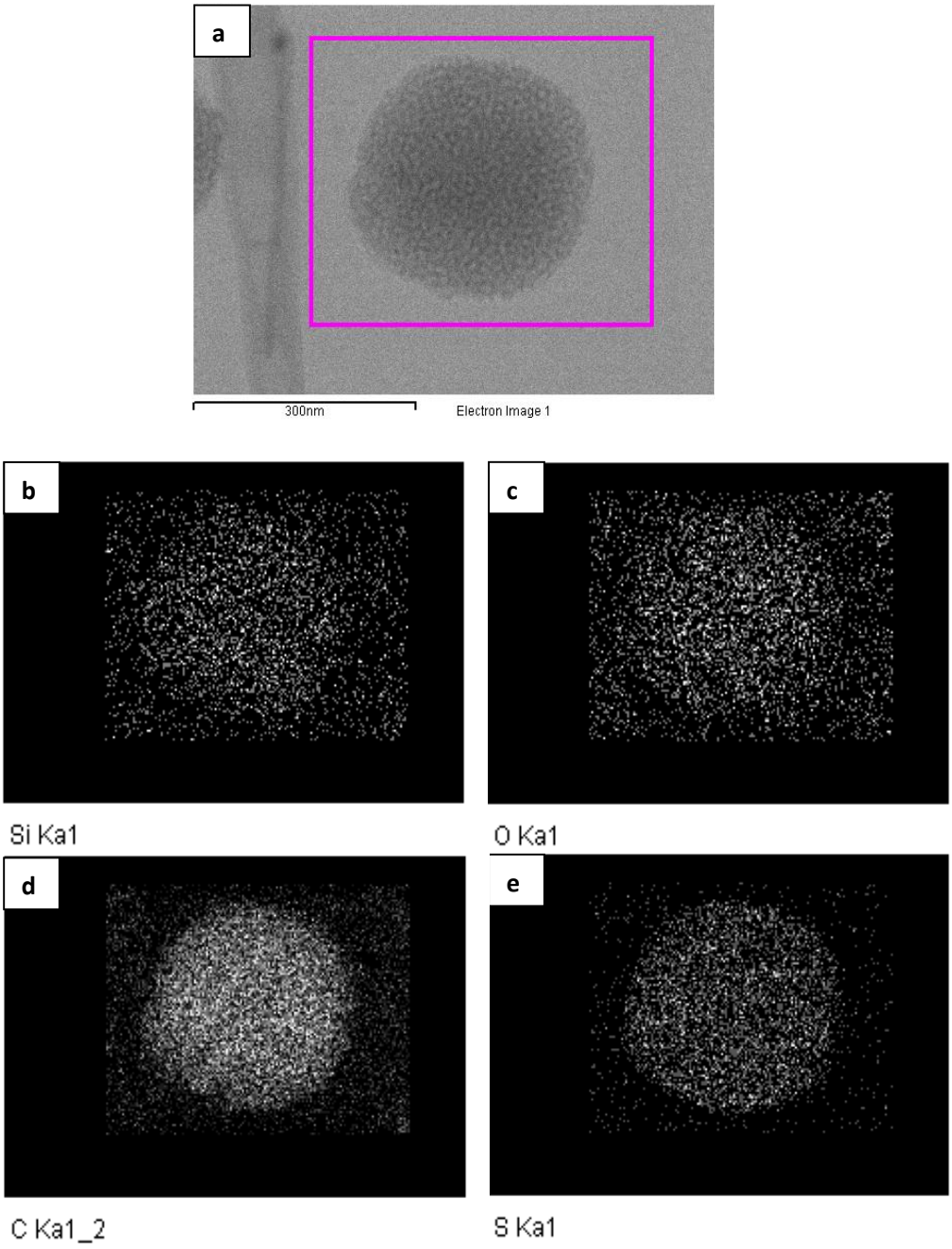

Figure 4.15 (a)TEM image of a single S-BMC/S-70-Si particle and the corresponding (b) silicon, (c) oxygen, (d) carbon and (e) sulfur elemental maps showing the homogeneous distribution of silica on the surface.

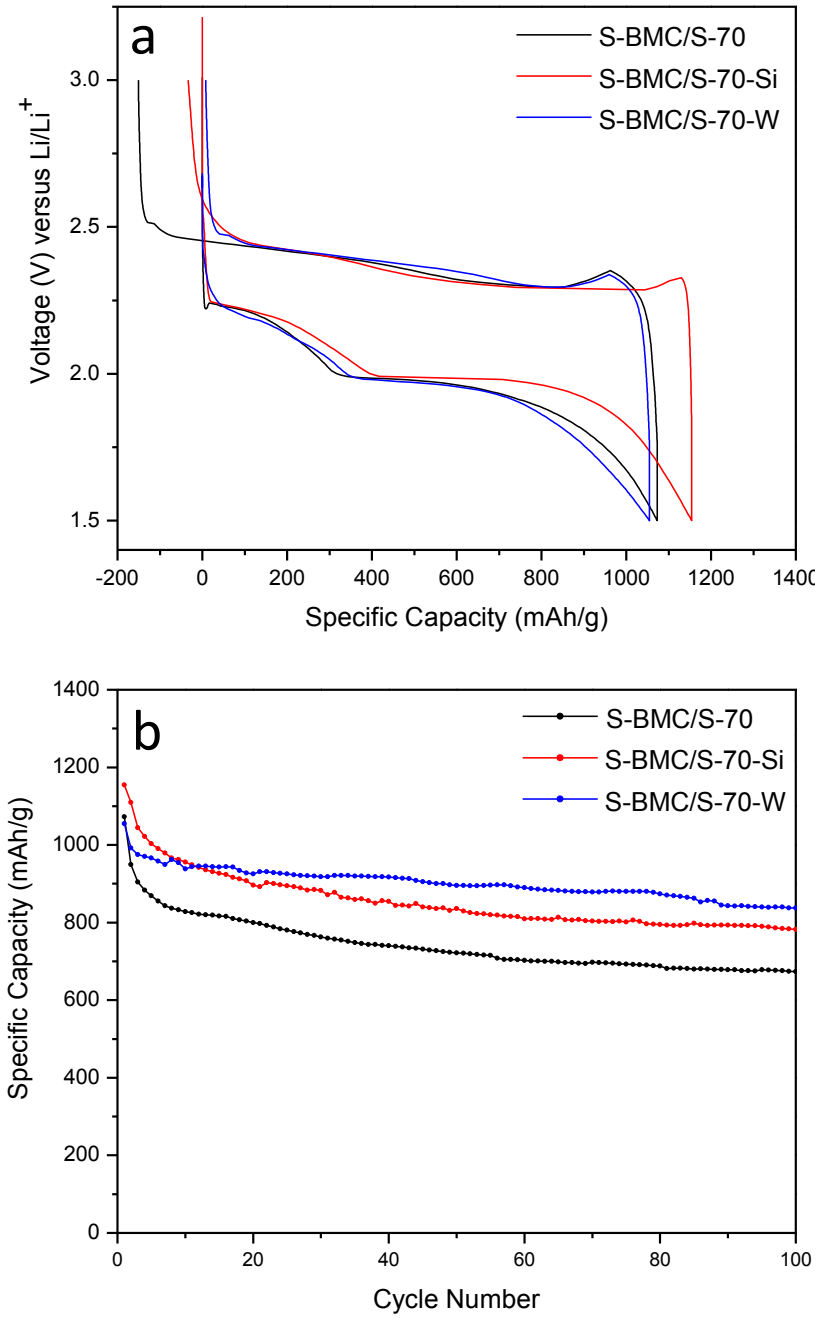

Figure 4.16 (a) Initial charge-discharge profiles of as-prepared S-BMC/S-70 versus post-treated samples by SiO_x coating or CS_2 washing and (b) Cycling stability of all the three "C/S-70" electrodes. All the cells were operated at a current rate of 1C (1675 mA/g) at room temperature.

The blue curve in Figure 4.16a shows that all the overcharge capacity disappeared in the first cycle of the washed sample (S-BMC/S-70-W), indicating that the undesired shuttle processes were completely suppressed. Similarly, the homogeneous SiO_x coating was also effective, because most of the over-discharge capacity was eliminated (Figure 4.16a, red curve). The sharp capacity drop at the 2nd cycle of both samples was also diminished (Figure 4.16b). In spite of some sulfur loss during the washing and filtration, the two samples retained higher capacities. For example, a capacity above 830 mAh/g was obtained for S-BMC/S-70-W sample, after 100 cycles at a current rate of 1C, much higher than the original S-BMC/S-70 electrode. Even compared with the S-BMC/S-50 and S-BMC/S-60 samples that have comparable sulfur content, S-BMC/S-70-W exhibits better capacity retention (Figure 4.17).

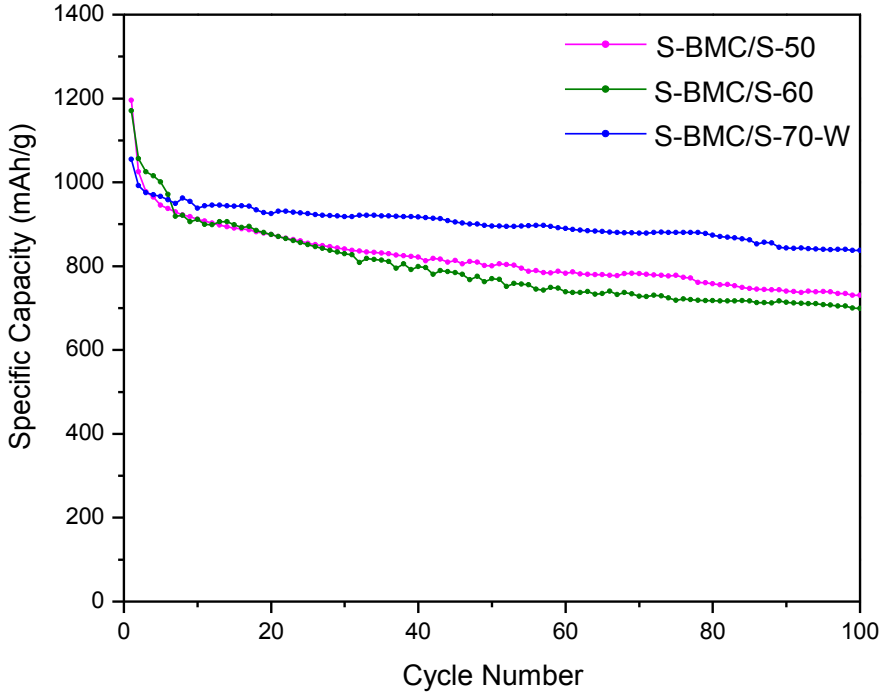

Figure 4.17 Comparison of S-BMC/S-70-W versus electrodes with similar sulfur content, S-BMC/S-50 and S-BMC/S-60 at C rate (1675 mA/g).

The efficacy of the S-BMC/S-70-W and S-BMC-70-Si could last to a long term cycling up to 200 cycles (Figure 4.18), and it seems with extended cycles, the protection layer SiO_x became more and more important to the retention of the capacity. Details of the electrochemical performance of various electrodes are summarized in Table 4.2.

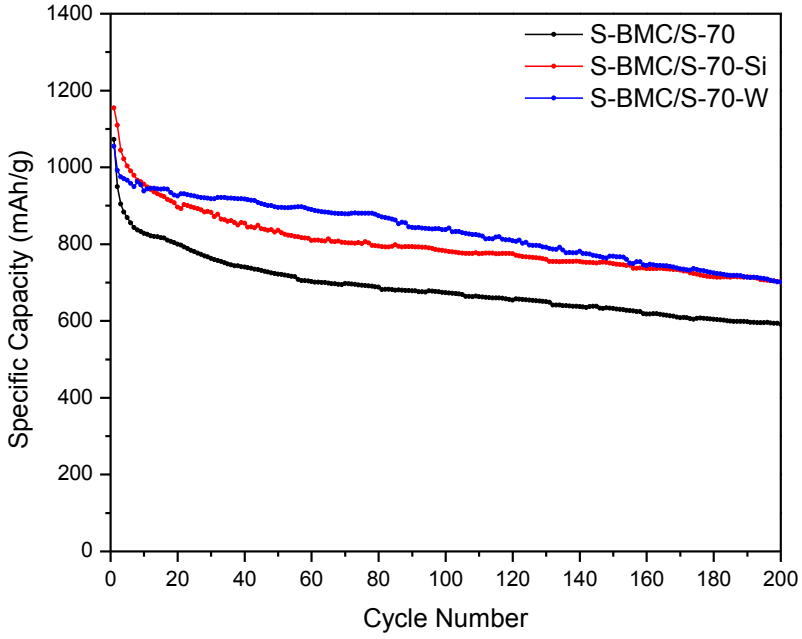

Figure 4.18 Comparison of electrodes in 200 cycles at C rate (1675 mA/g).

Table 4.2 Summary of capacity retention of various "S-BMC/S-70"electrodes.

	$C_{initial}$ (mAh/g)	C_{200} (mAh/g)	$C_{200}/C_{initial}$
S-BMC/S-70-W	1055	702	66.5%
S-BMC/S-70-Si	1154	702	60.8%
S-BMC/S-70	1073	592	55.2%

$C_{initial}$ is the initial discharge capacity and C_{200} is the discharge capacity at 200 cycles.

It must be pointed out that the overcharge capacity still exists for all the samples during cycles, revealing that the polysulfide shuttle phenomenon could not be inhibited completely. For example, the difference of the charge and discharge capacity of S-BMC/S-70-W became larger during the first 10 cycles and then maintained as a constant of ~100 mAh/g (Figure 4.19), giving a coulombic efficiency of ~90%. This is resulted by the high solubility of polysulfides in the electrolyte solvent DOL and DME, especially for DME. As discussed in **Chapter 1**, this electrolyte has relatively low viscosity, which facilitates the migration of lithium ions and provides good kinetics, but on the other hand, the polysulfide sulfide shuttle is more serious in this system than for those with tetraglyme and sulfone type electrolyte solvents that are more viscous.[9,16,17]

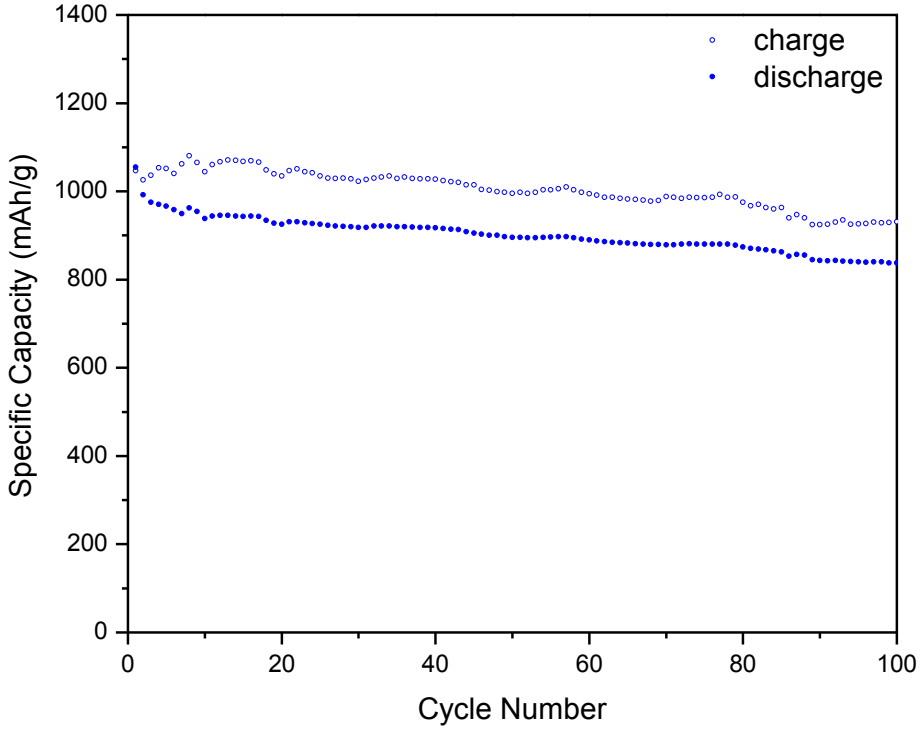

Figure 4.19 Charge-discharge capacity difference of S-BMC/S-70-W at C rate (1675 mA/g).

Initial discharge capacities of ~760 mAh/g and 480 mAh/g could be obtained for S-BMC/S-70-W, at a higher current density of 2C (3350 mA/g) and 4C (6700 mA/g), and with the increase of the current rates, the stability of the electrodes becomes better, as well as the coulombic efficiency, as shown in Figure 4.20.

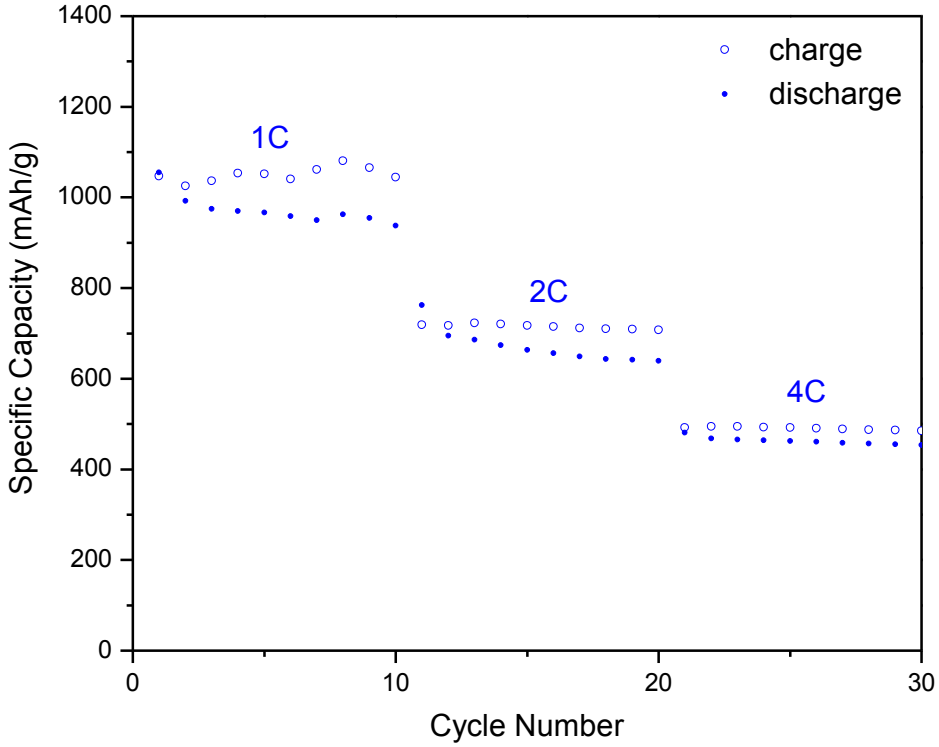

Figure 4.20 Charge-discharge capacities of S-BMC/S-70-W at different current rates of 1C (1675 mA/g), 2C (3350 mA/g) and 4C (6700 mA/g).

4.4 Conclusions

In summary, spherical OMC nanoparticles of 300 nm in diameter with a 2D-hexagonal mesostructure were developed. The material shows one of the highest inner pore volumes for

mesoporous carbon nanoparticles of 2.32 cm^3/g and also one of the highest surface areas of 2445 m^2/g with a bimodal pore size distribution of large and small mesopores of 6 nm and 3.1 nm. They were successfully applied as a scaffold of sulfur in Li-S batteries with as much as 70 wt% sulfur incorporated into the C/S nanocomposites by a melt-diffusion strategy. The corresponding electrodes showed a high initial discharge capacity up to 1200 mAh/g and 730 mAh/g after 100 cycles at a high current rate 1C (1675 mA/g). The stability of the cells could be further improved by either removal of the sulfur on the external surface of spherical particles or functionalization of the C/S composites via a simple TEOS induced SiO_x coating process. Mesoporous carbon nanofibers were also employed as a framework of sulfur cathodes, which displayed similar performance as the nanosheres. These results indicat the importance of particle size control of mesoporous carbons on electrochemical properties of the Li-S cells.[18]

Chapter 5

Hydrothermal Synthesis and Electrochemical Properties of Li_2CoSiO_4/C Nanospheres

5.1 Introduction

As discussed in **Chapter 1**, silicate-based cathode materials Li_2FeSiO_4 and Li_2MnSiO_4 have been drawing more and more attention since the first report in 2005.[1] However, very little progress has been made with Li_2CoSiO_4 so far. Studies are complicated by the fact that several polymorphs exist, which are structural variants of the Li_3PO_4 structure type. These are formed at different temperatures ranging from 700-900 °C. These three materials adopt different structural symmetries denoted by their space group: the β_I phase ($Pbn2_1$); the β_{II} phase ($Pmn2_1$) and the γ_0 phase ($P2_1$). Theoretical calculations suggest that the extraction of lithium ions from the cobalt silicate lattice is at about 4.4 V for the first Li ion; but it is around 5 V for the second lithium extraction and hence above the accessibility limit for most alkyl carbonate electrolytes.[2] However, subsequent computational studies found that the second extraction potential is somewhat lower than this for the $Pmn2_1$ and the $P2_1$ phases, where the latter is predicted to be 4.8V.[3] Bruce synthesized these three polymorphs of Li_2CoSiO_4 and investigated their electrochemical performance as cathode materials.[4,5] The β_{II} phase ($Pmn2_1$) electrode showed the highest charge capacity of ~180 mAh/g (1.1 Li per unit formula) after ball-milling with carbon, but a discharge capacity of only ~30 mAh/g. Direct carbon coating methods could be only accomplished with the β_I phase ($Pbn2_1$) since the cobalt (II) in the β_{II} phase was reduced to Co metal by carbon at high temperature. The coated β_I sample showed

much improved performance compared to the ball-milled β_{II}-phase material, suggesting that a successful homogeneous carbon coating was achieved. Similar work on the β_{II} phase of Li_2CoSiO_4 prepared by solution and hydrothermal routes with ball milled carbon (or graphite added) also showed high charge capacity but insertion of only about 0.25 - 0.4 Li on the discharge cycle.[6]

Herein, we address the challenge of carbon incorporation using a unique new strategy whereby the silica contained within a conductive carbon framework is used as the source precursor for growth of Li_2CoSiO_4 nanospheres. MCS is prepared by vaporation induced self-assembly (EISA) method, using water-soluble phenolic resin as the carbon source, tetraethyl orthosilicate (TEOS) as the silica source, and triblock copolymer poly(propylene oxide)-block-poly(ethylene oxide)-block-poly(propylene oxide) (F127, M_w=12,700) as a soft template, as discussed in **Chapter 3** but with some modifications. It possesses a highly ordered hexagonal mesoporous structure, with SiO_2 nanocrystallites (mean size of ~2 nm[7]) imbibed into the walls of the carbon framework. Owing to this special structure, a large number of carbon fragments that are produced on collapse of the porous framework are homogeneously incorporated in the Li_2CoSiO_4 nanoparticles during their formation. Additionally, it is found the morphology and particle size of the Li_2CoSiO_4/C nanocomposites were significantly influenced by the concentration of the $[OH]^-$ in the precursors. By carefully controlling the system PH as well as the precursor concentration, nanospherical Li_2CoSiO_4/C particles with a uniform size of 300-400 nm could be obtained, some of which exhibit an unusual hollow structure. This is the first report of such size control in silicates, especially in the presence of carbon incorporation which is explained with a proposed reaction mechanism. Electrochemical results showed that the

Li_2CoSiO_4/C cathodes with nano "internal" carbons exhibited superior properties compared to those synthesized from fumed silica.

5.2 Experimental

5.2.1 Synthesis of mesoporous MCS composites

Three MCS composites with different SiO_2 content were prepared via the evaporation-induced self-assembly (EISA) strategy, as described in **Chapter 3**. Briefly, 1.0-2.3 g of triblock copolymer poly(propylene oxide)-block-poly(ethylene oxide)-block-poly(propylene oxide) (F127, M_w=12,700) was dissolved in a solution of 6.0-10.0 g ethanol and 1.0 g 0.2 M HCl via stirring. Next, 2.08 g of tetraethyl orthosilicate (TEOS) and 2.5-10.0 g phenolic resin solution were added to this solution and stirred for 8 h at 40 ℃. The mixture was transferred to Petri dishes to evaporate the ethanol overnight and held at 100 ℃ for 24h to thermopolymerize the phenolic resin. The as-made product was collected from the dishes, hand milled in a mortar for 10 min, and heated under Ar flow at 900 ℃ for 4 h, at a rate of 1 ℃/min below 600 ℃ and 5 ℃/min above 600 ℃. Three mesoporous samples, denoted as MCS-1, MCS-2 and MCS-3, were physically ground in a mortar for 5 min before further use. The specific ratios of the precursors are listed in Table 5.1.

Table 5.1 Preparation conditions of the ordered MCS samples by the EISA method.

	Phenolic resin (g)	F127 (g)	TEOS (g)	Ethanol (g)
MCS-1	0.5	1.0	2.08	12
MCS-2	1.0	1.6	2.08	12
MCS-3	2.0	2.3	2.08	14

5.2.2 Synthesis of Li_2CoSiO_4/C nanocomposites

Li_2CoSiO_4/C nanocomposites were prepared hydrothermally following the previous literature.[4] Various parameters such as concentrations, reaction times, temperatures and $C_{[OH]}$- were investigated to optimize the product. These variations were specified in the '**Results and discussion**' section. Here, the general procedures are described as follows. First, 100 mg of MCS-1 is dispersed in 10 ml of deionized water by sonication for 60 min and then 230 mg of LiOH·H_2O was added and the mixture was sonicated for another 30 min. Next, 320 mg of $CoCl_2$·$6H_2O$ was dissolved in 7 ml of ethylene glycol to afford a clear solution by stirring. The above two solutions were then mixed together and stirred for 60 min at room temperature. The obtained slurry was transferred into a 23 ml Teflon-lined autoclave and the remaining volume was filled with deionized water. The concentration of SiO_2 was 3.5 mg/ml. The autoclave was heated at 150 ℃ for 72 h. The product was washed with deionized water and ethanol for 3 times and dried at 200 ℃ overnight under vacuum. Li_2CoSiO_4 with fume silica as the silicate precursor was also prepared (460 mg of LiOH·H_2O) to provide a comparison with the Li_2CoSiO_4/C sample.

5.2.3 Electrochemistry

Electrochemical performance of the Li_2CoSiO_4/C cathode materials was evaluated using lithium metal as the anode in coin cells. In a typical experiment, 10 wt% of the binder PVDF was first dissolved in *N*-Methyl-2-pyrrolidone (NMP). To it, 80 wt% of active material and 10 wt% of super P carbon were added. This mixture was ground for 30 min to obtain homogeneous slurry, which were then casted on aluminum foil current collector. The foil was dried at 100 ℃ in vacuum condition to evaporate NMP and moisture completely. Coin cells

were assembled and cycled at 30 ℃ between 2.0 V and 4.6 V, with 1 M $LiPF_6$ in ethylene carbonate (EC) and dimethyl carbonate (DMC) as the electrolyte (V:V = 1:1). The electrode formula of Li_2CoSiO_4/C-8-F (Li_2CoSiO_4 obtained from fume silica) is Li_2CoSiO_4/C-8-F:Super P:PVDF=75:15:10, in which the ratio of active material Li_2CoSiO_4 is similar to the one in the Li_2CoSiO_4/C electrodes.

5.3 Results and discussion

5.3.1 Synthesis of Li_2CoSiO_4/C nanocomposites with various MCSs

5.3.1.1 Characterization of mesoporous MCS frameworks

The Li_2CoSiO_4/C composites are synthesized by fixing the amount of MCS as a constant (100 mg) but the other precursors vary accordingly because the SiO_2:C ratios among MCS-1, MCS-2 and MCS-3 are different. The three final Li_2CoSiO_4/C products are denoted as Li_2CoSiO_4/C-1, Li_2CoSiO_4/C-2 and Li_2CoSiO_4/C-3, respectively.

The gravimetric silica content of each MCS sample was determined by TGA in air as shown in Figure 5.1. The first minor weight decrease up to 100 ℃ in the curves is caused by the physisorbed moisture and the sharp drops in weight above 500 ℃ represent the combustion of the carbon frameworks. Silica weight ratio of each sample is ~82 wt%, 68 wt% and 57 wt%. In the previous literature[7], carbon/silica composite prepared with a similar method showed much lower silica content in the composites. The main difference probably owes to the extension of contact time, which allowed more extensive hydrolysis of the silicate oligomers. The extended calcination (4 h) also favors more complete pyrolysis of the carbon and increase silica content in the composites. This is important as a higher ratio of silicate in the final MCS product results in a greater fraction of active material.

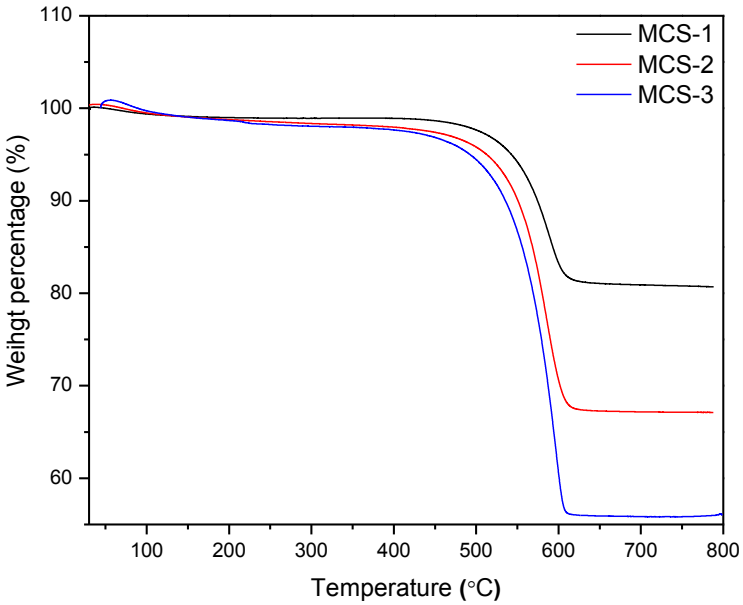

Figure 5.1 TGA data of the three MCS mesoporous frameworks under air.

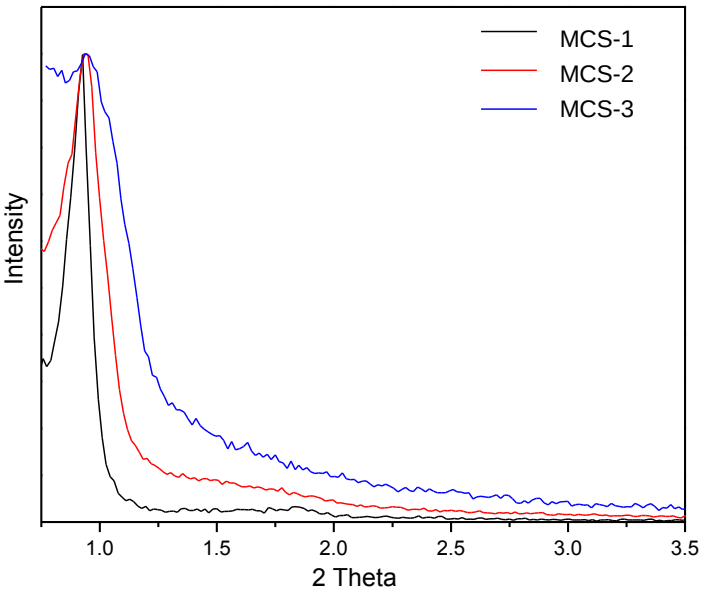

Figure 5.2 Low angle XRD patterns of the three MCS samples.

The mesoporous structure of the three MCSs was identified by their low angle XRD patterns in Figure 5.2. The sharp (100) peaks around 0.9 ° imply a well ordered hexagonal symmetry. As observed in the previous work,[7] the regularity of the structure gradually reduces with the increase of carbon content in the MCSs composites.

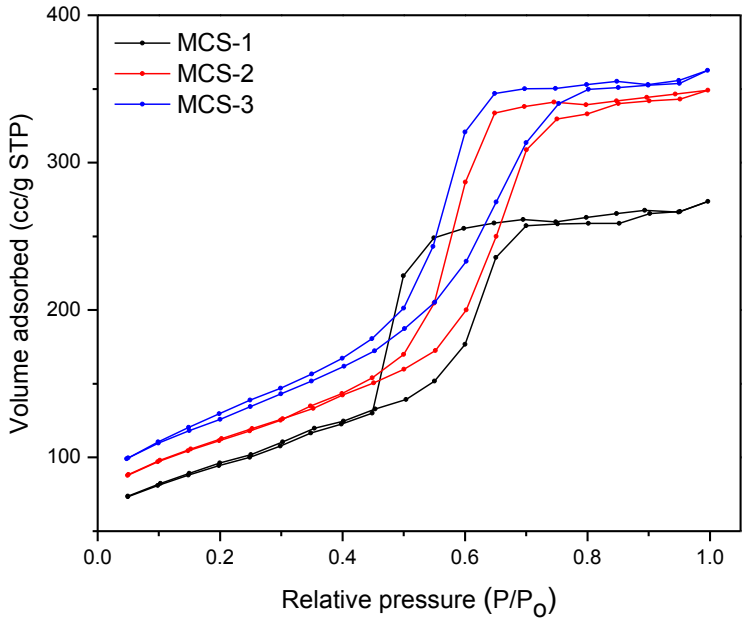

Figure 5.3 N_2 sorption isotherms of the three MCS samples.

All the three samples display type IV N_2 sorption isotherms (Figure 5.3), indicating the presence of the mesoporous channels. The specific BET surface areas enlarge from MCS-1 to MCS-3 due to the increase of the relatively low density of carbon in the composites (i.e. 320 m^2/g for MCS-1 but 424 m^2/g for MCS-3).

5.3.1.2 Characterization of Li_2CoSiO_4/C composites

The formation of Li_2CoSiO_4 was confirmed by the XRD patterns as shown in Figure 5.4. Consistent with previous studies,[4,5] all the three Li_2CoSiO_4 samples prepared by the hydrothermal method adopt the β_{II} phase ($Pmn2_1$). For Li_2CoSiO_4/C-3, a small peak appears at ~18 º, indicating the existence of Li_2SiO_3 (indicated by the asterisk in Figure 5.4) as impurity. Low angle XRD patterns (Figure 5.5) show that the mesostructure of MCSs largely collapse during the hydrothermal process to form the Li_2CoSiO_4/C composites, although a little poorly disordered porous structure residue remains.

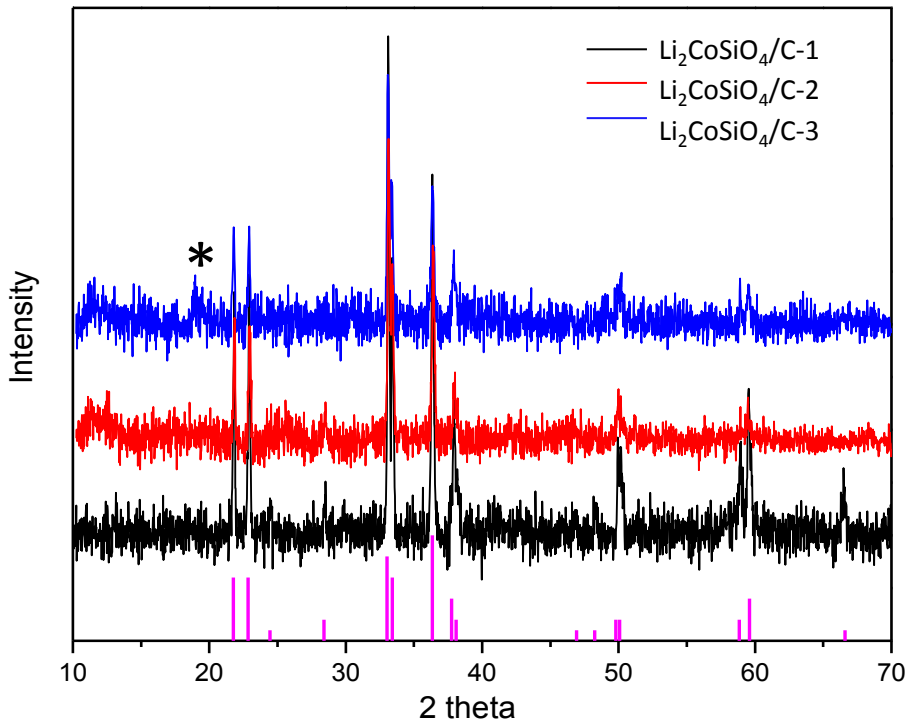

Figure 5.4 Wide angle XRD patterns of the three Li_2CoSiO_4/C samples.

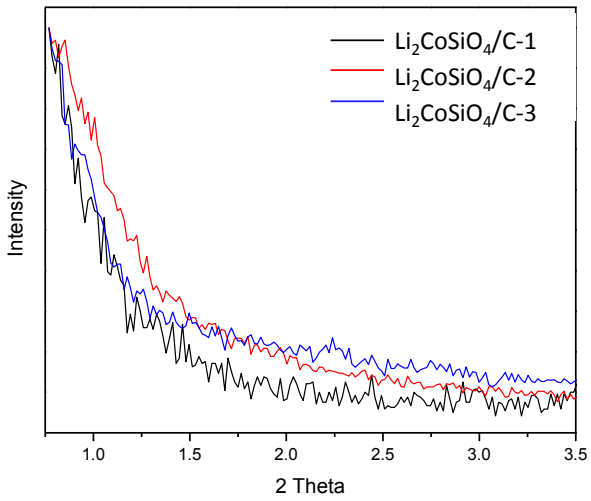

Figure 5.5 Low angle XRD patterns of the three Li_2CoSiO_4/C samples.

Figure 5.6 compares SEM images of MCS-1 and Li_2CoSiO_4/C composites obtained from MCS-1, MCS-2 and MCS-3 under similar magnifications. The silicate precursor MCS-1 has a film-like morphology with no uniform particle size due to the EISA procedure. (also the same result for MCS-2 and MCS-3). However, the three Li_2CoSiO_4/C composites are homogeneous spherical particles with a diameter of ~1-1.5 μm. Higher magnification images of Li_2CoSiO_4/C-1 (Figure 5.6e and f) indicate some of the homogeneous particles have hexagonal morphology. It is known that β_{II} phase of Li_2CoSiO_4 has tetrahedral structure ($Pmn2_1$), but it is also considered as a distorted hexagonal close packing.[8] This may explain the hexagonal crystal morphology of some of the Li_2CoSiO_4/C-1 particles. In addition, the morphology of the Li_2CoSiO_4/C product is also affected by the solvents used in the hydrothermal process, which will be illustrated in the following section **5.3.2.4**. It was noted that there were large pieces of black materials mixing with the homogeneous Li_2CoSiO_4/C particles (Figure 5.6b, c and d), and the more carbon was in the MCS precursors, the more large pieces of black materials appeared in the SEM images.

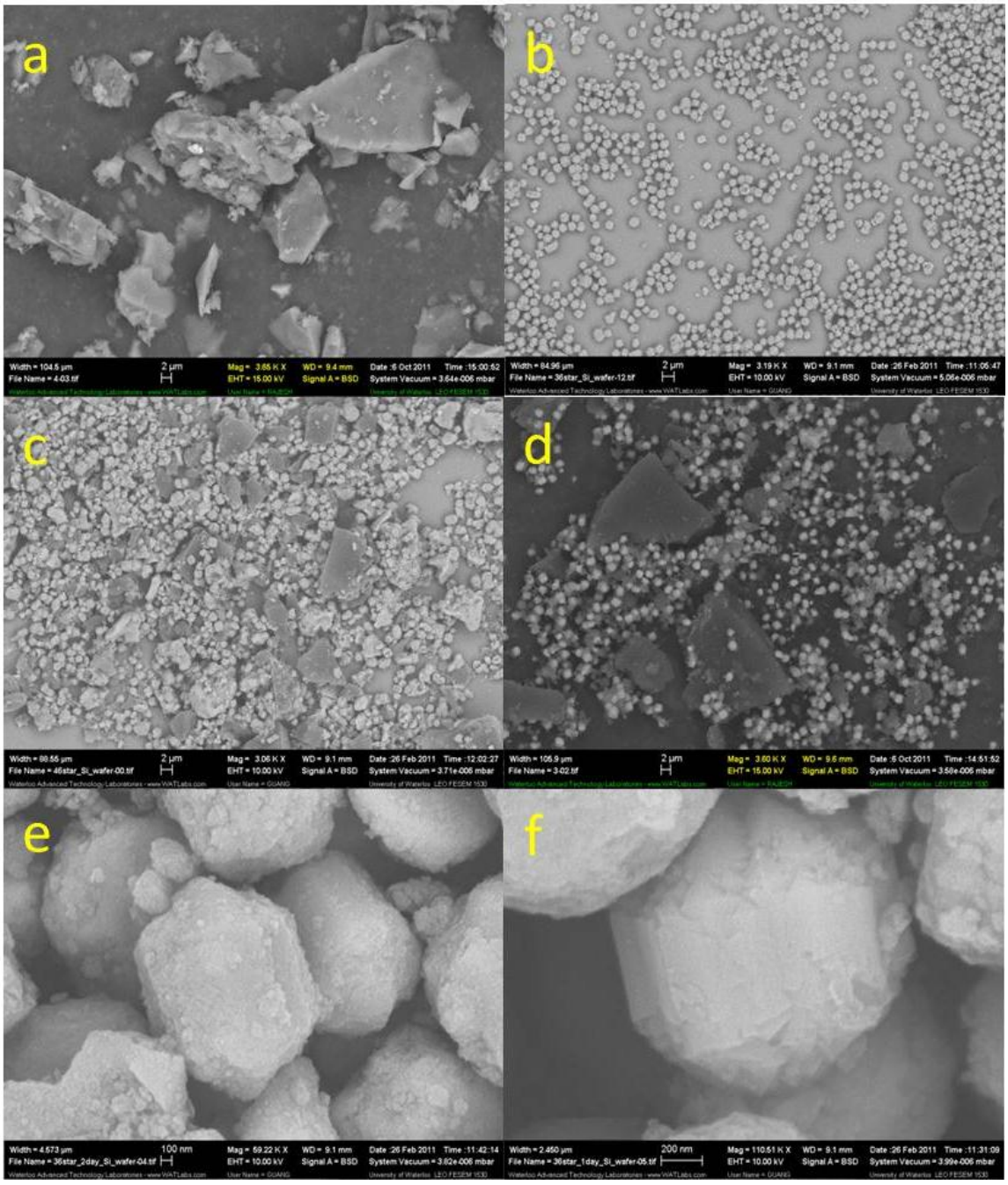

Figure 5.6 (a) SEM images of MCS-1 and (d-f) Li_2CoSiO_4/C composites. (b), (c) and (d) are Li_2CoSiO_4/C prepared from MCS-1, MCS-2 and MCS-3 composites. (e) and (f) are images of (b) at higher magnifications.

The composition of a single Li_2CoSiO_4/C-1 particle was determined by EDAX (Figure 5.7 and Table 5.2). In spite of no lithium could be detected due to the limitation of the technique, the atomic ratio of Co:Si:O almost ideally follows the theoretical ratio of 1:1:4, indicating the formation of Li_2CoSiO_4. The carbon content in the particle is ~5.2 wt%, lower than the theoretical calculation (theoretically, carbon ratio in the composites reduces from ~18 wt% to 7.4 wt% from MCS-1 to Li_2CoSiO_4/C-1). Since the substrate of the sample also contains carbonaceous material, the real carbon content in the particle is even lower than 5 wt%.

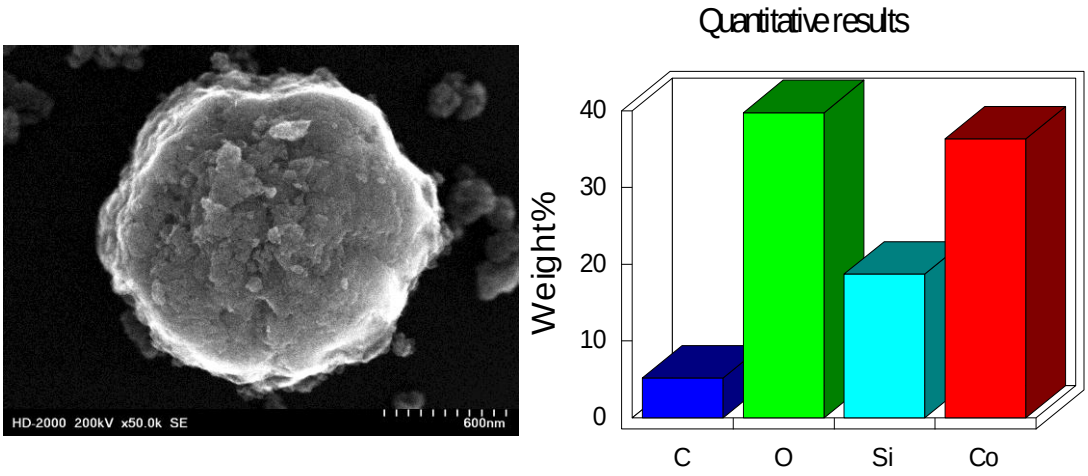

Figure 5.7 SEM image and EDAX analysis of a single Li_2CoSiO_4/C-1 particle.

Table 5.2 Detailed EDAX results of a single Li_2CoSiO_4/C-1 particle.

Element	Weight %	Atomic %
C	5.19	10.29
O	39.74	59.15
Si	18.74	15.89
Co	36.33	14.68
Totals	100.00	100.00

EDAX analysis of the large pieces of black particles confirms that carbon is the most abundant element, along with small fractions of O, Si, and Co (Figure 5.8). These particles are probably the carbon residues of the MCS composites after hydrothermal reactions, which account for the disordered porous structure (Figure 5.5) of the Li_2CoSiO_4/C product as well. These large carbon pieces, with a mean particle size above 10 μm, probably do not assist very much in improving the conductivity of the cathodes, but sacrifice the capacity and energy density of the cathodes. Therefore, Li_2CoSiO_4/C-2 and Li_2CoSiO_4/C-3 were not further investigated for morphology and particle size optimization. In the next section **5.3.2**, only Li_2CoSiO_4/C-1 was studied with various synthetic conditions, such as precursor concentrations, reaction temperatures, reaction duration, different solvent and system $C_{[OH]}$-. In order to make it easier to mark the Li_2CoSiO_4/C-1 sample, it will be labeled as Li_2CoSiO_4/C from now in this chapter.

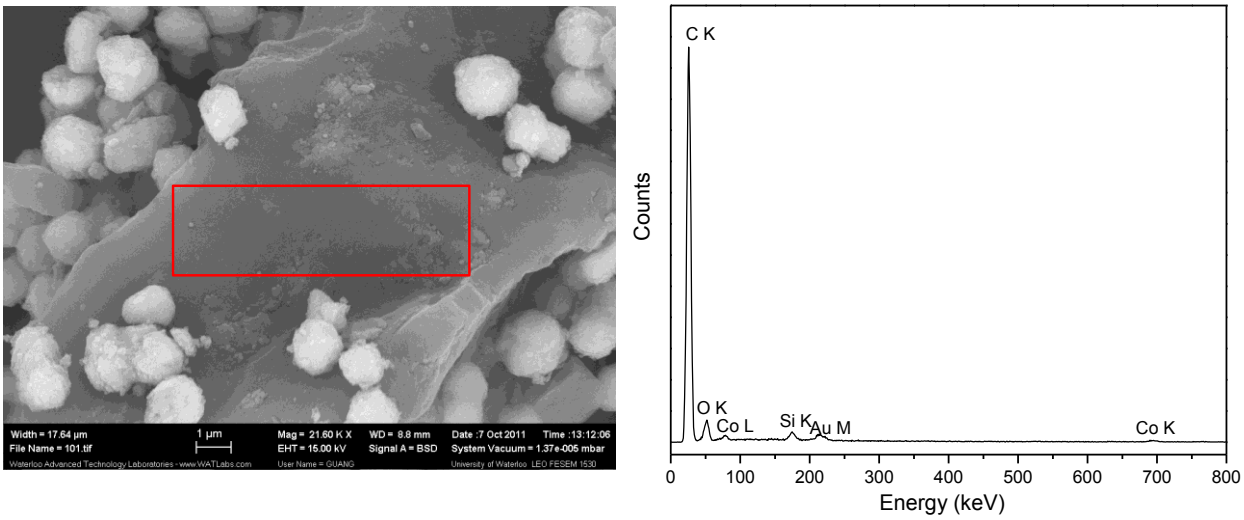

Figure 5.8 SEM image and EDAX analysis of a large piece of the black materials mixed with Li_2CoSiO_4/C-1.

5.3.2 Influence of various conditions on the synthesis of Li_2CoSiO_4/C composites

5.3.2.1 Influence of concentrations of precursors

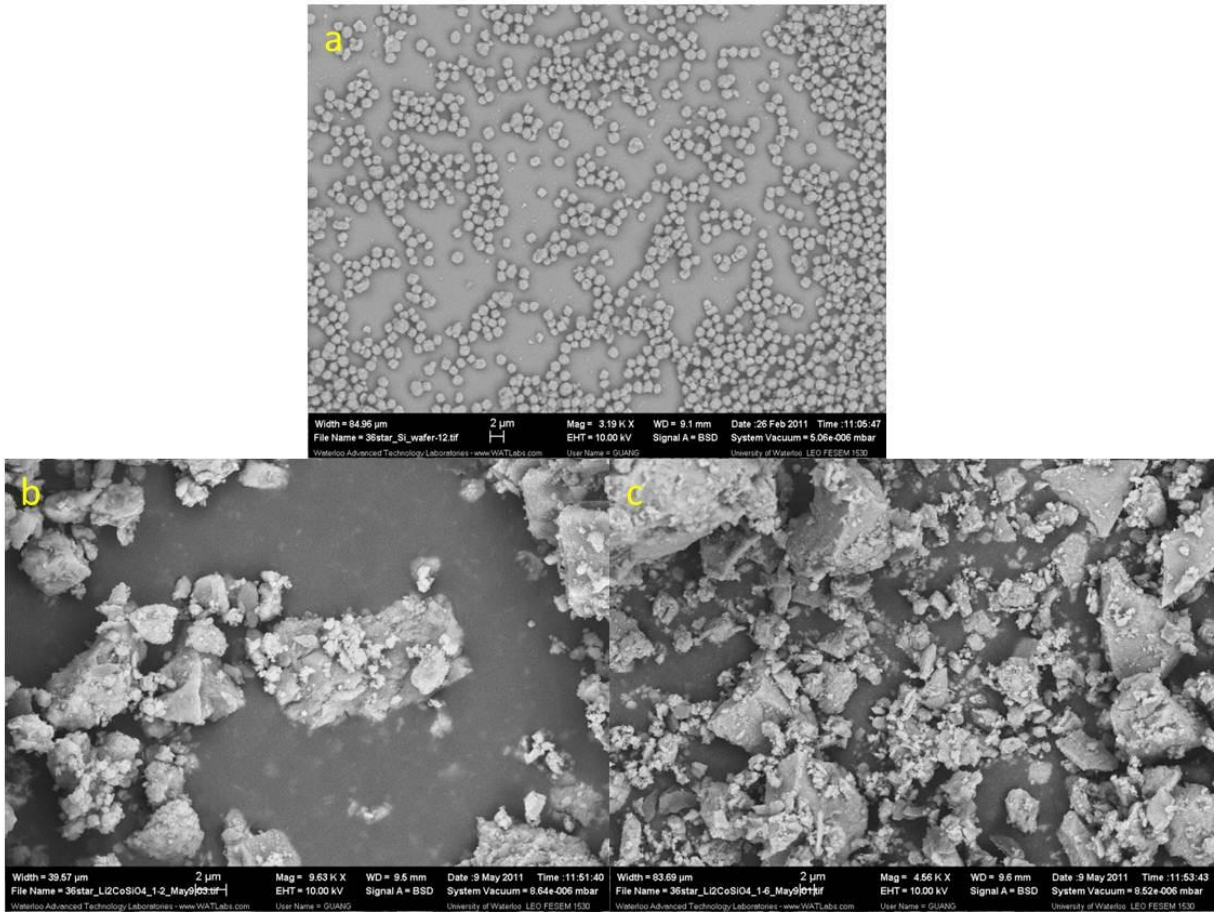

Figure 5.9 SEM images of Li_2CoSiO_4/C synthesized at different precursor concentrations (a) C, (b) 1/2C and (c) 1/6C.

The preparation of Li_2CoSiO_4/C composites was attempted by fixing other parameters as constants but diluting precursor concentrations to 1/2 and 1/6. No homogeneous particles result from the SEM images (Figure 5.9). XRD patterns of the three samples (Figure 5.10) imply that very poor Li_2CoSiO_4 crystallites yield when the precursor concentration was diluted to 1/2, whilst the products cannot be identified by XRD by further diluting the concentration to 1/6 because of their amorphous feature.

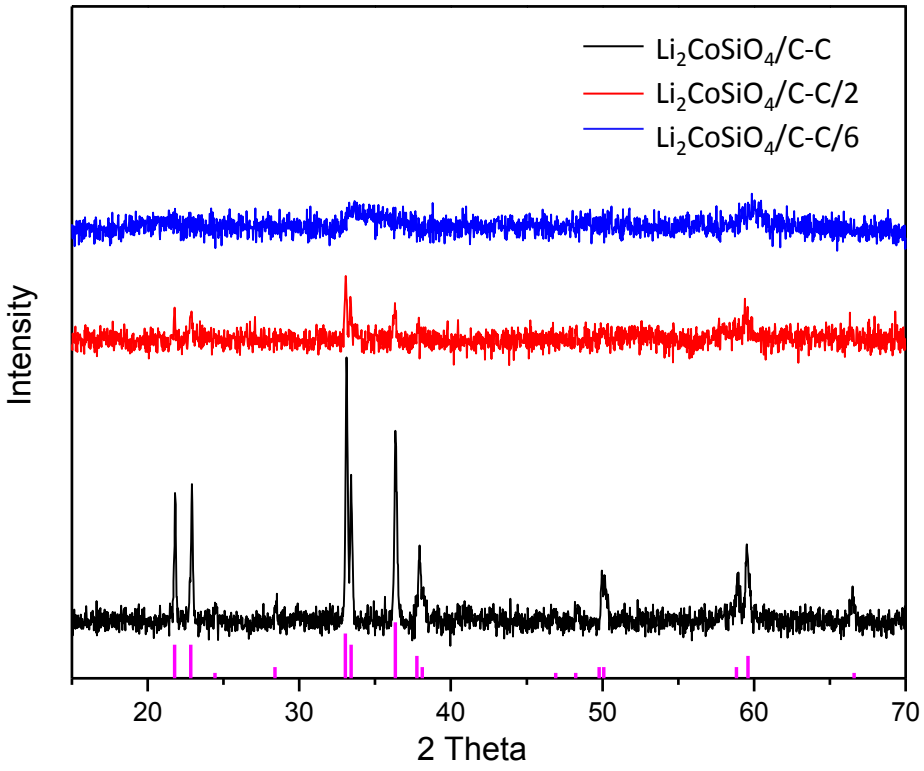

Figure 5.10 XRD patterns of Li_2CoSiO_4/C synthesized at different precursor concentrations.

5.3.2.2 Influence of reaction temperatures

Attempts were also made to prepare Li_2CoSiO_4/C composites at decreased temperatures of 120 ℃ and 100 ℃. Similar to the influence of temperatures on the products, Irregular large particles which have poor crystalline or amorphous structure resulted, as shown in Figure 5.11 and 5.12. The SEM image of the sample synthesized at 100 ℃ clearly exhibits different phases in Figure 5.11c, indicating incomplete reactions between LiOH, MCS and $CoCl_2$ at this low temperature.

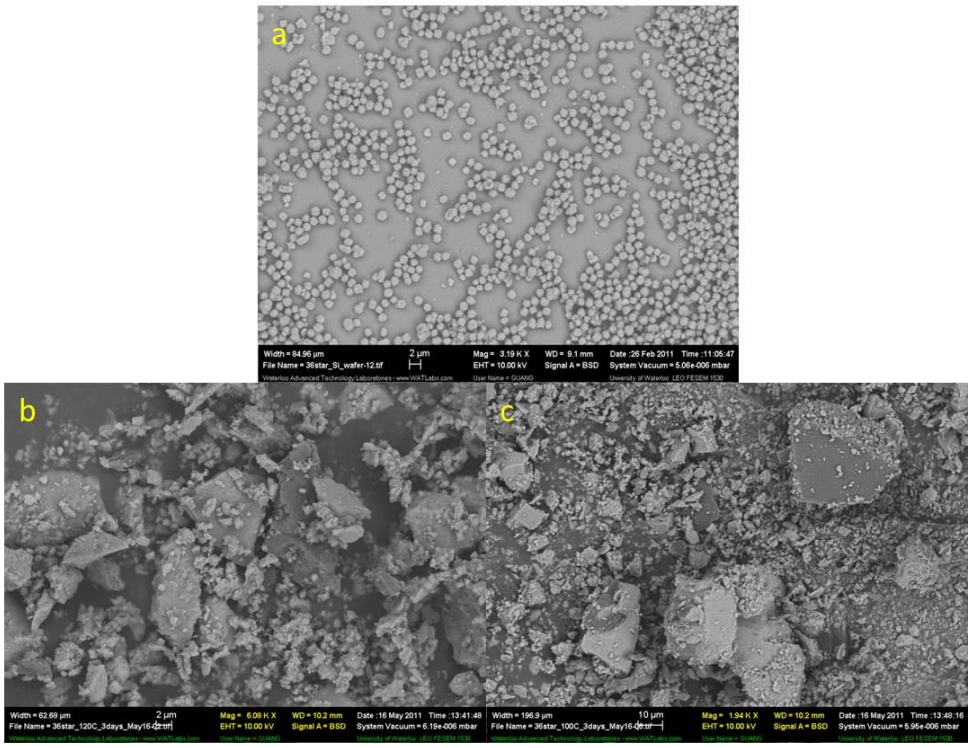

Figure 5.11 SEM images of Li_2CoSiO_4/C synthesized at different temperatures (a) 150 ℃, (b) 120 ℃ and (c) 100 ℃.

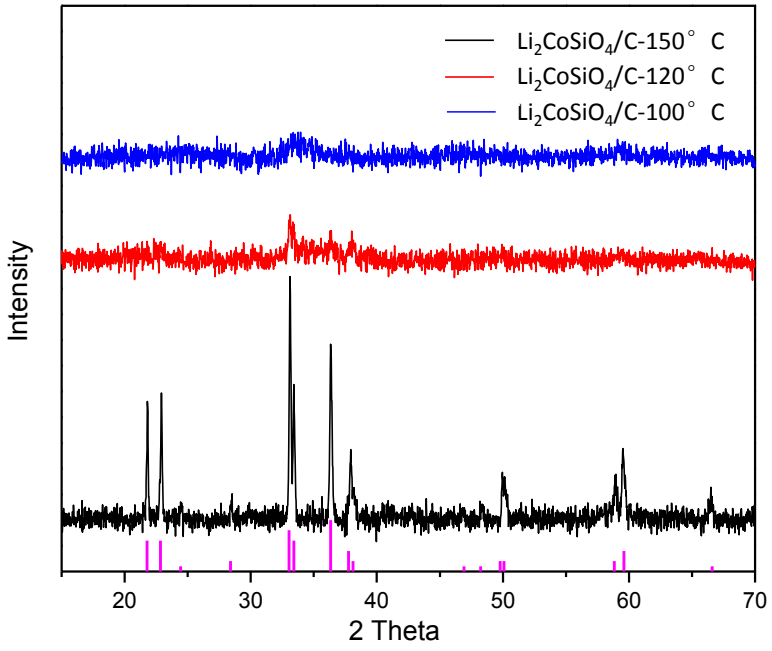

Figure 5.12 XRD patterns of Li_2CoSiO_4/C synthesized at different temperatures.

5.3.2.3 Influence of reaction duration

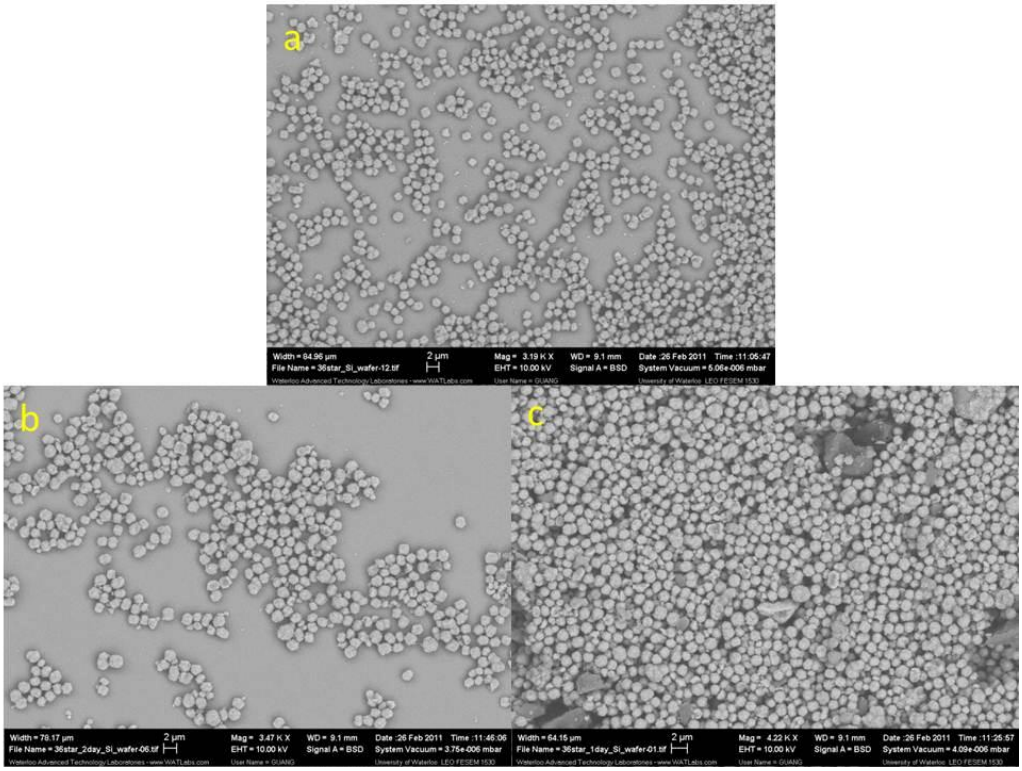

Figure 5.13 SEM images of Li_2CoSiO_4/C synthesized at different reaction duration (a) 72h, (b) 48h and (c) 24h.

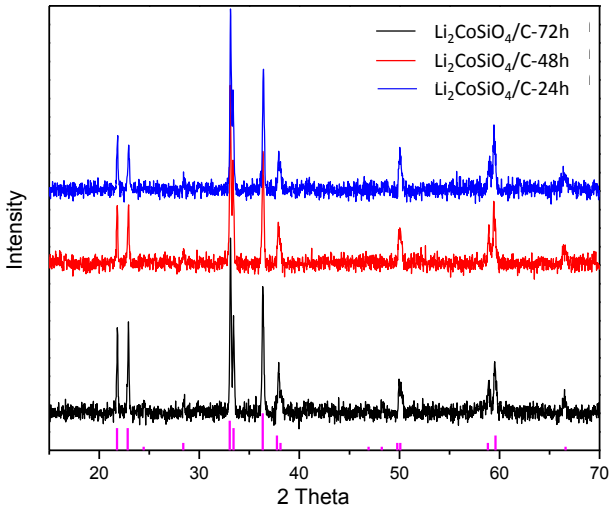

Figure 5.14 XRD patterns of Li_2CoSiO_4/C synthesized at different reaction duration.

By reducing the reaction duration to 48 h and 24 h, the Li_2CoSiO_4/C composites exhibit almost identical XRD patterns (Figure 5.13) and morphologies (Figure 5.14) to that synthesized under extended time of 72 h.

5.3.2.4 Influence of solvent

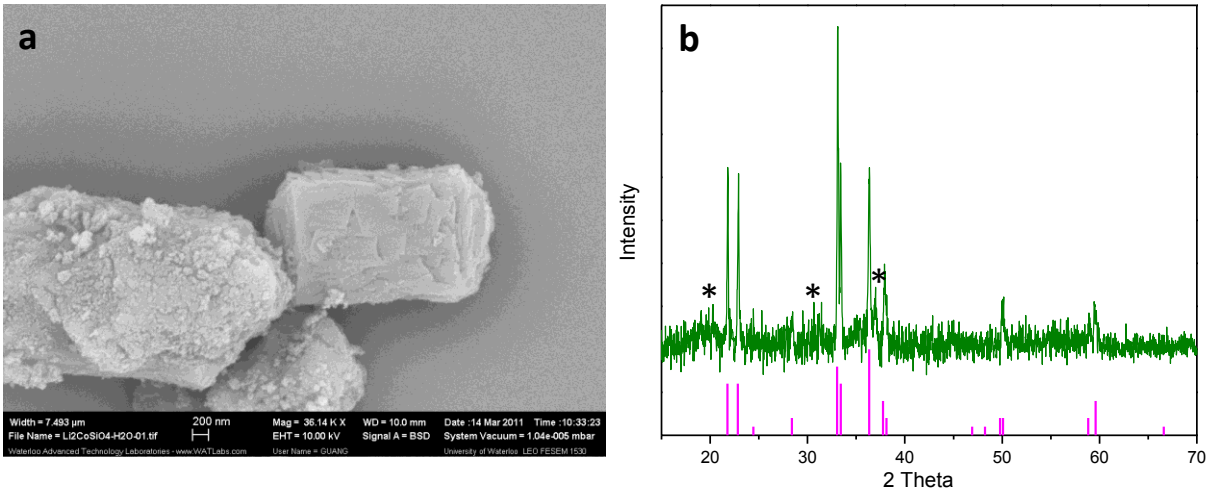

Figure 5.15 (a) SEM image and (b) XRD pattern of Li_2CoSiO_4/C synthesized in deionized H_2O.

Li_2CoSiO_4/C rods were obtained with only deionized water as solvent instead of a mixed solvent of water and ethylene glycol. The diameter of the rods is comparable with the spherical particles prepared in the mixed solvent, as shown in Figure 5.15a. Impurity of Co_3O_4 is observed in the diffraction pattern of the sample (Figure 5.15b, peaks indicated by the asterisks), which indicates ethylene glycol did not only serve as a solvent of the precursors, but has positive influence in the formation of the Li_2CoSiO_4 phase.

5.3.2.5 Influence of $C_{[OH]}$-

Influence of the $[OH]^-$ concentration on the morphology of the Li_2CoSiO_4/C product was studied by adjusting the amount of LiOH H_2O employed in the precursors. In all the above experiments, the molar ratio of LiOH:SiO_2:$CoCl_2$ was set to 4:1:1, but in this section, it is tuned to 0:1:1 (lithium acetate was used as the lithium source), 2:1:1, 8:1:1 and 16:1:1 and the duration of the reaction time was set to 24 h. No crystalline Li_2CoSiO_4 yielded when the concentration of the base (LiOH) was too low (0:1:1 and 2:1:1, Figure 5.16).

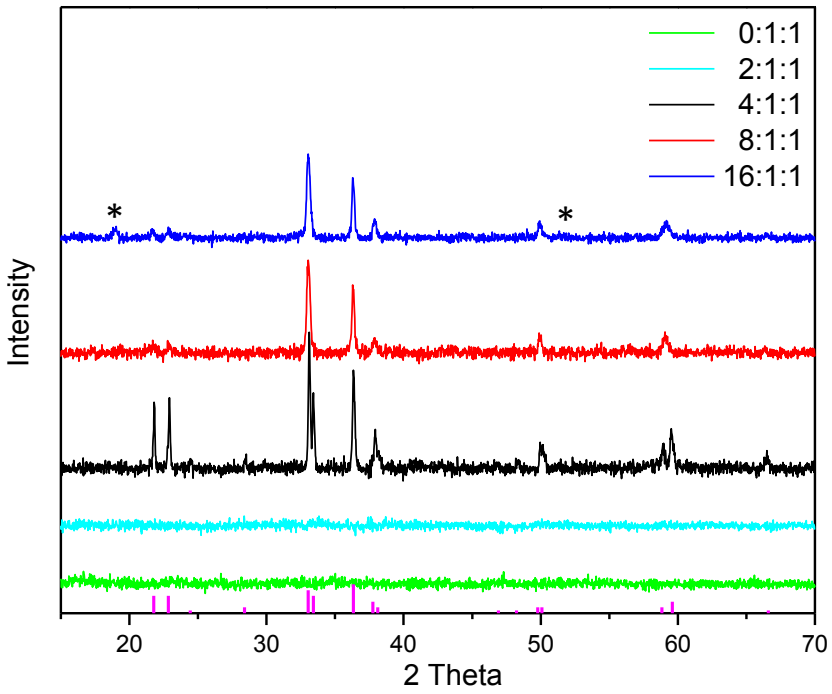

Figure 5.16 XRD patterns of Li_2CoSiO_4/C synthesized at various $[OH^-]$. The caption of the plot demonstrates ratios of [LiOH]/[SiO_2]/[$CoCl_2$].

As described in the experimental, three Li_2CoSiO_4/C samples were synthesized from MCS as a precursor using different LiOH:MCS:$CoCl_2$ ratios, where the silica in the MCS serves as the *in-situ* source of SiO_2. These are denoted as Li_2CoSiO_4/C-4 (4:1:1),

Li_2CoSiO_4/C-8 (8:1:1) and Li_2CoSiO_4/C-16 (16:1:1). The diffraction patterns shown in Figure 5.16 indicate that a well crystallized β_{II} phase is obtained for Li_2CoSiO_4/C-4. With increasing LiOH ratio, the crystallinity becomes a little poorer and the impurity β-$Co(OH)_2$ starts to appear in the highest LiOH content material, Li_2CoSiO_4/C-16. The low intensities of the first two peaks observed in the diffraction patterns of Li_2CoSiO_4/C-8 (and Li_2CoSiO_4/C-16) compared to Li_2CoSiO_4/C-4 simply results from slight differences in the unit cell parameters of these two samples. This was confirmed by Rietveld refinements of the patterns of Li_2CoSiO_4/C-4 and Li_2CoSiO_4/C-8, which yielded good agreement factors and unit cell parameters in accord with that previously reported for the β_{II} phase from combined X-ray and neutron measurements,[9] (namely: a=6.2558(2) Å, b=5.3584(2) Å, c=4.9357(2) Å), but which differed slightly for the two samples: (Li_2CoSiO_8/C-4: a=6.2694(6) Å, b=5.3715(5) Å, c=4.9436(4) Å, R_{wp}=2.198%; Li_2CoSiO_8/C-8: a=6.246(3) Å, b=5.419(3) Å, c=4.945(2) Å, R_{wp}=3.014%). The β_{II} phase Li_2CoSiO_4 with an orthorhombic structure ($Pmn2_1$) has a glide plane and a screw axis known to produce systematic extinctions. Small changes in lattice parameters and atomic position can lead to notable peak intensity redistribution.

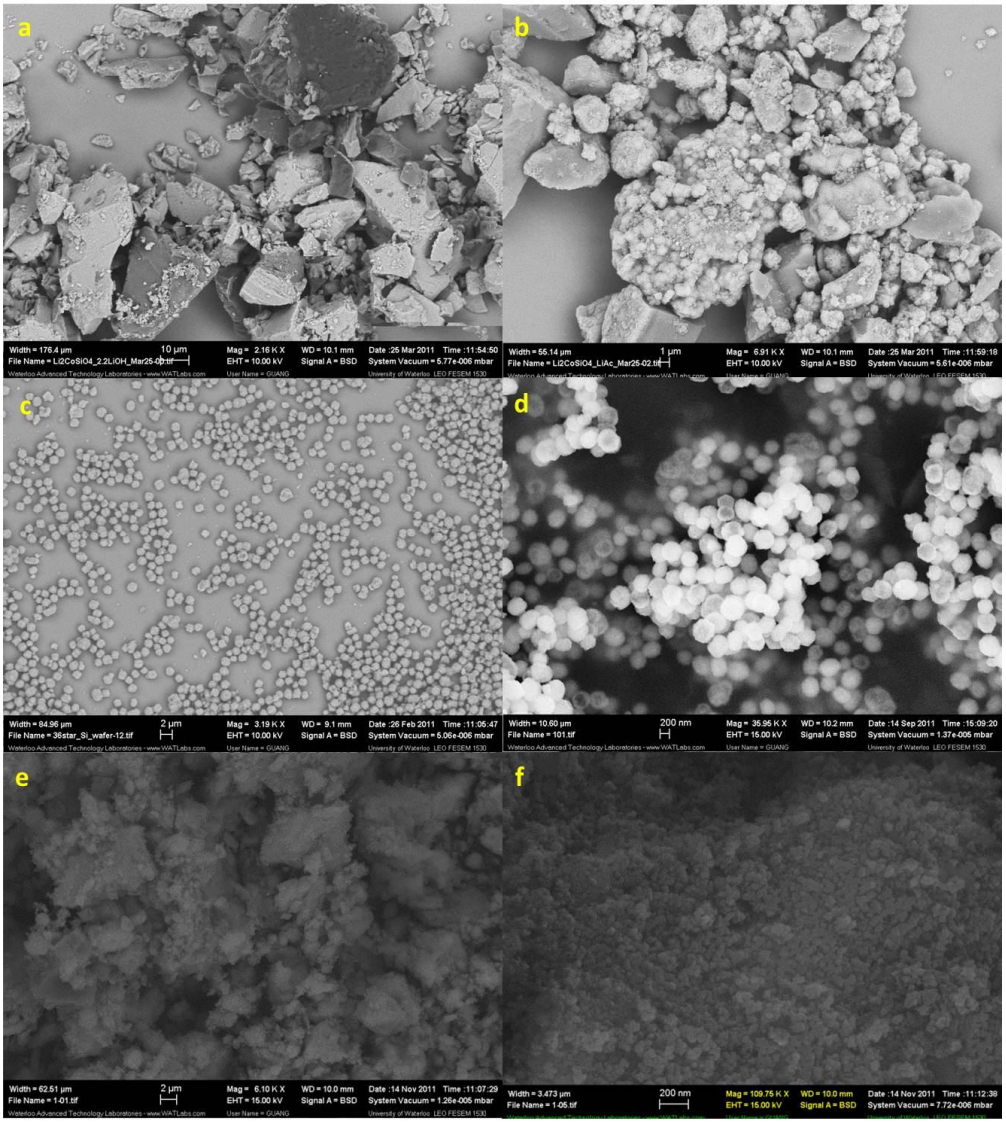

Figure 5.17 SEM images of Li_2CoSiO_4/C synthesized at various [OH^-]. The ratios of [LiOH]/[SiO_2]/[$CoCl_2$] are (a) 0:1:1, (b) 2:1:1, (c) 4:1:1, (d) 8:1:1 and (e) 16:1:1. (f) is the higher magnification of (e).

The morphologies of hydrothermal products are significantly affected by the $C_{[OH]}$-. No uniform particles form without LiOH (Figure 17a) or insufficient LiOH (Figure 17b) in the precursors. Conversely, both Li_2CoSiO_4/C-4 and Li_2CoSiO_4/C-8 exhibit spherical structures,

where the particle size is reduced from ~1-2 μm to 300-400 nm by simply controlling the concentration of LiOH in the precursors (Figure 5.17c and d, respectively). Higher magnification (Figure 5.18a), reveals that the spherical structure of the Li_2CoSiO_4/C-8 is similar to a raspberry composed of 30-50 nm nanocrystalline seeds. More interestingly, some of Li_2CoSiO_4/C-8 spheres exhibit a hollow structure, as shown in Figure 5.17d and Figure 5.18a. Hollow spheres could also be observed in the TEM image (Figure 5.18b), as well as a core-shell structure.

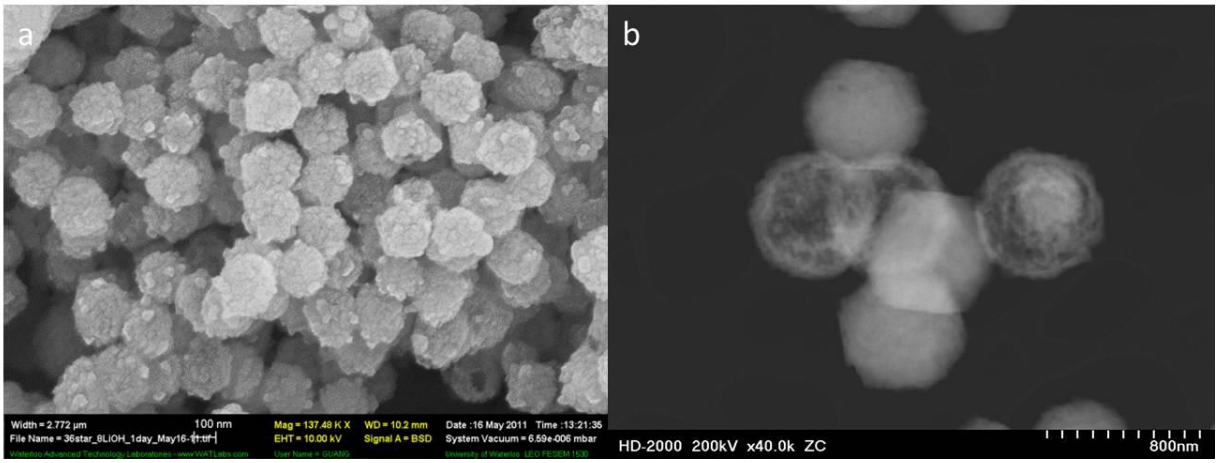

Figure 5.18 Higher magnification (a) SEM image and (b) TEM image of Li_2CoSiO_4/C-8 synthesized at the ratio [LiOH]/[SiO_2]/[$CoCl_2$]=8:1:1.

The uniform particles disappeared by further increasing the concentration of LiOH to 16:1:1 (Figure 5.17e). However, upon further increasing the ratio of LiOH to SiO_2 and $CoCl_2$ (ie Li_2CoSiO_4/C-16), the morphology of the material changed. The overall particle size is even larger than that of Li_2CoSiO_4/C-4, and the uniformly spherical structure disappeared (Figure 5.17e), although the material demonstrates a similar "raspberry structure" to that of

Li_2CoSiO_4/C-8. Small nanocrystallites of ~50 nm can be clearly seen under high magnification (Figure 5.17f).

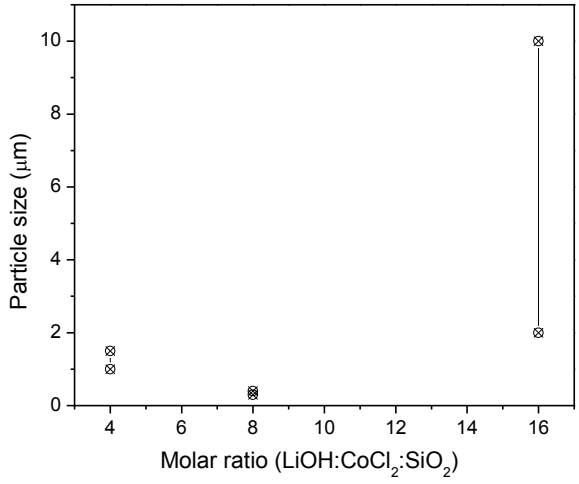

Figure 5.19 Particle size illustration of the three Li_2CoSiO_4/C composites, showing uniform nanoparticles could be obtained with the molar ratio of [LiOH]/[SiO_2]/[$CoCl_2$]=8:1:1.

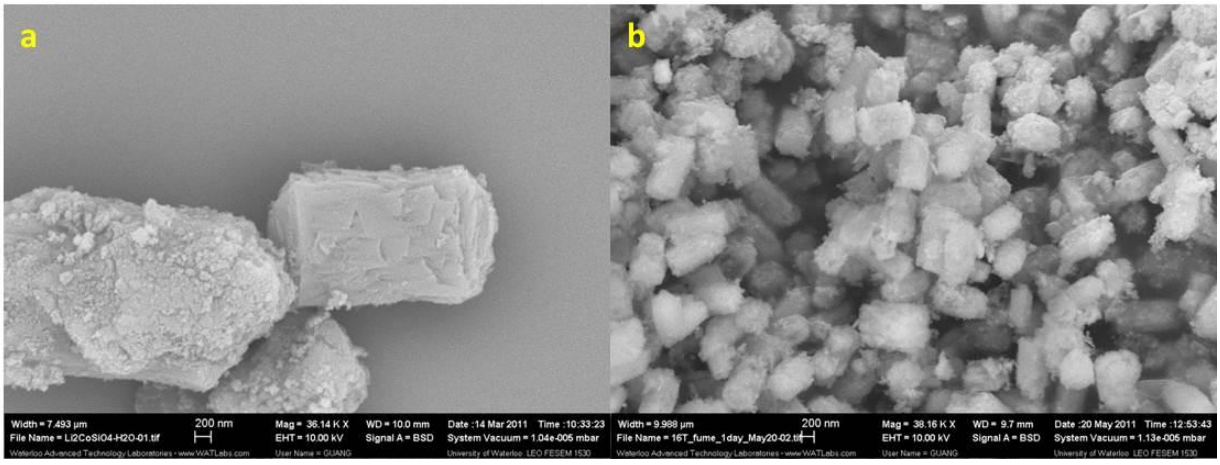

Figure 5.20 SEM images of Li_2CoSiO_4/C synthesized at the ratio of [LiOH]/[SiO_2]/[$CoCl_2$]= (a) 4:1:1 and (b) 8:1:1 in H_2O.

The mean particle sizes of all the three samples are summarized in Figure 5.19. The effect of $C_{[OH]}$- on morphology and particle size of the Li_2CoSiO_4/C composites is also

detected when a pure water solvent applied. The particle size was distinctly reduced by increasing the concentration of LiOH to 8 times of SiO_2 and $CoCl_2$ (Figure 5.20).

5.3.3 Formation mechanism of Li_2CoSiO_4/C nanocomposites

Both solid and hollow particles exhibited almost identical elemental compositions as determined by EDAX analysis (Figure 5.21), indicating that Li_2CoSiO_4 was formed in both cases, but in different morphologies.

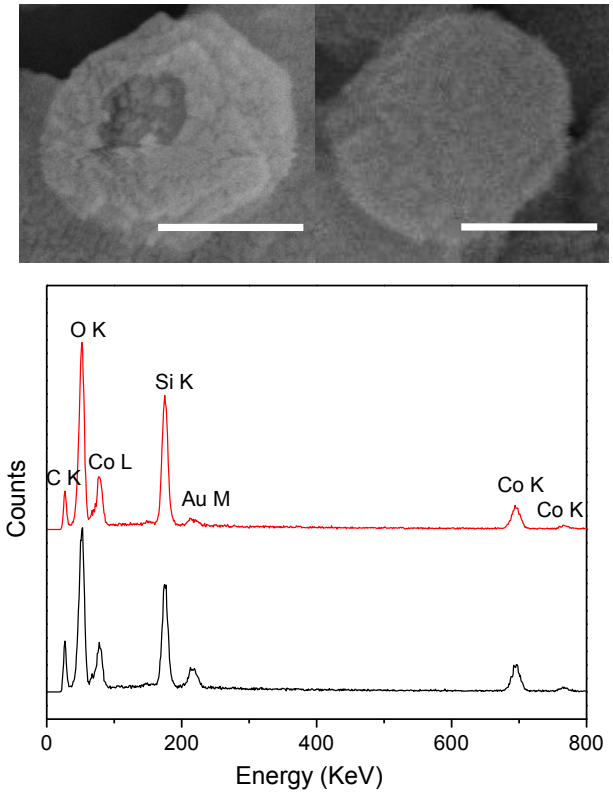

Figure 5.21. SEM images and EDAX analysis of both solid (red line) and hollow (black line) particles of Li_2CoSiO_4/C-8, confirming the same composition of the two particles in spite of different morphologies. The scale bars are 300 nm.

To confirm the formation of the $[CoSiO_4]^{2-}$ polyanion as the framework entity in Li_2CoSiO_4/C-8, we carried out multipoint EDAX measurements on more than 15 randomly selected spheres, all of which exhibited a Si and Co atomic ratio of 1:1 (Figure 5.22).

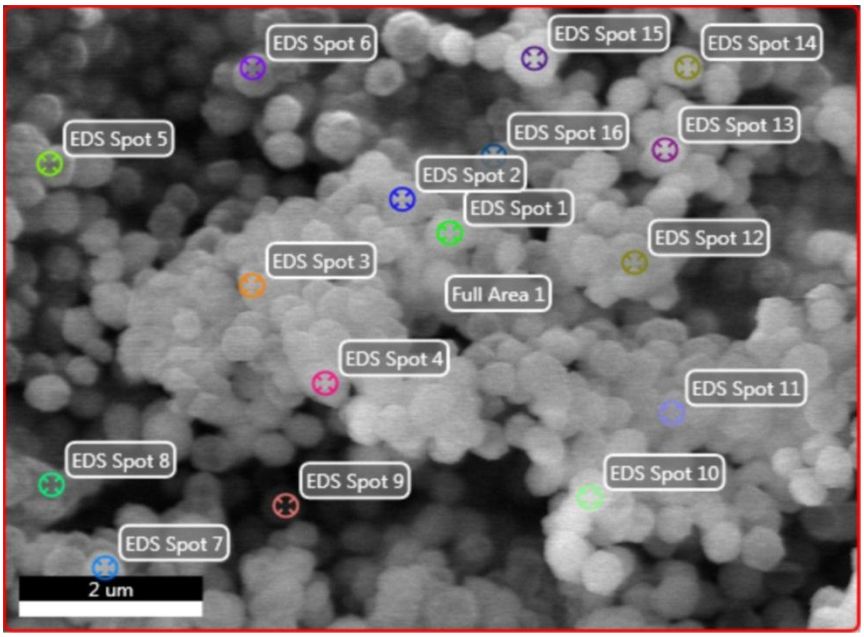

	Full area	EDS Spot 1	EDS Spot 2	EDS Spot 3	EDS Spot4	EDS Spot5	EDS Spot 6	EDS Spot 7
Si	49.4%	50.2%	49.9%	48.0%	48.6%	47.2%	49.0%	50.0%
Co	50.6%	49.8%	50.1%	52.0%	51.4%	52.8%	51.0%	50.0%

EDS Spot 8	EDS Spot 9	EDS Spot 10	EDS Spot 11	EDS Spot 12	EDS Spot 13	EDS Spot 14	EDS Spot 15	EDS Spot 16
49.8%	49.8%	48.8%	49.2%	49.1%	50.2%	49.1%	50.8%	48.3%
50.2%	50.2%	51.2%	50.8%	50.9%	49.8%	50.9%	49.2%	51.7%

Figure 5.22. SEM image and EDAX analysis summary of Li_2CoSiO_4/C-8 spheres.

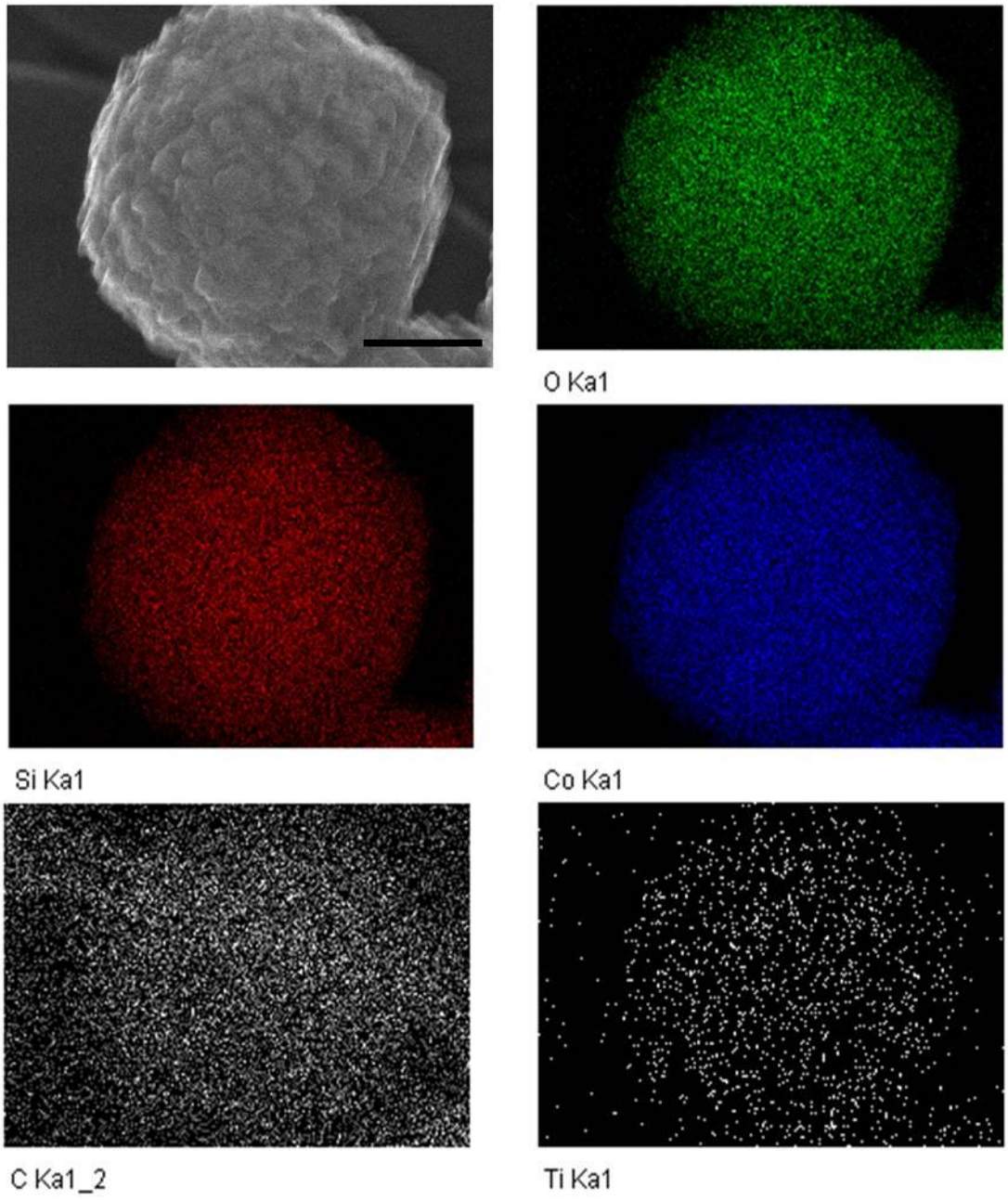

Figure 5.23 TEM image and the corresponding elemental maps of a single Li_2CoSiO_4/C-8 particle, showing a homogeneous distribution of carbon nanoparticles on Li_2CoSiO_4. The scale bar is 100 nm, and Ti is a reference element.

The elemental maps conducted on a single Li_2CoSiO_4/C-8 particle display a homogeneous distribution of carbon (Figure 5.23). However, the degree of nanocarbon incorporation cannot be determined by either the EDAX spectrum or elemental mapping analysis, due to the influence of the underlying carbon substrates. In addition, some of the carbon aggregates as large particles mixed in with the Li_2CoSiO_4/C spheres (Figure 5.8), present in all three Li_2CoSiO_4/C samples. We believe this arises from residual carbon in the mesoporous carbon-silica (MCS) precursor. As discussed above, the carbon content in MCS is determined to be ~18 wt%. However, the specific carbon ratio in various MCS particles may differ. For those particles with abundant carbon but significantly less SiO_2, the conversion from SiO_2 to Li_2SiO_3 probably would not fragment the micron-size MCS particles.

In order to estimate the amount of nano-carbon embedded in the silicate, thermogravimetric analysis of Li_2CoSiO_4/C-8 was carried out (Figure 5.24a). Under a N_2 atmosphere, three approximate weight losses in the curve are apparent. The first drop below 200 ℃ (region I, ~2 wt%) is attributed to the removal of adsorbed moisture by the material, similar to the behavior of MCS (Figure 5.1a). From 200 ℃ to 500 ℃, the weight loss (region II) is due to the "internal"oxidation of carbon by Li_2CoSiO_4 which evolve CO_2,

$$2Li_2CoSiO_4 + C = Li_2Si_2O_5 + Co + Li_2O + CO_2\uparrow$$

The XRD pattern of Li_2CoSiO_4/C-8 treated under a N_2 flow at 400 ℃ for 1h (Figure 5.24b) confirmed the formation of $Li_2Si_2O_5$ and metallic Co. The other presumed product Li_2O, is assumed to exist as an amorphous phase that is not visible in the XRD. Bruce *et al*. also reported that all the attempts to carbon "wire" the β_{II} - Li_2CoSiO_4 phase failed due to the formation of lithium silicate and Co metal,[4] which is consistent with our finding. The weight loss in the second stage (II) is ~5 wt%, which correlates to ~2 wt% carbon nanoparticles

encapsulated in Li_2CoSiO_4 calculated from the above equation. TGA only provides an approximate estimation of the amount of the nanoscale carbon, which may deviate from the actual content. However, this estimation is still helpful in considering the electrochemical performance of this material, which will be discussed later.

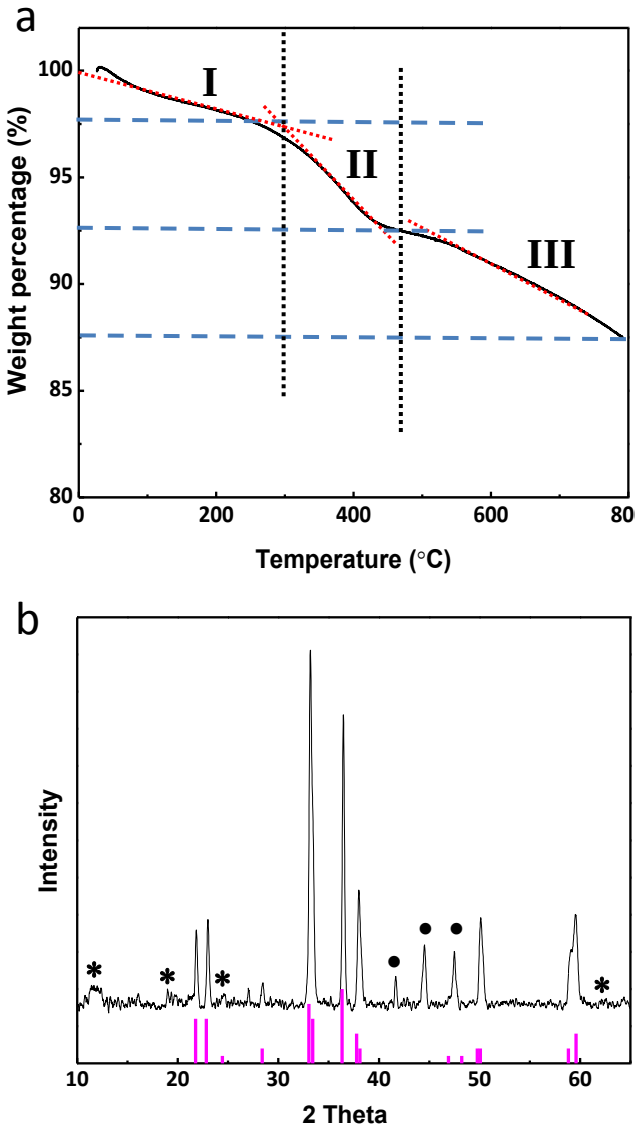

Figure 5.24 (a) TGA of Li_2CoSiO_4/C-8 spheres under N_2 (10 ℃/min), and (b) XRD pattern of Li_2CoSiO_4/C-8 after treated in N_2 at 400 ℃ for 1 h. Peaks labeled by asterisks and cycles indicate the formation of Li_2SiO_5 and metallic Co.

Because the carbon involved in the reaction in region II is homogeneously mixed with Li_2CoSiO_4 particles at the nanoscale, reactivity in the solid-solid reaction at low temperature is more facile than for the large carbon particles (see Figure 5.8) the latter of which account for the final, third weight loss in the TGA curve (above 500 ℃; region III). In accord, the diffraction pattern of the material heated at 800 ℃ shows only the presence of $Li_2Si_2O_5$ and Co, with no Li_2CoSiO_4 remaining.

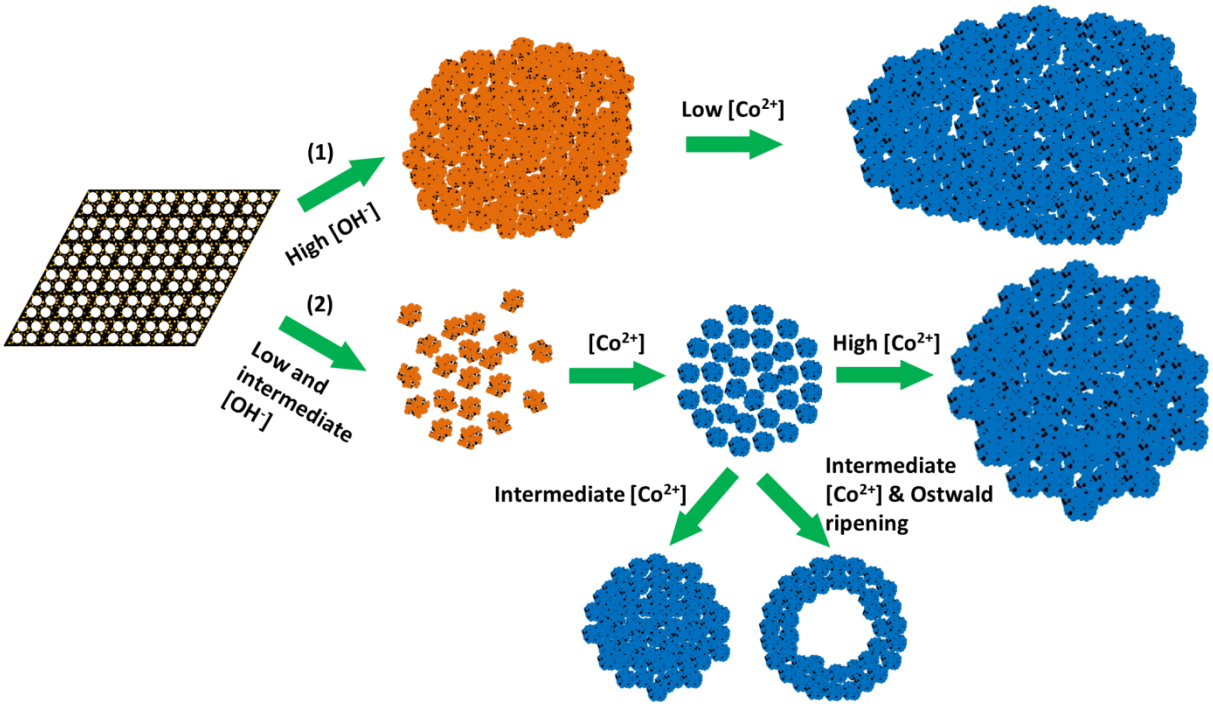

Figure 5.25 Schematic representation of the synthetic mechanism of Li_2CoSiO_4/C composites from highly ordered mesoporous framework MCS.

A possible mechanism to account for the formation of the encapsulated Li_2CoSiO_4/C is illustrated in Figure 5.25. At either high or low [OH^-] concentrations, MCS-1 is etched in the presence of LiOH at elevated temperature; the intermediate product in this step is probably

Li_2SiO_3 (shown in orange). This differs from the synthesis of ordered mesoporous carbons from their silica replicas, where aqueous NaOH is used as the etchant which reacts with SiO_2 to form highly soluble water glass (Na_2SiO_3).[10,11] Thus, the underlying carbon mesostructure is fully maintained. However, Li_2SiO_3 has very low solubility under alkaline conditions even at 175 ℃,[12] which would account for the collapse of the ordered mesostructure of the MCS, because it does not dissolve but rather fragments.

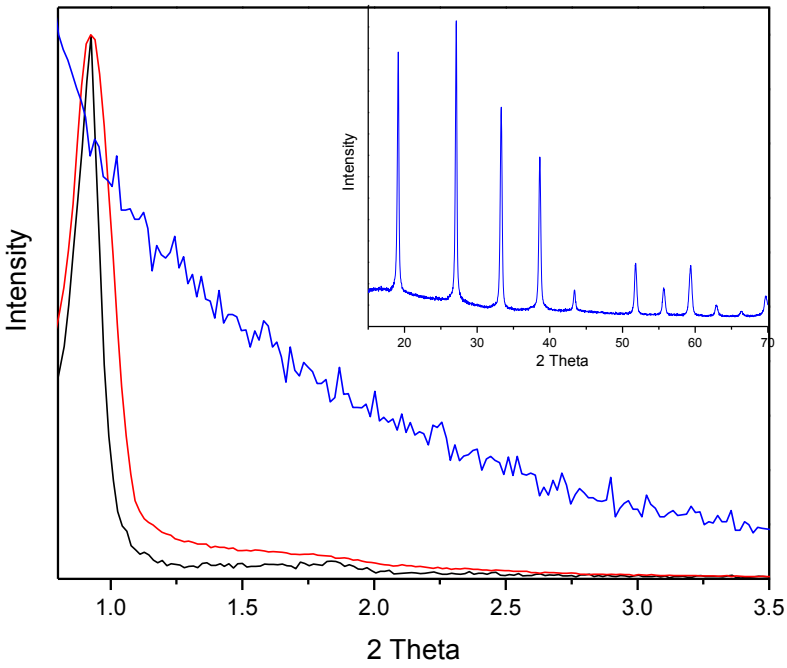

Figure 5.26 Low angle XRD patterns of the highly ordered MCS-1 framework (black curve) and the product of MCS-1 after hydrothermal treatment at 150 ℃ with (blue curve) and without LiOH (red curve). Inset is the wide angle XRD pattern of the product obtained from MCS-1 treated with LiOH, indicating the formation of Li_2SiO_3.

Figure 5.26 compares low angle XRD patterns of the as-prepared MCS-1 (black curve), and those treated hydrothermally with and without LiOH. As expected, the highly ordered MCS-1 framework is very stable under a hydrothermal condition at 150 ℃ up to 24 h (red curve), but collapsed within 6 h in the presence of LiOH. The product of the latter reaction is identified to

be Li_2SiO_3 (inset blue curve in Figure 5.26). The mean diameter of the hexagonal pores in MCS-1 is ~6 nm, analyzed based on the pore size distribution curve (Figure 5.27a). The collapse of the carbon framework creates a large number of carbon nanoparticles, since the wall thickness of the mesopores are only ~5 nm (Figure 5.27b) as calculated from the low angle XRD and pore size distribution results. These nanocarbon particles are intimately mixed with the Li_2SiO_3 nanocrystallites (~30-50 nm) and became the "seeds" of the "raspberry" structure. At low or intermediate [OH^-] concentrations (path 2), the seeds are formed relatively slowly and their aggregation is isotropic. Therefore, a spherical morphology results for Li_2CoSiO_4/C-4 and Li_2CoSiO_4/C-8. When the [OH^-] concentration is quite high (path 1), both the silica etching and the seed aggregation takes place very quickly and no regular morphology is exhibited, as in the case of Li_2CoSiO_4/C-16. The next step involves reaction of the Li_2SiO_3 with cobalt in solution to form Li_2CoSiO_4, a process that is strongly affected by the concentration of [Co^{2+}]. In turn, the [Co^{2+}] is dependent upon the hydroxyl concentration, because the reaction of $CoCl_2$ with LiOH immediately precipitates $Co(OH)_2$ owing to its low solubility. Thus in the case of Li_2CoSiO_4/C-4, the very low [OH^-] concentration after silica etching in the MCS composites results in little precipitation of $Co(OH)_2$, and hence a higher [Co^{2+}] than in the other two cases. Accordingly, growth of Li_2CoSiO_4 crystals is relatively faster, which explains the larger particle size of Li_2CoSiO_4/C-4 vs that of Li_2CoSiO_4/C-8, as well as its higher crystallinity as exhibited by its XRD pattern. In contrast, for the other end member, Li_2CoSiO_4/C-16, the β-$Co(OH)_2$ impurity (Figure 5.16) is probably due to an insufficient [Co^{2+}] concentration, which limits the complete conversion of [$Co(OH)_2 + Li_2SiO_3$] $\rightarrow$ Li_2CoSiO_4.

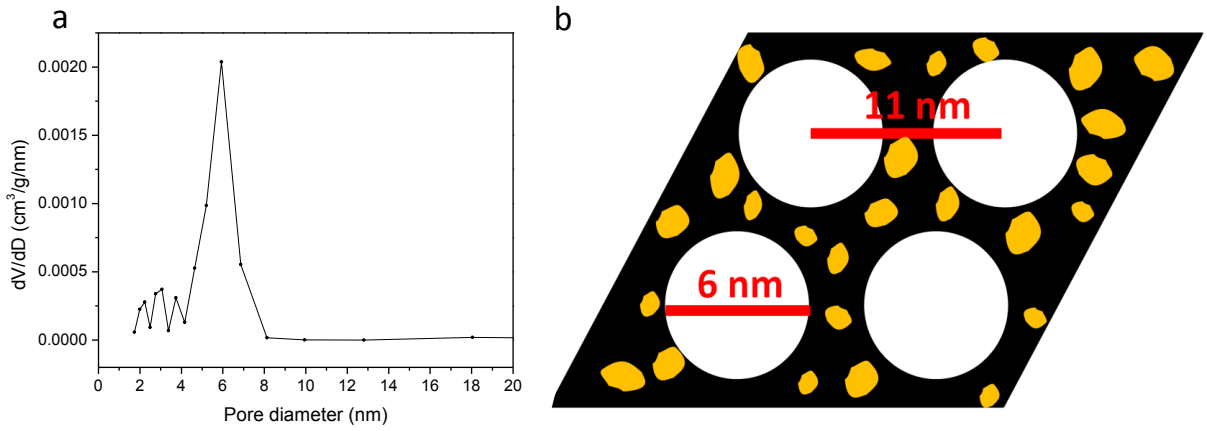

Figure 5.27 (a) Pore size distribution by the BJH method of the ordered mesoporous MCS-1 framework and (b) the corresponding schematic representation of its pore size and the wall thickness.

The hollow and core-shell morphologies of Li_2CoSiO_4/C-8 could be attributed to the Oswald ripening effect. Zeng and co-workers first reported the preparation of hollow or core-shell nanomaterials following this strategy in 2004.[13] Briefly, when a solid particle is comprised of smaller crystallites, or seeds of the raspberry structure, the crystallites locate in the inner cores always have less dense but higher surface energy than those in the outer surfaces. In order to decrease the system energy, they tend to dissolve and re-deposit on the outer part, resulting in the formation of hollow structures.[14] Various nano hollow spheres, as well as core-shell materials have been synthesized following this mechanism, such as TiO_2,[15] ZnS,[16] Co_3O_4,[14] Cu_2O[17,18] and Li_2SiO_3[11]. Similar effect is believed to occur on Li_2CoSiO_4/C-8 during the synthesis.

5.3.4 Electrochemical performance of Li_2CoSiO_4/C-8

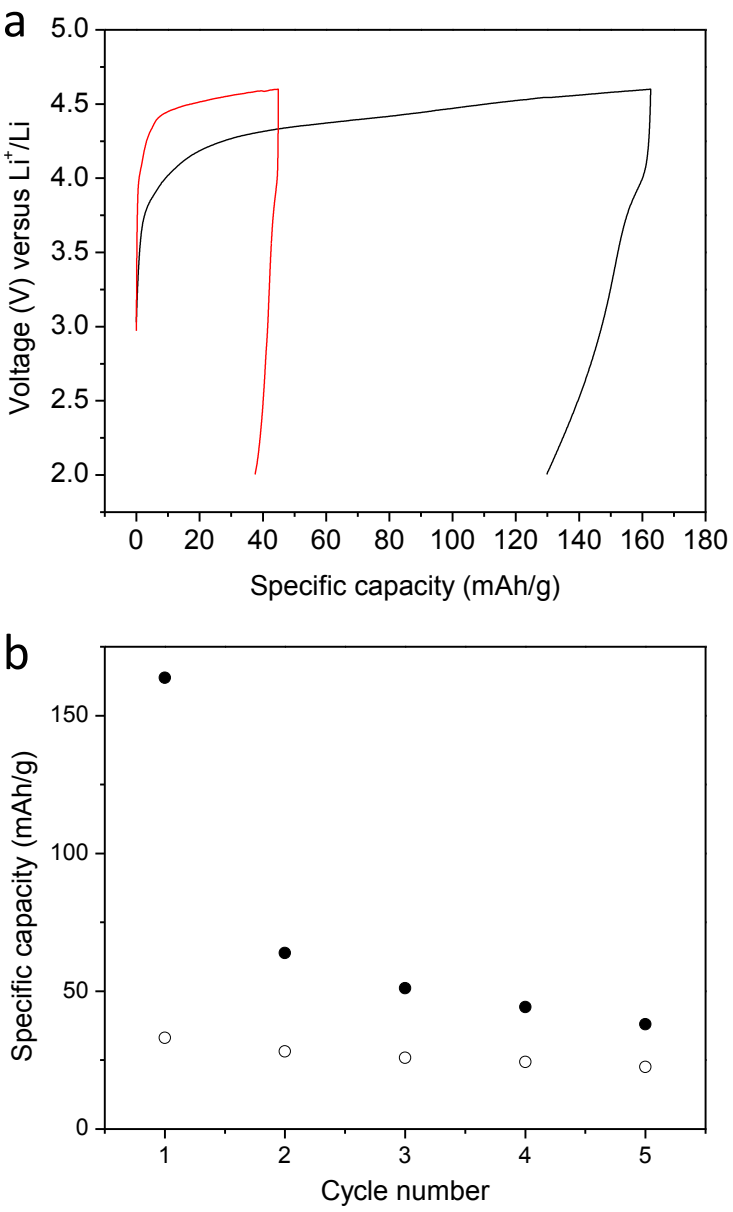

Figure 5.28. (a) Initial profiles of Li_2CoSiO_4/C-8 (black curve) and Li_2CoSiO_4/C-8-F (red curve), and (b) cycling charge-discharge capacities of Li_2CoSiO_4/C-8.

The electrochemical performance of Li_2CoSiO_4/C-8 was evaluated in a half-cell configuration using metallic lithium as the anode and 1 M $LiPF_6$ in EC/DMC as the electrolyte

at room temperature. The current rate and voltage window were set as C/30 (~11 mA/g) and 2.0 V-4.6 V respectively. The initial charge curve displays a plateau above 4.2 V (Figure 5.28a, black curve), much higher than that of iron and manganese silicate cathodes, but consistent with previous results for Li_2CoSiO_4.[4] The charge capacity is 162 mAh/g. This corresponds to the extraction of 1.0 Li, although the shape of the curve suggests that other processes are also at play, such as electrolyte oxidation. Similar to other reports of this material,[4,19] the reversible discharge capacity (~33 mAh/g) is much less, indicating the difficulty of reinserting lithium ions back into the structure. Severe capacity fading occurs after the first cycle and then stabilizes (Figure 5.28b), which is indicative of a structural change that presumably accompanies all members of the Li_2MSiO_4 family.[4,20,21] The significance of the nanoscale "intenral" carbon is clearly demonstrated by comparing the initial charge-discharge profiles of Li_2CoSiO_4/C-8 and Li_2CoSiO_4/C-8-F. The Li_2CoSiO_4/C-8-F electrode was prepared by simply mixing conductive carbon and the active material Li_2CoSiO_4/C-8-F which was synthesized using the same conditions as Li_2CoSiO_4/C-8, but using fumed silica. Thus no "internal" carbon is present. Although both electrodes contained comparable total carbon content (~15 wt%), the Li_2CoSiO_4/C-8-F exhibits a charge capacity of only ~70 mAh/g and the discharge capacity is almost negligible (Figure 5.28a, red curve). Therefore, the homogeneous carbon incorporation on the nanoscale is indeed a key factor in obtaining improved electrochemical results for silicate cathodes. It is worth noting that the significant electrochemical enhancement in our experiments arises from only ~2 wt% "internal' nanocarbon. Further fine-tuning of the synthesis conditions to result in a larger nanocarbon fraction would undoubtedly further improve the network conductivity of the silicate electrodes.

5.4 Conclusions.

Li_2CoSiO_4/C nanocomposites were synthesized via a facile hydrothermal method, by selecting a unique carbon/silica mesoporous framework (MCS) as the silicate precursor as well as the carbon source. The morphology and particle size of the composites could be tailored by simply adjusting the concentration of the LiOH etching agent, and adjusting the ratio of LiOH:Si:Co in the precursors. At a molar ratio of 8:1:1, uniform spheres with a mean diameter of 300-400 nm were obtained, among which both hollow and core shell structures were observed. The proposed reaction mechanism suggests that a higher concentration of [OH^-] favors the formation of Li_2SiO_3 but hinders the subsequent conversion to Li_2CoSiO_4. Approximately 2 wt% of nanoscale carbon was distributed on/in the Li_2CoSiO_4, which arises from the collapse of the highly ordered porous structure of the mesporous carbon/silica framework. The released carbon nanoparticles play a significant role in improving the electrochemical performance of the electrode compared to materials that lack the encapsulated "nanocarbon". This strategy can be potentially extended to other lithium metal silicate compounds such as Li_2FeSiO_4 and Li_2MnSiO_4. However, it also illustrates the difficulty in achieving suitable electrochemical properties for this class of materials, even with mixing of conductive carbon at the nanoscale.[22]

Chapter 6

Investigation of Hydrogen Storage in Lithium Transition Metal Nitride Li-M-N (M = V and Mn) Systems

6.1 Introduction

Li_3N is a well-known hydrogen storage compound which remarkably stores up to 11.4 wt% hydrogen according to the equation:[1] $Li_3N + 2\ H_2 \leftrightarrow Li_2NH + LiH + H_2 \leftrightarrow LiNH_2 + 2\ LiH$. One of the major limitations of this system is that the high storage capacity can only be achieved at a temperature of 400 ℃, however, the reaction temperature can be decreased by incorporating other light elements such as Mg, B, Al, and K into this system[2,3,4,5]. Recently, Langmi et al.[6] have reported a reversible hydrogen storage system based on a Li-Fe-N phase, revealing the possible potential of hydrogen storage by lithium transition metal nitrides. Such materials might be expected to function midway between intermetallic alloy systems and the complex hydrides. Interesting new lithium transition metal nitrides[7] have also been recently discovered that are considered as potential hydrogen storage materials. In this chapter, Li_7VN_4 and Li_7MnN_4 were synthesized by high-temperature solid state reactions, and the hydrogen storage properties are explored both by density functional theory (DFT) calculations and experiments. The results show that Li_7VN_4 did not absorb hydrogen under our experimental conditions, and Li_7MnN_4 was observed to absorb 7 hydrogen atoms through the formation of LiH, Mn_4N, and ammonia gas. While these results for Li_7VN_4 and Li_7MnN_4 differ in detail, they are in overall

qualitative agreement with our theoretical work, which strongly suggests that both compounds are unlikely to form quaternary hydrides.

6.2 Computational procedures

Total electronic energies were calculated with the Vienna ab initio Simulation Package (VASP), which implements density functional theory[8] with a plane wave basis set.[9 10] Potentials obtained via the projector-augmented wave approach[11 12] were employed for the elements in conjunction with the generalized gradient approximation of Perdew and Wang[13 14] for the exchange-correlation energy functional. The Li, V, Mn, N, and H potentials contained 3, 23, 25, 7, and 1 electrons and were constructed with augmentation wave energy cutoffs of 272 eV, 264 eV, 270 eV, 700 eV, and 700 eV, respectively. In all calculations, a plane wave cutoff energy of 900 eV was imposed, and the k-point spacings of the reciprocal space meshes were no larger than 0.1/Å. At least two full-cell optimizations of the lattice parameters and nuclear coordinates were performed for each material of interest; the total energies were converged to 10^{-6} eV/cell and the forces relaxed to 10^{-5} eV/Å. Calculations for the N_2 and H_2 molecules were done with the same potentials in boxes large enough to ensure isolation.

6.3 Experimental

6.3.1 Design of reaction container and XRD holder

Since both the precursors (Li_3N and transition metals) and the products (Li_7VN_4 and Li_7MnN_4) are very sensitive to oxygen and moisture, all the operations including the loading of precursors and unloading of the final products, should be performed in inert conditions. In this case, a reaction container with special design is necessary to synthesize pure lithium metal

nitride compounds. The whole reaction container is comprised of 4 parts: the stainless steel body tube, a pair of O-ring adapters, a pair of Swagelok quick-connectors and a pair of clams, as shown in Figure 6.1a. Compared with quartz tubes, there are a couple of merits of this special container:

1) It allows to load and unload samples in the glove box;

2) The quick-connectors seal both ends of the container automatically as long as the male parts are pulled out.

The contamination from air was completely eliminated by using this kind of reaction container and pure target materials were obtained. The XRD holder is also specially made with Capton[@] film as a roof to protect samples from air during measurements (Figure 6.1).

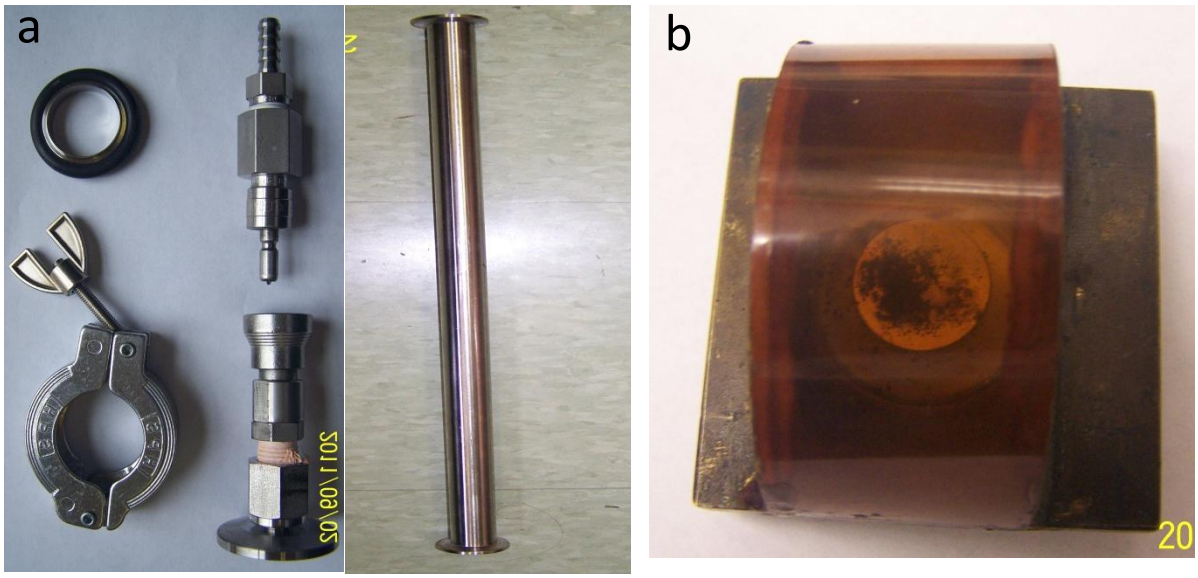

Figure 6.1 a) Reaction tube and Swagelok accessories and b) air-tight XRD holder.

6.3.2 Synthesis of Li_7VN_4 and Li_7MnN_4

Li_7VN_4 and Li_7MnN_4 were synthesized by a high temperature solid-state reaction of Li_3N and V/Mn metal. Typically, Li_3N (0.600 g; 10% molar excess) and V powder (325 mesh, 99.5%) (0.338 g) were hand-milled for 15 min and pressed into a pellet at 3 MP pressure under an inert Ar atmosphere. This pellet was heated under high-purity N_2 at 700 ℃ for 24 h. A similar process was applied to synthesize Li_7MnN_4, replacing V powder with Mn (325 mesh, 99+ %).

Hydrogenation experiments were conducted in a Cahn2151 high pressure thermal gravimetric analyzer (TGA). Approximately, 200 mg of powdered sample was loaded into an open stainless steel sample bucket in the Ar glove box and protected during transfer to the TGA by covering the sample with anhydrous pentane. The TGA was purged with He gas while the pentane evaporated. After pressurizing to 8.3 MPa of H_2 gas, Li_7VN_4 was heated to 600 ℃ at 5 ℃/min in flowing H_2 gas. Li_7MnN_4 was heated to 600 ℃ in 50 ℃ steps, with a 45 min soak at each temperature. The TGA exhaust gas was sampled using an SRS model CIS-100 mass spectrometer operated in residual gas analysis (RGA) mode to identify the constituents in the evolved gas. The RGA monitored mass channels at 2 amu (H_2), 4amu (He), 16amu (CH_4, NH_2 crack of ammonia), 17 amu (NH_3, OH crack of water), 18 amu (H_2O), 28 amu (N_2), 32 amu (O_2), and 44 amu (CO_2). Mixed gas experiments were conducted in a Hiden Model IGA-3 thermogravimetric analyzer (IGA). Approximately, 80 mg of powdered sample was placed into an open stainless steel bucket, sealed into a transfer container, and transferred into the IGA instrument without air exposure using a removable interlock chamber. Sample densities were obtained from weight changes due to buoyancy during pressurization to 20 bar. Li_7VN_4

was heated in 50 ℃ steps with variable soak times up to 425 ℃ in flowing pure H_2 gas at 20 bar. Li_7MnN_4 was similarly heated to 400 ℃ in 50 ℃ steps in a mixture of 50% H_2/50% N_2 at 20 bar, mixed 50% H_2/50% Ar at 20 bar, or pure H_2 at 10 bar.

Post-heat treatment XRD measurements were performed with a Siemens D5000 diffractometer (CuKα radiation, λ=1.5418A). Sample powders were compacted onto XRD slides and then sealed under a Kapton film to help protect the sample from atmospheric exposure during the XRD measurement.

6.4 Results and discussions

6.4.1 Theoretical investigations

Enthalpies of formation ΔH for the Li_7VN_4 and Li_7MnN_4 compounds as well as enthalpies of hydride formation ΔH* for model hydrides of them were calculated. Using Li_7VN_4 as a specific example, we express ΔH as:

$$\Delta H(Li_7VN_4) = E(Li_7VN_4) - 7\,E(Li) - E(V) - 2\,E(N_2), \qquad (6.1)$$

where E denotes the electronic total energy emerging from the VASP computations for the relevant materials (Li_7VN_4, Li and V metals, and the N_2 molecule). Defined this way, ΔH is the calculated standard enthalpy of formation at zero temperature in the absence of zero point energy contributions - which are small on the scale of the electronic terms - making Eq. (1) a good approximation.[15]

For the low temperature γ-phase of Li_7VN_4 having the cubic *P*-43*n* (space group No. 218) structure[16 17] whose synthesis is described below we find

$$\Delta H(\gamma\text{-}Li_7VN_4) = -928 \text{ kJ/mole f. u.}$$

(f. u. ≡ formula unit). Calculations for the tetragonal $P4_2/nmc$ (No. 137) α-phase[16] yield

$$\Delta H(\alpha\text{-}Li_7VN_4) = -923 \text{ kJ/mole f. u.} \quad ;$$

the higher value is consistent with the fact that the α-phase is a high temperature modification. Both materials are semiconductors with calculated bands gaps of 2.8 eV (γ-Li_7VN_4) and 2.2 eV (α-Li_7VN_4).

In the case of Li_7MnN_4, only known to form in the cubic *P*-43*n* structure,[18] non-magnetic as well as magnetic calculations were performed since susceptibility measurements indicate weak ferromagnetism below about 8K.[19] In the ferromagnetic state we obtain

$$\Delta H(Li_7MnN_4) = -661 \text{ kJ/mole f. u.} \quad ,$$

which is 49 kJ/mole f. u. lower than for the non-magnetic configuration and thus consistent with experiment. The spin-only calculated moment is 2.0 μ_B/Mn, identical to the value inferred from the measured susceptibility.[19]

These findings make it clear that both compounds are quite stable thermodynamically and suggest that Li_7VN_4, with a significantly more negative formation enthalpy, is less likely to sorb hydrogen. To assess hydride formation more specifically, calculations were performed for five hypothetical quaternary hydrides whose crystal structures were constructed by placing hydrogen into the largest holes in the parent compound: (i) 8e and 24i vacancy sites in cubic Li_7MnN_4 and (ii) 8g and two distinct 16h sites in tetragonal α-Li_7VN_4. Each structure was fully optimized with VASP and the enthalpy ΔH* of hydride formation computed, e. g.:

$$\Delta H^*[Li_7MnN_4H(8e)] \equiv E[Li_7MnN_4H(8e)] - E(Li_7MnN_4) \qquad (6.2)$$

As Table 6.1 shows, we obtain large and positive values of ΔH* for all five models, strongly suggesting that neither Li_7MnN_4 nor Li_7VN_4 is likely to form a quaternary hydride. The entries for $Li_7MnN_4H_n$ are undoubtedly also reflective of γ-$Li_7VN_4H_n$ having the same cubic structure, and the ΔH* values for α-Li_7VN_4 illustrate that not even the lower tetragonal symmetry offers any prospect for changing the sign of ΔH*. As described below, our experimental results confirm the inferences from our theoretical modeling work.

Table 6.1. Enthalpies of hydride formation ΔH* calculated for quaternary hydrides modeled by inserting H atoms into the indicated vacancy sites in cubic Li_7MnN_4 (8 f. u. per unit cell) and tetragonal α-Li_7VN_4 (2 f. u. per primitive cell).

Model hydride	H site	ΔH* (kJ/mole H_2)
Li_7MnN_4H	8e	+33
$Li_7MnN_4H_3$	24i	+91
$Li_7VN_4H_4$	8g	+170
$Li_7VN_4H_8$	$16h_1$	+118
$Li_7VN_4H_8$	$16h_2$	+202

6.4.2 Experimental investigations

The X-ray powder diffraction patterns of the prepared Li_7VN_4 and Li_7MnN_4 are shown in Figure 6.2. Previous studies[20,21] have classified the crystal structures of lithiated transition metal nitrides of the first row into two groups: the ionic anti-fluorite structure for elements in the early series where the metal is present in its group oxidation state,[16,19,22,23] and a layered

structure based on α-Li_3N for elements in the late series that exist in the univalent state.[24,25,26] In this paper, the studied elements vanadium and manganese are within the range of the early series, therefore they both form an anti-fluorite structure. For the Li_3N/V system, Li_7VN_4 (P-43n) was obtained as a major phase with trace quantities of VN and Li_7VN_4 (Pa3-). In the case of Li_3N/Mn a similar XRD pattern is observed, which can be assigned to Li_7MnN_4, an isostructure of Li_7VN_4. It is notable that as manganese is in the middle of the first row transition metals, its lithiated nitrides can adopt anti-fluorite or layered structures. Moreover, a new composition $Li_xMn_{2-x}N$ with an anti-rutile structure was also prepared by Niewa's group.[27] The various possible structures of the Li-Mn-N system can complicate the preparation of a single Li_7MnN_4 phase, however no layered $Li_2[(Li_{1-x}M_x)N]$ or anti-rutile $Li_xMn_{2-x}N$

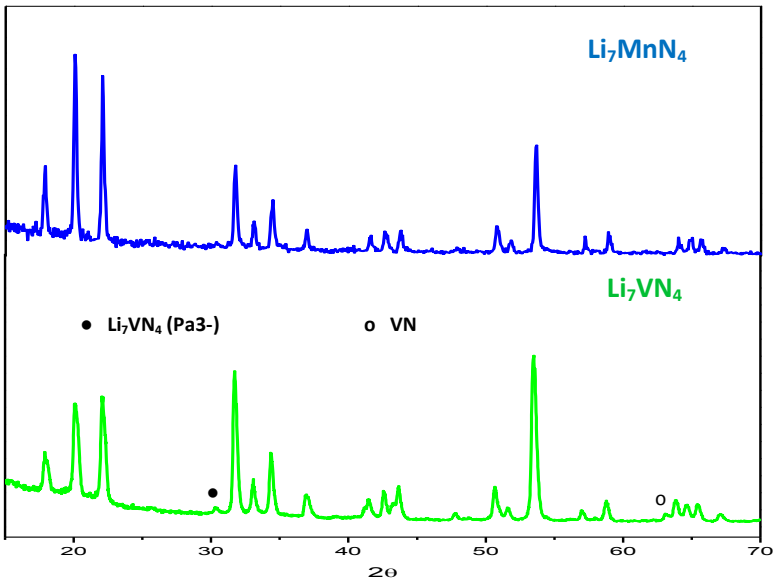

Figure 6.2 XRD patterns of as-synthesized Li_7VN_4 and Li_7MnN_4 samples showing the (almost) pure single phase nature of the product.

structures are observed in the XRD pattern. Therefore, a pure phase of Li_7MnN_4 was obtained by a simple high temperature solid-state process.

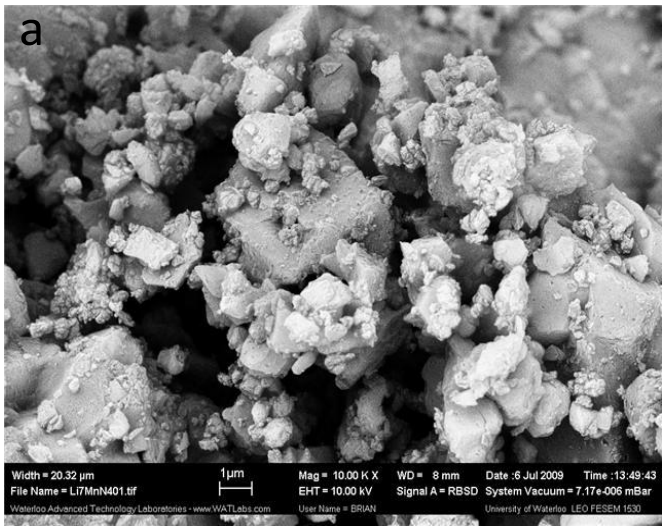

element	Wt %	At %
N	26.55	46.70
O	22.45	34.57
Au	12.84	1.61
Mn	38.17	17.12

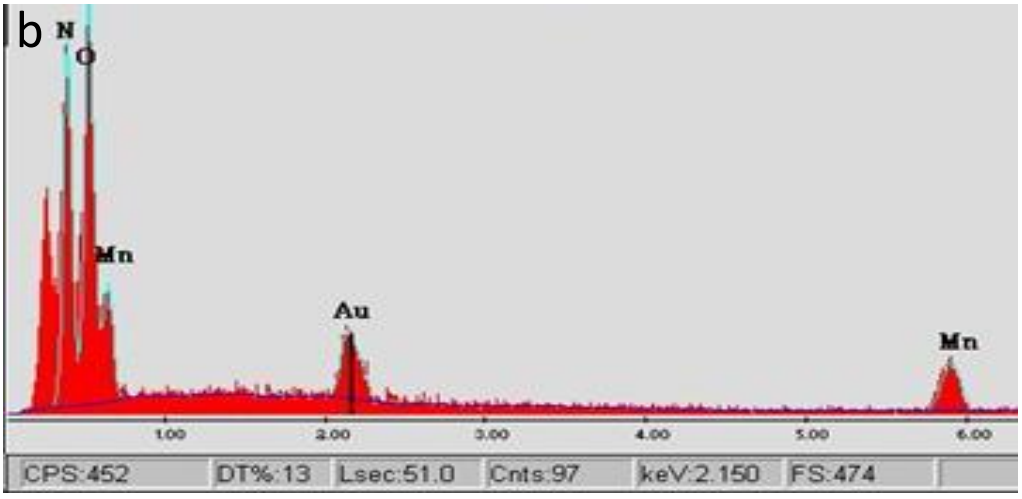

Figure 6.3 a) SEM image and b) EDAX of the as-synthesized Li_7MnN_4. Detailed EDAX results are shown in the table.

The SEM image of Li_7MnN_4 Figure 6.3a shows the particle size is in microns, a regular dimension for products prepared by solid state reactions. Surprisingly, a huge amount of oxygen - much higher content than nitrogen - is observed by the corresponding EDAX

measurement (Figure 6.3b), which is contradicted with the XRD result. This is probably due to the extremely high sensitivity of the nitrides to air. Since samples with poor electronic conductivity, like nitrides, usually tend to charge when scanned by the electron beam in a secondary electron imaging mode, a thin layer of gold was deposited on Li_7MnN_4 by a sputter coating process for a couple of minutes before SEM operations. Despite a short period, this procedure, as well as the following loading sample on the SEM station, caused oxidation of the sample on the surface which seems to accounts for the 34.57 at% oxygen in the sample from EDAX.

Attempts were made to induce H_2 absorption in both samples. Figure 6.4 shows the thermogravimetric profile of Li_7VN_4. The slight increase in weight at the beginning of the temperature ramp is a convection cell artifact of the high pressure TGA. The change in weight during depressurization suggests that the sample became less dense during the temperature profile. Excluding these weight changes, only 1 wt % loss is observed after 7 h, even with high temperature and pressure conditions (600 ℃ and 83 bar). IGA measurement similarly observed a weight loss of about 0.35 wt% even after 47 hrs at 425 ℃ in 20 bar H_2. These results confirm that Li_7VN_4 is very stable and hydrogen cannot be easily absorbed. A concurrent mass spectrographic measurement shows the small weight change might be due to the production of N_2.

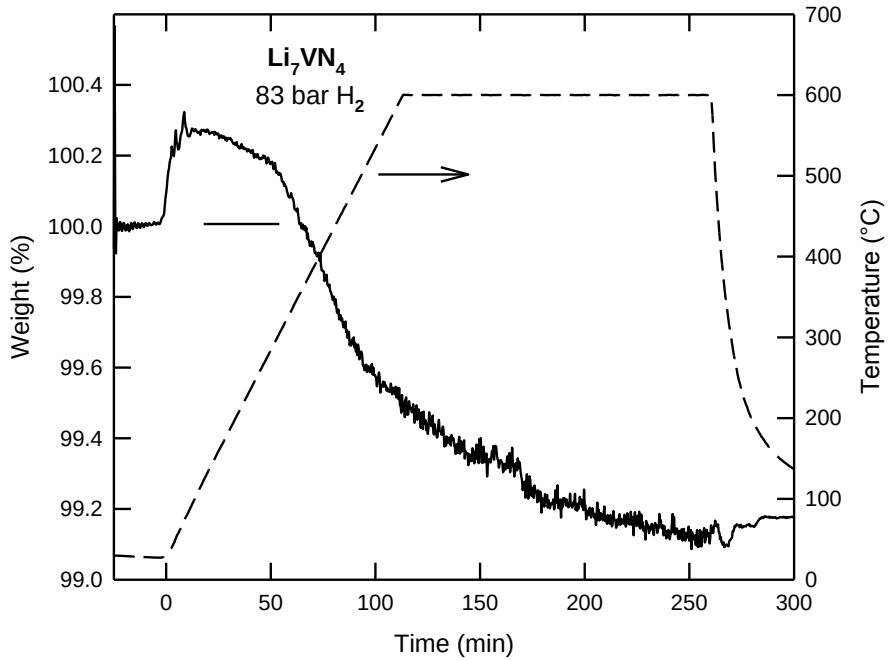

Figure 6.4 TGA profile of Li_7VN_4 in 83 bar of hydrogen (conducted by GM).

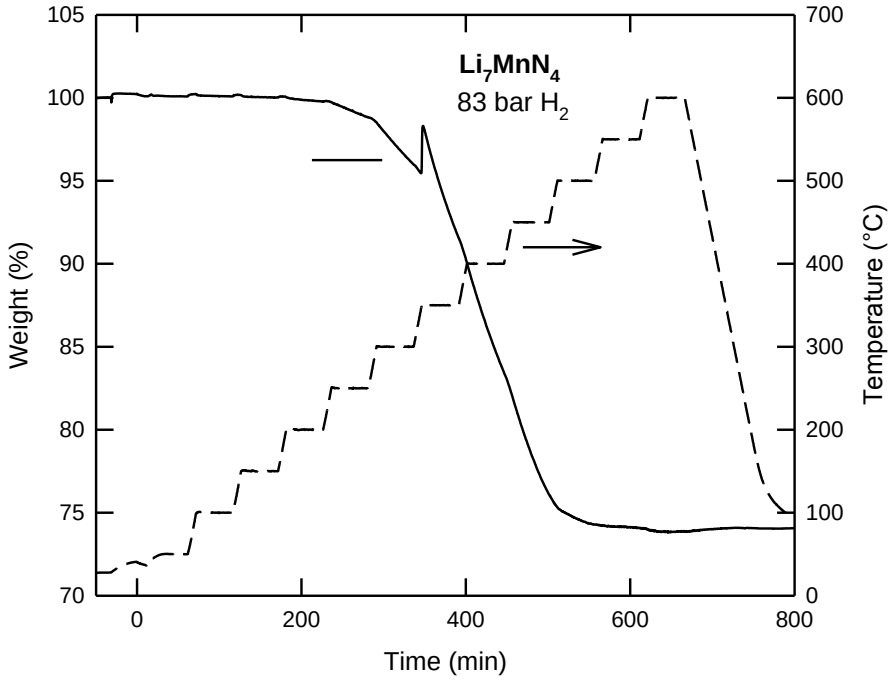

Figure 6.5 TGA profile of Li_7MnN_4 in 83 bar of hydrogen (conducted by GM).

The thermogravimetric profile of Li_7MnN_4 is given in Figure 6.5 Instead of H_2 adsorption, there is a weight loss of roughly 26 wt% under 83 bar of H_2. A slight weight gain of 2.6% occurred near 350 ℃, corresponding to an uptake of approximately 4 H atoms per formula unit associated with the formation of LiH. Niewa et al.[19] found that the reduction, or decomposition reaction of Li_7MnN_4, took place in the presence of Li above 250 ℃, to produce a series of Li-Mn-N compounds such as $Li_5[(Li_{1-x}Mn_x)]_3$ and $Li_2[(Li_{1-x}M_x)N]$. In our case, H_2 gas played a similar role as Li by reducing Mn (V) in Li_7MnN_4 to a lower oxidation state. A quantity of LiH was probably formed during this process, as some Li atoms were released from Li_7MnN_4 with the reduction of Mn (V). The large weight loss above 350 ℃ should be attributed to the complete decomposition of the Li-Mn-N system to form binary Mn_xN and LiH.

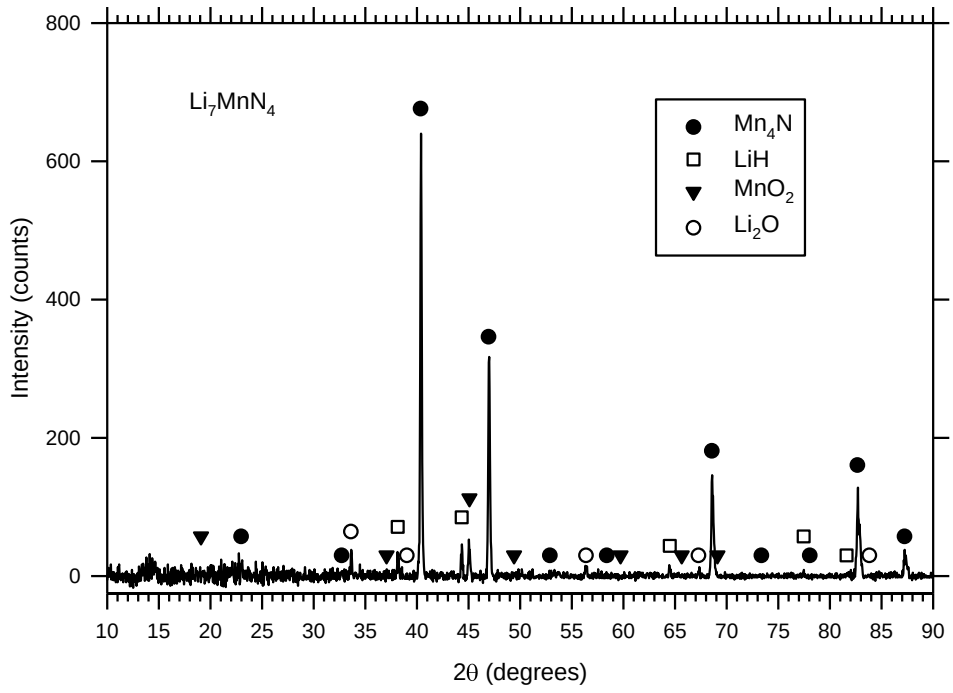

Figure 6.6 XRD pattern of Li_7MnN_4 after attempted hydrogenation (conducted by GM).

This assumption is confirmed by an XRD pattern of the final material after attempted hydrogenation (Figure 6.6), that shows the presence of Mn_4N, LiH and some Li_2O and MnO_2. The overall sample density of the decomposed sample is 1.43 g/cm^3, determined by pressure buoyancy, which is in excellent agreement with the expected value of 1.43 g/cm^3 for mixed LiH and Mn_4N. As mass spectrometer measurements obtained during the observed weight losses show the evolved gas to be NH_3, the overall reaction of the process should be:

$$Li_7MnN_4 + 73/8\ H_2 \rightarrow 7\ LiH + 1/4\ Mn_4N + 15/4\ NH_3 \qquad (6.3)$$

According to this reaction, the predicted weight loss is 28 wt%, which is consistent with the measured weight loss (26 wt %). It should be noted that LiH reacts with NH_3 very fast at elevated temperature to give rise to Li_2NH and $LiNH_2$, which probably explains the weight increase at ~350 ℃ in Figure 6.5. However, both of these two intermediate products decompose at the subsequent higher temperatures above 500 ℃, so they are not detected by XRD. The presence of Li_2O and MnO_2 in the product is unusual. The experimental section has specified that the samples were loaded to the TGA under inert gas protection, so it is most likely that the products were partly oxidized during the improper XRD operations, because no any oxides are observed in Figure 6.8 which is the XRD of the hydrogenation products treated in NH_3 atmosphere.

The experimental results are in accord with our calculations insofar as Li_7MnN_4 is much less stable than Li_7VN_4 and can be hydrogenated at elevated temperatures. Moreover, conducting VASP computations for Mn_4N and the NH_3 molecule, we find that the left side of reaction 6.3 is thermodynamically unstable with respect to the right side (by 104 kJ/mole Li_7MnN_4), consistent with the inference of reaction 6.3 from our measurements. It is noted that

different Li-M-N systems have different hydrogen absorptions and final products. For example, Li_3FeN_2 absorbed H_2 at a relatively low temperature and produced $Fe+LiNH_2+LiH$ in the products in Ref. 6. For Li_7VN_4 and Li_7MnN_4, despite isostructure of the two compounds, they show different performance of hydrogen absorption. However, all the three compounds are unlikely to be used in FCV for hydrogen storage since these transition metal doped nitrides are much more stable with hydrogen gas than pure Li_3N.

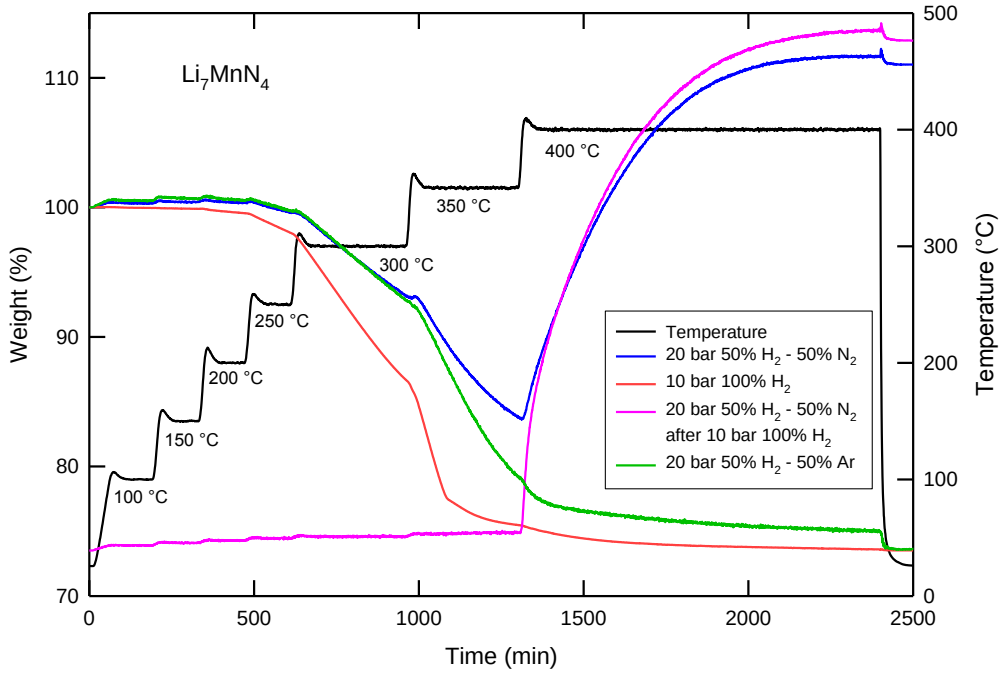

Figure 6.7 IGA results of the attempts to suppress NH_3 formation using N_2 or Ar gas, and subsequent nitriding above 350 ℃ when N_2 gas is present (conducted by GM).

As we have had previous success in suppressing NH_3 formation with a partial pressure of N_2 mixed with the H_2, this was attempted with the TGA, which can supply multiple gases simultaneously. Figure 6.7 shows the weight change in 10 bar of pure H_2 (red curve), 20 bar 50% H_2/50% N_2 (blue curve), and 20 bar 50% H_2/50% Ar (green curve). A second gas mixed with

H_2, whether N_2 or Ar, does appear to suppress the NH_3 production by moving the reaction to a higher temperature. All samples still lost weight due to nitrogen release in the form of NH_3. However, when N_2 gas is present the sample gains weight due to re-nitriding of the materials above 350 ℃, as shown in the blue curve of Figure 6.7. A similar result can be obtained by treating a fully desorbed sample (red curve) with a gas mixture containing N_2 (magenta curve), which exhibits similar absorption temperature and gaining weight.

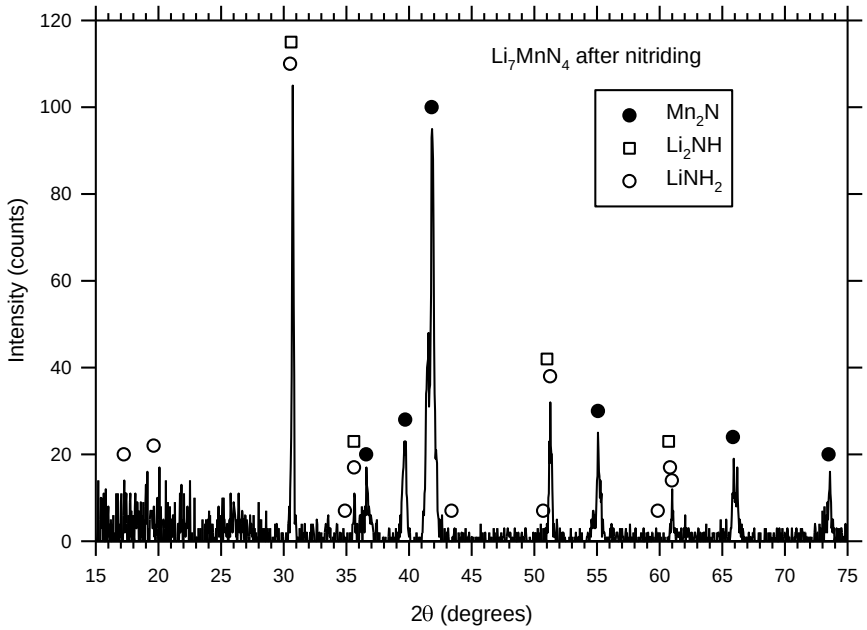

Figure 6.8 XRD pattern of Li_7MnN_4 produced by decomposition in H_2 followed by a subsequent nitriding (conducted by GM).

The XRD pattern of the final product produced by desorption in H_2 followed by a subsequent nitriding (Figure 6.8) shows the presence of Mn_2N plus Li_2NH and $LiNH_2$, which further corroborates the re-nitriding assumption.

6.5 Conclusions

Lithium transition metal nitrides Li_7VN_4 and Li_7MnN_4 were successfully prepared by a high temperature solid-state synthesis. No hydrogen absorption is observed for Li_7VN_4 at high temperature and pressure conditions, while Li_7MnN_4 can react with H_2 and produce LiH, Mn_4N, and NH_3. Although as many as 7 H atoms can be absorbed per unit of Li_7MnN_4, the release of NH_3 and the relatively high absorption temperature prevent its application in FCVs. A mixture of H_2/N_2, or H_2/Ar was found to be helpful for suppressing the release of NH_3 by shifting the reaction to a higher temperature. In addition, a weight gain is observed above 350 ℃ in the presence of N_2 gas due to the re-nitriding of the desorbed products. Computational modeling work indicates that Li_7VN_4 and Li_7MnN_4 are unlikely to form quaternary hydrides, in qualitative agreement with the experimental results.[28]

References

Chapter 1

1 M. S. Dresselhaus and I. L. Thomas, *Nature*, **414**, 332, (2001).

2 M. S. Whittingham, *Science*, **192**, 1126, (1976).

3 K. Mitzushima, P. C. Jones, P. J. Wiseman and J. B. Goodenough, *Mater. Res. Bull.*, **15**, 783, (1980).

4 K. Xu, *Chem. Rev.*, **104**, 4303, (2004).

5 R. Fong, U. von Sacken and J. R. Dahn, *J. Electrochem. Soc.*, **137**, 2009, (1990).

6 J.-M. Tarascon and M. Armand, *Nature*, **414**, 359, (2001).

7 M. Winter, J. O. Besenhard, M. E. Spahr and P. Novák, *Adv. Mater.*, **10**, 725, (1998).

8 M. S. Whittingham, *Chem. Rev.*, **104**, 4271, (2004).

9 G. G. Amatucci, J. M. Tarascon, L. C. Klein, *J. Electrochem. Soc.*, **143**, 1114, (1996).

10 J. Cho, Y. J. Kim, J. T. Kim and B. Park, *Angew. Chem. Int. Ed.*, **40**, 3367, (2001).

11 Z. Wang, C. Wu, L. Liu, L. Chen and X. Huang, *J. Electrochem. Soc.*, **149**, A466, (2002).

12 Z. Chen and J. R. Dahn, *Electrochim. Acta*, **49**, 1079, (2004).

13 A. Rougier, P. Gravereau and C. Delmas, *J. Electrochem. Soc.*, **143**, 1168, (1996).

14 P. G. Bruce, A. R. Armstrong and R. L. Gitzendanner, *J. Mater. Chem.*, **9**, 193, (1999).

15 G. Prado, A. Rougier, L. Fournes and C. Dlmas, *J. Electrochem. Soc.*, **147**, 2880, (2000).

16 G. Prado, A. Rougier, L. Fournes and C. Delmas, *J. Solid State Chem.*, **159**, 103, (2001).

17 A. R. Armstrong, R. Gitzendanner, A. D. Robertson and P. G. Bruce, *Chem. Commun.*, 1833, (1998).

18 A. R. Armstrong, A. D. Robertson and P. G. Bruce, *Electrochim. Acta*, **45**, 285, (1999).

29 A. R. Armstrong, A. J. Paterson, A. D. Robertson and P G. Bruce, *Chem. Mater.*, **14**, 710, (2002).

20 Z. Liu, A. Yu and J. Y. Lee, *J. Power Sources*, **81-82**, 416, (1999).

21 M. Yoshio, H. Noguchi, J. Itoh, M. Okada and T. Mouri, *J. Power Sources*, **90**, 176, (2000).

22 T. Ohzuku and Y. Makimura, *Chem. Lett.*, 642, (2001).

23 B. L. Ellis, K. T. Lee and L. F. Nazar, *Chem. Mater.*, **22**, 691, (2010).

24 Z. H. Chen and J. R. Dahn, *Electrochem. Solid-State Lett.*, **7**, A11, (2004).

25 http://pubs.acs.org/cen/science/85/8551sci1.html

26 M. M. Thackeray, S.-H. Yang, A. J. Kahaian, K. D. Kepler, J. T. Vaugher and S. A. Hackney, *Electrochem. Solid-State Lett.*, **1**, 7, (1998).

27 A. K. Padhi, K. S. Nanjundaswamy and J. B. Goodenough, *J. Electrochem. Soc.*, **144**, 1188, (1997).

28 J. B. Goodenough and Y. Kim, *Chem. Mater.*, **22**, 587, (2010).

29 J.-M. Tarascon and M. Armand, *Nature*, **414**, 359, (2001).

30 H. Huang, S.-C. Yin and L. F. Nazar, *Electrochem. Solid-State Lett.*, **4**, A170, (2001).

31 D. Lepage, C. Michot, G. Liang, M. Gauthier and S. B. Schougaard, *Angew. Chem. Int. Ed.*, **50**, 1, (2011).

32 P. S. Herle, B. L. Ellis, N. Coombs and L. F. Nazar, *Nat. Mater.*, **3**, 147, (2004).

33 C. Delacourt, P. Poizot, M. Morcrette, J. M. Tarascon and C. Masquelier, *Chem. Mater.*, **16**, 93, (2004).

34 J. Liu, T. E. Conry, X. Song, L. Yang, M. M. Doeff and T. J. Richardson, *J. Mater. Chem.*, **21**, 9984, (2011).

35 A. Nytén, A. Abouimrane, M. Armand, T. Gustafsson and J. O. Thomas, *Electrochem. Commun.*, **7**, 156, (2005).

36 M. S. Islam, R. Dominko, C. Masquelier, C. Sirisopanaporn, A. R. Armstrong and P. G. Bruce, *J. Mater. Chem*., **21**, 9811, (2011).

37 R. Dominko, *J. Power Sources*, **184**, 4621, (2008).

38 A. Kokalj, R. Dominko, G. Mali, A. Meden, M. Gaberscek and J. Jamnik, *Chem. Mater.*, **19**, 3633, (2007).

39 R. Dominko, M. Bele, M. Gaberscek, A. Meden, M. Remskar and J. Jamnik, *Electrochem.Commun.*, **8**, 217, (2006).

40 C. Lyness, B. Delobel, A. R. Armstrong and P. G. Bruce, *Chem. Commun.*, 4890, (2007).

41 T. Muraliganth, K. R. Stroukoff and A. Manthiram, *Chem. Mater.*, **22**, 5754, (2010).

42 T. Ohzuku, M. Kitagawa and T. Hirai, *J. Electrochem. Soc.*, 1990, **137**, 769.

43 D. Lv, W. Wen, X. Huang, J. Bai, J. Mi, S. Wu and Y. Yang, *J. Mater. Chem.*, **21**, 9506, (2011).

44 D. Rangappa, K. D. Murukanahally, T. Tomai, A. Unemoto and I. Honma, *Nano Lett*., **12**, 1146, (2012).

45 D. M. Kempaiah, D. Rangappa and I. Honma, *Chem. Commun.*, **48**, 2698, (2012).

46 N. Recham, J-N. Chotard, L. Dupont, C. Delacourt, W. Walker, M. Armand and J-M. Tarascon, *Nat. Mater.*, **9**, 68, (2010).

47 P. Barpanda, M. Ati, B. C. Melot, G. Rousse, J.-N. Chotard, M.-L. Doublet, M. T. Sougrati, S. A. Corr, J.-C. Jumas and J.-M. Tarascon, *Nat. Mater.*, **10**, 772, (2011).

48 J. Cabana, L. Monconduit, D. Larcher and M. R. Palac ń, *Adv. Mater.*, **22**, E170, (2010).

49 J. R. Dahn, T. Zheng, Y. Liu and J. S. Xue, *Science*, 270, 590, (1995).

50 E. Peled, *J. Electrochem. Soc.*, **126**, 2047, (1979).

51 P. W. Stephens, L. Mihaly, P. L. Lee, R. L. Whetten, S.-M. Huang, R. Kaner, F. Diederich and K. Holczer, *Nature*, **351**, 632, (1991).

52 G. Che, B. B. Lakshmi, E. R. Fischer and C. M. Martin, *Nature*, **393**, 346, (1998).

53 H. Zhou, S. Zhu, M. Hibino, I. Honma and M. Ichihara, *Adv., Mater.*, **15**, 2107, (2003).

54 E.-J. Yoo, J. Kim, E. Hosono, H. Zhou, T. Kudo and I. Honma, *Nano Lett.*, **8**, 2277, (2008).

55 P. Poizot, S. Laruelle, S. Grugeon, L. Dupont and J.-M. Tarascon, *Nature*, **407**, 496, (2000).

56 F. Cheng, J. Liang, Z, Tao and J. Chen, *Adv. Mater.*, **23**, 1695, (2011).

57 A. S. Aric ò, P. Bruce, B. Scrosati, J.-M. Tarascon and W. V. Schalkwijk, *Nat. Mater.*, **4**, 366, (2005).

58 Z.-W. Fu, Y. Wang, X.-L. Yue, S.-L. Zhao and Q.-Z. Qin, *J. Phys. Chem. B*, **108**, 2236, (2004).

59 Q. Sun and Z. W. Fu, *Electrochem. Solid-State Lett.*, **11**, A233, (2008).

60 D. C. S. Souza, V. Pralong, A. J. Jacobson and L. F. Nazar, *Science*, **296**, 2012, (2002).

61 V. Pralong, D. C. S. Souza, K. T. Leung and L. F. Nazar, *Electrochem. Commun.*, **4**, 516, (2002).

62 M. Winter and J. O. Besenhard, *Electrochim. Acta*, **45**, 31, (1999).

63 Y. Yu, L. Gu, C. Wang, A. Dhanabalan, P. A. van Aken and J. Maier, *Angew. Chem. Int. Ed.*, **48**, 6485, (2009).

64 H. X. Zhang, C. Feng, Y. C. Zhai, K. L. Jiang, Q. Q. Li and S. S. Fan, *Adv. Mater.*, **21**, 2299, (2009).

65 M. G. Kim and J. Cho, *Adv. Funct. Mater.*, **19**, 1497, (2009).

66 J. Cho, *J. Mater. Chem.*, **20**, 4009, (2010).

67 Y.-M. Kang, S.-M. Lee, S.-J. Kim, G.-J. Jeong, M.-S. Sung, W.-U. Choi and S.-S. Kim, *Electochem. Commun.*, **9**, 959, (2007).

68 J. R. Szczech and S. Jin, *Energy Environ. Sci.*, **4**, 56, (2011).

69 H. Kim, M. Seo, M.-H. Park and J. Cho, *Angew. Chem. Int. Ed.*, **49**, 2146, (2010).

70 H. Kim, B. Han, J. Choo and J. Cho, *Angew. Chem. Int. Ed.*, **47**, 10151, (2008).

71 L.-F. Cui, Y. Yang, C.-M. Hsu and Y. Cui, *Nano Lett.*, **9**, 3370, (2009).

72 C. K. Chan, R. N. Patel, M. J. O'Connell, B. A. Korgel and Y. Cui, *Acs Nano*, **4**, 1443, (2010).

73 Y. Yao, M. T. Mcdowell, I. Ryu, H. Wu, N. Liu, L. Hu, W. D. Nix and Y. Cui, *Nano Lett.*, **11**, 2949, (2011).

74 A. Magasinski, P. Dixon, B. Herzberg, A. Kvit, J. Ayala and G. Yushin, *Nat. Mater.*, **9**, 353, (2010).

75 I. Kovalenko, B. Zdyrko, A. Magasinski, B. Herzberg, Z. Milicev, R. Brutovyy, I. Luzinov and G. Yushin, *Science*, **334**, 75, (2011).

76 X. Ji and L. F. Nazar, *J. Mater. Chem.*, **20**, 9821, (2010).

77 T. Ogasawara, A. Debart, M. Holzapfel, P. Novak and P. G. Bruce, *J. Am. Chem. Soc.*, **128**, 1390, (2006).

78 J.-S. Lee, S. T. Kim, R. Cao, N.-S. Choi, M. Liu, K. T. Lee and J. Cho, *Adv. Energy Mater.*, **1**, 34, (2011).

79 B. H. Jeon, J. H. Yeon, K. M. Kim and I. J. Chung, *J. Power Sources*, **109**, 89, (2002).

80 H. Yamin, J. Penciner, A. Gorenshtain, M. Elam and E. Peled, *J. Power Sources*, **14**, 129, (1985).

81 N. Jayaprakash, J. Shen, S. S. Moganty, A. Corona and L. A. Archer, *Angew. Chem. Int. Ed.*, **50**, 5904, (2011)

82 D. Peramunage and S. Licht, *Science*, **261**, 1029, (1993).

83 S. Levasseur, M. Menetrier, E. Suard and C. Delmas, *Solid State Ionics*, **128**, 11, (2000).

84 J. A. Dean, *Handbook of Chemistry, 3rd ed.*; McGraw-Hill: New York, 1985.

85 J. Shim, K. A. Striebel, and E. J. Cairns, *J. Electrochem. Soc.*, 2002, **149**, A1321.

86 B. M. L. Rao, and J. A. Shrophire, *J. Electrochem. Soc.*, **128**, 942, (1981).

87 E. Peled, Y. Sternberg, A. Gorenshtein, and Y. Lavi, *J. Electrochem. Soc.*, **136**, 1621, (1989).

88 S. E. Cheon, K. S. Ko, J. H. Cho, S. W. Kim, E. Y. Chin, and H. T. Kim, *J. Electrochem. Soc.*, **150**, A796, (2003).

89 H. S. Ryu, H. J. Ahn, K. W. Kim, J. H. Ahn, J. Y. Lee, and E. J. Cairns, *J. Power Sources*, **140**, 365, (2005).

90 H. S. Ryu, H. J. Ahn, K. W. Kim, J. H. Ahn, K. K. Cho, and T. H. Nam, *Electrochim. Acta*, **52**, 1563, (2006).

91 Y. Mikhaylik and J. R. Akridge, *J. Electrochem. Soc.*, **151,** A1969. (2004).

92 K. Kumaresan, Y. Mikhaylik and R. E. White, *J. Electrochem. Soc.*, **155,** A576. (2008).

93 J. Wang, L. Liu, Z. Ling, J. Yang, C. Wan and C. Jiang, *Electrochim. Acta*, **48**, 1861, (2003).

94 S.-C. Han, M.-S. Song, H. Lee, H.-S. Kim, H.-J. Ahn, J.-Y. Lee, *J. Electrochem. Soc.* **150**, A889, (2003).

95 W. Zheng, Y. W. Liu, X. G. Hu, C. F. Zhang, *Electrochim. Acta*, **51**, 1330, (2006).

96 M. S. Song, S. C. Han, H. S. Kim, J. H. Kim, K. T. Kim, Y. M. Kang, H. J. Ahn, S. X. Dou and J. Y. Lee, *J. Electrochem. Soc.*, **151**, A791, (2004).

97 Y. J. Choi, B. S. Jung, D. J. Lee, J. J. Jeong, K. W. Kim, H. J. Ahn, K. K. Cho and H. B. Gu, *Phys. Scr.*, **T129**, 62, (2007).

98 D. Aurbach, E. Pollk, R. Elazari, G. Salitra, C. S. Kelley and J. Affinito, *J. Electrochem. Soc.* **156**, A694, (2009).

99 J. Wang, J. Yang, J. Xie and N. Xu, *Adv. Mater.*, **14**, 963, (2002).

100 J. Wang, J. Yang, C. Wan, K. Du, J. Xie and N. Xu, *Adv. Funct. Mater.*, **13**, 487, (2002).

101 X. Yu, J. Xie, Y. Li, H. Huang, C. Lai and K. Wang, *J. Power Sources*, **146**, 335, (2005).

102 X. Ji, K. T. Lee, and L. F. Nazar, *Nat. Mater.* **8**, 500, (2009).

103 X. Ji, S. Evers, R. Black and L. F. Nazar, *Nat. Commun.*, **2**. 325, (2011).

104 H. Wang, Y. Yang, Y. Liang, J. T. Robinson, Y. Li, A. Jackson, Y. Cui and H. Dai, *Nano Lett*., **11**, 2644, (2011).

105 G. Zheng, Y. Yang, J. J. Cha, S. S. Hong, Y. Cui, *Nano Lett*., **11**, 4462, (2011).

106 J. Guo, Y. Xu and C. Wang, *Nano Lett*., **11**, 4288, (2011).

107 N. Tachikawa, K. Yamauchi, E. Takashima, J.-W. Park, K. Dokko and M. Watanabe, *Chem. Commun.*, **47**, 8157, (2011).

108 R. Demir-Cakan, M. Morcrette, F. Nouar, C. Davoisne, T. Devic, D. Gonbeau, R. Dominko, C. Serre, G. Férey and J.-M. Tarascon, *J. Am. Chem. Soc.*, **133**, 16154, (2011).

109 X. Liang, Y. Liu, Z. Wen, L. Huang, X. Wang and H. Zhang, *J. Power Sources*, **196**, 6951, (2011).

110 F. Wu, J. Chen, R. Chen, S. Wu, L. Li, S. Chen and T. Zhao, *J. Phys. Chem. C*, **155**, 6057, (2011).

111 C. Lai. X. P. Gao, B. Zhang, T. Y. Yan and Z. Zhou, *J. Phys. Chem. C*, **113**, 4712, (2009).

112 B. Zhang, X. Qin, G. R. Li and X. P. Gao, *Energy Environ. Sci*., **3**, 1531, (2010).

113 X. Li, Y. Cao, W. Qi, L. V. Saraf, J. Xiao, Z. Xie, J. Mietek, J.-G. Zhang, B. Schwenzer and J. Liu, *J. Mater. Chem.*, **21**, 16603, (2011).

114 R. D. Rauh K. M. Abraham, G. F. Pearson, J. K. Supernant and S. B. Brummer, *J. Electrochem. Soc.*, **126,** 523, (1979).

115 C. D. Liang, N. J. Dudney, and J. Y. Howe, *Chem. Mater.*, **21**, 4724, (2009).

116 Y. Ren, A. R. Armstrong, F. Jiao, and P. G. Bruce, *J. Am. Chem. Soc*., **132,** 996, (2010).

117 N. Liu, L. Hu, M. T. McDowell, A. Jackson and Y. Cui, *ACS Nano*, **5**, 6487, (2011).

118 Y. Yang, M. T. McDowell, A. Jackson, J. J. Cha, S. S. Hong and Y. Cui, *Nano Lett.*, **10**, 1486, (2010).

119 M. N. Obrovac and J. R. Ahn, *Electrochem. Solid-State Lett*., **5**, A70, (2002).

120 A. Hayashi, R. Ohtsubo, T. Ohtomo, F. Mizuno and M. Tatsumisago, *J. Power Sources*, **183**, 422, (2008).

121 Y. Zhou, C. Wu, H. Zhang, X. Wu and Z. Fu, *Electrochim. Acta*, **52**, 3130, (2007).

122 Y. Mikhaylik, I. Kovalev, R. Schock, K. Kumaresan, J. Xu and J. Affinito, *ECS Transaction*s, **25**, 23, (2010).

123 W. Wang, Y. Wang, Y. Huang, C. Huang, Z. Yu, H. Zhang, A. Wang and K. Yuan, *J. Appl. Electrochem.*, **40**, 321, (2010).

124 L. X. Yuan, J. K. Feng, X. P. Ai, Y. L. Cao, S. L. Chen and H. X. Yang, *Electrochem. Commun*., **8**, 610, (2006).

125 J. Wang, S. Y. chew, Z. W. Zhao, S. Ashraf, D. Wexler, J. Chen, S. J. Ng, S. L. Chou and H. K. Liu, *Carbon*, **46**, 229, (2008).

126 J. Hassoun and B. Scrosati, *Adv. Mater.*, **22**, 5198, (2010).

127 J. Hassoun and B. Scrosati, *Angew. Chem. Int. Ed.*, **49**, 2371, (2010).

128 J. Hassoun, Y.-K. Sun and B. Scrosati, *J. Power Sources*, **196**, 343, (2011).

129 M. Nagao, A. Hayashi and M. Tatsumisago, *Electrochim. Acta*, **56** 6055, (2011).

130 K. Hong, *J. Power Sources*, **96**, 85, (2001).

131 Y. Liu, H. Pan, M. Gao and Q. Wang, *J. Mater. Chem*., **21**, 4743, (2011).

132 L. Schlapbach and A. Züttel, *Nature*, **414**, 353, (2001).

133 B. Bogdanovic and M. Schwickardi, *J. Alloys Compds*, **253**, 1, (1997).

134 B. Bogdanovic, R. A. Brand, A. Marjanovic, M. Schwickardi and J. Tölle, *J. Alloys Compds*, **302**, 36, (2000).

135 A. Züttel, P. Wenger, S. Rentsch and P. Sudan, *J. Power Sources*, **118**, 1, (2003).

136 H.-W. Li, Y. Yan, S.-I. Orimo, A. Züttel and C. M. Jensen, *Energies*, **4**, 185, (2011).

137 S. Orimo, Y. Nakamori, J. Eliseo, A. Züttel and C. M. Jensen, *Chem. Rev.*, **107**, 4111, (2007).

138 P. Chen, Z. T. Xiong, J. Z. Luo, J. Y. Lin and K. L. Tan, *Nature*, **420**, 302, (2002).

139 Z. T. Xiong, G. T. Wu, J. Q. Hu and P. Chen, *Adv. Mater.*, **16**, 1522, (2004).

140 F. E. Pinkerton, G. P. Meisner, M. S. Meyer, M. P. Balogh and M. D. Kundrat, *J. Phys. Chem. B*, **109**, 6, (2005).

141 Z. T. Xiong, G. T. Wu, J. Q. Hu and P. Chen, *J. Power Sources*, **159**, 167, (2006).

142 J. Wang, T. Liu, G. Wu, W. Li, Y. Liu, C. M. Araujo, R. H. Scheicher, A. Blomqvist, R. Ahuja, Z. Xiong, P. Yang, M. Gao, H. Pan and P. Chen, *Angew. Chem. Int. Ed.*, **48**, 5828, (2009).

143 T. Hügle, M. Hartl and D. Lentz, *Chem. Eur. J.*, **17**, 10184, (2011).

144 Z. Xiong, C. K. Yong, G. Wu, P. Chen, W. Shaw, A. Karkamkar, T. Autrey, M. O. Jones, S. R. Johnson, P. P. Edwards and W. I. F. David, *Nat. Mater.*, **7**, 138, (2007).

145 Z. Xiong, Y. S. Chua, G. Wu, W. Xu, P. Chen, W. Shaw, A. Karkamkar, J. Linehan, T. Smurthwaite and T. Autrey, *Chem. Commun.*, **43**, 5595, (2008).

146 K. J. Fijalkowski and W. Grochala, *J. Mater. Chem.*, **19**, 2043, (2009).

147 H. Wu, W. Zhou, T. Yildirim, *J. Am. Chem. Soc.*, **130**, 14834, (2008).

148 C. Wu, G. Wu, Z. Xiong, T. He and P. Chen, *Chem. Mater.*, **21**, 4899, (2009).

149 V. Bérube, G. Radtke, M. Dresselhaus and G. Chen, *Int. J. Energy Res*., **31**, 637, (2007).

150 T. K. Nielsen, F. Besenbacher and T. R. Jensen, *Nanoscale*, **3**, 2086, (2011).

151 L. Mosegaard, B. Møller, J. E. Jørgensen, Y. Filinchuk, Y. Cerenius, J. C. Hanson, E. Dimasi, F. Besenbacher and T. R. Jensen, *J. Phys. Chem. C*, **112**, 1299, (2008).

152 P. Ngene, P. Adelhel, A. M. Beale, K. P. de Jong and P. E. de Jongh, *J. Phys. Chem. C*, **114**, 6163, (2010).

153 C. P. Baldé, B. P. C. Hereijgers, J. H. Bitt and K. P. de Jong, *J. Am. Chem. Soc*., **130**, 6761, (2008).

154 A. Gutowska, L. Li, Y. Shin, C. M. Wang, X. S. Li, J. C.Linehan, R. S. Smith, B. D. Kay, B. Schmid, W. Shaw, M. Gutowski and T. Autrey, *Angew. Chem. Int. Ed*., **44**, 3578, (2005).

155 L. Li, X. Yao, C. Sun, A. Du, L. Cheng, Z. Zhu, C. Yu, J. Zou, S. C. Smith, P. Wang, H.-M. Cheng, R. L. Frost and G. Q. Lu, *Adv. Funct. Mater*., **19**, 265, (2009).

156 T. K. Nielsen, K. Manickam, M. Hirscher, F. Besenbacher and T. R. Jensen, *ACS Nano*, **3**, 3521, (2009).

157 K.-J. Jeon, H. R. Moon, A. M. Ruminski, B. Jiang, C. Kisielowski, R. Bardhan and J. J. Urban, *Nat. Mater*., **10**, 286, (2011).

158 C. T. Kresge, M. E. Leonowicz, W. J. Roth, J. C. Vartuli and J. S. Beck, *Nature*, **359**, 710, (1992).

159 J. S. Beck, J. C. Vartuli, W. J. Roth, M. E. Leonowicz, C. T. Kresge, K. D. Schmitt, C. T-W. Chu, D. H. Olson, E. W. Sheppard, S. B. McCullen, J. B. Higgins and J. L. Schlenker, *J. Am. Chem. Soc*., **114**, 10834, (1992).

160 Y. Wan and D. Zhao, *Chem. Rev*., **107**, 2821, (2007).

161 Q. Huo, R. Leon, P. M. Petroff and G. D. Stucky, *Science*, **268**, 1324, (1995).

162 S. A. Bagshaw, E. Prouzet and T. J. Pinnavaia, *Science*, **269**, 1242, (1995).

163 M. Kruk, M. Jaroniec, R. Ryoo and J. M. Kim, *Microporous Materials*, **12**, 93, (1997).

164 D. Zhao, J. Feng, Q. Huo, N. Melosh, G. H. Fredrickson, B. F. Chmelka and G. D. Stucky, *Science*, **279**, 548, (1998).

165 Y. Sakamoto, M. Kaneda, O. Terasaki, D. Zhao, J. M. Kim, G. D. Stucky, H. J. Shim and R. Ryoo, *Nature*, **408**, 449, (2000).

166 D. Zhao, Q. Huo, J. Feng, B. F. Chmelka and G. D. Stucky, *J. Am. Chem. Soc*., **120,** 6024, (1998).

167 P. Schmidt-Winkel, W. W. Lukens, D. Zhao, P. Yang, B. F. Chmelka and G. D. Stucky, *J. Am. Chem. Soc*., **121,** 254, (1999).

168 J. Fan, C. Yu, J. Lei, Q. Zhang, T. Li, B Tu, W. Zhou and D. Zhao, *J. Am. Chem. Soc*., **127,** 10794, (2005).

169 M. Templin, A. Franck, A. D. Chesne, H. Leist, Y. Zhang, R. Ulrich, V. Schädler and U. Wiesner, *Science*, **278**, 1795, (1997).

170 K. Schumacher, M. Grün and K. K. Unger, *Microporous Mesoporous Mater*., **27**, 201, (1999).

171 K. Yano and Y. Fukushima, *Bull. Chem. Soc. Jp*., **75**, 1977, (2003).

172 K. Yano and Y. Fukushima, *J. Mater. Chem*., **14**, 1579, (2004).

173 C. Yu, J. Fan, B. Tian and D. Zhao, *Chem. Mater*., **16**, 889, (2004).

174 X. Ji, K. T. Lee, M. Monjauze and L. F. Nazar, *Chem. Commun*., 4288, (2008).

175 S. Che, Z. Liu, T. Ohsuna, K. Sakamoto, Osamu and T. Tatsumi, *Nature*, **429**, 281, (2004).

176 X. Wu, H. Jin, Z. Liu, T. Ohsuna, O. Terasaki, K. Sakamoto and S. Che, *Chem. Mater*., **18**, 241, (2006).

177 S. Yang, L. Zhao, C. Yu, X. Zhou, J. Tang, P. Yuan, D. Chen and D. Zhao, *J. Am. Chem. Soc*., **128,** 10460, (2006).

178 Y. Snir and R. D. Kamien, *Science*, **307**, 1067, (2005).

179 Y. Han, L. Zhao and J. Y. Ying, *Adv. Mater*., **19**, 2454, (2007).

180 C. Liang, Z. Li and S Dai, *Angew. Chem. Int. Ed*., **47**, 3696, (2008).

181 J. H. Knox, B. Kaur and G. R. Millward, *J. Chromatogr*., **352**, 3, (1986).

182 C.-G. Wu and T. Bein, *Science*, **266**, 1013, (1994).

183 C. Yu, B. Tian and D. Zhao, *Curr. Opin. Solid St. M*., **7**, 191, (2003).

184 R. Ryoo, S. H. Joo and S. Jun, *J. Phys. Chem. B*, **103**, 7743, (1999).

185 M. Kaneda, T. Tsubakiyama, A. Carlsson, Y. Sakamoto, T. Ohsuma, O. Terasaki, S. H. Joo and R. Ryoo, *J. Phys. Chem. B*, **106**, 1256, (2002).

186 S. Jun, S. H. Joo, R. Ryoo, M. Kruk, M. Jaroniec, Z. Liu, T. Ohsuna and O. Terasaki, *J. Am. Chem. Soc*., **122,** 10712, (2000).

187 M. Impéror-Clerc, P. Davidson and P. Davidson, *J. Am. Chem. Soc*., **122,** 11925, (2000).

188 S. H. Joo, S. J. Choi, I. Oh, J. Kwak, Z. Liu, O. Terasaki and R. Ryoo, *Nature*, **412**, 169, (2001).

189 A. B. Fuertes and S. Alvarez, *Carbon*, **42**, 3049, (2004).

190 F. Kleitz, S. Choi and R. Ryoo, *Chem. Commun*., 2136, (2003).

191 J. E. Hampsey, Q. Y. Hu, L. Rice, J. B. Pang, Z. W. Wu and Y. F. Lu, *Chem. Commun*., 3606, (2005).

192 K. P. Gierszal and M. Jaroniec, *J. Am. Chem. Soc*., **128,** 10026, (2006).

193 J. Kim, J. Lee and T. Hyeon, *Carbon*, **42**, 2711, (2004).

194 P. Valle-Vigón, M. Sevilla and A. B. Fuertes, *Microporous Mesoporous Mater*., **134**, 165, (2010).

195 Y. Zhai, Y. Dou, D. Zhao, P. F. Fulvio, R. T. Mayes and S. Dai, *Adv. Mater*., **23**, 4828, (2011).

196 C. Liang, K. Hong, G. A. Guiochon, J. W. Mays and S. Dai, *Angew. Chem. Int. Ed*., **43**, 5785, (2004).

197 X. Wang, C. Liang and S. Dai, *Langmuir*, **24**, 7500, (2008).

198 C. Liang and S. Dai, *J. Am. Chem. Soc*., **128,** 5316, (2006).

199 Y. Wan, Y. Feng and D. Zhao, *Chem. Commun*., 897, (2007).

200 Z. Li, W. Yan and S. Dai, *Carbon*, **42**, 767, (2004).

201 I. Morguchi, A. Ozono, K. Mikuriya, Y. Teraoka, S. Kagawa and M. Kodama, *Chem. Lett*., 1171, (1999).

202 Y. Meng, D. Gu, F. Zhang, Y. Shi, H. yang, Z. Li, C. Yu, B. Tu and D. Zhao, *Angew. Chem. Int. Ed*., **44**, 7053, (2005).

203 Y. Lu, R. Ganuli, C. A. Drewien, M. T. Anderson, C. J. Brinker, W. Gong, Y. Guo, H. Soyez, B. Dunn, M. H. Huang and J. I. Zink, *Nature*, **389**, 364, (1997).

204 C. J. Brinker, Y. Lu, A. Sellinger and H. Fan, *Adv. Mater*., **11**, 579, (1999).

205 D. Grosso, F. Cagnol, G. Soler-Illoa, E. L. Crepaldi, H. Amenitsch, A. Brunet-Bruneau, A. Bourgeois and C. Sanchez, *Adv. Funct. Mater*., **14**, 309, (2004).

206 Y. Meng, D. Gu, F. Zhang, Y. Shi, L. Cheng, D. Feng, Z. Wu, Z. Chen, Y. Wan, A. Stein and D. Zhao, *Chem. Mater*., **18**, 4447, (2006).

207 R. T. Mayes, C. Tsouris, J. O. Kiggans, S. M. Mahurin, D. W. Depaoli and S. Dai, *J. Mater. Chem*., **20**, 8674, (2010).

208 Y. Wan, Y. Shi and D. Zhao, *Chem. Mater*., **20**, 932, (2008).

209 R. Liu, Y. Shi, Y. Wan, Y. Meng, F. Zhang, D. Gu, Z. Chen, B. Tu and D. Zhao, *J. Am. Chem. Soc*., **128,** 11652, (2006).

210 H. Wei, Y. Lv, L. Han, B. Tu and D. Zhao, *Chem. Mater*., **23**, 2353, (2011).

211 S. Tanaka, Y. Katayama, M. P. Tate, H. W. Hillhouse and Y. Miyake, *J. Mater. Chem*., **17**, 3639, (2007).

212 D. Feng, Y. Lv, Z. Wu, Y. Dou, L. Han, Z. Sun, Y. Xia, G. Zheng and D. Zhao, *J. Am. Chem. Soc*., **133,** 15148, (2011).

213 M. Zheng, J. Cao, X. Ke, G. Ji, Y. Chen, K. Shen and J. Tao, *Carbon*, **45**, 1105, (2007).

214 M. Steinhart, C. Liang, G. W. Lynn, U. Gösele and S. Dai, *Chem. Mater*., **19**, 2383, (2007).

215 A. T. Rodriguez, M. Chen, Z. Chen, C. J. Brinker and H. Fan, *J. Am. Chem. Soc*., **128,** 9276, (2006).

216 Y. Yan, F. Zhang, Y. Meng, B. Tu and D. Zhao, *Chem.Commun*., **2867**, (2007).

217 D. Long, F. Lu, R. Zhang, W. Qiao, L. Zhan, X. Liang and L. Ling, *Chem.Commun*., **2647**, (2008).

218 Y. Fang, D. Gu, Y. Zhou, Z. Wu, F. Li, R. Che, Y. Deng, B. Tu and D. Zhao, *Angew. Chem. Int. Ed*., **49**, 7987, (2010).

219 P. Yang, D. Zhao, D. I. Margolese, B. F. Chmelka and G. D. Stucky, *Nature*, **396**, 152, (1998)

220 P. Yang, D. Zhao, D. I. Margolese, B. F. Chmelka and G. D. Stucky, *Chem. Mater*., **11**, 2813, (1999).

221 B. Tian, X. Liu, b. Tu, C. Yu, J. Fan, L. Wang, S. Xie, G. D. Stucky and D. Yang, *Nat. Mater*., **2**, 159, (2003).

222 F. Jiao, K. M. Shaju and P. G. Bruce, *Angew. Chem. Int. Ed*., **44**, 6550, (2005).

223 F. Jiao, A. Harrison, J.-C. Jumas, A. V. Chadwick, W. Kockelmann and P. G. Bruce, *J. Am. Chem. Soc*., **128,** 5468, (2006).

224 F. Jiao, J. Bao, A. H. Hill and P. G. Bruce, *Angew. Chem. Int. Ed*., **47**, 9711, (2008).

225 Y. Ren, L. J. Harwick and P. G. Bruce, *Angew. Chem. Int. Ed*., **49**, 2570, (2010).

226 Y. Ren, Z. Ma, L. Qian, S. Dai, H. He and P. G. Bruce, *Catal. Lett*., **131**, 146, (2009).

227 J. Roggenbuck and M. Tiemann, *J. Am. Chem. Soc*., **127,** 1096, (2005).

228 J. Roggenbuck, G. Koch and M. Tiemann, *Chem. Mater*., **18,** 4151, (2006).

229 M. Groenewolt and M. Antonietti, *Adv. Mater*., **17**, 1789, (2005).

230 F. Goettmann, A. Fischer, M. Antonietti and A. Thomas, *Angew. Chem. Int. Ed*., **45**, 4467, (2006)

231 X. Chen, Y.-S. Jun, K. Takanabe, K. Maeda, K. Domen, X. Fu, M. Antonietti and X. Wang, *Chem. Mater*., **21**, 4093, (2009).

232 B. Jürgens, E. Irran, J. Senker, P. Kroll, H. Müller and W. Schnick, *J. Am. Chem. Soc*., **125,** 10288, (2003).

233 A. Fischer, M. Antonietti and A. Thomas, *Adv. Mater*., **19**, 264, (2007).

Chapter 2

1 A. R. West, *Solid State Chemistry and Its Applications*, John Willey&Sons Ltd., (1984).

2 G. Cao, *Nanostructures&Nanomaterials-Synthesis, Properties&Applications*, Imperial Colleage Press, (2004).

3 K. S. W. Sing, D. H. Everett, R. A. W. Haul, L. Moscou, R. A. Pierotti, J. Rouquerol and T. Siemieniewska, *Pure Appl. Chem*., **57**, 63, (1985).

4 *Operating Manual*, Quantachrome Instrument, (2006).

5 T. L. Hill, *J. Phys. Chem*., **519**, 1065, (1955).

6 http://saf.chem.ox.ac.uk/Instruments/BET/sorpoptprin.html.

7 S. Brunauer, P. Emmett and E. Teller, *J. Am. Chem. Soc*., **60**, 309, (1938).

8 B. C. Lippens and J. H. de Boer, *J. Catal*., **4**, 319, (1965).

9 A. W. Marczewski, *A Partical Guide to Isotherms of Adsorption on Hterogeneous Surfaces*, http://awm.sorption.org.

10 E. P. Barrett, B. L. Joyner, and P. P. Halenda, *J. Am. Chem. Soc.*, **73**, 373, (1951).

Chapter 3

1 D. Peramunage and S. Licht, *Science*, **261**, 1029, (1993).

2 J. Wang, S. Y. Chew, Z. W. Zhao, S. Ashraf, D. Wexler, J. Chen, S. H. Ng, S. L. Chou and H. K. Liu, *Carbon*, **46**, 229, (2008).

3 C. Liang, N. J. Dudney, J. Y. Howe, *Chem. Mater*., **21**, 4724, (2009).

4 S.-E. Cheon, K.-S. Ko, J.-H. Cho, S.-W. Kim, E.-Y. Chin and H.-T. Kim, *J. Electrochem. Soc.*, **150**, A800, (2003).

5 Y. V. Mikkhaylik, and J. R. Akridge, *J. Electrochem. Soc.*, **151**, A1969, (2004).

6 X. Ji and L. F. Nazar, *J. Mater. Chem*., **20**, 9821, (2010)

7 H. S. Ryu, H. J. Ahn, K. W. Kim, J. H. Ahn, J. Y. Lee and E. J. Clairns, *J. Power Sources*, **140**, 365, (2005).

8 H. S. Ryu, H. J. Ahn, K. W. Kim, J. H. Ahn, K. K. Cho and T. H. Nam, *Electrochim. Acta*, **52**, 1563, (2006).

9 X. Ji, K. T. Lee, and L. F. Nazar, *Nat. Mater.*, **8**, 500, (2009).

10 C. J. Brinker, Y. Lu, A. Sellinger and H. Fan, *Adv. Mater.*, **11**, 579, (1999).

11 D. Grosso, F. Cagnol, G. J. A. A. Soler-Illia, E. L. Crepaldi, H. Amenitsch, A. Brunet-Bruneau, A. Bourgeois and C. Sanchez, *Adv. Funct. Mater.*, **14**, 309, (2004).

12 H. Yang, A. Kuperman, N. Coombs, S. Mamiche-Afara, G. A. Ozin, *Nature*, **379**, 703, (1996).

13 R. L. Liu, Y. F. Shi, Y. Wan, Y. Meng, F. Q. Zhang; D. Gu, Z. X. Chen, B. Tu, and D. Y. Zhao, *J. Am. Chem. Soc.*, **128**, 11652, (2006).

14 C. Z. Yu, J. Fan, B. Z. Tian, and D. Y. Zhao, *Chem. Mater.*, **16**, 889, (2004).

15 Y. Meng, D. Gu, F. Zhang, Y. Shi, H. Yang, Z. Li, C. Yu, B. Tu and D. Zhao, *Angew. Chem. Int. Ed.*, **44**, 7053, (2004).

16 G. L. Miessler and D. A. Tarr, *Inorganic Chemistry*, Pearson Education, (2008).

17 S. Tanaka, N. Nishiyama, Y. Egashira and K. Ueyama, *Chem. Commun.*, **16**, 2125, (2005).

18 L. Song, D. Feng, H.-J. Lee, C. Wang, Q. Wu, D. Zhao and B. D. Vogt, *J. Phys. Chem. C*, **114**, 9618, (2010).

19 J. Schuster, R. Köhn, A. Keilbach, M. Döblinger, H. Amenitsch and T. Bein, *Chem. Mater.*, **21**, 5754, (2009).

20 D. Feng, Y. Lv, Z. Wu, Y. Dou, L. Han, Z. Sun, Y. Xia, G. Zheng and D. Zhao, *J. Am. Chem. Soc.*, **133**, 15148, (2011).

21 L. Song, D. Feng, N. J. Fredin, K. G. Yager, R. L. Jones, Q. Wu, D. Zhao and B. D. Vogt, *ACS Nano*, **4**, 189, (2010).

22 J. H. Shin and E. J. Cairns, *J. Electrochem. Soc.*, **155**, A368, (2008).

23 E. Peled, Y. Sternberg, A. Gorenshtein and Y. Lavi, *J. Electrochem. Soc.*, **136**, 1621, (1989).

24 Y. Mikhaylik, I. Kovalev, R. Schock, K. Kumaresan, J. Xu and J. Affinito, *ECS Transactions*, **25**, 23, (2010).

25 M.-S. Song, S.-C. Han, H.-S. Kim, J.-H. Kim, K.-T. Kim, Y.-M. Kang, H.-J. Ahn, S. X. Dou and J.-Y. Lee, *J. Electrochem. Soc.*, **151**, A791, (2004).

26 J. Shim, K. A. Striebel and E. J. Cairns, *J. Electrochem. Soc.*, **149**, A1321, (2002).

27 Y. Meng, D. Gu, F. Zhang, Y. Shi, L. Cheng, D. Feng, Z. Wu, Z. Chen, Y. Wan, A. Stein and D. Zhao, *Chem. Mater.*, **18**, 4447, (2006).

28 C. Lai, X. P. Gao, B. Zhang, T. Y. Yan and Z. Zhou, *J. Phys. Chem. C*, **113**, 4712, (2009).

29 B. Zhang, X. Qin, G. R. Li and X. P. Gao, *Energy Enviro. Sci.*, **3**, 1531, (2010).

30 J. L. Wang, J. Yang, J. Y. Xie, and N. Xu, *Adv. Mater.*, **14,** 963, (2002).

31 J. Wang, J. Chen, K. Konstantinov, L. Zhao, S. H. Ng, G. X. Wang, Z. P. Guo, H. K. Liu, *Electrochim. Acta*, **51**, 4634, (2006).

32 X. Ji, S. Evers, R. Black and L. F. Nazar, *Nat. Commun.*, **2,** 325, (2011).

33 L. Cao, T. Man and M. Kruk, *Chem. Mater.*, **21**, 1144, (2009).

34 H. Zhang, J. Sun, D. Ma, G. Weinberg, D. S. Su and X. Bao, *J.Phys. Chem. B*, **110**, 25908, (2006).

35 J. Fan, C. Yu, T. Gao, J. Lei, B. Tian, L. Wang, Q. Luo, B. Tu, W. Zhou and D. Zhao, *Angew. Chem. Int. Ed*., **42**, 3146, (2003).

36 L. Wang, H. Fan, B. Tian, H. Yang, C. yu, B. Tu and D. Zhao, *Microporous Mesoporous Mater*., **67**, 135, (2004).

37 C. T. Kresge, M. E. Leonowicz, W. J. Roth, J. C. Vartuli and J. S. Beck, *Nature*, **359**, 710, (1992).

38 S. Jun, S. Joo, R. Ryoo, M. Kruk, M. Jaroniec, Z. Liu, T. Ohsuna and O. Terasaki, *J. Am. Chem. Soc.*, **122**, 10712, (2000).

39 Y. Wan and D. Zhao, *Chem. Rev.*, **101**, 2821, (2007).

40 J. Fan, C. Yu, J. Lei, Q. Zhang, T. Li, B. Tu, W. Zhou and D. Zhao, *J. Am. Chem. Soc.*, **127**, 10794, (2005).

41 G. He, X. Ji and L. Nazar, *Energy Environ. Sci*., **4**, 2878, (2011).

Chapter 4

1 T.-W. Kim, P.-W. Chung, I. I. Slowing, M. Tsunoda, E. S. Yeung and V. S. Y. Lin, *Nano Lett.*, **8**, 3724, (2008).

2 Y. Yan, F. Zhang, Y. Meng, B. Tu and D. Zhao, *Chem. Commun.*, 2867, (2007).

3 N. Tonanon, W. Intarapanya, W. Tanthapanichakoon, H. Nishihara, S. Mukai and H. Tamon, *J. Porous Mater.*, **15**, 265, (2008).

4 Y. Fang, D. Gu, Y. Zou, Z. Wu, F. Li, R. Che, Y. Deng, B. Tu and D. Zhao, *Angew. Chem. Int. Ed.*, **122**, 8159, (2010).

5 H.-J. Liu, W.-J. Cui, L.-H. Jin, C.-X. Wang and Y.-Y. Xia, *J. Mater. Chem.*, **19**, 3661, (2009).

6 Z. Lei, N. Christov, L. L. Zhang and X. S. Zhao, *J. Mater. Chem.*, **21**, 2274, (2009).

7 R. Liu, Y. Shi, Y. Wan, Y. Meng, F. Zhang, D. Gu, Z. Chen, B. Tu and D. Zhao, *J. Am. Chem. Soc.*, **128**, 11652, (2006).

8 X. Ji, K. T. Lee and L. F. Nazar, *Nat. Mater.*, **8**, 500, (2009).

9 X. Ji, S. Evers, K. T. Lee, L. F. Nazar, *Chem. Commun.*, **46**, 1658, (2010).

10 M.-S. Song, S.-C. Han, H.-S. Kim, J.-H. Kim, K.-T. Kim, Y.-M. Kang, H.-J. Ahn, S. X. Dou and J.-Y. Lee, *J. Electrochem. Soc.*, **151**, A791, (2004).

11 J. Wang, J. Yang, J. Xie and N. Xu, *Adv. Mater.*, **14**, 963, (2002).

12 H. Wang, Y. Yang, Y. Liang, J. T. Robinson, Y. Li, A. Jackson, Y. Cui and H. Dai, *Nano Lett.*, **11**, 2644, (2011).

13 J. Hassoun and B. Scrosati, *Angew. Chem. Int. Ed.*, **49**, 2371, (2010).

14 J. Hassoun and B. Scrosati, *Adv. Mater.*, **22**, 5198, (2010).

15 X. Ji, S. Evers, R. Black and L. F. Nazar, *Nat. Commun.*, **2,** 325, (2011).

16 Y. Mikhaylik, I. Kovaley, R. Schock, K. Kumaresan, J. Xu and J. Affinito, *ECS Transactions*, **25**, 23, (2010).

17 J. Guo, Y. Xu and C. Wang, *Nano Lett*., **11**, 4288, (2011).

18 J. Schuster, G. He, B. Mandlmeier, T. Yim, K. T. Lee, T. Bein and L. F. Nazar, *Angew. Chem. Int. Ed.*, **51**, 3591, (2012).

Chapter 5

1 A. Nytén, A. Abouimrane, M. Armand, T. Gustafsson and J. O. Thomas, *Electrochem. Commun.*, **7**, 156, (2005).

2 M. E. A. Dompablo, M. Armand. J. M. Tarascon and U. Amador, *Electrochem. Commun.*, **8**, 1292, (2006).

3 G. Zhong, Y. Li, P. Yan, Z. Liu, M. Xie and H. Lin, *J. Phys. Chem. C*, **114**, 3693, (2010).

4 C. Lyness, B. Delobel, A. R. Armstrong and P. G. Bruce, *Chem. Commun.*, 4890, (2007).

5 A. R. Armstrong, C. Lyness, M. Ménétrier and P. G. Bruce, *Chem. Mater*., **22**, 1892, (2010).

6 Z. L. Gong, Y. X. Li and Y. Yang, *J. Power Sources*, **174**, 524, (2007).

7 R. L. Liu, Y. F. Shi, Y. Wan, Y. Meng, F. Q. Zhang; D. Gu, Z. X. Chen, B. Tu, and D. Y. Zhao, *J. Am. Chem. Soc.*, **128**, 11652, (2006).

8 M. S. Islam, R. Dominko, C. Masquelier, C. Sirisopanaporn, A. R. Armstrong and P. G. Bruce, *J. Mater. Chem.*, **21**, 9811, (2011).

9 A. R. Armstrong, C. Lyness, M. Ménétrier, P. G. Bruce, *Chem. Mater*., **22**, 1892, (2010).

10 S. Jun, S. H. Joo, R. Ryoo, M. Kruk, M. Jaroniec, Z. Liu, T. Ohsuna and O. Terasaki. *J. Am. Chem. Soc.*, **122**, 10712, (2000).

11 Y. Shi, Y. Wan, R. Zhang and D. Zhao, *Adv. Funct. Mater*., **18**, 2436, (2008).

12 J. Ortiz-Landeros, M. E. Contreras-García, C. Gómez-Yáñez, and H. Pfeiffer, *J. Solid. State. Chem.*, **184**, 1304, (2011).

13 H. G. Yang and H. C. Zeng, *J. Phys. Chem. B*, **108**, 3492, (2004).

14 H. C. Zeng, *Curr. Nanosci*., **3**, 177, (2007).

15 J. Li and H. C. Zeng, *J. Am. Chem. Soc*., **129**, 15839, (2007).

16 B. Liu and H. C. Zeng, *Small*, **1**, 566, (2005).

17 Y. Chang, J. J. Teo and H. C. Zeng, *Langmuir*, **21**, 1074, (2005).

18 J. J. Teo, Y. Chang and H. C. Zeng, *Langmuir*, **22**, 7369, (2006).

19 Y. Li, Z. Gong and Y. Yang, *J. Power Sources*, **174**, 528, (2007).

20 A. R. Armstrong, N. Kuganathan, M. S. Islam and P. G. Bruce, *J. Am. Chem. Soc.*, **133**, 13031, (2011).

21 R. Dominko, M. Bele, A. Kokalj, M. Gaberscek and J. Jamnik, *J. Power Sources*, **174**, 457, (2007).

22 G. He, G. Popov and L. F. Nazar, *Chem. Mater*., submitted.

Chapter 6

1 P. Chen, Z. T. Xiong, J. Z. Luo, J. Y. Lin and K. L. Tan, *Nature*, **420**, 302, (2002).

2 Z. T. Xiong, G. T. Wu, J. Q. Hu and P. Chen, *Adv. Mater.*, **16**, 1522, (2004).

3 F. E. Pinkerton, G. P. Meisner, M. S. Meyer, M. P. Balogh and M. D. Kundrat, *J. Phys. Chem.* ***B***, **109**, 6, (2005).

4 Z. T. Xiong, G. T. Wu, J. Q. Hu and P. Chen, *J. Power Sources*, **159**, 167, (2006).

5 J. Wang, T. Liu, G. Wu, W. Li, Y. Liu, C. M. Araujo, R. H. Scheicher, A. Blomqvist, R. Ahuja, Z. Xiong, P. Yang, M. Gao, H. Pan and P. Chen, *Angew. Chem. Int. Ed.*, **48**, 5828, (2009).

6 H. W. Langmi, S. D. Culligan and G. S. Mcgrady, *Int. J. Hydrogen Energy*, **34**, 8108, (2009).

7 A. Yamada, S. Mori, H. Iyama, R. Kanno and M. Shibata, *J. Ceram. Soc. Jp.*, ***117***, *52*, (2009).

8 W. Kohn and L. Sham, *Phys. Rev.*, **140**, A1133, (1965).

9 G. Kresse and J. Hafner, *Phys. Rev. B*, **49**, 14251, (1994).

10 G. Kresse and J. Furthmüller, *Comput. Mater. Sci.*, **6**, 15, (1996).

11 P. E. Blöchl, *Phys. Rev. B*, **50**, 17953, (1994).

12 G. Kresse and D. Joubert, *Phys. Rev. B*, **59**, 1758, (1999).

13 J. P. Perdew and Y. Wang, *Phys. Rev. B*, **45**, 13244, (1992).

14 J. P. Perdew, J. A. Chevary, S. H. Vosko, K. A. Jackson, M. R. Pederson, D. J. Singh and C. Fiolhais, *Phys. Rev. B*, **46**, 6671, (1992).

15 J. F. Herbst and M. S. Meyer, *J. Alloys. Compd.*, **492**, 65, (2010).

16 R. Niewa, D. Zherebtsov and Z. Hu, *Inorg. Chem.*, **42**, 2538, (2003).

17 K. Kushida, Y. Ichihashi, Y. Suzuki and K. Kuriyama, *Physica B*, **405**, 2305, (2010).

18 R. Juza, E. Anschütz and H. Puff, *Angew. Chem. Int. Ed.*, **71**, 161, (1959).

19 R. Niewa, F. R. Wagner, W. Schnelle, O. Hochrein and R. Kniep, *Inorg. Chem.*, **40**, 5215, (2001).

20 R, Juza, K. Langer and K. V.Benda, *Angew. Chem. Int. Ed.*, **7**, 360, (1968).

21 R. Niewa and F. J. Disalvo, *Chem. Mater.*, **10**, 2733, (1998).

22 R. Niewa, D. Zherebtsov and S. Leoni, *Chem. Eur. J.*, **9**, 4255, (2003).

23 A. Gudat, R. Kniep and A. Abenau, *J. Less-Common Met.*, **161**, 31, (1990).

24 J. L. C. Rowsell, V. Pralong and L. F. Nazar, *J. Am. Chem. Soc.*, **123**, 8598, (2001).

25 M. Nishijima, T. Kagohashi, Y. Takeda, M. Imanishi and O. Yamamoto, *J. Power Sources*, **68**, 510, (1997).

26 R. Niewa, Z. L. Huang, W. Schnelle, Z. Hu and R. Kniep, *Z. Anorg. Allg. Chem.*, **629**, 1778, (2003).

27 R. Niewa, F. J. Disalvo, D. K. Yang, D. B. Zax, H. Luo and W. B. Yelon, *J. Alloys. Compd.*, **266**, 32, (1998).

28 G. He, J. F. Herbst, T. N. Ramesh, F. E. Pinkerton, M. S. Meyer and L. Nazar, *Phys. Chem. Chem. Phys.*, **13**, 8889, (2011).